ANL/RAS 79-8

Final Report on TREAT Tests R4 and R5; Seven-pin, Loss-of-flow Tests with Full-length, Unirradiated FFTF-type Fuel Pins

Prepared by:

B. W. Spencer

With Contributors:

M. A. Grolmes

R. E. Holtz

G. Hoppner

N. A. Kramer

W. F. Murphy

F. J. Testa

April 1979

NOTICE: This informal document contains preliminary information prepared primarily for interim use in fast breeder reactor programs in the U.S. Since it does not constitute a final report, it should be cited as a reference only in special circumstances, such as requirements for regulatory needs.

Reactor Analysis and Safety Division
ARGONNE NATIONAL LABORATORY
9700 S. Cass Avenue
Argonne, Illinois 60439

The facilities of Argonne National Laboratory are owned by the United States Government. Under the terms of a contract (W-31-109-Eng-38) among the U. S. Department of Energy, Argonne Universities Association and The University of Chicago, the University employs the staff and operates the Laboratory in accordance with policies and programs formulated, approved and reviewed by the Association.

MEMBERS OF ARGONNE UNIVERSITIES ASSOCIATION

The University of Arizona
Carnegie-Mellon University
Case Western Reserve University
The University of Chicago
University of Cincinnati
Illinois Institute of Technology
University of Illinois
Indiana University
The University of Iowa
Iowa State University
The University of Kansas
Kansas State University
Loyola University of Chicago
Marquette University
The University of Michigan
Michigan State University
University of Minnesota
University of Missouri
Northwestern University
University of Notre Dame
The Ohio State University
Ohio University
The Pennsylvania State University
Purdue University
Saint Louis University
Southern Illinois University
The University of Texas at Austin
Washington University
Wayne State University
The University of Wisconsin-Madison

NOTICE

This report was prepared as an account of work sponsored by the United States Government. Neither the United States nor the United States Department of Energy, nor any of their employees, nor any of their contractors, subcontractors, or their employees, makes any warranty, express or implied, or assumes any legal liability or responsibility for the accuracy, completeness or usefulness of any information, apparatus, product or process disclosed, or represents that its use would not infringe privately-owned rights. Mention of commercial products, their manufacturers, or their suppliers in this publication does not imply or connote approval or disapproval of the product by Argonne National Laboratory or the U. S. Department of Energy.

ANL/RAS 79-8

Final Report on TREAT Tests R4 and R5; Seven-pin, Loss-of-flow Tests with Full-length, Unirradiated FFTF-type Fuel Pins

Prepared by:

B. W. Spencer

With Contributors:

M. A. Grolmes
R. E. Holtz
G. Hoppner
N. A. Kramer
W. F. Murphy
F. J. Testa

April 1979

NOTICE: This informal document contains preliminary information prepared primarily for interim use in fast breeder reactor programs in the U.S. Since it does not constitute a final report, it should be cited as a reference only in special circumstances, such as requirements for regulatory needs.

Reactor Analysis and Safety Division
ARGONNE NATIONAL LABORATORY
9700 S. Cass Avenue
Argonne, Illinois 60439

ABSTRACT

Two seven-pin loss-of-flow simulation tests have been performed in-pile in support of LMFBR safety analyses. These integral-type tests were executed in the R-series test apparatus at TREAT, designed to provide a prototypic thermal hydraulic flowing sodium system. The test fuel pins were full-length FFTF-type, containing unirradiated UO_2 fuel. In LOF test R4, the sequence was run at constant fuel power well beyond the inception of molten fuel motion; in R5, the sequence was terminated prior to fuel melting to preserve evidence of early molten cladding motion. The tests were consistent with one another, showing the anticipated sequence of sodium boiling, channel voiding, cladding dryout, cladding failures, molten cladding motion and, for R4, fuel melting and motion. Thin planar upper cladding blockages were formed as were thick lower blockages, effectively plugging the bundle at the extremities of the active fuel region. There was no sodium reentry, and there were no significant pressurization events. Comparison of test results with SAS code calculations revealed differences associated with early voiding behavior, release of noncondensible fuel pin plenum gas, and the thickness and location of the upper blockage. In general, however, the overall sequence of significant events observed in R4 and R5 is in quite good agreement with SAS code analysis of the test conditions. Features of SAS related to overall voiding, cladding motion, and to some extent fuel motion have been substantiated in these results.

TABLE OF CONTENTS

TABLE OF CONTENTS (cont'd)

TABLE OF CONTENTS (cont'd)

List of Figures

List of Figures (Cont'd)

List of Figures (cont'd)

List of Figures (Cont'd

List of Figures (Cont'd)

List of Figures (Cont'd)

List of Figures (Cont'd)

List of Figures (Cont'd)

LIST OF TABLES

1.0 INTRODUCTION

In recent years, the development of analytical models for describing a mechanistic sequence of events related to LMFBR hypothetical accident conditions has progressed to the point where large-scale integrated in-reactor tests are needed to provide verification of model capabilities. Specifically, for the LMFBR unprotected-pump-failure analysis, the progression of the accident sequence from the onset of sodium boiling involves connected phenomena of sodium voiding, fission-gas release, clad melting and relocation, and fuel motion. The connection between the various phenomena becomes important in model development and code verification. The R-series tests, together with complementing in- and out-of-pile testing programs, provide a data base with which the validity of code predictions may be assessed. The overall objective of the R-series LOF tests has been to support development of the SAS accident analysis code[1] in the areas of the coolant dynamics and molten cladding behavior for the initiating phase of the hypothetical LOF accident under FTR-type conditions.

The R-series test apparatus was designed specifically to perform these tests at the TREAT reactor facility. The apparatus combines the unique capabilities of accomodating full-length LMFBR pins together with providing the essential hydraulic and thermal features of LMFBR operation, features which are necessary for performing meaningful sodium voiding and cladding relocation tests. The experiment equipment and procedures were checked out during the single-pin R3 test. Shortly afterward, the R4 and R5 7-pin tests were performed back-to-back. Three additional 7-pin LOF tests were performed at later times, completing the LOF-supportive task. Additional background information, the R-series test approach, and brief discussion of related LOF tests are presented in the remainder of this section. Section 2 presents details of the experiment configuration, instrumentation, operation, and test conditions. A summary of the test outcomes as well as detailed descriptions of test data are given in Sect. 3; a complete set of instrumentation data has been included in the appendix for reference. Results of the posttest metalographic examinations and the comparisons with SAS code predictions are presented in Sects. 4 and 5, respectively, followed by an overall interpretation of the test sequence and a summary of test findings.

1.1 Test Objectives

The overall objective of the R-series tests was to examine the integrated sequence of events resulting from sustained full power operation of test fuel pins accompanied by a controlled reduction of the coolant driving pressure. This is equivalent in the reactor case to the hypothetical loss of power to the coolant pumps with simultaneous failure to scram.

In both the R4 and R5 tests, the basic objective was to obtain experimental information about specific phenomena and about the interrelation of the various phenomena during the integrated LOF sequence for comparison with SAS accident analysis code predictions. Specific phenomena of interest included incipient boiling superheat, the inception and progression of channel voiding, cladding melting and motion under the influence of sodium vapor streaming, cladding relocation and freezing resulting in channel blockages, the reentry of sodium into the region of molten steel and fuel, and energetics of any reentry interactions. The objective of R4 was to allow the test to proceed as far into the destructive stage of the sequence as the TREAT limitation on integrated power would permit, predicted by SAS to result in substantial fuel melting and relocation. The objective of R5 was to terminate earlier in the sequence preserving evidence of early cladding relocation.

1.2 Approach

The R-series approach was to first to create an in-reactor test apparatus which would meet the technical criteria for performing meaningful tests of coolant voiding and molten cladding motion. Sodium boiling and sodium vapor streaming could be shown to effect clad failure, gas release, and clad motion. Clad motion could be shown to influence fuel melting and fuel relocation. From a thermohydraulic argument, these effects can be related to length of heated and unheated zone, flow rate at time of boiling, and temperature distribution in unheated parts of the reactor, or test section. Therefore, it was considered necessary to the design of such an integrated test to accomodate full-length LMFBR fuel pins. This alone was a major step in providing improved thermal hydraulic simulation in terms of heat flux, temperature profiles, and system hydraulic resistance. In addition, a once-through two-tank system was designed into the R-series test vehicle, providing improved simulation of the imposed pressure boundary conditions for LOF tests over the loop-type test apparatus. The R-series gas-driven approach inherently provides an effectively infinite bypass-flow simulation, assuring that the prescribed boundary conditions would not be altered by channel voiding of test section pressurization events. These considerations led to development of the R-series test apparatus described in Sect. 2

Although the first test in the series, the R3 proof test, was performed with a single pin, the basic test section was selected to contain seven pins. Heat losses from the single pin precluded meaningful extended tests of this type. From a TREAT reactivity standpoint, the 7-pin bundle was the largest capable of undergoing the integral, extended meltdown tests planned. The test approach is illustrated in Fig. 1. The behavior of the full-size 217-pin subassembly, represented by a one-dimensional, single-channel model in SAS, was to be represented experimentally using a 7-pin test bundle. Consistent with the SAS single-channel thermal-hydraulic model, the 7-pin test section was designed to provide nominally coherent temperature conditions, representative of the central region of the subassembly. Moreover, conditions were selected to represent an FTR high power-to-flow subassembly (initial core operation, beginning of life fuel cycle), first experiencing disruption during the hypothetical accident. Four measures were taken to provide nominally one-dimensional bundle temperature conditions: 1) The pin-to-pin enrichment was varied to give nominally equal power generation in all seven pins, 2) the outer-row wire wraps were reduced in diameter to lessen overcooling at the walls, 3) the hex-can flats had filler rods also to lessen the outer over-cooling, and 4) the hex can itself was made as thin as practical (20-mil) to minimize heat capacity effects during the transient undercooling.

The approach to conducting the tests was to first establish quasi-steady hydraulic and thermal conditions, representative of reactor conditions, during a preheat stage of the TREAT experiment transient. During this early planned stage of the transient, the sodium velocity in the pin bundle was about 7.2 m/s (23 fps), test fuel power generation was nominally 30 kW/pin, the sodium inlet temperature was about 316°C (600°F), the inlet plenum pressure was about 8.5 atm, and the upper plenum pressure was about 1.3 atm. The flow coastdown

Fig. 1 SAS Single-Channel Representation of Small and Large Fuel Pin Bundles.

	SAS	*R-SERIES	SUBASSEMBLY
Configuration	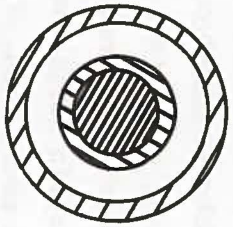	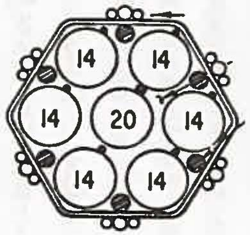	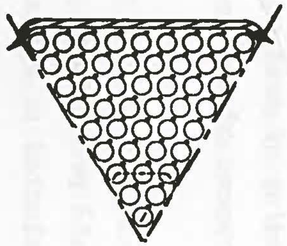
Size	1-Channel	7-Pin	217-Pin
Coolant radial temperature variation at boiling inception	None	50°C	250°C
Pin power loss at fuel incipient melting	Variable	$\lesssim$70%	$\lesssim$5%

* Numbers in pins show UO_2 enrichments.

was programmed to be initially more rapid than in FTR to conserve TREAT run time, but to level off and enter sodium boiling at about the same rate of flow decay. This is illustrated in Fig. 2 which shows how the FTR pump coastdown requiring about 14 s to boiling inception was reduced to about 6 s for the R-series tests. The tests were eventually terminated by TREAT reactor scram.

1.3 Relationship to Other Tests

The R-series apparatus differs from the present Mark-II sodium in-pile test vehicle[2] in its ability to accommodate full-length fuel and provide full-scale hydraulic resistance through all stages of a simulated flow coastdown. However, the present Mark-II test vehicle can accommodate preirradiated or mixed oxide fuel while the R-series is limited to fresh fuel. The Static Autoclave test capsule used for S-series TREAT Experiments[3] is unsuited for loss-of-flow simulation tests by design. The R-series test vehicle is, however, closely related to the out-of-pile OPERA test facility[4] in capability for loss-of-flow simulation.

The relationship of LOF Tests R4 and R5 to other in-reactor and out-of-reactor tests is summarized in Table 1. The out-of-reactor OPERA 7-pin test[4] focused on details of sodium boiling and voiding during the pump coastdown. The voiding process could be characterized in detail using voltage tap void detector techniques. This test utilized electric heaters to simulate the fuel pins; no information was obtained past the time of heater failures which occurred prior to cladding melting. The L-series LOF tests, performed in the Mark-II loop, have contributed principally to understanding of fuel melting, fission gas release, and molten fuel motion aspects of the accident sequence. These tests used considerably shorter pins than the FTR-type used in the R-series tests, and the loop had only about one-tenth the prototypic system hydraulic resistance. Although these tests were not intended to key on coolant and cladding behavior upper cladding blockages were found to varying degrees in L2, L3, and L4[5].

The complete program of R-series LOF tests, R3 through R8, is listed in Tables 1 and 2. Test R3[6] was a single-pin proof test which led into the series of seven-pin tests. Test R6[7] reproduced R4 as closely as possible in order to

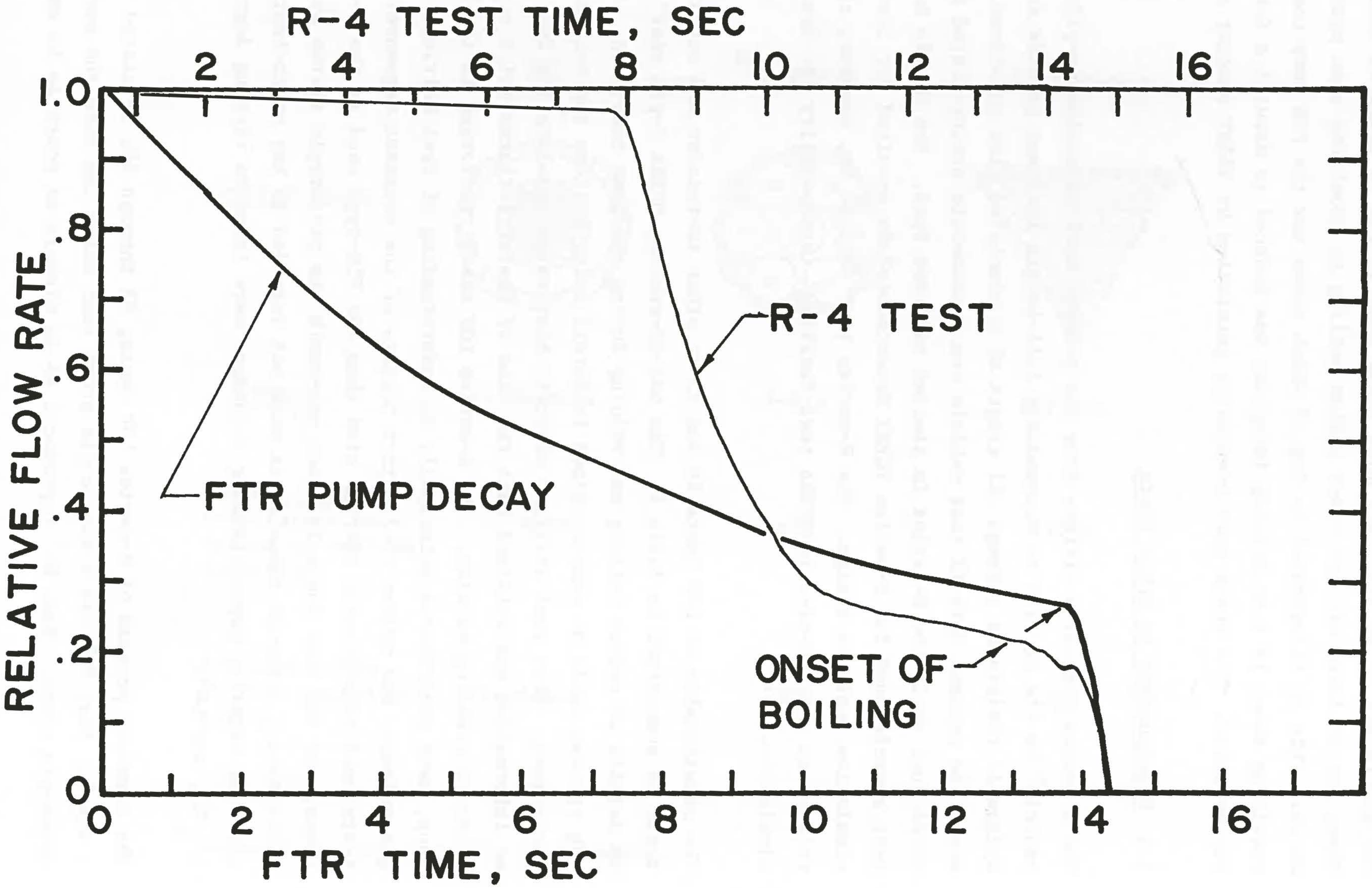

Fig. 2 Illustration of Experimental Approach to Simulate FTR Pump Coastdown Accident.

Table 1. In-reactor and Out-of-reactor Test Relating to Initiating Phase of LMFBR Loss-of-flow Accident

Test	Type	No. Pins	Fuel	Plenum Volume	Plenum Gas and Pressure	Contribution
OPERA	Out-of-Pile	7	Electric-resistance heater rods simulating fuel elements	Similar to FTR-type fuel element; contained 1 atm Xe @ 75°F; for thermal and hydraulic simulation only; no gas communication with cladding rupture location		Provided detailed description of coolant boiling and voiding for uniform axial power generation; cladding motion not investigated because of heater rod limitations.
L2	TREAT (Mark-II loop)	7	Fresh UO_2; 30-7/8" pin length, 13-1/2" active fuel region	0.15 $in.^3$	He; 1 atm @ 67°F	First TREAT LOF test; proof test relating to coolant, cladding, and fuel motion (constant power) within confines of Mark-II apparatus.
L3	TREAT (Mark-II loop)	7	PNL-17 low power irradiated to 3.5% nominal burnup; 30-7/8" length	0.32 $in.^3$	He fill gas plus fission gas to ∿75 psia @ 67°F	Comparison of fuel dynamic behavior for low power irradiated fuel (constant power).
L4	TREAT (Mark-II loop)	7	NUMEC-F high power irradiated to 4.3% nominal burnup; 30-7/8" length	0.34 $in.^3$	He fill gas plus fission gas to ∿165 psia @ 67°F	Comparison of fuel dynamic behavior for high power irradiated fuel (constant power).
L5	TREAT (Mark-IIC stretch loop)	3	HEDL-59 low power irradiated to 8% nominal burnup; 60 in. length	0.27 $in.^3$	Xe; 1 atm @ 75°F	Comparison of fuel dynamic behavior for low power irradiated, high burnup fuel for near full-length fuel column (34 in.) with power spike at initiation of cladding melting.
R3	TREAT (R-apparatus)	1	Fresh UO_2; full size FTR-type fuel element, 93.4 in. long	1.14 $in.^3$	He; 1 atm @ 75°F	R-series proof test.
R4,R6	TREAT (R-apparatus)	7	Fresh UO_2; full size FTR-type fuel element, 93.4 in. long	1.14 $in.^3$	He; 1 atm @ 75°F	R4-first in-reactor verification of SAS voiding model. Coolant and cladding behavior for high power-to-flow fuel in FTR-simulating thermal and hydraulic environment; varying degrees of fuel melting at constant power.
R5	TREAT (R-apparatus)	7	Fresh UO_2; full size FTR-type fuel element, 93.4 in. long	1.14 $in.^3$	He; 1 atm @ 75°F	Same as R4 except power terminated early to examine initial cladding motion caused by vapor streaming; no fuel melting.
R7	TREAT (R-apparatus)	7	Fresh UO_2; full size FTR-type fuel element, 93.4 in. long	1.14 $in.^3$	He; 1 atm @ 75°F	Same as R4 except with power pulse at inception of fuel motion simulating reactivity effect; examine vapor-driven fuel dispersal.
R8	TREAT (R-apparatus)	7	Fresh UO_2; full size FTR-type fuel element, 93.4 in. long	1.14 $in.^3$	4 pins unpressurized; same as R4; 3 pins pressurized with Xe to 210 psia @ 75°F (585 psia @ 1040°F)	Examine influence of pressurized plenum gas release from initial coherent pin failures on established accident sequence; significance relates to existence of flow channel blockages potentially constraining subsequent fuel dispersal.

Accident.

TABLE 2

Summary of TREAT/R-series Tests Performed in Support of FTR TUC Accident Analysis

Test	No. Pins	Plenum Gas (STP)	Test Fuel Power/Termination	Purpose
R3	1	He at 1 atm	10kw/ft flattop; 10.5 s after FR	R-series proof test
R4	7	He at 1 atm	10kw/ft flattop; 10.1 s after FR	Reference test: integrated sequence at nominal power
R5	7	He at 1 atm	10kw/ft flattop; 4.4 s after FR	Early termination, cladding relocation test
R6	7	He at 1 atm	10kw/ft flattop; 8.2 s after FR	Hodoscope assessment of fresh UO_2 slumping
R7	7	He at 1 atm	10kw/ft flattop; 6.2 s after FR, 15x power burst	Vapor-driven fuel dispersal in presence of upper and lower cladding blockages
R8	7	3-Xe at 14.2 atm 4-Xe at 1 atm	10kw/ft flattop; 7.1 s after FR	Effect of pressurized plenum-gas release on coolant voiding and cladding relocation

obtain hodoscope fuel-motion data. The R7 test[8] was also the same as R4 except that a power spike was initiated at incipient fuel slumping, simulating the slumping reactivity effect as calculated by SAS. This test produced a vapor-driven dispersal of molten fuel which was prevented from leaving the core region by the previously-formed upper and lower cladding blockages. Test R8[9] was also similar to R4 except that three of the test fuel pins had been pressurized to examine the effect on the accident sequence of release of the pressurized plenum gas upon cladding failures. The channel pressurization caused accelerated sodium voiding and pin dryout. At incipient cladding motion there was no sodium vapor streaming, and the planar upper blockage of the type found in R4 and R5 was not formed.

2.0 EXPERIMENT EQUIPMENT AND OPERATION

2.1 R-series Test Apparatus

The R-series test apparatus, Figs. 3 through 7, was designed for use in TREAT to provide a flowing-sodium system capable of providing prototypic thermal and hydraulic conditions for performing tests of hypothetical LMFBR whole-core accidents[10]. It contains the essential features of the current design LMFBR core including high pressure inlet plenum, inlet flow orificing, fuel bundle comprised of full-length FTR fuel pins, and an upper plenum having a sodium free surface and inert cover gas. The interconnecting piping routes through the TREAT core in a U-bend such that the active fuel region of the test fuel pins is approximately centered in the TREAT core with upward-directed sodium flow. Sodium flow was driven through the apparatus by differential gas pressure. This provides prototypic sodium velocity through the 7-pin test section while effectively simulating an infinite bypass flow. The apparatus inlet and outlet inertial lengths closely matched the corresponding subassembly parameters, as was the case for the axial pressure distribution. Hence, the combination of matched sodium velocity, infinite bypass ratio, matched inertial lengths, and matched system pressures provided simulation of dynamic as well as static system hydraulic behavior.

The entire system was heated to the desired sodium inlet temperature of 316°C (600°F), based upon FFTF planned initial core operation. The 7-pin test section, Fig. 8, was designed to minimize radial noncoherence. This was accomplished by grading the pin enrichments to give nominally uniform power generation (20% enriched center pin, 14% enriched edge pins), and by minimizing overcooling at the wraps on the outer pins, and by using filter rods on the inside flats of the hexagonal fuel holder). With these design provisions the test fuel bundle resembled the central region of an LMFBR high power-to-flow subassembly, minimizing the effects of both radial power skewing and radial temperature variation. Details of the experiment apparatus, operating charcteristics, and test procedures are presented in the following sections.

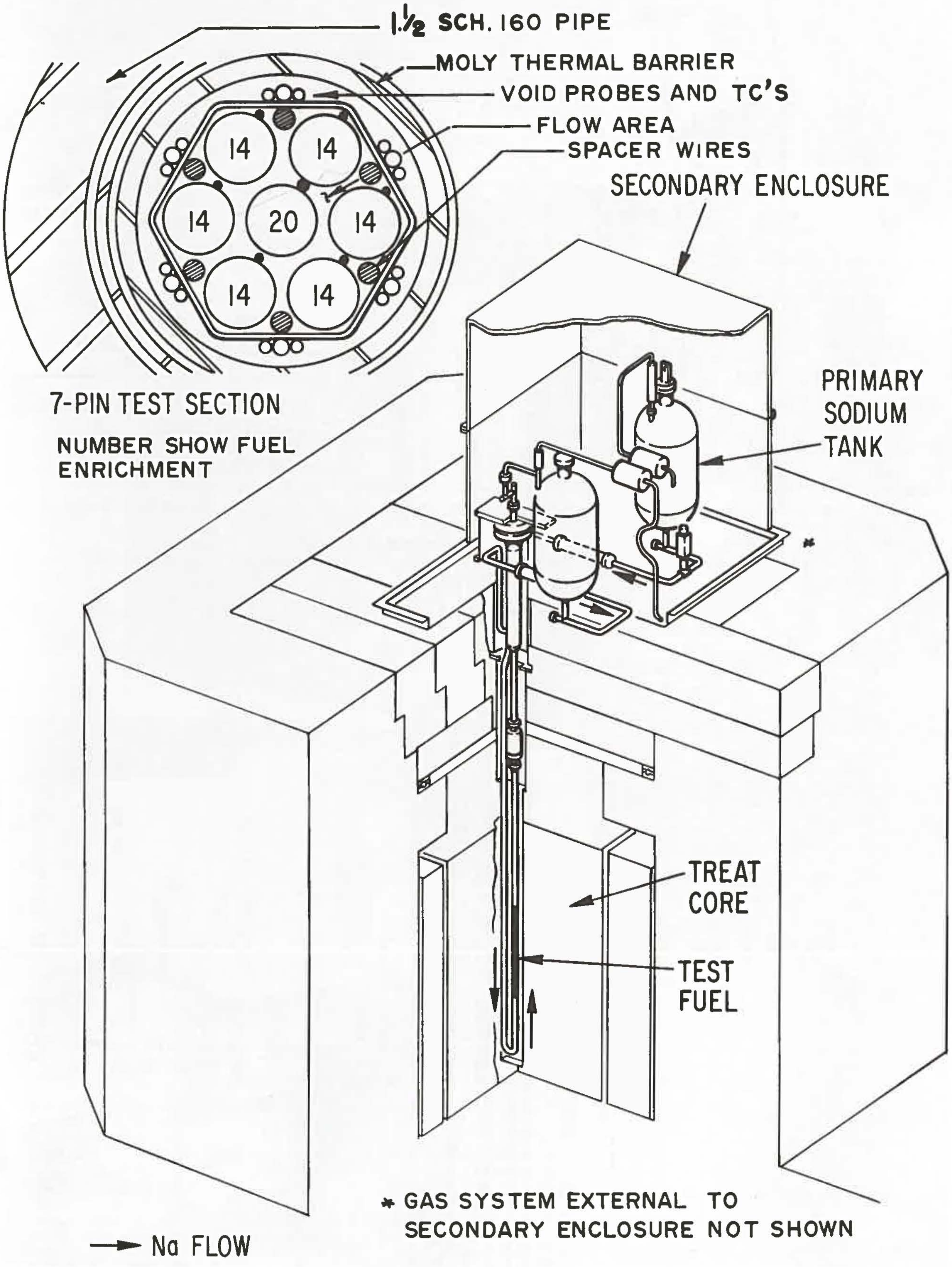

Fig. 3 The R-Series Test Apparatus.

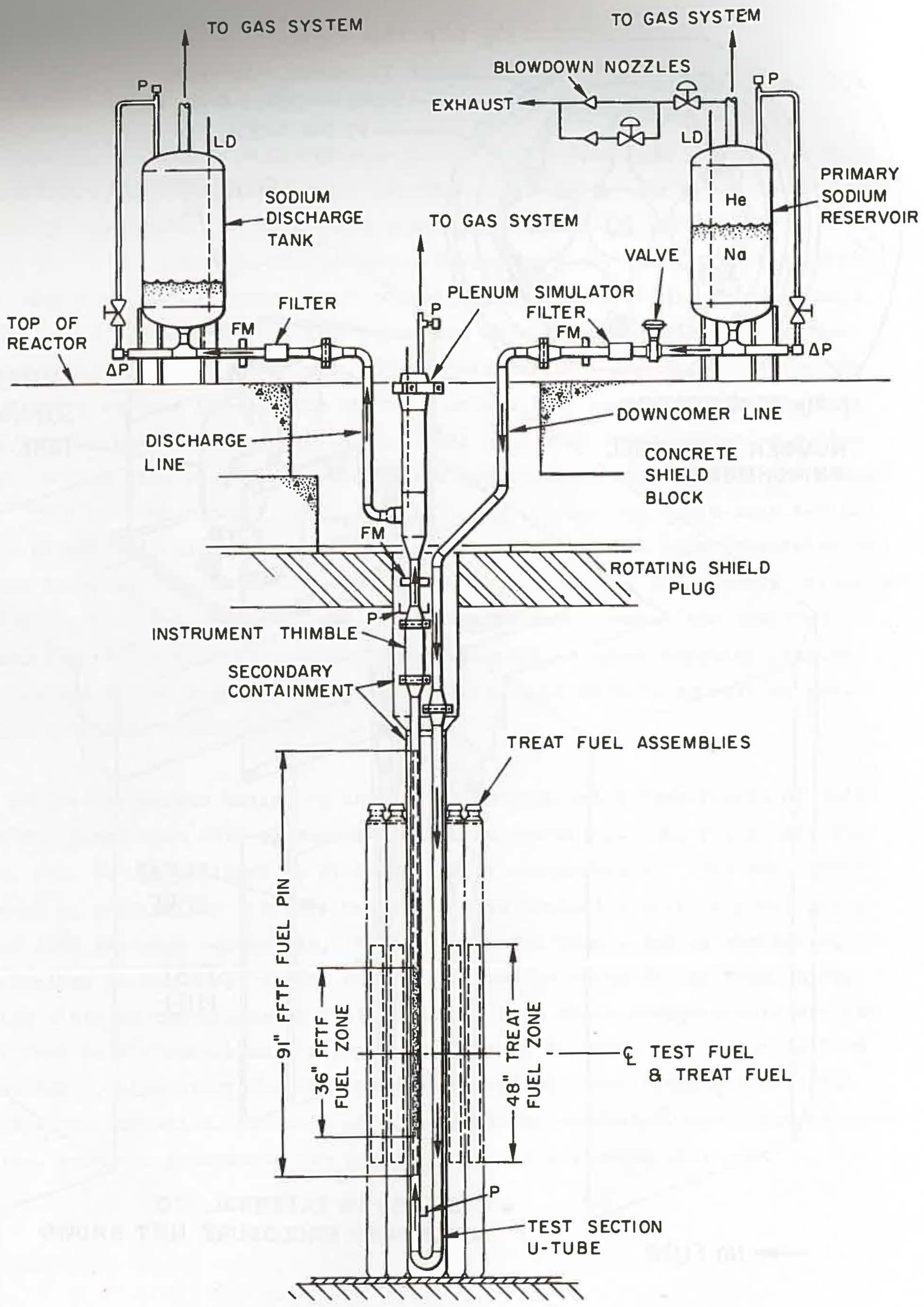

Fig. 4 Illustration of R-Series Apparatus in TREAT.

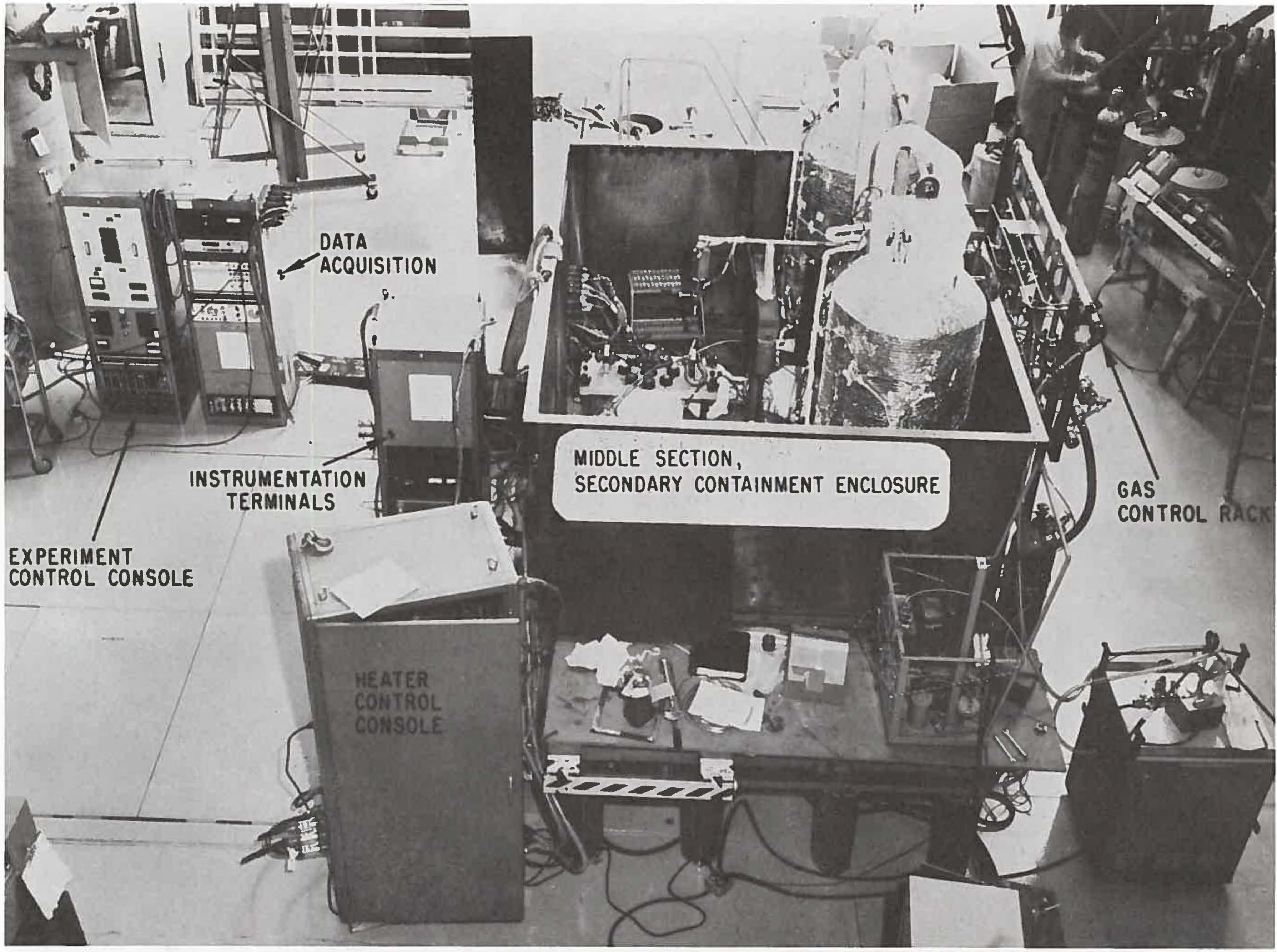

Fig. 5 Photo of R-Series Equipment During Floor Checkout at TREAT.

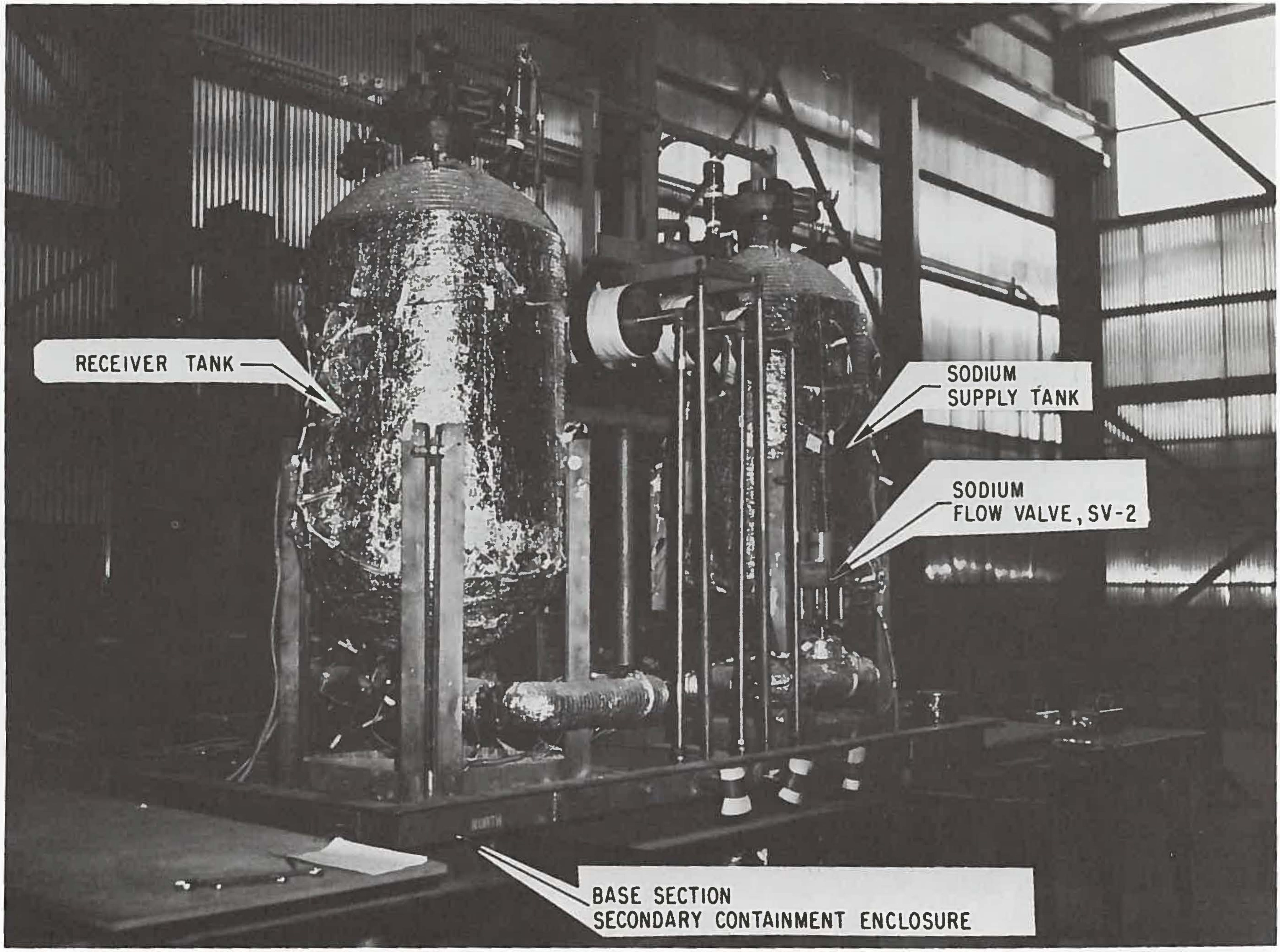

Fig. 6 R-Series Sodium Tanks.

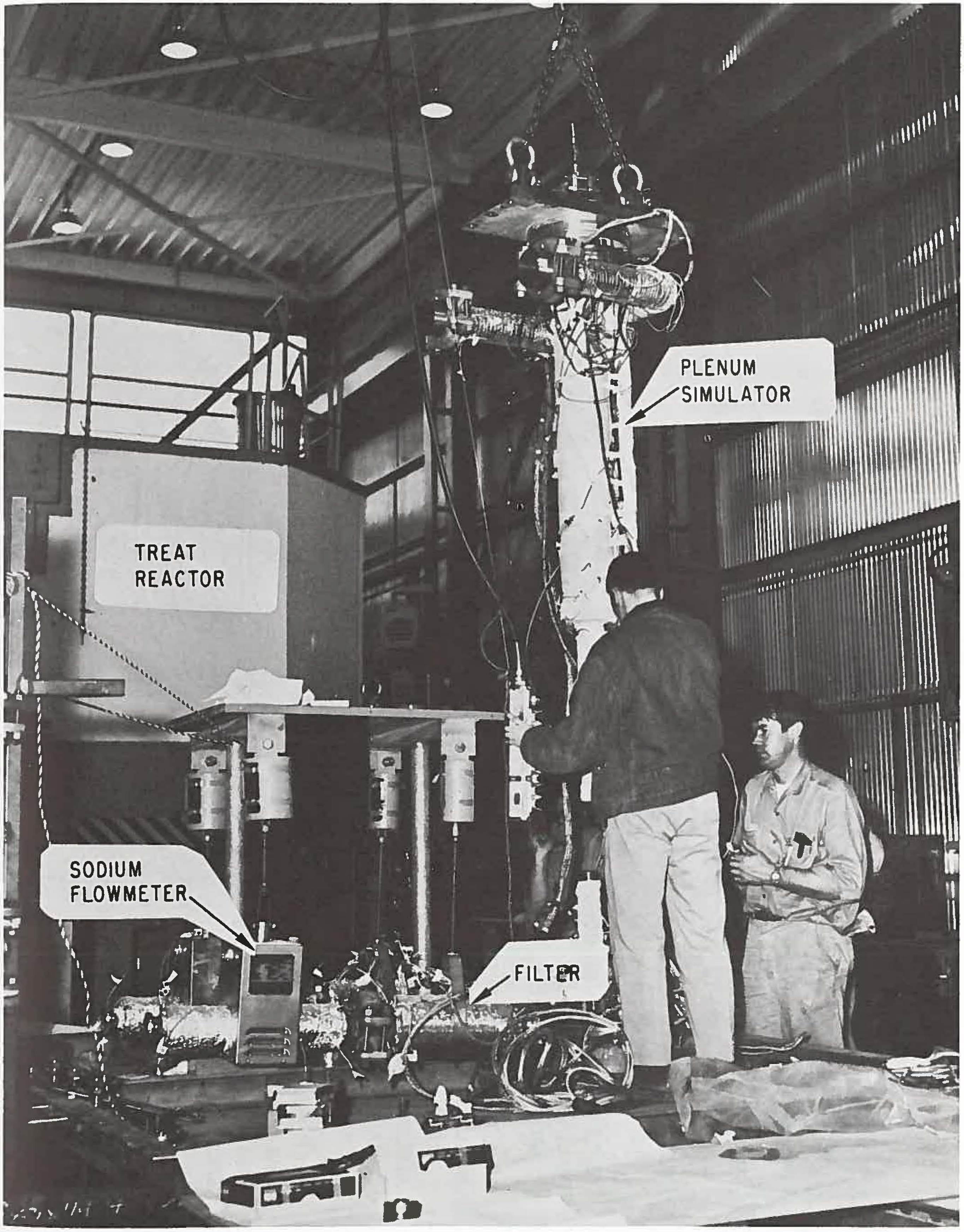

Fig. 7 Components of R-Series Apparatus During Assembly.

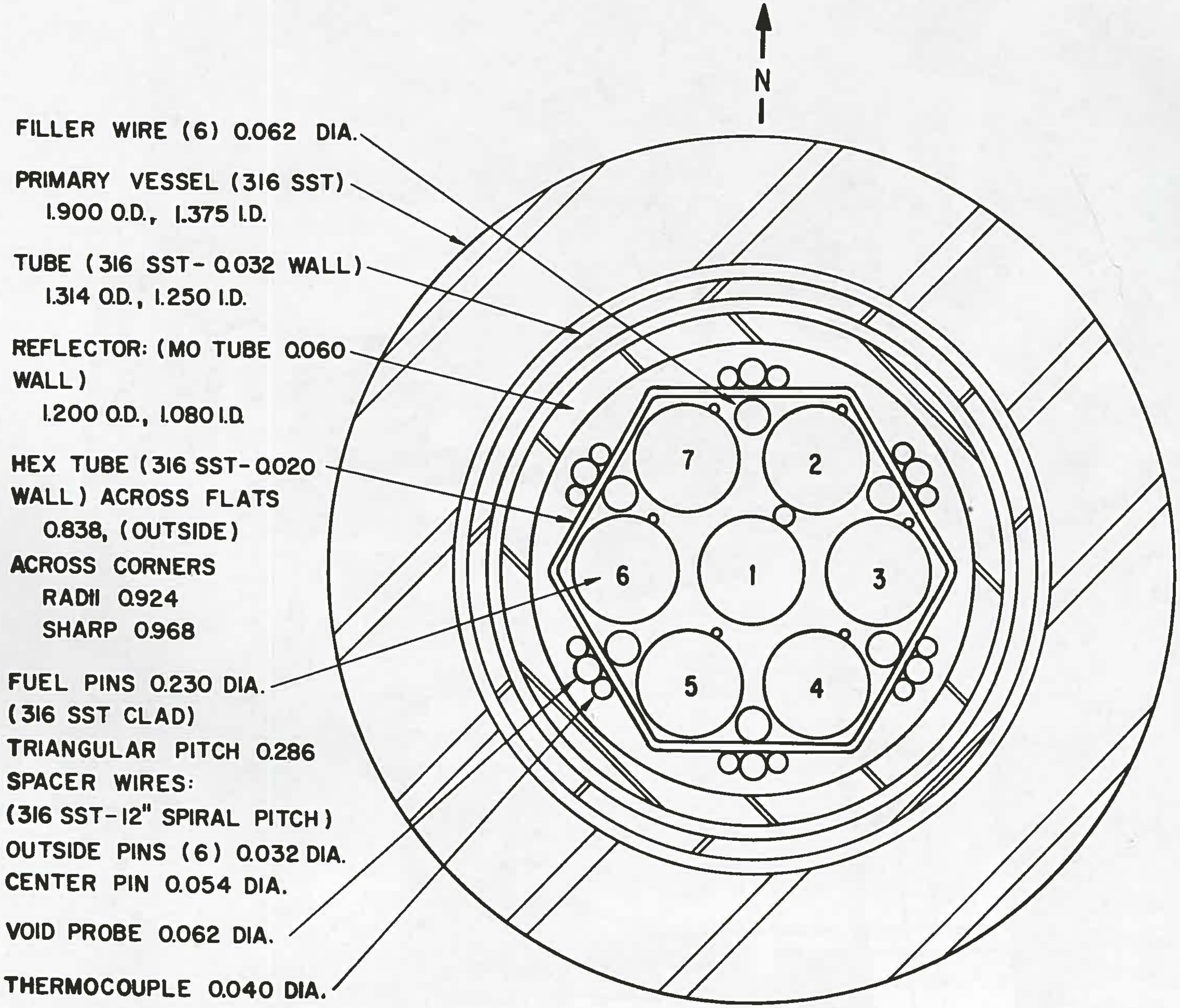

Fig. 8 Plan View of R-Series 7-pin Test Section.

2.2 Test Section

The R-series 7-pin test section is shown in Figs. 8 and 9. The seven FTR-type fuel pins were contained inside a thin-walled hexagonal flow tube fabricated from type 316 stainless steel with wall thickness of 0.51 mm (0.020 in.). A 1.57-mm (0.062-in.) diameter filler rod was spot welded to each of the inner hex flats, decreasing the flow area and decreasing the hydraulic diameter in these edge subchannels. The hex flow tube formed the inside boundary of a gas cavity through which instrumentation leads were routed. The outer boundary of the gas space was the 0.81-mm (0.032-in.) type 316 stainless steel dewar tube. A bellows was provided at the lower end of the assembly, connecting the hex tube to the dewar tube, which permitted about 3 cm of differential axial thermal expansion. The elevation of the active fuel midplane was centered on the TREAT core midplane at thermal conditions encountered during the quasi-steady stage of test operation (immediately prior to entering the transient undercooling stage). A 1.52-mm (0.060-in.) wall molybdenum tube was placed in the gas cavity between the hex flow tube and dewar tube to serve as a meltthrough barrier, preventing molten fuel from contacting the outer primary vessel. The entire 7-pin test section was placed inside 1-1/2 in. schedule 160 type 316 stainless steel pipe which served as the primary system containment vessel. The primary vessel and the dewar tube were connected at the instrument thimble; the gap between the two was filled with sodium as a consequence of filling the system under vacuum. The instrument thimble connects the top of the test section assembly with the upper plenum simulator. Test section instrumentation penetrated the primary containment at the instrument thimble and atop the plenum simulator.

The seven fuel pins were held inside the hex flow tube by a locking assembly located at the bottom of the hex, directly downstream from the bellows assembly. This formed the inlet to the pin bundle region of the test section. There was no restraint at the top ends of the pins. Inlet flow restriction was provided by a 8.38-mm (0.33-in.) diameter by 181-mm (7.12-in.) long nozzle located on the upstream side of the inlet bellows, on the opposite side of the U-bend. This flow restrictor provided the inlet pressure drop required to simulate the zone orificing ΔP at the entrance to the LMFBR subassembly.

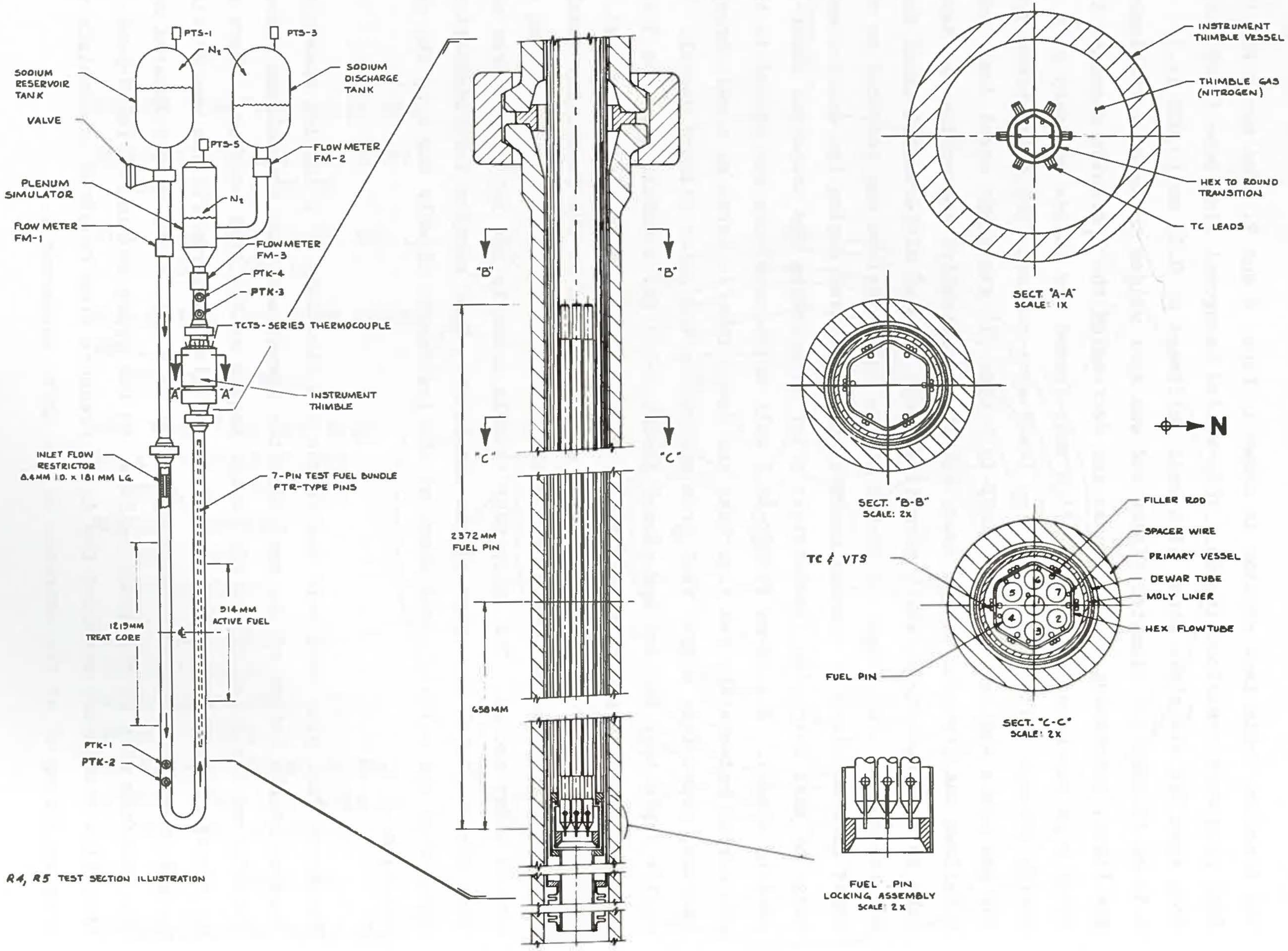

Fig. 9 Illustration of R-Series 7-pin Test Train.

Heat sinks were located on the outside of the primary vessel, covering the bottom region of the fuel pins and downward to the U-bend. These 11.4-mm-thick stainless steel heat sinks were a safety precaution to protect the primary vessel from excessively high temperature in the case of molten fuel compaction inside the test assembly.

2.3 Test Fuel Pins

The identification of the R4 and R5 test fuel pins is given in Table 3. These pins were full-size FTR-type containing fresh UO_2 fuel; the pin configuration is illustrated in Fig. 10. The enrichments were 20% for the center pin and 14% for the edge pins; the wire wrap diameters were 1.37 mm (0.054 in.) for the center pin and 0.81 mm (0.032 in.) for the edge pins. The wire wrap pitch was 30.2 cm (11.9 in.). All pins were nominally unpressurized; that is, they were filled with helium gas to 1 atm pressure at 24°C. All the test fuel pins were fabricated and filled with gas by the Hanford Engineering Development Laboratory, Richland, WA. Details of the pin design parameters are given in Appendix A.

2.4 Hydraulic Performance

The hydraulic performance of the loop with the 7-pin test fuel bundle was assessed prior to both tests. The overall pressure drop at 316°C is shown versus sodium flow rate in Fig. 11. The flow data are well represented by:

$$\dot{m}(\text{lbm/sec}) = 0.195 \sqrt{\Delta P}\ (\text{psid}).$$

The coefficient of 0.195 was consistent to within 2% for tests R4 through R8, indicating an excellent consistency in hydraulic behavior for all the 7-pin LOF tests.

The pressure drop distribution through the loop has been evaluated from:

$$\Delta P = \frac{10^{-7}\ \dot{m}^2}{2\rho\ A_r^2} \sum_i \left(\frac{A_r}{A_i}\right)^2 (k + f\ \ell/d)_i\ ,$$

where

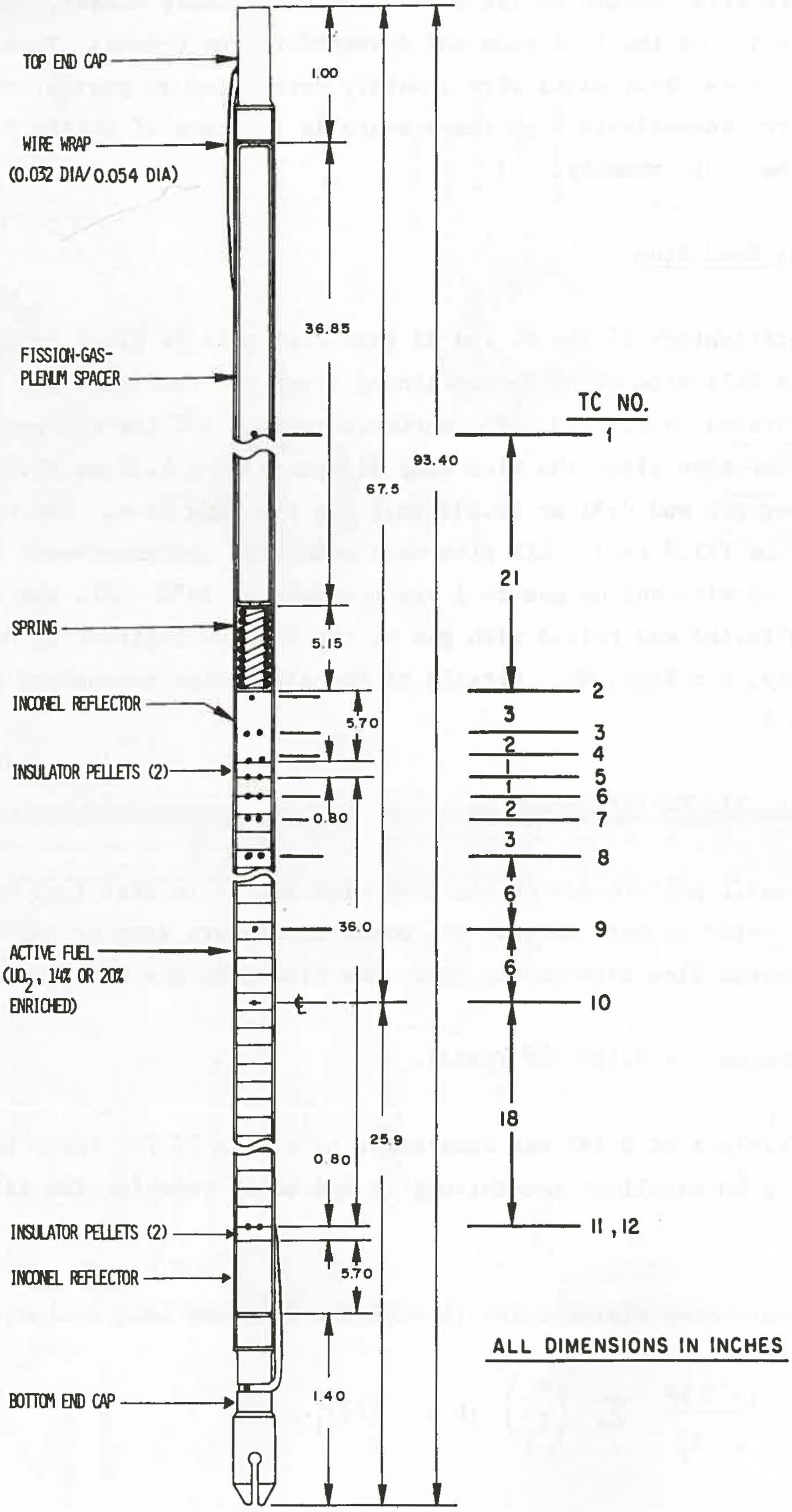

Fig. 10 FTR-type Fuel Pin used in R-Series Tests; Also Shows Locations of Test Section TC's for R4 and R5.

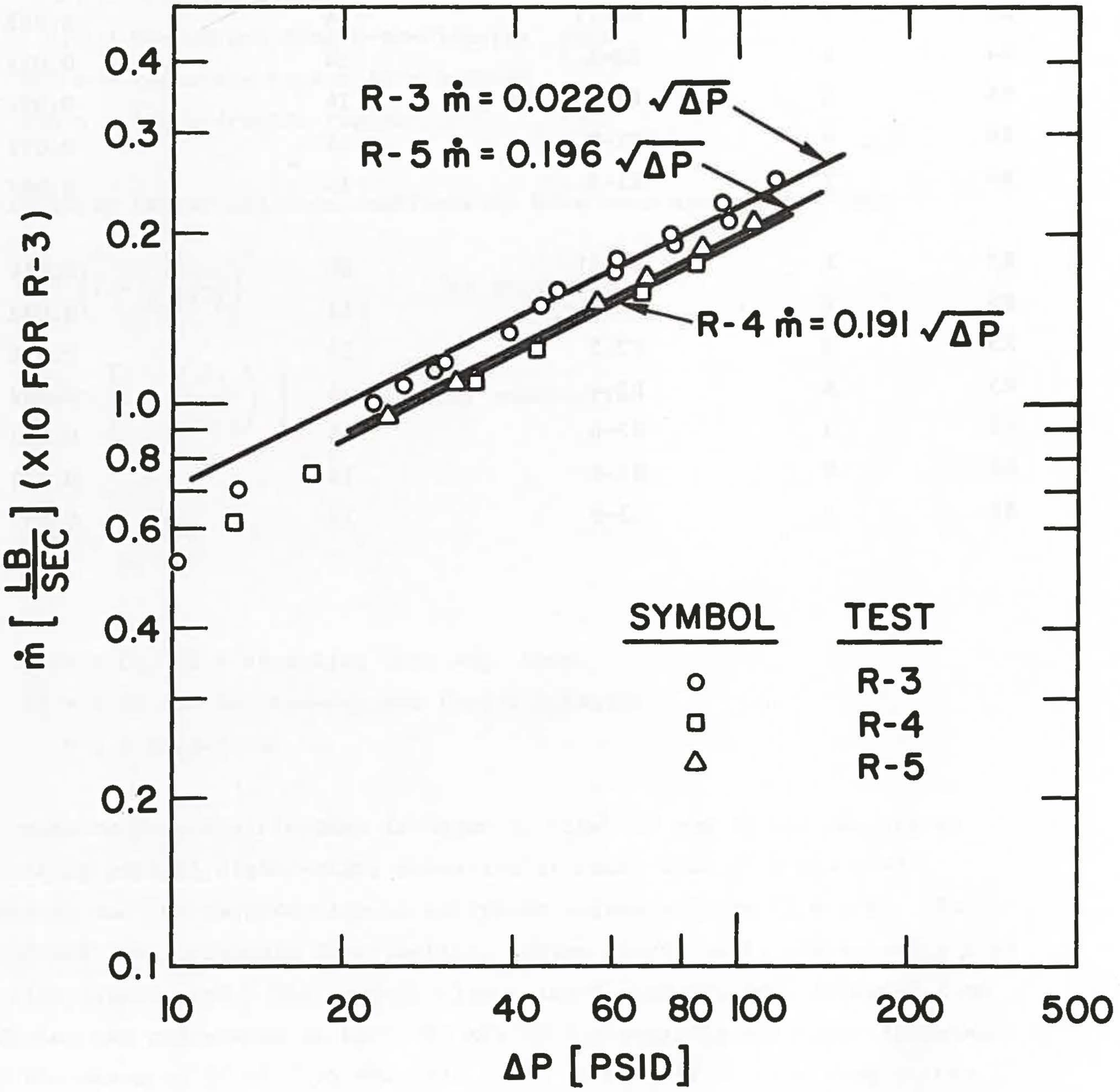

Fig. 11 System Steady-State Hydraulic Performance; T = 316°C.

Table 3. Test Fuel Pin Identifications for R4 and R5

Test	Pin No.	Serial No.	Enrichment (%)	Wire Wrap (in.)
R4	1	R1-1	20	0.054
R4	2	R2-2	14	0.032
R4	3	R1-11	14	0.032
R4	4	R2-1	14	0.032
R4	5	R1-6	14	0.032
R4	6	R1-9	14	0.032
R4	7	R1-5	14	0.032
R5	1	R3-21	20	0.054
R5	2	R2-3	14	0.032
R5	3	R2-5	14	0.032
R5	4	R2-4	14	0.032
R5	5	R2-6	14	0.032
R5	6	R2-8	14	0.032
R5	7	R3-9	14	0.032

ΔP = flow pressure drop, MPa

$\dot{m}$ = sodium mass flow rate, g/s

ρ = sodium density, g/cm^3

A = flow area, cm^2

k = loss coefficient (expansion, contraction, etc.)

f = friction factor

ℓ/d = equivalent length-to-diameter ratio

sub r = reference region (pin bundle)

sub i = ith hydraulic region

The friction factor and loss coefficients have been determined from:

$$k = \left(1 - \frac{A_i}{A_i + 1}\right)^2 \qquad \text{for expansion}$$

$$k = C_1\left[1 - \left(\frac{A_i}{A_{i-1}}\right)^2\right] \qquad \text{for contraction}$$

and

$$f = C_2 \frac{0.316}{Re^{0.25}}$$

where

$0.04 \leq C_1 \leq 0.4$ depending upon edge shape

C_2 = 1.05 in the wire-wrapped fuel pin region

= 1.0 elsewhere.

The pressure drop distribution is shown in Figs. 12 and 13 for conditions reflecting nominal steady-state operation at rated flow (7.3 m/s bundle velocity) and for reduced flow at incipient sodium voiding (2.0 m/s). The calculated total pressure distribution, sodium static head, and velocity head are also illustrated. The overall flow-related pressure drop at rated flow condition was calculated to be 0.785 MPa (113.8 psi), in excellent agreement with the measured ΔP of 0.79 MPa (115 psi). About 31% of this drop occurs across the inlet orifice and about 66% across the full-length, wire-wrapped fuel region. In the FTR subassembly, the overall flow pressure drop is about 0.75 MPa (109 psi) of which about 52% occurs at the inlet and about 40% occurs across the fuel region. The difference reflects the smaller hydraulic diameter

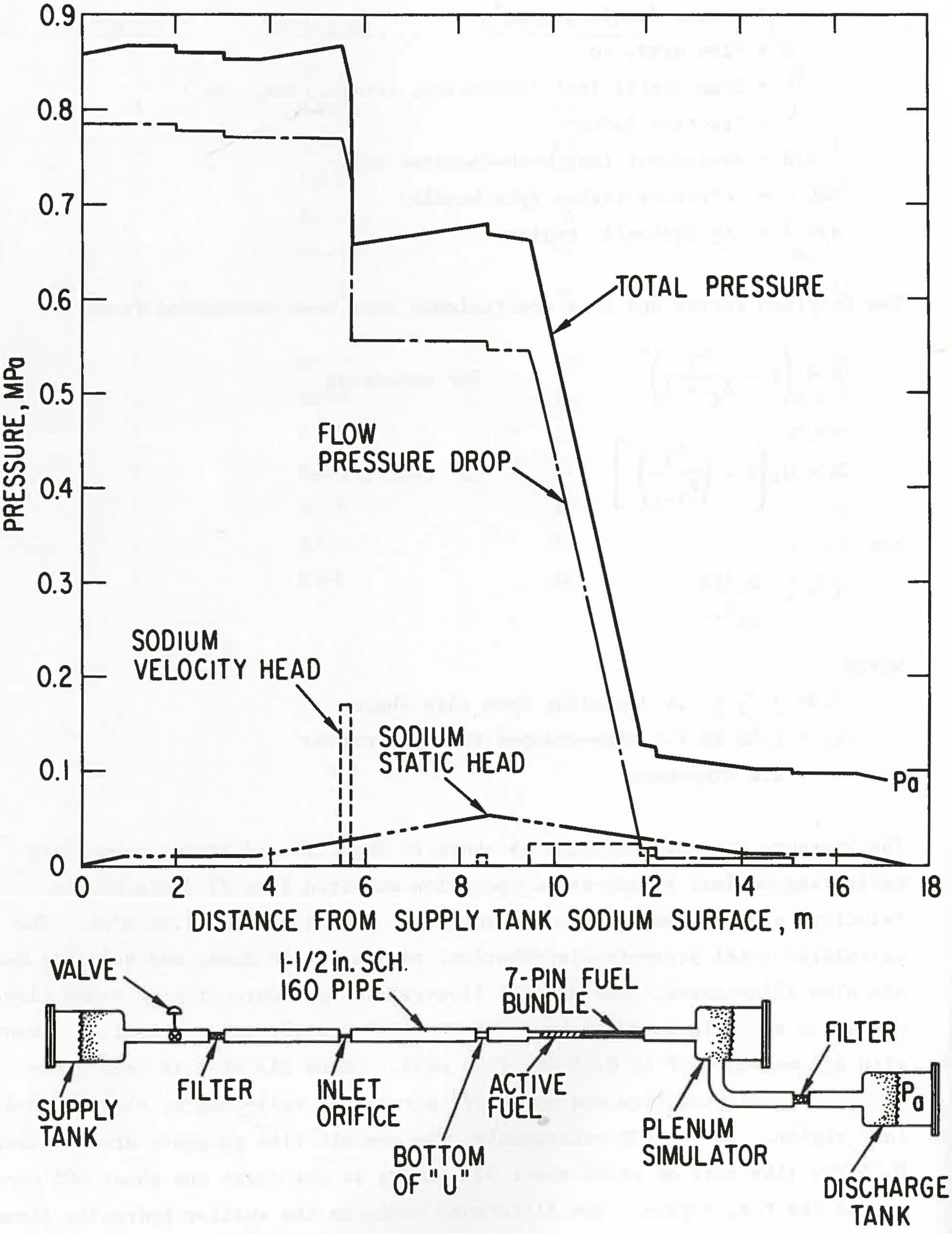

Fig. 12 System Pressure Drop Distribution at Nominal Steady-State Operating Condition; T = 316°C.

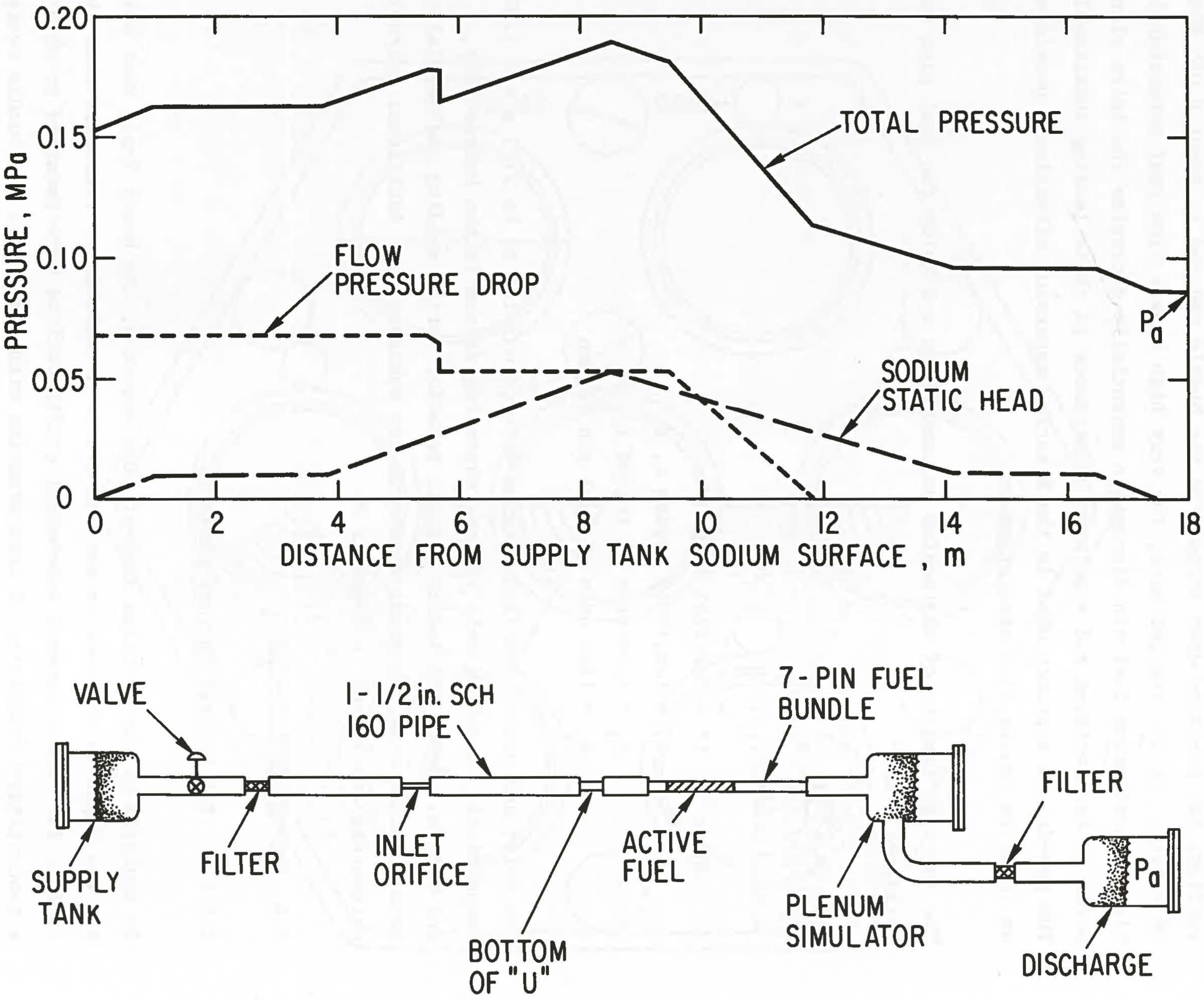

Fig. 13 System Pressure Drop Distribution at Incipient Boiling; T = 316°C.

of the 7-pin bundle (2.46 mm vs. 3.25 mm for the subassembly) due to the presence of the filler rods at the inside surfaces of the hex flats. At incipient voiding, the pressure drop across the pin bundle reduced to about 0.055 MPa (8.0 psi). In the reactor core, the very high bypass flow past subassemblies first experiencing fuel pin disruption essentially decouples the inlet plenum pressure from voiding and expulsion occurrences in these leading subassemblies. The gas-driven approach used in the R-series apparatus effectively provides an infinite bypass flow simulation.

The inertial lengths of the sodium columns above and below the fuel pins were evaluated from[11]:

$$L^* = \sum \ell_i \frac{A_r}{A_i}$$

where L^* = inertial length, m

ℓ_i = length of region i, m

A_i = flow area of region i

A_r = flow area of fuel pin region

The inlet and outlet inertial lengths were calculated to be 2.03 m and 0.29 m, respectively, matching well the corresponding values in the subassembly, 1.74 and 0.18 m. Hence the sodium dynamic behavior during voiding and expulsive events should well represent events in the subassembly. Additional hydraulic parameters are listed in Appendix B.

2.5 Thermal Performance

2.5.1 SAS Pretest Thermal Analysis

In analysis of the R-series loss-of-flow sequence, the basic 7-pin test assembly was input to SAS code in several different subchannel configurations shown in Fig. 14. These several subchannel configurations were examined to obtain a quantitative evaluation of incoherencies with respect to the bundle average input case in both boiling initiation and clad motion. A comparison of key input parameters to SAS code for the FTR case, the R-series average case, and

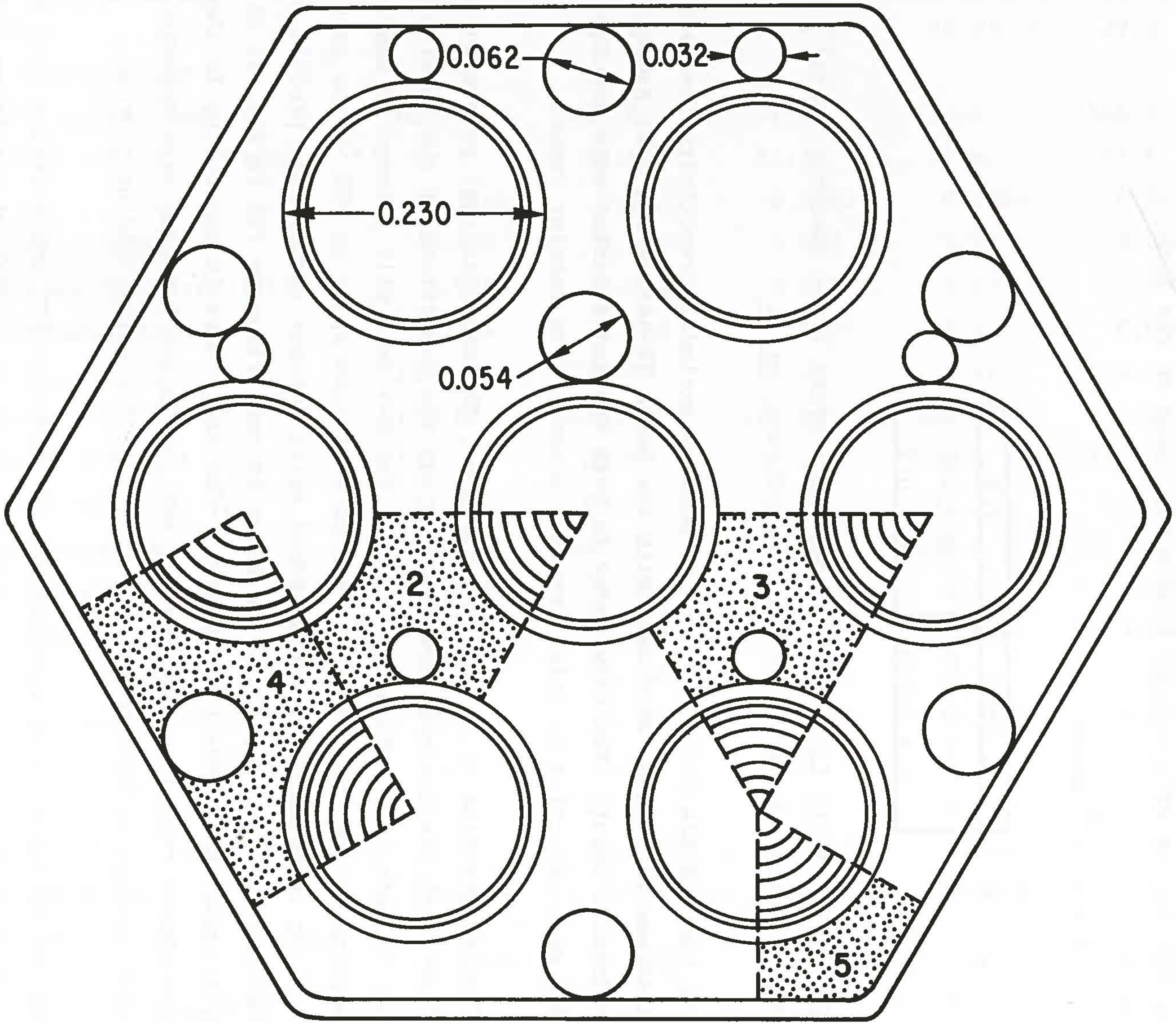

Fig. 14 SAS Subchannel Configuration for R-Series Incoherency Evaluation.

the several subchannels is listed in Table 4.

The reference conditions were based on nearly identical pin power (31 kW/pin FTR, 30 R-series) and sodium velocity (21.5 ft/sec FTR, 20.8 ft/sec R-4) at initiation of flow coastdown. The SAS calculation of the single-phase friction factor in the wire wrapped bundle was input in the form

$f = a\,Re^{-b}$ where

R-4	FTR
a = 0.175 b = 0.175	a = 0.2 b = 0.2

The coefficients for R-4 were taken from OPERA 7-pin checkout tests[12] and compare favorably with the test data of Okamoto _et al._[13]

The basic SAS2A thermal hydraulic modules excluding reactivity feedback and disassembly options were used with the basic (R-series and FTR) geometric and hydraulic input. The flow decay in both FTR and R-series were described in SAS as a reduction in inlet pressure according to tabular input.

From the results of the SAS calculations, the basic initial or steady conditions from which the loss-of-flow proceeds and the conditions at the onset of boiling are illustrated in Figs. 15 and 16. The R-4 test will attempt to approach boiling at the same flow rate and rate of flow decay as FTR $\sim$4 sec prior to boiling inception. The anticipated axial coolant temperature profile which results from this operation is shown in comparison to FTR in Fig. 15 at steady state and at the onset of boiling. The difference in subcooling in the fission-gas plenum region at the onset of boiling in the R-series case appears to be small enough to have negligible effect on the early voiding process.

Figure 16 illustrates a comparison of reference FTR and R-series test fuel conditions at steady state and at the onset of boiling clad melting. The

Table 4. SAS Input Parameters for $R\text{-}4_{avg}$, FTR, $R\text{-}4_{sub\#2\rightarrow5}$

Parameter	$R\text{-}4_{avg}$	FTR	$R\text{-}4_2$	$R\text{-}4_3$	$R\text{-}4_4$	$R\text{-}4_5$
Pin power [kW]	30	31.2	32.4	28.05	29.7	31.42
Radial power distribution						
SS coolant flux [g/cm^2 sec]	613.5	623.0	751.0	751.0	568.2	541.2
SS pressure drop along pin [psig]	81.7	44.1	81.5	81.6	81.6	81.6
D_h [cm]	0.2454	0.3873	0.3363	0.3363	0.2181	0.2022
Volume fraction of coolant	0.448	0.427	0.403	0.403	0.480	0.473
Structure-clad surface area ratio	0.932	0.124	0.171	0.171	1.470	1.592
Structural thickness [cm]	0.049	0.134	0.027	0.027	0.044	0.048
Length of fuel pin [cm]	124.46	124.46	124.46	124.46	124.46	124.46
Height of plenum [cm]	106.68	106.68	106.68	106.68	106.68	106.68
Height of lower reflector [cm]	151.0	82.8	151.0	151.0	151.0	151.0
Height of upper reflector [cm]	41.3	102.0	41.3	41.3	41.3	41.3
Coolant inlet temperature [°C]	315.6	316.0	315.6	315.6	315.6	315.6
Coolant exit pressure [atm]	1.075	1.353	1.075	1.075	1.075	1.075
Fuel pellet diameter [cm]	0.508	0.508	0.508	0.508	0.508	0.508
Fuel pin diameter [cm]	0.584	0.584	0.584	0.584	0.584	0.584
Bond conductance parameter HBPAR	0.0028	0.002	0.0028	0.0028	0.0028	0.0028
Maximum bond conductance [W/cm^2 °C]	1.0	1.0	1.0	1.0	1.0	1.0
Sodium superheat [°C]	10.0	10.0	10.0	10.0	10.0	10.0
Initial film thickness [cm]	0.0111	0.0128	0.0111	0.0111	0.0111	0.0111
Minimum film thickness [cm]	0.0074	0.0085	0.0074	0.0074	0.0074	0.0074
Fuel thermal conductance at 1600°C [W/cm °C]	0.0207	0.0193	0.0207	0.0207	0.0207	0.0207
Fuel density at 2000°C [g/cm^3]	9.2	9.3	9.2	9.2	9.2	9.2
Fuel specific heat at 1600°C [J/g°C]	0.350	0.384	0.350	0.350	0.350	0.350

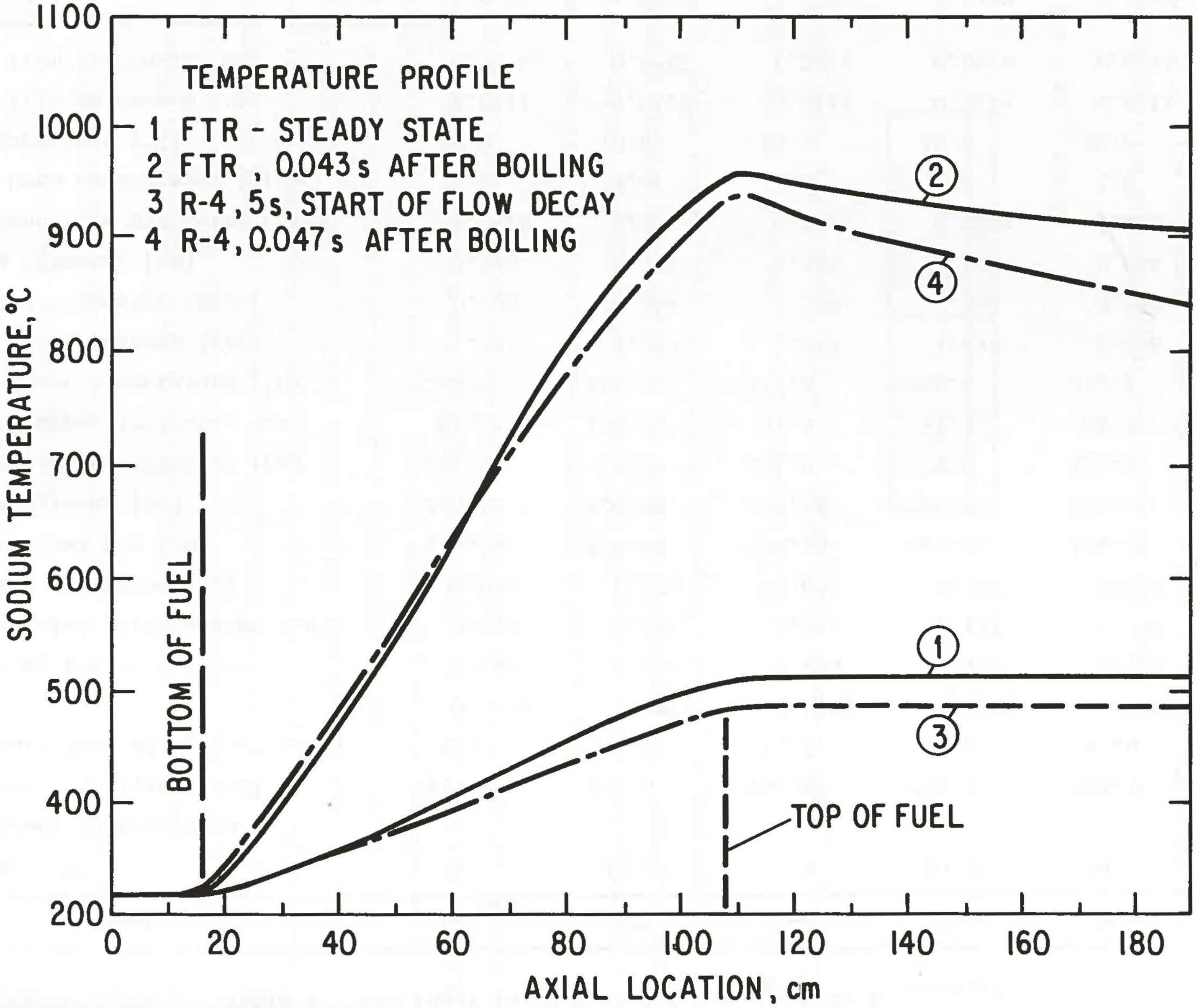

Fig. 15 SAS Calculations of Axial Coolant Temperature Profiles at Steady-State and Onset of Voiding.

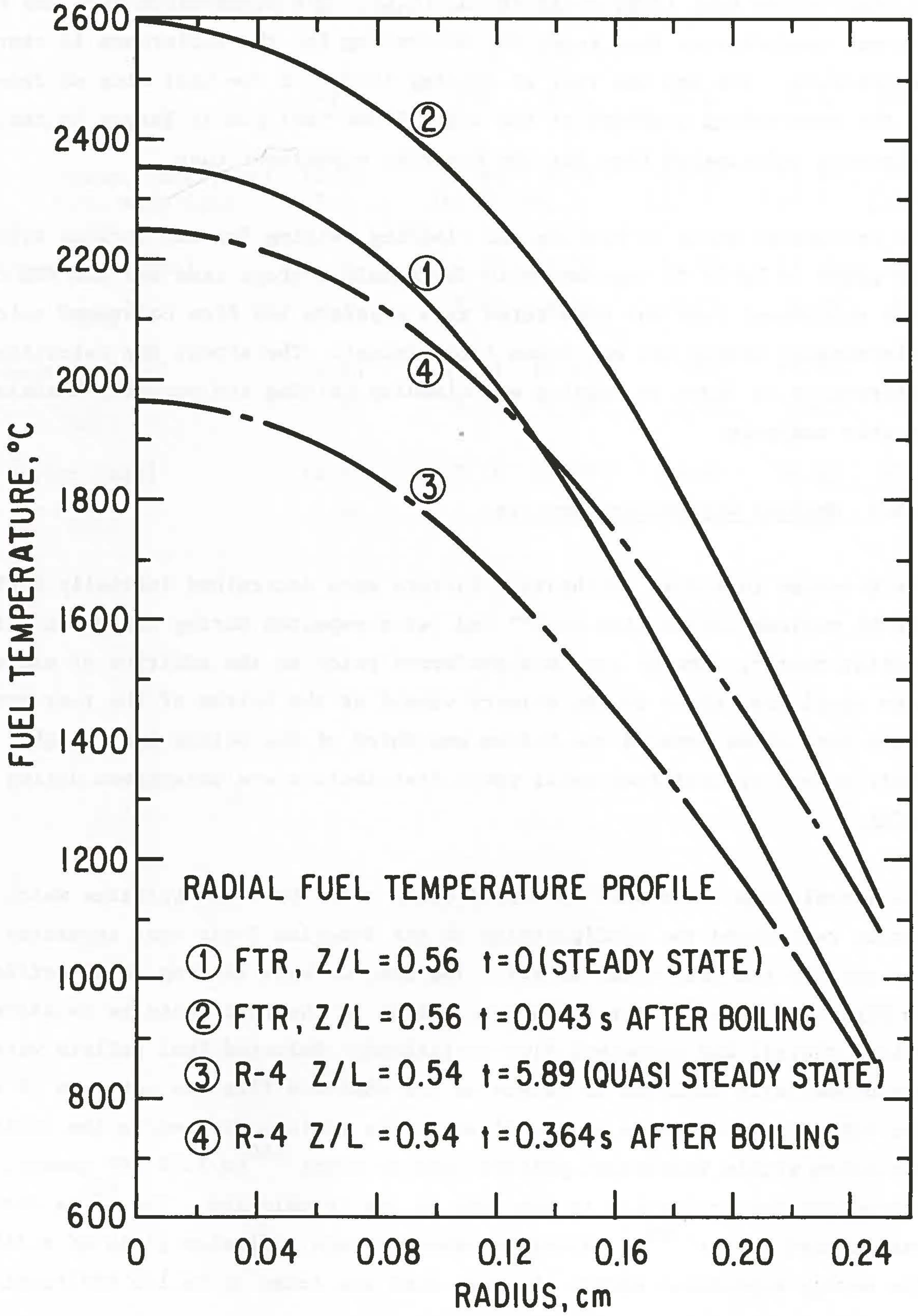

Fig. 16 SAS Calculations of Fuel Midplane Temperature Profiles at Steady-State and Onset of Boiling.

differences illustrated here show some quantitative evaluation of the effects of mixed-oxide fuel (FTR) vs fresh UO_2 (R-4). The mixed-oxide fuel has a lower thermal conductivity than fresh UO_2 accounting for the difference in centerline temperature. One can see that at boiling inception the heat flux as determined by the temperature gradient at the edge of the fuel pin is larger in the FTR reference calculation than for the R-series experiment case.

The calculated times to boiling and cladding melting for the various subchannels are given in Table 5, together with the bundle average case and the FTR case. Each subchannel case was considered in a separate SAS flow coastdown calculation; interchannel mixing was not taken into account. Therefore, the calculated differences in times to voiding and cladding melting are probably maximized in this analysis.

2.5.2 Nuclear Calibration Results

The R-series test fuel calibration factors were determined initially during the R1 nuclear calibration test[14] and later repeated during the R8CAL calibration test[15]. The R1 test was performed prior to the addition of stainless steel heat sinks on the primary vessel at the bottom of the test train. These heat sinks covered the bottom one-third of the active fuel height. Their effect on test fuel axial power distribution was determined during R8CAL.

The irradiation tests were performed using a calibration apparatus which accurately reproduced the configuration of the R-series 7-pin test apparatus (except for the heat sinks in R1). The reactor core loading is illustrated in Fig. 17. Flux monitor wires were placed in the test vehicles to assess axial, radial, and azimuthal flux variations. Selected fuel pellets were radiochemically analyzed to determine the absolute fissions per gram of UO_2. The laboratory procedure was to dissolve the pellets (to remove the radial variation within individual pellets) and to count ^{140}La 1.59 MEV gammas, correcting the activation to the time of the irradiation. The ^{140}La activity was related to the ^{140}Ba parent, assumed to have a fission yield of 6.51%. The energy deposition within the test fuel was taken to be 175 MEV/fission.

TABLE 5 Summary Table of R-series Subchannel and FTR Times to Boiling, Dryout, and Melting

	$R\text{-}4_{avg}$	FTR	$R\text{-}4_2$	$R\text{-}4_3$	$R\text{-}4_4$	$R\text{-}5_5$
Boiling (t_{boil} = 0.0)						
Trans. Time [sec]	11.02	13.86	9.78	12.20	12.29	10.50
Cod. mass flux	149.5	164.0	191.0	177.7	135.7	136.6
Na film dryout [sec]	11.94	14.50	10.34	12.80	13.14	11.30
t_{boil}	0.92	0.74	0.56	0.60	0.85	0.80
Clad melting [sec]	12.63	15.11	11.03	13.62	13.52	12.23
t_{boil}	1.61	1.25	1.25	1.42	1.63	1.73
Clad Motion [sec]	13.50	15.78	11.76	14.52	14.87	12.96
t_{boil}	2.48	1.92	1.98	2.32	2.58	2.46

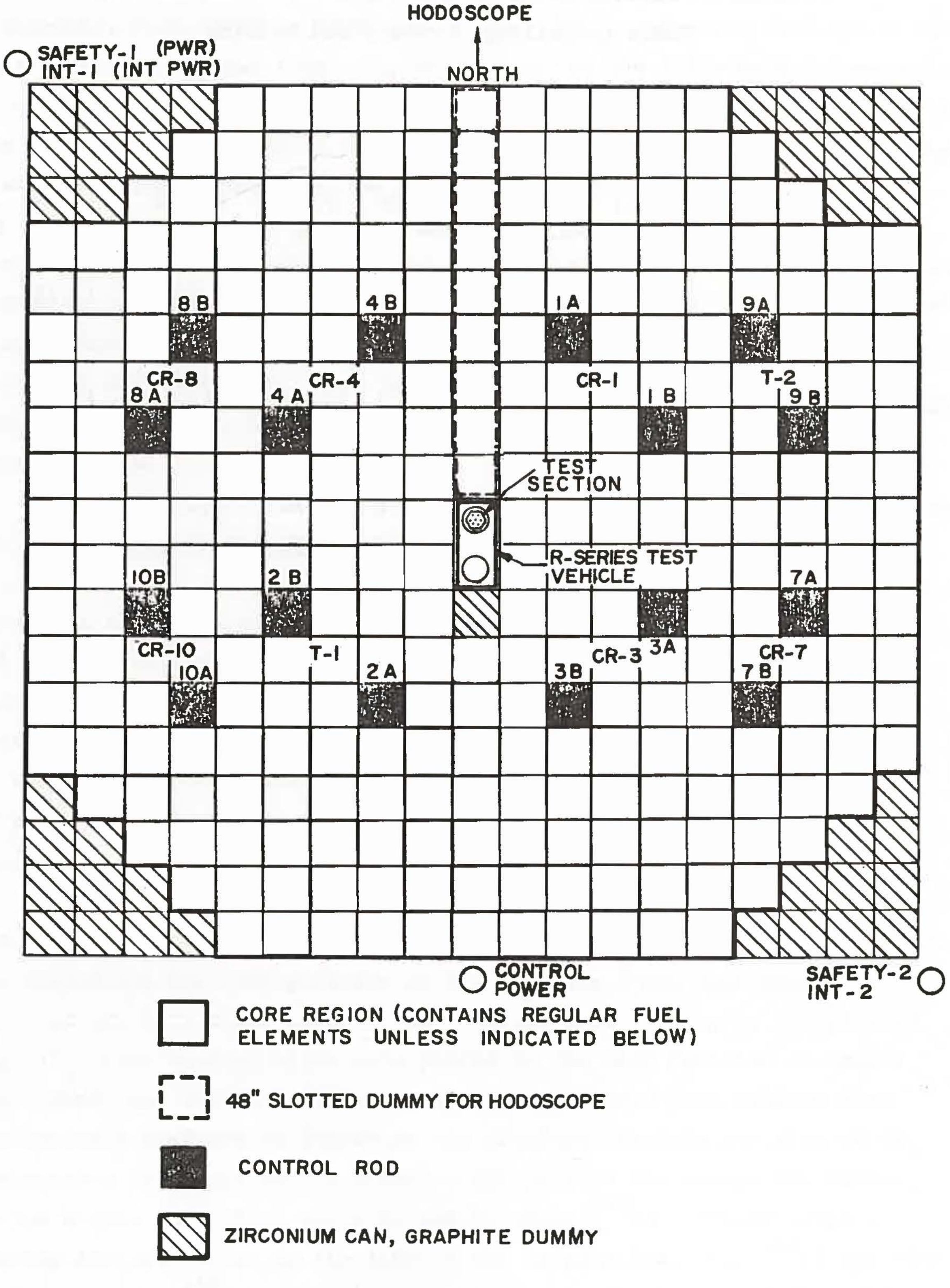

Fig. 9 TREAT Core Loading and Instrumentation for R8CAL

Fig. 17 TREAT Core Loading and Instrumentation for R4 and R5.

The results of the nuclear calibration tests applicable for the R4 and R5 tests with the stainless steel heat sinks are summarized in Table 6. A comparison is also included with the results of the earlier R1 test without the heat sinks. The test results indicate that about 20% more power was generated in the center pin than in an average edge pin. Among the edge pins, the max-to-average power variation was only about 1%, indicating negligible power skewing. The axial power distribution was about 1.25 max-to-average, as illustrated in Fig. 18. The effect of the heat sinks in causing a power depression at the bottom one-third of the fuel column is evident in this figure. The overall calibration factor, averaged lengthwise, radially, and azimuthally, was 2.51 watts/gm UO_2-MW_{TREAT}. Based upon 173.7 gm UO_2 per pin, the power calibration factor was 0.436 kW/pin-MW. To operate at a test fuel power of 28 kW/pin average required a TREAT power level of 64.2 MW.

Selected fuel pellets were also analyzed for their internal radial fission distribution by the method of radial sampling[15]. An ultrasonic technique developed at ANL[16] was used to cut the pellets into concentric hollow cylinders, each of which was radiochemically analyzed for fissions. The test results, Fig. 19, illustrate that the maximum-to-minimum power variation across the pellets amounts to approximately 1.12 and 1.16 for a 14% enriched edge pin and 20% enriched center pin, respectively. The data illustrate that the power depression is essentially independent of the axial location.

2.6 Instrumentation

Instrumentation used for tests R4 and R5 were identical to one another and are summarized in Table 7. Details on instrument selection and utilization are given in Table 8. Locations of the various instruments are shown in Fig. 20.

2.6.1 Sodium Flowmeters

Flowmeters FM-1 and FM-2 were located in the supply and discharge pipes, respectively. These assemblies were permanent-magnet type, mounted on the exterior of 1-1/2 in. diameter Schedule 160 pipe, with signal electrodes tack welded to the pipe. The magnets were Alnico V, temperature stabilized to 800°F, which provided field strengths of approximately 1260 gauss. Flowmeter

Table 6. Summary of Calibration Results for R-Series 7-pin Test Section

Parameter	R4-R5 (Ref. 15) SST Heat Sinks	R1 (Ref. 14) No Heat Sinks
Calibration factor; center pin, lengthwise average (watts/gm-MW)	2.93	3.08
Calibration factor; edge pins, lengthwise and azimuthal average (watts/gm-MW)	2.44	(a) 2.74
Calibration factor; all pins, lengthwise and azimuthal average (watts/gm-MW)	2.51	(b) 2.78
Radial Power Ratio,		
Center Pin/avg. edge pin	1.20	1.12
Center Pin/avg. all pins	1.17	--
Azimuthal Power Shape (edge pins) max-to-avg.	1.011	--
Axial Power Shape, max-to-avg. (Fig. 18)	(d) 1.25	(c) 1.12
Mass of Active Fuel per Pin, avg. (gm)	173.7	173.7
Power calibration factor for 7-pin test (bundle (kW/test pin/MW TREAT)	0.436	0.483
TREAT power required for 23 kW/pin avg. (MW, Safety #1)	64.2	58.0

Notes:

(a) For one edge pin, location unspecified.

(b) Edge pins not azimuthally averaged.

(c) Without 0.45-in.-thick heat sink at bottom 13 in. of active fuel.

(d) Max-to-avg. value is misleading since profile is affected by heat sinks.

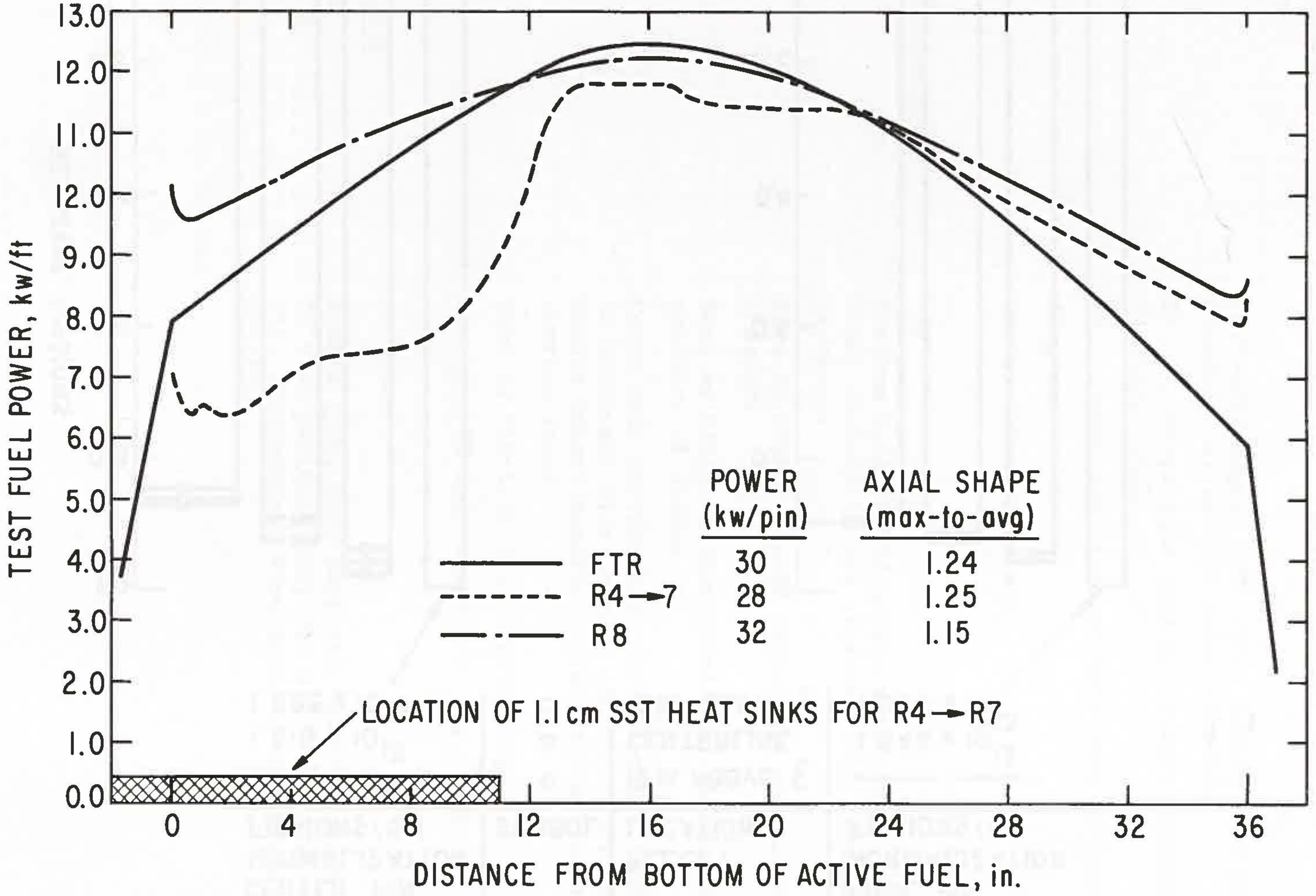

Fig. 18 Fuel Axial Power Distribution from Calibration Irradiation (Ref. 15).

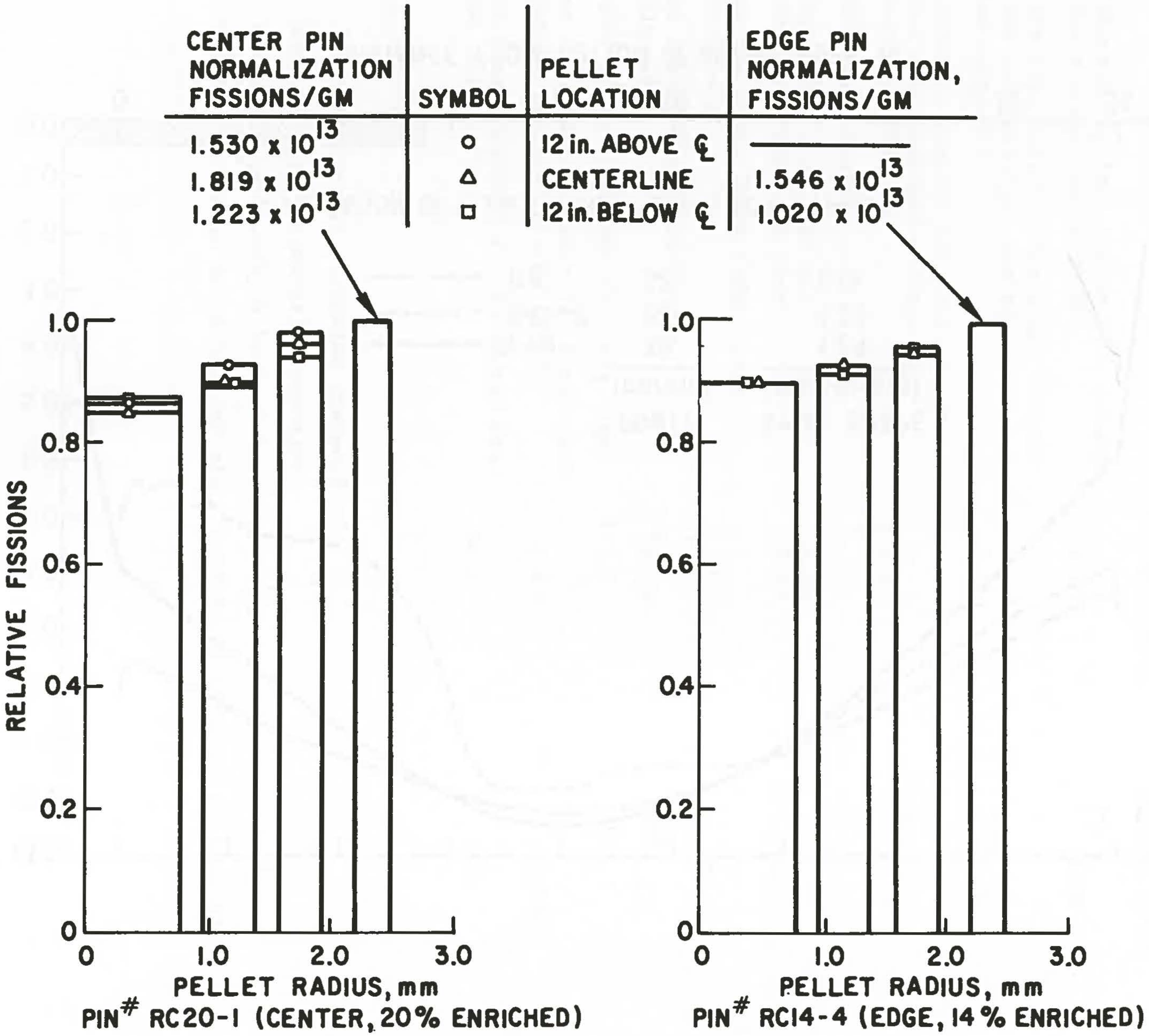

Fig. 19 Fuel Radial Power Generation from Calibration Irradiation with Radial Pellet Sampling (Refs. 15 and 16).

TABLE 7 Description of R4 and R5 Test Instrumentation

Instrument	Type/Location/Function
Flowmeters	
FM-1	Permanent magnet (PM) type; supply line piping; measure test section inlet flowrate
FM-2	PM; discharge line piping; between simulator and discharge tank
FM-3	PM; plenum simulator; measure test section outlet flowrate
FM-4	Backup inlet flowmeter
Pressure Transducers	
PTS-1	Statham Model PA822 bonded strain gage type; supply tank; measure ST gas pressure (LOF pressure blowdown)
PTS-3	Same as PTS-1; plenum simulator; measure DT gas pressure
PTS-5	Same as PTS-1; plenum simulator; measure absolute pressure of plenum gas
PTK-1	Kamam eddy current type (0-200 psia); flush mounted in downcomer pipe between inlet orifice and fuel bundle inlet; measure sodium pressure at test section inlet
PTK-2	Same as PTK-1,2; 0-3000 psia range
PTK-3,4	Same as PTK-1,2; located at top of pin bundle
Thermocouples	
*TCTS-i i = 1 - 12	Sheath type, bare intrinsic junction type K; 12 TC's at various locations along flow tube (see Fig. 10); measure flow tube axial temperature profile

TABLE 8

Operating Characteristics of Test Instrumentation

Test Variable and Inst.	Transducer	Range	Accuracy	Response	Project SIG Conditioning	Output	Parameter Range	Output Range	Function and Failure Contingency
Pressure									
PTS-1	Statham PA-822 S/N 12765 (525°F)	0-150 psia	±3% FR	7.5 KHz (Nat Freq)	V_{ex} - 4.543 vdc Zero at 0 psig	0.0675 mv/psi	0-150 psig	0-10.1 mvdc	Supply tank abs. pres. Do not proceed until functioning properly
PTS-3	Statham PA-822 S/N 12766 (525°F)	0-150 psia	±3% FR	7.5 KHz (Nat Freq)	V_{ex} - 4.777 vdc Zero at 0 psig	0.0650 mv/psi	0-25 psig	0-1.63 mvdc	Discharge tank abs. pres. Proceed
PTS-5	Statham PA-822 S/N 12782 (525°F)	0-50 psia	±3% FR	7.5 KHz (Nat Freq)	V_{ex} = 4.600 vdc Zero at 0 psig	0.0201 mv/psi	0-25 psig	0-0.51 mvdc	Plco. Sim. abs. pres. Proceed
PTK-1	Kaman K1908 S/N 2865 (1200°F)	0-200 psia	±5% FR	dc - 3 KHz	Kaman Uni-vit Sys. Zero at 0 psig	0-300 mvdc (nom.)	0-150 psig	0-225 mvdc	T.S. entrance pres. Proceed
PTK-2	Kaman K1908 S/N 2869 (1200°F)	0-3000 psia	±5% FR	dc - 10 KHz	Kaman Uni-vit Sys. Zero at 0 psig	0-300 mvdc (nom.)	0-3000 psig	0-300 mvdc	T.S. entrance pres. Proceed
PTK-3	Kaman K1908 S/N 2866 (1200°F)	0-3000 psia	±5% FR	dc - 10 KHz	Kaman Uni-vit Sys. Zero at 0 psig	0-300 mvdc (nom.)	0-3000 psig	0-300 mvdc	T.S. exit pres. Proceed
PTK-4	Kaman K1908 S/N 2867 (1200°F)	0-200 psia	±5% FR	dc - 3 KHz	Kaman Uni-vit Sys. Zero at 0 psig	0-300 mvdc (nom.)	0-50 psig	0-75 mvdc	T.S. exit pres. Proceed
Sodium Flow									
FM-1	Tem Tex S/N 001 (Mfg. Special)	0-20 gpm	±5% meas.	-	-	2.10 mv/lbm/sec	0-2.5 lbm/sec	0-5.3 mv	Supply line flow rate Used for exp. control (A/D-6). Do not proceed until functioning properly
	Tem Tex S/N 001 (Mfg. Special)	0-20 gpm	±5% meas.	-	-	2.10 mv/lbm/sec	0-12.5 lbm/sec	0-27 mv	
FM-2	Tem Tex S/N 002 (Mfg. Special)	0-20 gpm	±5% meas.	-	-	2.05 mv/lbm/sec	0-2.5 lbm/sec	0-5.2 mv	Discharge line flow. Proceed
FM-3	ANL PM Flowmeter	0-100 gpm	±5% meas.	-	-	0.877 mv/lbm/sec	0-2.5 lbm/sec	0-2.19 mv	Test section exit. Do not proceed until functioning properly
	ANL PM Flowmeter	0-100 gpm	±5%	-	-	0.877 mv/lbm/sec	0-12.5 lbm/sec	0-11.0 mv	
Temperature									
TCTS-j	Weld attachment to test section; Type K, intrinsic	32-2300°F	±3% Reading	Same as hex can (~35 msec)	"Hotbox" 150°F Ref Junction		550-2600°F	8.0-55 mv	T.S. Outlet Temp. used for exp. control (A/D-8). Change to TCTS-[illegible].

TABLE 8 (Cont'd)

Test Variable and Inst.	Transducer	Range	Accuracy	Response	Project SIG Conditioning	Output	Parameter Range	Output Range	Function and Failure Contingency
Sodium Level									
PTS-2	Statham PM732TC S/N 2293 (600°F)	±2.5 psid	±5% FR	3.1 KHz (Nat Freq)	V_{ex} = 4.600 vdc	2.446 mv/psi (.0774 mv/in Na)	15-35 in Na	1.16-2.71 mv (dc)	Supply tank Na level. Exp. Control (A/D-7) Do not proceed.
PTS-4	Statham PM732TC S/N 2294 (600°F)	±2.5 psid	±5% FR	3.1 KHz (Nat Freq)	V_{ex} = 4.802 vdc	2.661 mv/psi (.0842 mv/in Na)	15-35 in Na	1.26-2.95 mv (dc)	Discharge tank Na level. Proceed.
Sodium Voiding									
VP-1	Electrode attached to test section	Na short/open between electrodes	-	300 μsec	-	Diff Voltage Hi VP-1 Lo VP-2	-	±6 mvdc	Voltage tap
VP-2	Electrode attached to test section	Na short/open between electrodes	-	300 μsec	-	Diff Voltage Hi VP-2 Lo VP-3	-	±6 mvdc	Voltage tap
VP-3	Electrode attached to test section	Na short/open between electrodes	-	300 μsec	-	Diff Voltage Hi VP-3 Lo VP-4	-	±6 mvdc	Voltage tap
VP-4	Electrode attached to test section	Na short/open between electrodes	-	300 μsec	-	Diff Voltage Hi VP-4 Lo VP-5	-	±6 mvdc	Voltage tap
VP-5	Electrode attached to test section	Na short/open between electrodes	-	300 μsec	-	Diff Voltage Hi VP-5 Lo VP-6	-	±6 mvdc	Voltage tap
VP-6	Electrode attached to test section	Na short/open between electrodes	-	300 μsec	-	-	-	-	Voltage tap
EVP	Sorensen SRL 60-35 Power Supply	0-60 vdc	-	150 μsec	-	-	-	4-7 vdc	Power supply output voltage. Proceed.

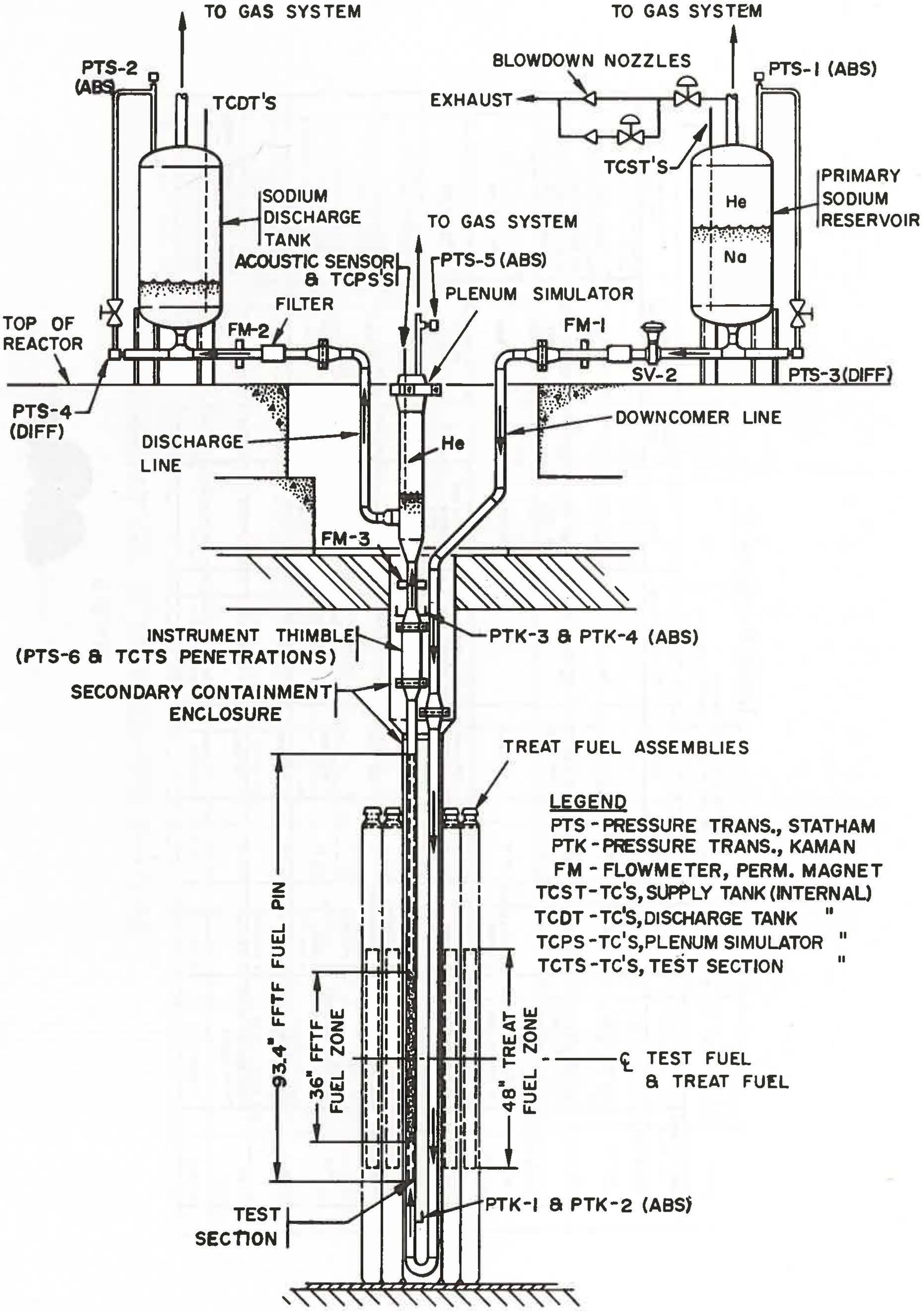

Fig. 20 Locations of Instrumentation in R-Series Test Apparatus.

FM-3 was also of the permanent-magnet type, located on the plenum simulator. lower pipe section outlet flowrate. This compact "pipe hugger" assembly consisted of two Alnico V magnets and two soft iron pole pieces isolated from the 1.9 in. O.D. pipe by mica sheet. The field strength was approximately 500 gauss. The flowmeters were all located far outside the TREAT core region to avoid fluxrelated signal anomolies. The apparatus was filled with sodium in-situ under vacumn to avoid entrapment of gas between the test section and the inlet and outlet flowmeters. Both the inlet and outlet flowmeters were located far from the test bundle to enable test section voiding rates to be measured prior to gas or vapor passing through the flowmeters themselves. Upstream voiding during the test was not extensive enough for the gas to flow around the bottom of the "U"-bend; hence, no voiding whatsoever took place at the inlet flowmeter. The downstream (upper) voiding FM-3 eventually experienced signal dropout as noncondensible gas released during the test passed upward into the upper plenum.

The sodium flowmeters were calibrated as a part of loop pre-test operations. The apparatus was heated to the 316°C operating temperature and held at that temperature for 7 hours prior to the calibration, to promote pipe wetting. The calibration was performed in-situ under isothermal but otherwise identical conditions to the subsequent tests. A volumetric displacement method was used in which the time required for a known volume of sodium to be transferred from the supply tank to the discharge tank was measured. The calibration results are shown in Fig. 21, and the flowmeter sensitivities are summarized in Table 9.

TABLE 9 Summary of Flowmeter Calibration Results for R4 and R5; T = 316°C

Flowmeter	Sensitivity, mv/(lb$_m$/s)
FM-1	2.00 ± .06
FM-2	2.04 ± .06
FM-3	0.66 ± .03

2.6.2 Loop Pressure Transducers

Strain-guage pressure transducers were mounted at various locations in the apparatus to measure operating parameters including supply tank absolute pressure (PTS-1), discharge tank absolute pressure (PTS-3), and upper plenum cover

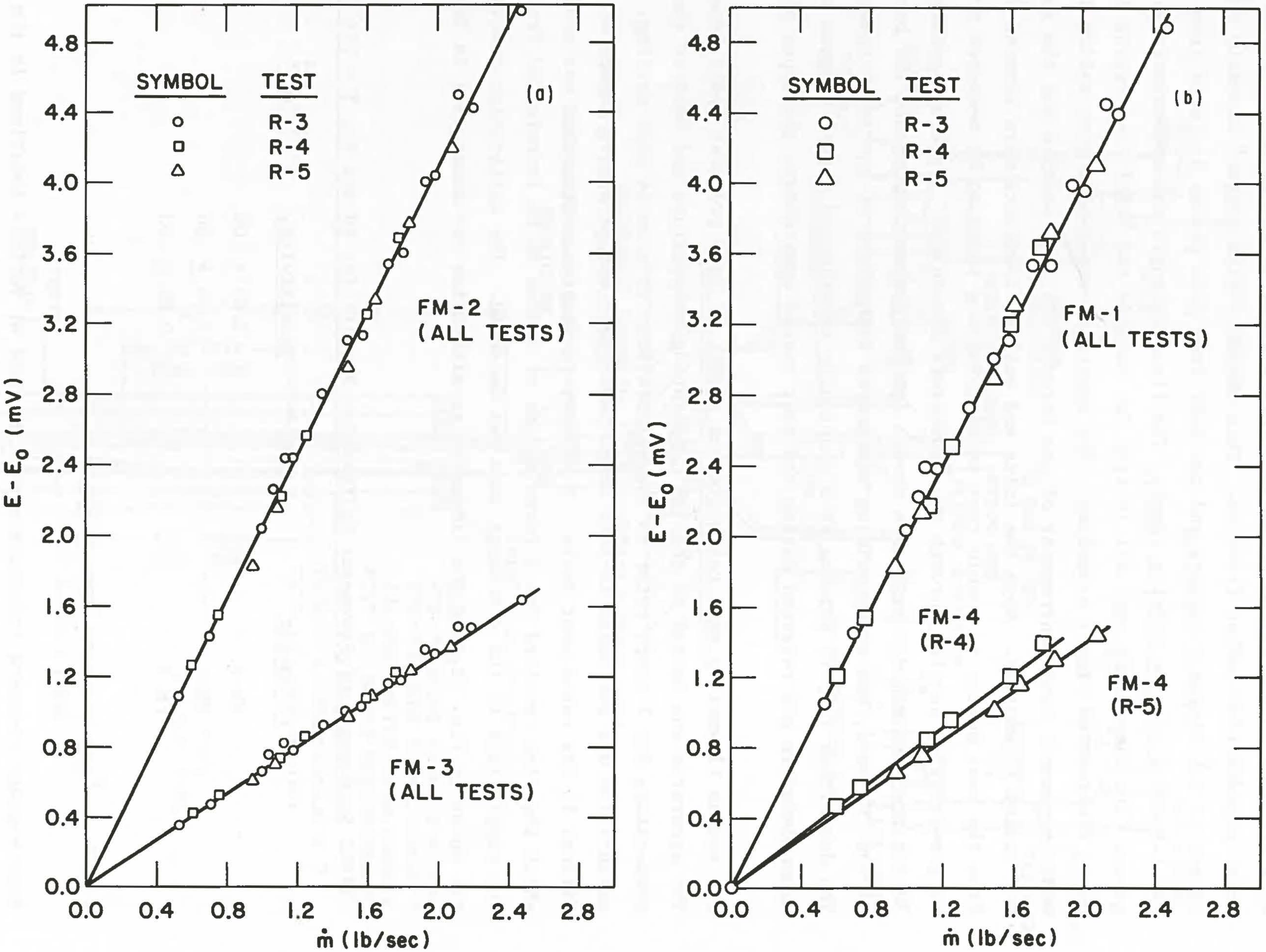

Fig. 21 Results of Flowmeter Calibrations; T = 316°C.

gas pressure (PTS-5). Fast response eddy-current transducers were flush mounted on the inside of the sodium pipe at the entrance and exit of the pin bundle (PTK-1 and PTK-4, respectively). These 200 psia transducers were used to monitor both steady-state and transient test section pressure. High range 3000 psia transducers, PTK-2 and PTK-3, were also located at the test section entrance and exit as a contingency to record any high-amplitude transient pressurization events which might occur. (No such events were expected nor occured during the LOF tests.) Both the PTS and PTK series transducers were calibrated in the loop following heatup to operating temperature. The pressure transducer calibration results were generally consistent with manufacturer's data. The PTK transducers exhibited slow zero shift due to transient heating of their flush-mounted diaphrams by the flowing sodium. All transducers were located outside the TREAT core, and no flux-related signal anomalies were present in test data.

2.6.3 Temperature Measurement

Thermocouples were located throughout the apparatus to monitor both system operating temperatures and test fuel bundle temperatures. The test section thermocouples (TCTS-1-12) were located on the outside surface of the hex flow-tube. Their elevations are shown in relation to the test fuel bundle in Fig. 10.

The intrinsic junction thermocouple design is shown in Fig. 22. The thermocouple wires were individually spot-welded to the fuel holder wall. The fuel holder thereby became an integral part of the thermocouple junction, adding negligible thermal inertia at the heated surface. The thermocouple assemblies were comprised of 0.040-in. O.D. 316 SS sheaths, chromel/alumel TC wire (nominal 6-mil diameter), and MgO insulation. Weld tabs were affixed to the sheath near the junction-end of the assemblies. During installation, these tabs were spot welded to the fuel holder, firmly attaching the sheath to the wall. The remainder of the sheath was loosely banded to the fuel holder so that differential thermal expansion was permitted. The bare TC wires, about 1/4-inch long, were flattened in a vise and were individually spot welded to the wall at a seperation of about 1/32 in. The bare, hot end of the sheath was potted with Aremco Cerama-Dip 538 which severd both as a sealant and as a protection against the wires shorting either to the sheath or to one another away from the wall.

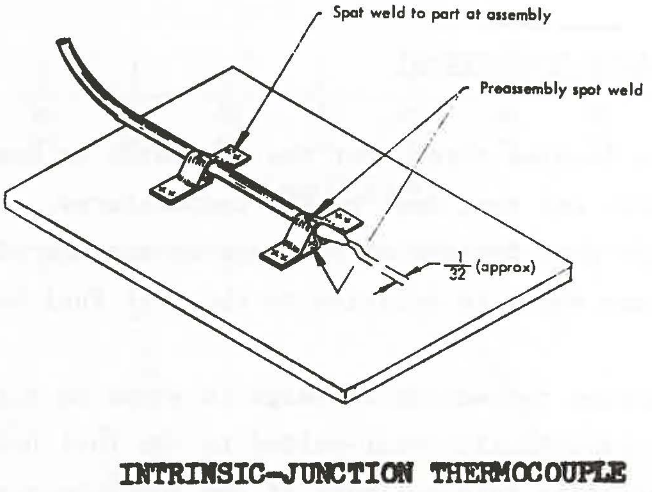

Fig. 22 Illustration of Intrinsic-junction Thermocouple used along Outside Surface of Thin-walled Flowtube.

The 63% time constant for this surface temperature measurement is estimated to be about 40 msec based upon internal resistance to heat flow within the 20 mil flowtube wall (Biot Modulus ≈ 70). Transient test data generally verified that the TC's responded adequately fast for the time scale of events during LOF-type tests. As an illustration, R4 test data in Fig. 23 show the relation between inlet sodium flowrate and measured wall temperature at the inlet plane of the test fuel column. At about 14.8 sec, the coolant reversed flow direction at the inlet and thereafter became oscillatory with alternating inward and outward flow. The flowtube thermocouple at the fuel inlet plane, TCTS-12, responded as expected to these changes in direction of the coolant motion. Prior to flow reversal the temperature was steady at 316°C; upon reversal, the temperature rapidly increased as the heated sodium was expelled back into the inlet plenum. The wall heating thereafter became cyclic, in response to the oscillating coolant flow. The time lag for this measurement was about 50 msec.

2.7 Data Acquisition

All test instrumentation was recorded wideband on TREAT analog data acquisition equipment. The recording setup, Fig. 24, utilized two 14-channel FM tape recorders operated at 60 ips, 20 kHz bandwidth. Additional channels for slow time response signals were provided by a 15-channel multiplexer whose output was fed to one of the tape recorder channels. Two oscillographic recorders were used on-line for redundancy on key instrumentation channels and for immediate indication of the test outcome.

Selected instruments were recorded on two data channels at varying gains to accomodate uncertainty in parameter ranges during the tests. The signal leads were routed from the experiment instrumentation console to the nearby TREAT input terminal board. From there, the signal leads were routed to the TREAT calibration and to the appropriate recorder amplifier and channel. All gains were set for nominally 1 VDC output at expected parameter full range signal level. The TREAT calibrator was used to record calibration signals at 0, ± 1/4, ± 1/2, ± 3/4, and ± 1 times full range signal level for each channel prior to the test.

2.8 Test Operation

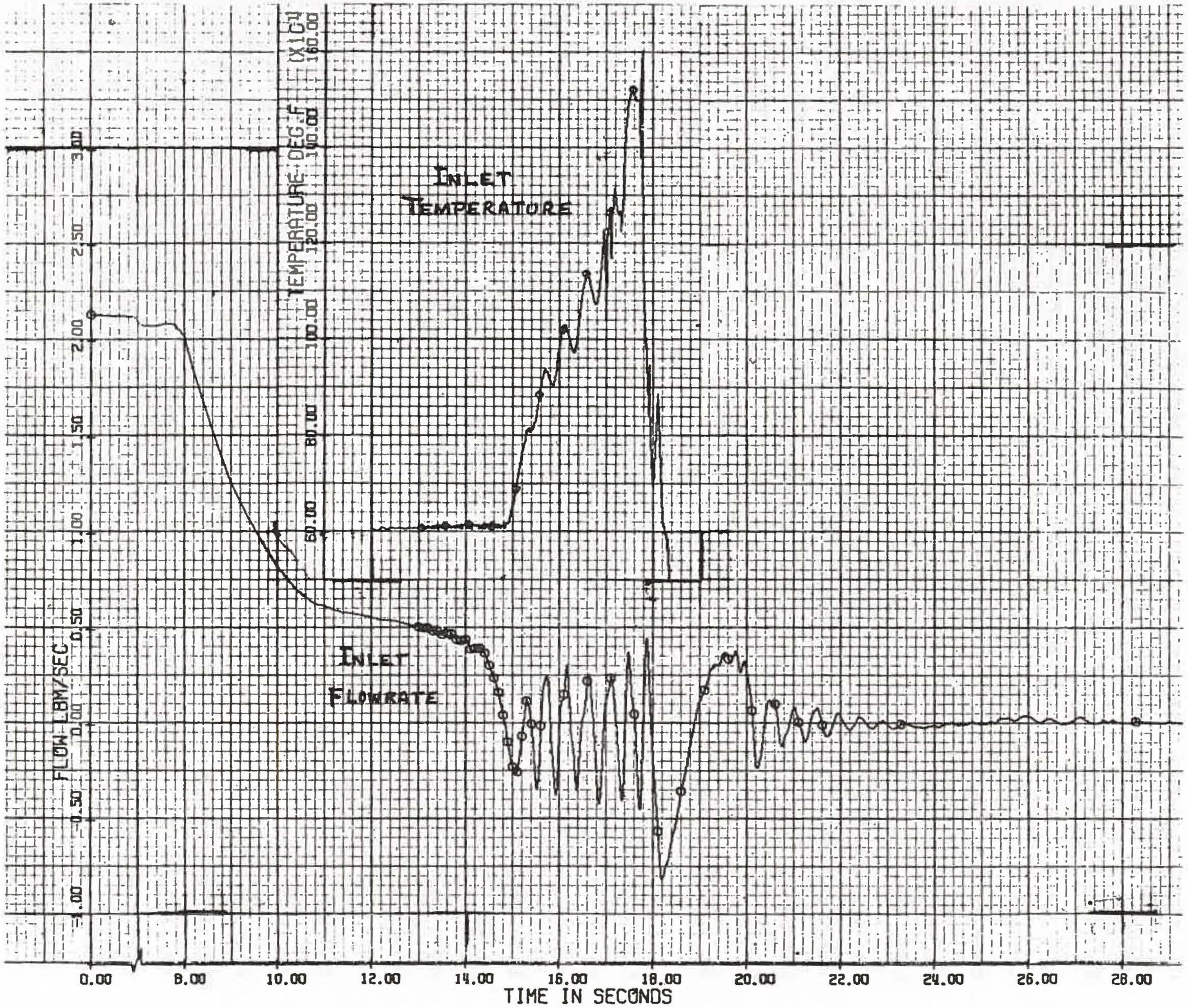

Fig. 23 R4 Test Data Illustrating Response of Intrinsic-junction TC Located at Entrance of Active Fuel Region.

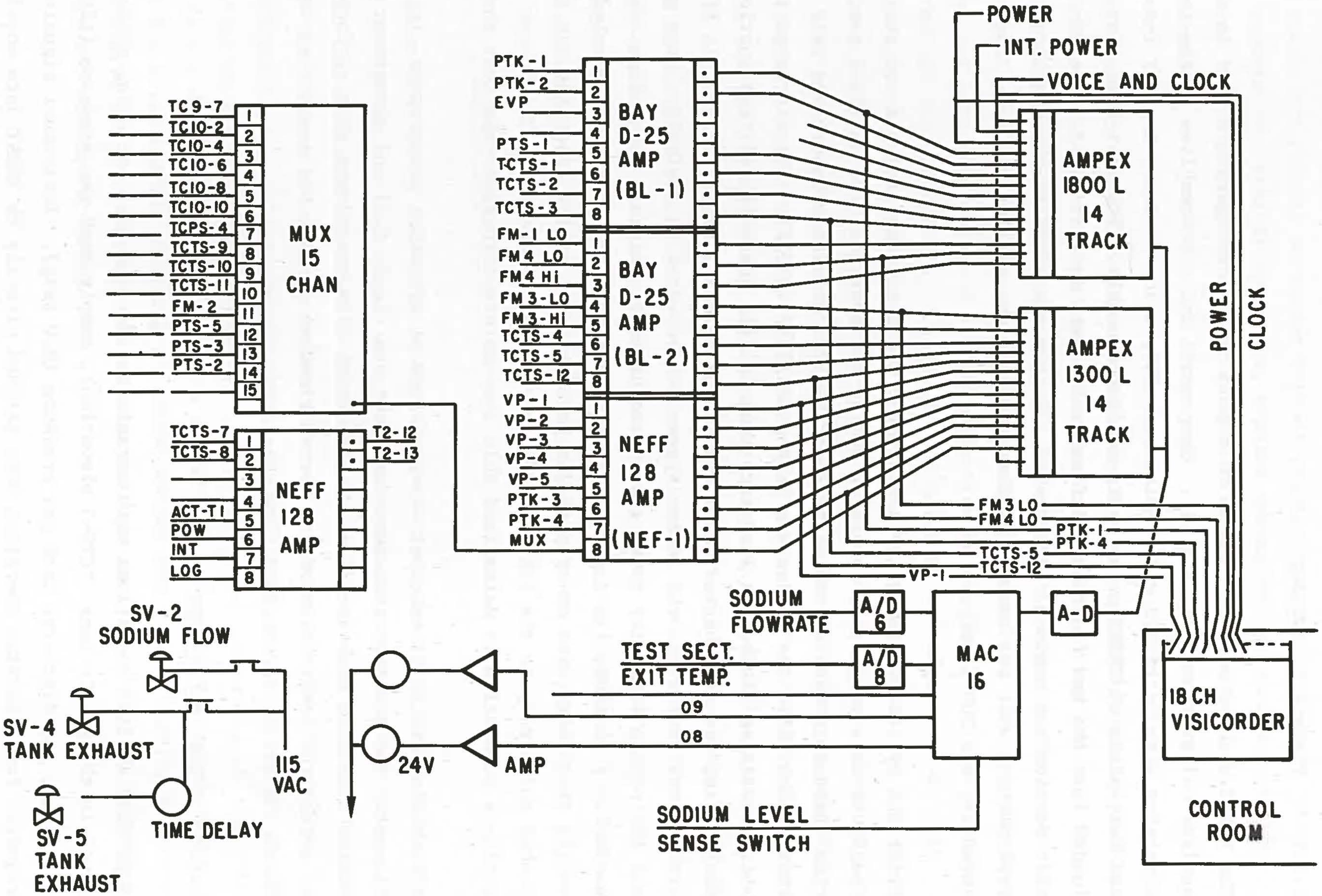

Fig. 24 Schematic Illustration of Data Acquisition and Experiment Control for R4 and R5.

2.8.1 Pretest Activities

The TREAT reactor core was loaded to reproduce the configuration used in the earlier calibration test, Fig. 17. Components and subassemblies of the test apparatus were outfitted with instrumentation, trace heaters, thermal insulation and heat sinks at TREAT prior to in-reactor assembly. The test fuel pins were loaded into the hex flowtube and final welds were made at TREAT. The completed test section was neutron radiographed. Sodium was added to the discharge tank, replenishing what was removed in components of the earlier R3 test. The sodium inventory was 200 liters.

After the system was secondary containment was sealed and inerted and preliminary checkouts were completed, apparatus heatup was started. The unfilled test section components were evacuated to less than 200 microns pressure and held at that vacumn while the system was heated to 177°C (350°F). The discharge tank, which contained the sodium inventory used to fill the unfilled test section components, was then heated until the sodium melted through. When this filling process was completed, the sodium system was returned to nominally 1 atm pressure, and the plenum simulator cover gas was adjusted to maintain the sodium level at nominally 5 cm above its discharge line elevation. The system was checked to verify that there were no trapped gas pockets. The entire apparatus was then heated uniformaly to the 316°C (600°F) operating temperature. The heater controllers automatically maintained this temperature throughout the test duration.

A complete functional checkout was performed at operating temperature, including flowmeter and pressure transducer calibrations (Sect. 2.6) and assessment of system hydraulic behavior (Sect. 2.4). Trial flow coastdowns were performed to select the combination of gas system blowdown nozzels and sequential valve operation giving the desired flow coastdown.

2.8.2 Test Activities

Apparatus initial conditions were established for the test including sodium level in the supply tank (TCTS-3 elevation), supply tank gas pressure (126 ± 2 psig), and discharge tank gas pressure (0.0 psig). Instrument signals not required for apparatus operation were patched directly to TREAT data acquisition.

A functional dry run was performed without reactor operation to check interfaces between test vehicle operation, reactor operation, and data acquisition equipment. Upon completion of test ready activities, the reactor building was evacuated.

The test sequence was initiated remotely from the control building, 1/2 mile away. Electrical power to the apparatus heaters was off during the test to minimize noise pickup. The test sequence illustrated in Fig. 25 was controlled automatically by the TREAT program timer and MAC-16 computer. The program timer started the data recorders and started execution of the MAC-16 initiated sodium flow through the apparatus by opening sodium valve SV-2. After a 7 sec wait the flowrate was sensed (using FM-1) to verify that it was within the prescribed flowrate window, 2.0 ± 0.4 lbm/sec., for a duration of 3.0 sec. Upon satisfying this condition, MAC-16 initiated the shaped power transient by transient rod withdrawl. After a 250 MJ initial preheat stage, both the sodium flowrate and the reactor flattop power were confirmed to be within their prescribed ranges, and the test was continued into the planned loss-of-flow stage. MAC-16 initiated the flow coastdown by opening supply tank blowdown valve SV-4. The reactor was scramed at the specified integrated power, terminating the test sequence. MAC-16 closed the sodium flow valve 30 sec later and stopped the data recorders 3 min. later. The apparatus heater power was restored.

2.8.3 Posttest Activities

Following approval by radiation protection personnel, test activities were resumed at the reactor building. An attempt was made to restore sodium flow through the apparatus in order to determine whether channel blockages were complet. The apparatus heater power was eventually turned off and the apparatus was allowed to cool to room temperature. Sodium, which typically reentered the test section after the test, froze during the cooldown, preserving the test debris intact during subsequent handling operations. Test R4 was one exception since the total channel plugging prevented sodium reentry. Following apparatus disassembly, the test section was neutron radiographed and placed in temporary storage for subsequent cutup.

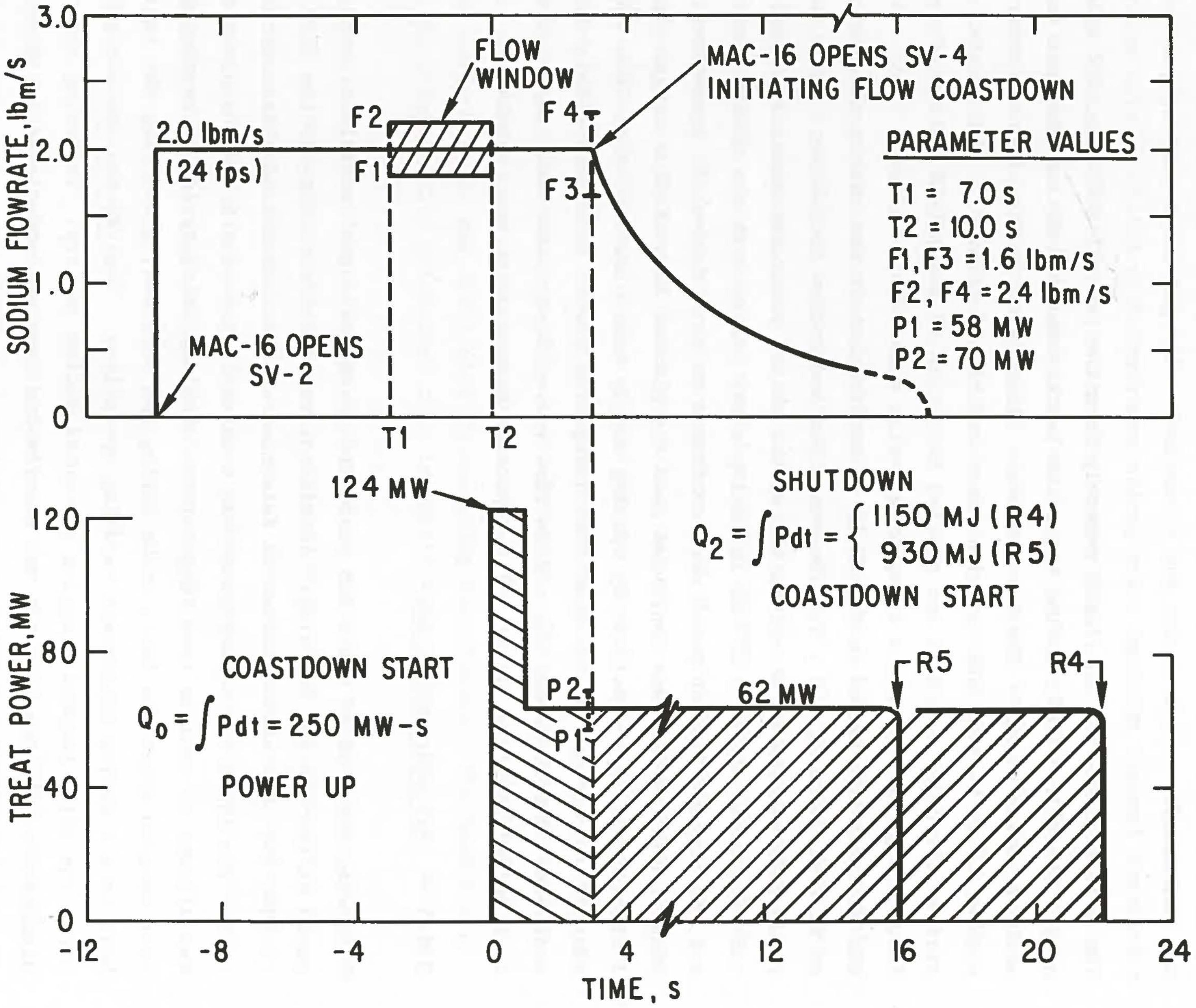

Fig. 25 Illustration of R-Series Automatic Experiment Control and Parameter Values.

2.9 Data Processing

The recorded data tapes were first scanned and duplicated. All channels were replayed onto the visicorder for preliminary examination. Subsequently, the analog data was digitized at sampling intervals ranging from 1 to 50 msec, depending upon the rate of signal change. The digitized data had the appropriate calibration factors applied for conversion to engineering units. The thermocouple data was reduced using a 4th order polynomial fitting of the Type-K thermocouple calibration. All data was plotted on a CALCOMP plotter and is included in Appendices C and D for tests R4 and R5, respectively.

3.0 TEST RESULTS

3.1 Summary of R4 Test Outcome

Test R4 was the first in the series of full-length seven-pin LOF-type tests to be carried out in the R-series apparatus at TREAT. The test was successfully performed November 9, 1973. The test sequence, test instrumentation, and data acquisition equipment functioned as planned with the exception of the loss of hodoscope data. This test was run at flattop power to the allowable limit of TREAT integrated power, resulting in substantial fuel melting and relocation. The timing of events established from this late termination test was used to plan the shutdown time for the R5 cladding relocation test which followed.

The TREAT reactor power for R4, TREAT transient #1527, is shown together with key test data in Fig. 26. The initial preheat stage of the transient, from power startup at 3.0 sec (TREAT program time) until start of the flow coastdown at 7.90 sec, brought the test bundle into quasi-steady thermal and hydraulic conditions representative of normal operation of an FTR high power-to-flow subassembly. The TREAT flattop power was approximately constant at 64.9 MW, corresponding to an average pin power of 28.3 kW. This nominal pin power lasted until 25.02 sec when TREAT reactor scram terminated the test sequence. The overall TREAT energy release was 1400 MJ, the maximum permitted for a shaped transient. During the flattop power operation, the programmed flow coastdown led to the destructive test sequence comprising coolant voiding, cladding dryout and failures, cladding melting and relocation, and fuel melting and relocation.

A summary of the timing of key test events is given in Table 10. The coolant flow coastdown was initiated at 7.90 sec, at which time the sodium inlet temperature was 327°C and the coolant velocity through the pin bundle was 7.15 m/s. Local sodium boiling was first detected at 13.15 s. A vapor bubble formed and collapsed from 13.8 to 14.1 s. Sustained channel voiding began at 14.15 s; at that time the coolant velocity was down to 1.83 m/s, 26% of the initial flowrate, and the rate of flow decay was 12%/sec. Inlet flow reversal (FR) followed 0.72 sec later at 14.87 sec. The first of the cladding failures was detected 1.13 sec after FR. The helium fill gas contained in the fuel pin fission gas

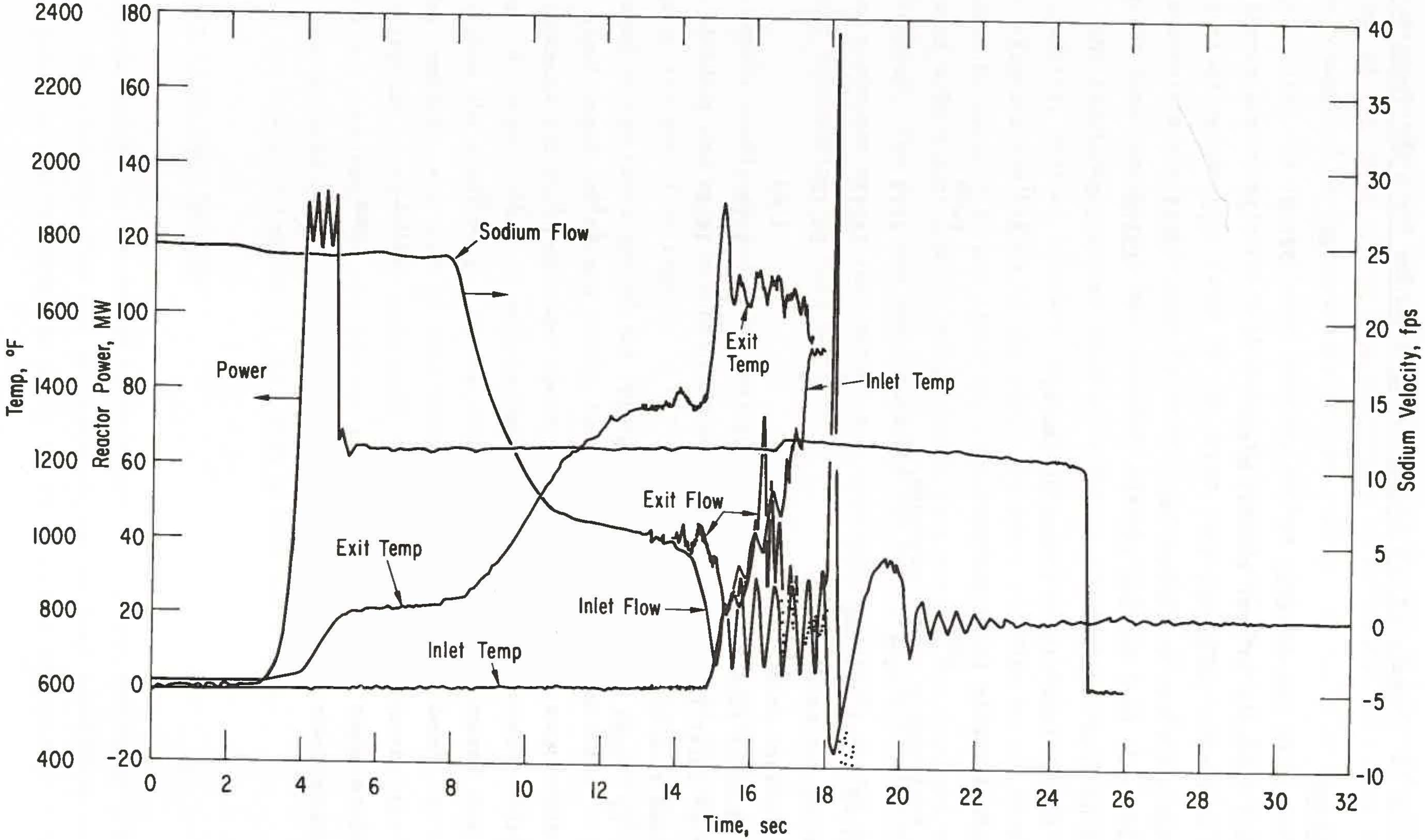

Fig. 26 Test Sequence for R-Series 7-pin Loss-of-flow Test R4, showing power, flow, and temperature history.

TABLE 10 Summary of Key Events During R-series 7-pin LOF Tests R4 and R5

Parameter	R4	R5
Coolant inlet temperature, °C	327.0	338.0
Coolant velocity in test bundle, m/sec	7.15	7.32
Time of reactor power up, sec	3.0	3.2
Average power/pin at flattop kw	28.3	28.3
Quasi-steady test section ΔT, °C	133.0	139.0
Start of flow coastdown, sec	7.90	7.95
Supply tank (inlet plenum pressure, atm	8.61	8.40
Fuel bundle inlet pressure, atm	6.88	6.67
Fuel bundle outlet pressure, atm	1.29	1.30
Onset of local boiling, sec	13.15	12.5
Onset of net voiding, sec	14.15	13.65
Coolant velocity, m/sec	1.83	1.83
Rate of flow decay, %/sec	12.0	12.0
Time of inlet flow reversal, sec	14.87	14.56
Elapsed time from FR to:		
i) onset of cladding failures (plenum gas release)	1.13	1.14
ii) upper cladding blockage	2.5	2.6
iii) flowtube failure	3.14	3.29
iv) lower cladding blockage	5.20	6.20
v) onset of fuel motion		
vi) power termination	10.15	4.45
Complete upper blockage	yes	no
Complete lower blockage	yes	no

plena was released into the vapor-filled channels, causing an enhanced upward displacement of the upper sodium slug but having no detectable influence on the sodium "chugging" at the lower active fuel region. As cladding melting began, shortly after the pin failures occured, molten cladding was swept upward by shear forces associated with high-velocity upward sodium vapor streaming. The molten cladding material froze in the upper insulator region of the pins creating a complete planar blockage by about 2.5 sec after FR. About 0.6 sec later a major flow pertubation was recorded, caused by failure of the hexagonal flowtube. The flowtube structure eventually melted along with the remaining fuel pin cladding, drained downward under gravity influence, and solidified in the lower reflector rod region of the pin. The lower blockage became complete and permanent by about 5.20 sec after FR. The test continued at full power for an additional 4.95 s during which considerable fuel melting and downward relocation occured. The fuel was constrained at the bottom by the thick pool of accumulated stainless steel; fuel motion was constrained radially by the molybdenum liner surrounding the test section.

The final debris configuration found during posttest examination showed that the steel cladding and structure had been completely removed from the upper two-thirds of the test fuel region. A 0.3 cm thick complete planar steel blockage was found at the elevation of the upper insulator pellets. At the bottom a massive steel ingot had formed within the moly liner which was about 15 cm in overall thickness and which extended about 5 cm down into the lower reflector rod region. A large clinker of once-molten fuel was found atop and partially imbedded within the steel plug. In the vicinity of the fuel midplane the fuel melting was complete, and most of this material had drained downward leaving a thick, irregular crust on the moly wall. In the upper fuel pin region, fuel melting was not complete, but was limited to varying degrees of pellet center melting. The sintered pellets retained their stacked configuration despite the melting and downward removal of fuel from within the stacks.

3.2 Summary of R5 Test Outcome

Test R5 was the second in the series of R-series full-length seven-pin LOF-type tests. The test objective was to reproduce the R4 test conditions as closely as possible and to terminate early in the sequence to preserve evidence of early cladding relocation. The test was successfully performed December 6, 1973. The test sequence, test instrumentation, and data acquisition equipment functioned as planned.

The TREAT reactor power for R5, TREAT transient #1528, is shown together with key test data in Fig. 27. The power and flow conditions were almost identical to R4. Figure 28 shows a comparison of the inlet flowrate behavior for the two tests which illustrates the very close similarity. In general, the R5 test sequence was nearly identical to the R4 sequence up to the time of R5 termination, about 5.7 s earlier (after FR) than R4. The test objective was achieved in the sense that extensive cladding melting and relocation took place while little trace of fuel melting was found.

As in the R4 test, the average pin power was 28.3 kW. The TREAT energy release at the reactor scram time of 19.0 s was 1038 MJ. The summary of event timing is given in Table 10 together with the R4 results. The coolant flow coastdown was initiated at 7.95 s, at which time the sodium inlet temperature was 338°C and the coolant velocity through the pin bundle was 7.32 m/s. Local sodium boiling was first detected at 12.5 s. Sustained channel voiding began at 13.65 s, at which time the coolant velocity was down to 1.83 m/s and the rate of flow decay was 12%/s. Inlet flow reversal (FR) followed 0.91 s later at 14.56 s. The pin failures and resulting helium fill-gas release began at 1.14 s after FR, and appeared nearly identical to R4 data. The upper cladding blockage formed at about 2.6 s after FR, and 0.7 s later the same major flow perturbation was recorded as occured in R4. This event was attributable to failure of the thin-walled hexagonal flowtube which permitted nitrogrn gas to enter the channel from the surrounding instrumentation annulus. Test data showed that the channel pressurization upon failure was about 1.3 atm, resulting in downward expulsion of the lower sodium slug which had been undergoing chugging oscillations at the bottom of the active fuel region. Reactor power scram terminated the test sequence 1.16 s later. Test data indicates that the molten steel which was relocating downward formed a solid plug at about 6.20 s after FR (1.75 s after power termination).

The final debris configuration showed that steel cladding and structure had been completely removed from the upper two-thirds of the test fuel region. A

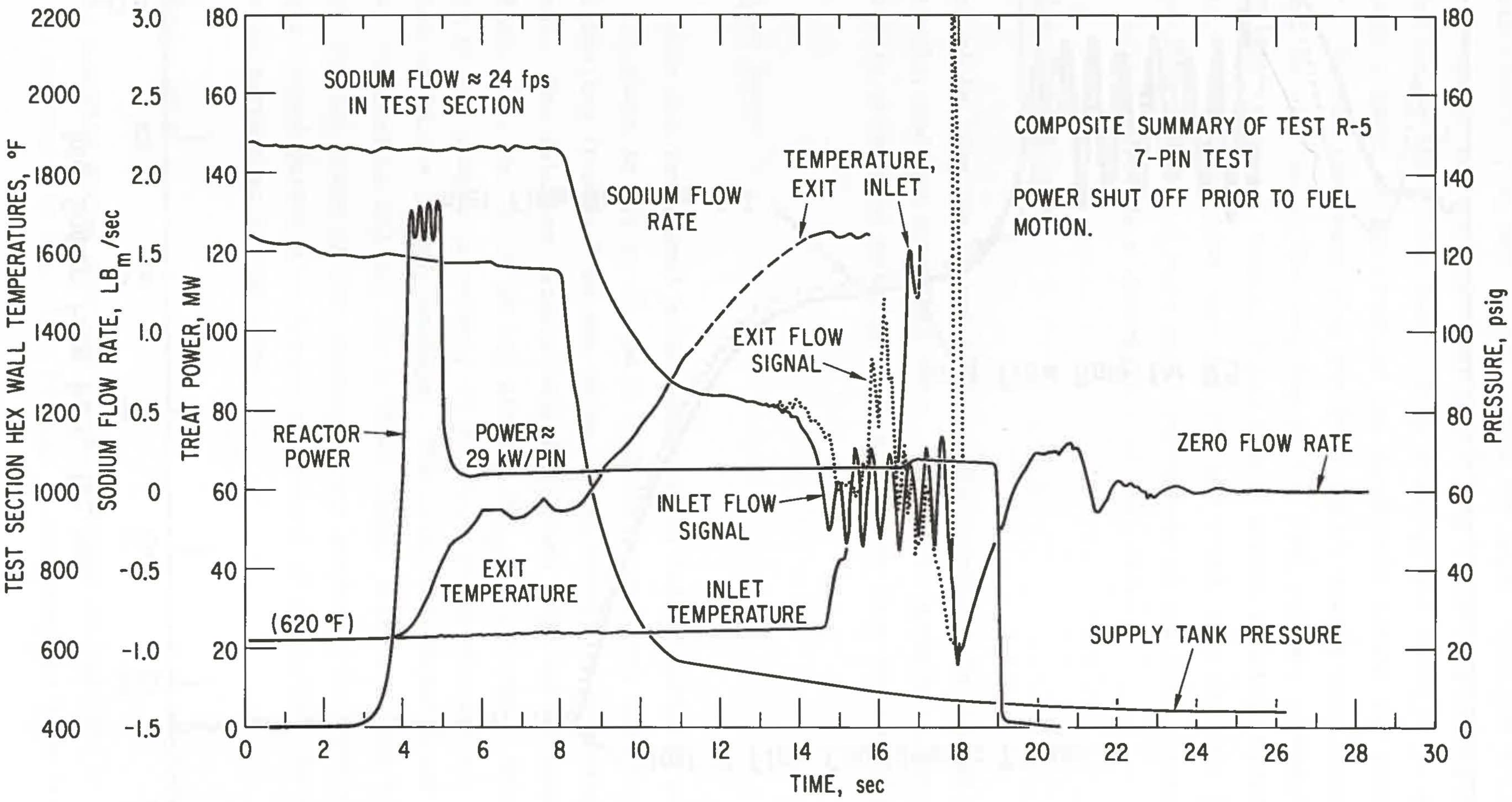

Fig. 27 Operating Sequence for R-Series Loss-of-flow Test R5 illustrating flow, power, temperature, and supply tank pressure variation during experiment sequence.

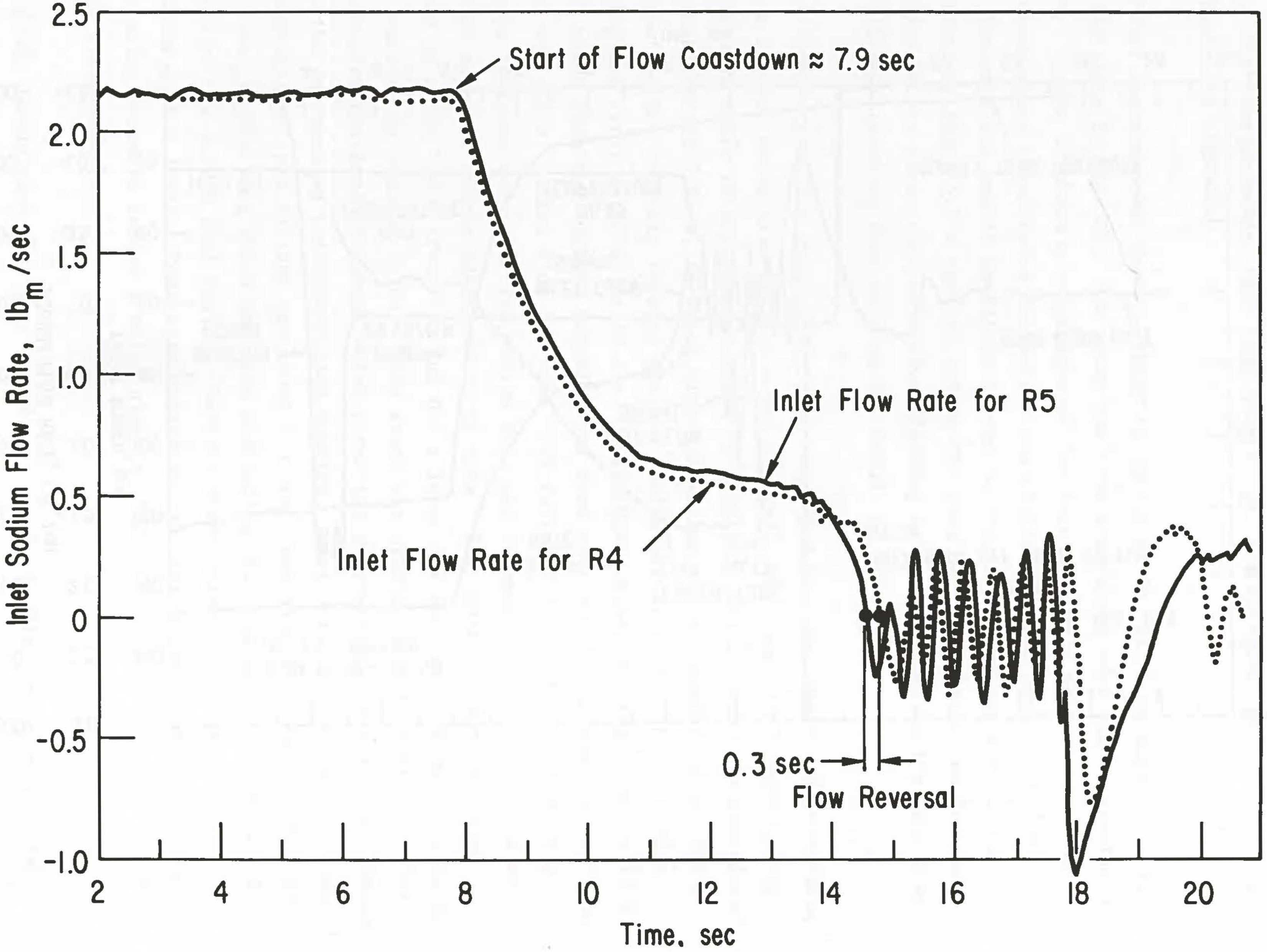

Fig. 28 Comparison of Inlet Flowrates for R4 and R5.

thin, incomplete channel plug was formed around the upper insulator pellets. Some holes were evident in plug. A lower steel plug of about 8 cm depth was found at the bottom of the active fuel. This blockage was found to be nearly complete although a small sodium flowrate was measurable during the posttest reflow attempt. Within the lower plug the fuel pellet stacks were intact. Above this plug, as well as at the very top of the fuel column, considerable pellet jumbling had occured. Intact, fused pellet stacks remained between the jumbled pellets. Some centerline fuel melting was found, particularly for the center pin, but this involved a very small percentage of the fuel present. The following sections provide a description of test data.

3.3 Description of Test Data

Individual data plots from the R4 and R5 tests are presented in Appendices C and D, respectively, and are described here. The square symbols on several of the data plots were printed at every 50th data point to show the sampling time intervals.

3.3.1 Reactor Power

TREAT reactor power and integrated power, measured by meters SAFETY-1 and INT-1, respectively, are shown in Fig's. C1 and D1. These meters were used consistently during the calibration irradiations and tests as the basis for assessing test fuel power level. The relation between test fuel power and reactor power, as described in Sect. 2.5, was 0.436 kW per pin per MW_{TREAT}, average. Hence the flattop portion of the shaped transient, 65 ± 3 MW, corresponds to test fuel power generation of 28.3 ± 1.3 MW, average. The total integrated power was 1400 MJ for R4, the maximum allowed for a TREAT shaped transient, and 1038 MJ for R5. The initial stage of the transients was programed for nominally 2X power for one-second duration to hasten attainment of prototypic fuel temperature and to conserve reactor run time.

3.3.2 Pressure Data

System pressure behavior during both the R4 and R5 tests is typified by the R4 data shown in composite in Fig. 29. Details of the pressure behavior are

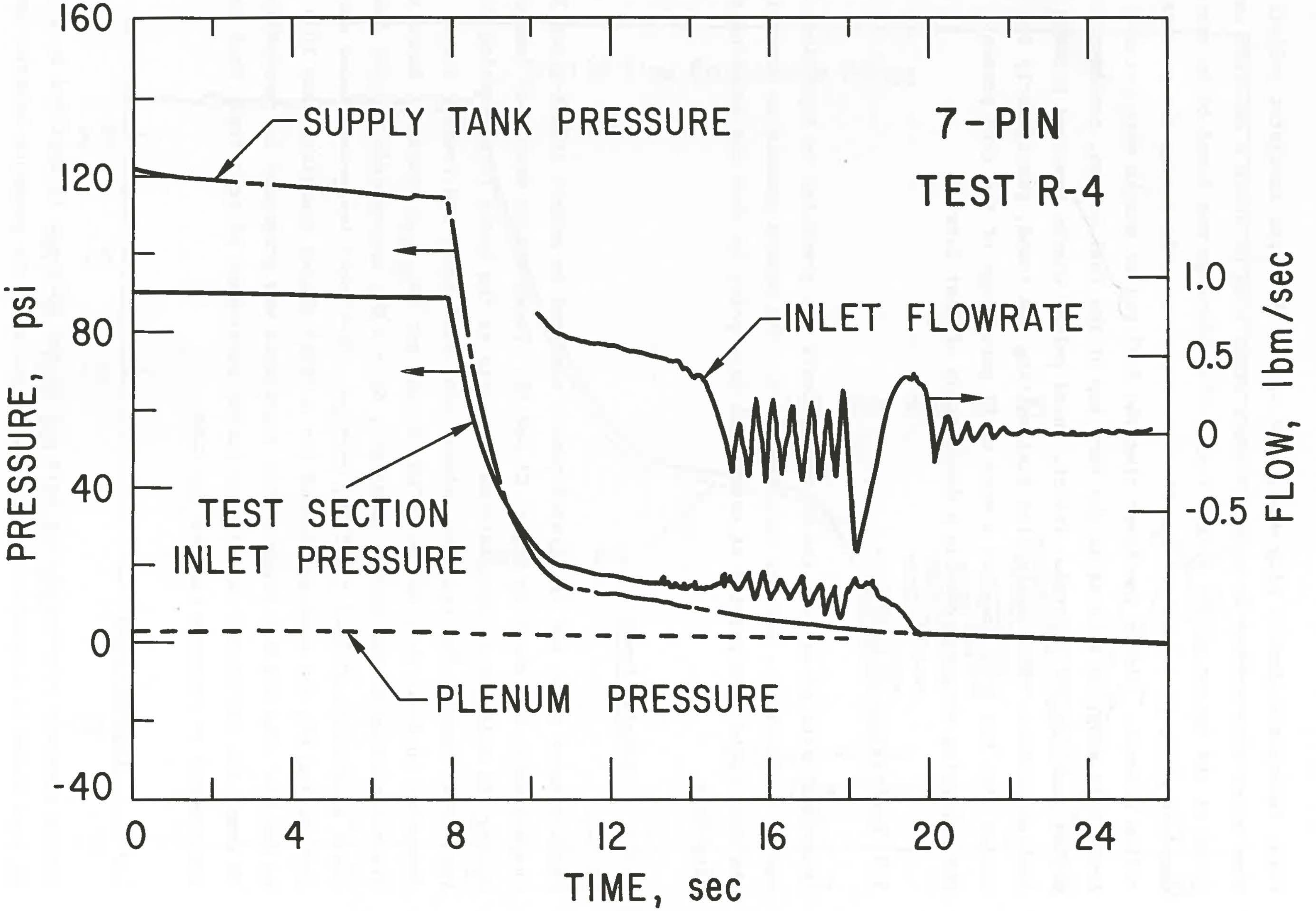

Fig. 29 Composit of R4 Pressure Data.

shown in the individual data plots in Fig's. C2 through C5 and D2 through D5 for R4 and R5, respectively. The supply tank pressure is equivalent to the inlet plenum pressure in the reactor system. The nitrogen driver gas pressure was initially set at 0.99 MPa (142.7 psia) with the sodium flow valve closed. When the flow valve was automatically opened during the programed test seqence, the system pressure differential drove sodium through the once-through test apparatus. At zero test time in the data plots, the sodium valve had already been opened and sodium had been flowing through the system for about 5 s. The slight decrease in supply tank pressure during this initial full-flow stage reflects the increasing volume of the fixed gas mass in the tank as the sodium was discharged through the system. At t = 7.95 s, when the supply tank pressure was 0.86 MPa (124.6 psia), the flow coastdown stage of the test sequence was entered. The supply tank blowdown valve SV-4 was automatically opened by MAC-16 command initiating the tank depressurization. As indicated by the data, the depressurization was initially rapid, occuring through both nozzels N1 and N2 (shown in the apparatus gas system schematic, Fig. 30). At a preset delay time of 1.1 s, valve SV-5 was closed, leaving only the smaller N2 nozzel for continued blowdown. This produced the desired gradual coastdown rate as the destructive stage of the transient was entered. Eventually, the supply tank depressurized to ambient pressure, 0.086 MPa (12.6 psia). Events occuring in the test section such as sodium voiding and channel pressurization had no effect on the system driving pressure since the flow bypass rates for a gas-driven system is effectively infinite.

Figures C3 and D3 show the pressures in the sodium discharge tank (PTS-3) and in the plenum simulator, 3 m above the test fuel bundle. The initial cover gas pressure in the discharge tank was atmospheric, 0.086 MPa (12.5 psia). The tank exhaust valve, SV-7, was closed during the test so that sodium which accumulated in the tank during the course of the test resulted in a gradual pressure buildup. The amplitude fluctuation exhibited by the data reflects signal noise which appears large on the expanded amplitude scale of these data plots.

The plenum simulator region of the test apparatus represents the upper plenum region of the reactor system, having both a very large coolant area expansion from the pin bundle (40-to-1) and a sodium/cover gas free surface. The level

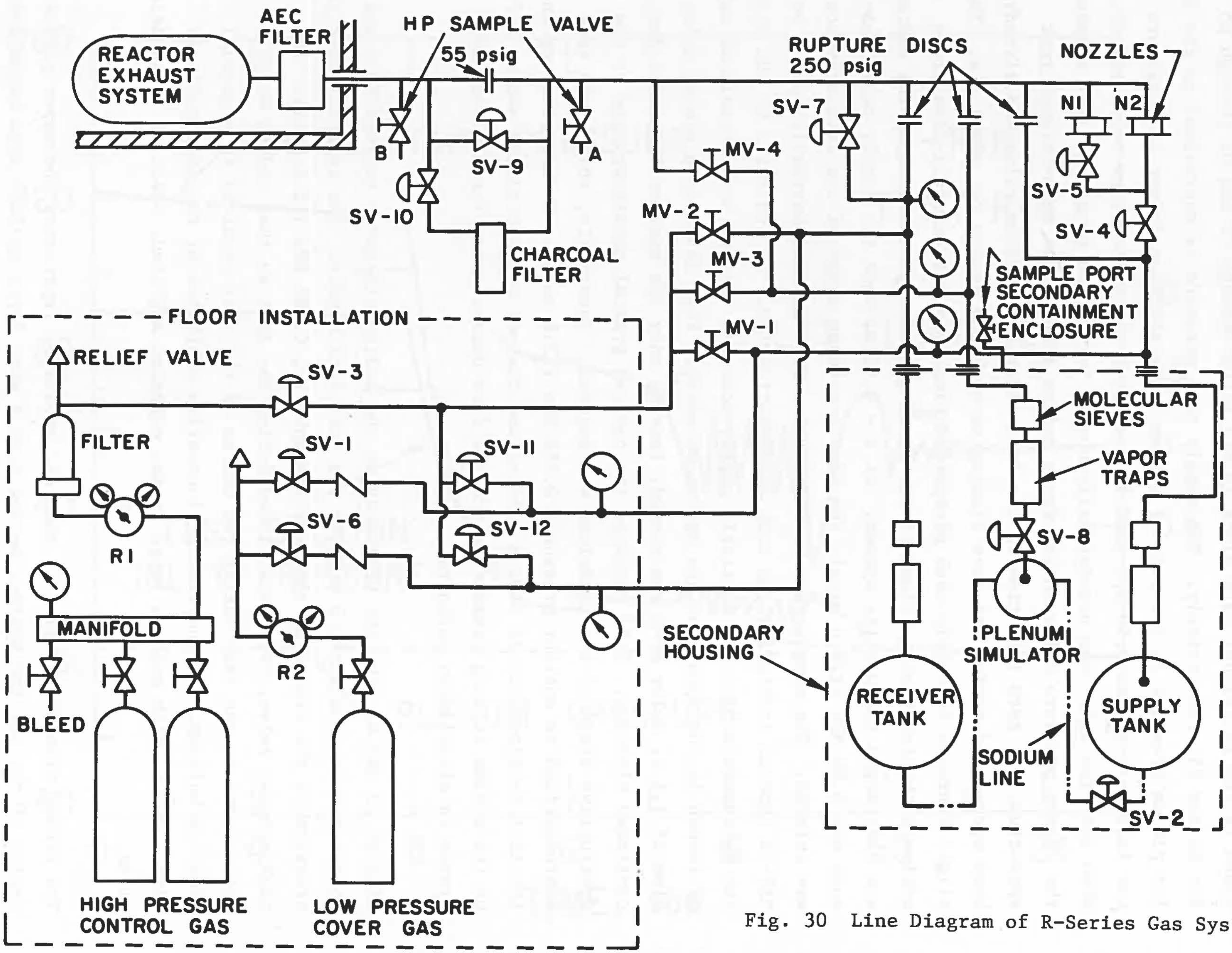

Fig. 30 Line Diagram of R-Series Gas Systems.

of sodium in this component was about 5-10 cm above the discharge line elevation. The cover gas pressure was approximately constant at 0.1 MPa following the flow coastdown until the sodium expulsion from the test section at about 17.8 s. The measured pressurization to about 0.12 MPa was caused by the sodium expelled into this upper plenum compressing the fixed volume of cover gas. The plenum simulator pressure eventually returned to near normal as the sodium was discharged toward the receiver tank.

Figures C4 and D4 show the transient pressure measured by PTK-1 between the inlet flow restrictor and the entrance to the pin bundle. This fast response pressure sensor was flush-mounted at the inside of the sodium pipe for optimal transient performance. However it was found that temperature variations in the flowing sodium, even when very mild, would introduce transient diaphram heating effects which were not compensated out in this otherwise temperature-compensated transducer. Hence the test data contains DC drift in addition to the expected pressure response. The temperature-drift effects were relatively slow and did not detract from interpretation of the transient pressure events although the DC pressure magnitudes may be slightly in error. The test data shows the inlet plenum depressurization starting at about 7.9 s. At about 13 s small pressure pertubations were recorded, indicative of sodium boiling in the test section. At about 13 s small pressure pertubations were recorded, indicative of sodium boiling in the test section. At about 14 s the pressure began to rise noticeably, reflecting the buildup of vapor pressure in the pin bundle and the corresponding deceleration of the inlet flow as it approached reversal. The sodium "chugging" pressure oscillations are visible from about 15 to 18 s. The peak-to-peak pressure amplitude was about 0.05 MPa (7 psia), and their frequency was about 2.2 Hz. The chugging oscillations were interrupted just prior to 18 s when the thin-walled hyxagonal flowtube failed. In both tests the flowtube failure resulted in noncondensible gas from the surrounding instrumentation annulus entering the previously-voided channels. In R4, the breech occured at a high-pressure peak of the chugging oscillations. The measured incremental pressurization was about 0.02 MPa (3 psi) above the peak. This higher channel pressure was sustained for about 0.6 s before the pressure began to decay away. The channel pressure was higher than the average level prior to failure for a duration of about 1.0 s. In the R5 test, the flowtube breech occured during a low-pressure phase of the chugging oscillations, and in this case the channel abruptly pressurized by about 0.12 MPa (18 psi). Again, the pressure was higher than the prefailure average for about 1.0 s. During this interval of channel overpressurization, sodium was expelled both upward and downward away from the test bundle. The sodium at the inlet eventually reversal direction and re-approached the pin bundle after the thimble gas pressure had been relieved.

Data from the bundle-outlet pressure transducers is shown in Figs. C5 and D5. This data is plotted in the form of raw millivolt output since transient temperature effects dominated the signal output for these downstream transducers. The data has been included to illustrate that there were no significant pressurization events measured downstream.

3.3.3 Flowrate Data

System flowrate data is shown in Figs. C6 through C9 and Figs. D6 through D9 for R4 and R5. The initial mass flowrate through the system was about 0.95 kg/s, corresponding to a bundle velocity of 7.6 m/s. Upon supply tank depressurization, the flowrate coasted down, initially rapidly, to about 2.4 m/s at 10.8 s. At that time the coastdown rate was reduced to about 12% s, nominally matching the FTR coastdown behavior.

Expanded analog data records showed mild bursts of oscillatory flow behavior, interpreted as local subcooled boiling, beginning at 13.15 s for R4 and at 12.50 s for R5. This stage of local boiling lasted for about 1 s. The analog records showed net divergence of inlet and outlet flowrate data, interpreted as net void growth, beginning at 14.15 s for R4 and at 13.65 s for R5. At that time in the test sequence the inlet flowrate was down to 1.83 m/s, 24% of the initial full flowrate, and the pressure at the top of the active fuel region was 0.15 MPa. The corresponding sodium saturation temperature was 903°C (1655°F).

In test R4, 0.72 s elapsed from the time of net void production to reversal of the inlet flowrate at 14.87 s. In test R5, the elapsed time was 0.91s to reversal at 14.56 s. The test data shows that the inlet sodium column began oscillating after reversal. The sodium velocity during the chugging stage was approximately -0.2 ± 1.2 m/s. Hence there was a slow, downward net motion of the sodium slug. Physically, the sodium interface level was oscillating upward and downward approximately ±12 cm about its mean, as the mean level itself was slowly moving downward. The period of oscillation was approximately 0.45 s, as described previously for the corresponding pressure behavior.

The chugging oscillations were abruptly halted just prior to 18 s by the flowtube failures. The ensuing channel pressurizations accelerated the inlet slug downward out of the pin bundle. In R4, the downward expulsion continued for about 0.9 s until at t = 18.9 s the slug reversed direction and began reapproaching the test fuel bundle. The maximum approach velocity was 1.2 m/s (in terms of equivalent bundle flowrate). At about 20.0 s the rate of return was sharply diminished, and thereafter the inlet sodium slug exhibited a damped oscillation to quiescense. It is interpreted that the disruption of test section geometry caused by melting cladding and structure resulted in a complete (and permanent) inlet blockage at that time. The inlet blockage, which formed before the sodium could reenter the pin bundle, trapped noncondensible gas below it, permitting the sodium column to oscillate between the supply tank and the trapped gas pocket.

The situation was very similar in the R5 test, despite the earlier power termination at 20.0 s. The data shows a more rapid and larger overall sodium expulsion, attributable to the higher channel pressurization at flowtube failure. The sodium reversed direction and began reapproaching the test section at 19.4 s. The return flowrate was smooth until, at about 20 s (the time the R4 inlet blockage became complete), a noticeable disturbance caused the flowrate to temporarily level off. Since the test fuel power was now terminated, any subsequent material motion would occur on a lengthed time scale since there was only stored energy for continued cladding melting. At about 21 s the inlet flow began to diminish and thereafter showed a damped oscillation to quiescence. The blockage was estimated to have become essentially complete at about 20.76 s.

Figures C7 and D7 show the test section exit flowrate measured by FM-3. This data tracked the inlet flowrate almost perfectly, as expected, until the time of net channel voiding at 14.1 s (R4) and 13.6 s (R5). At those times, the bundle outlet flow began to level off while the inlet flow continued to diminish, reflecting the void formation and growth in the coolant channel. The upward void growth continued for about 0.4 s past the time of inlet flow reversal, at which time the upper slug velocity went to about zero. At that time the liquid/vapor interface was located near the tops of the pins. The upper slug remained approximately stationary for an additional 0.5 to 0.6 s, until, at approximately 15.7 s, the upper sodium slug again began to be displaced upward.

This renewed upward motion was caused by failures of the fuel pin cladding which released helium fill gas into the previously-voided, vapor-filled channel. There was no significant channel pressurization since the fuel pins were nominally unpressurized. (The pin internal pressure would not have exceeded about 0.4 MPa at this stage of the transient). The released noncondensible gas had no detectable influence on the chugging behavior of the inlet slug; it mearly caused an upward displacement of the upper sodium slug as it expanded toward the upper plenum. The upward growth of the vapor/fill gas lasted for about 1-2 s before the gas release effects ceased. Thereafter, in test R4, there was minor downward motion of the upper slug, although for all practical purposes it was quiescent. In test R5, the net downward motion of the upper slug was more pronounced during this time interval. This lasted until flowtube failure just prior to 18 s. The failure caused abrupt upward expulsion of the upper sodium slugs. Figures C8 and D8, showing the FM-3 data on a compressed scale, show that the ejection was very rapid, peaking at about 3.6 and 7.4 times the initial full flowrate for R4 and R5, respectively. As the expanding gas and vapor passed upward through the flowmeter pipe, the normal flowmeter signal was lost. The negative-going signal level that followed does not represent slug reentry, but rather upward passage of gas and vapor and simultaneous downward draining of the sodium film on the inside surface of the pipe. This type of behavior was exhibited intermittantly for the duration of the test. The flowmeter signals eventually returned to zero after the test.

Figures C9 and D9 show the sodium flowrate from the plenum simulator to the discharge tank measured by FM-2. This data tracks the system flowrate almost perfectly except for a large degree of damping introduced by the cover gas volume in the plenum simulator. The two expulsion events after the coastdown were caused first by the pin failures and secondly by the flowtube failure.

3.3.4 Thermocouple Data

Test section thermocouple data is shown in Figs. C10 through C19 for R4 and D10 through D19 for R5. These intrinsec-junction, fast response TC's were located along the outside surface of the thin-walled flowtube at axial positions illustrated in Fig. 10; their distances above the active fuel entrance are given in the figure captions.

In general, the TC data reflects the axial variation of bundle heatup during the quasi-steady and flow coastdown stages of the test. The occurance of voiding is typified by a plateau wall temperature of near T_{sat}, approximately 900°C (1650°F) for the R4 and R5 test conditions. Where applicable in the active fuel region, the TC's also indicate the time of film dryout as the wall heatup resumed beyond T_{sat}, the ensuing structure heatup toward steel melting, and occasionally transient wall heatup associated with molten cladding moving within the test bundle and bridging to the adjacent wall. Up until the time of sodium voiding, the wall TC's effectively measured the temperature of the sodium in the subchannels of the bundle adjacent to the wall with about a 40 ms time constant. The bundle assembly tolerance of nominally 5 ± 4 mils permitted some lateral motion of the pins within the flowtube. This resulted in local variations of cooling along the wall subchannels, and is evidenced in test data by occasional abrupt or cyclic temperature variations. After sodium voiding, the measured wall dryout and heatup necessarily lagged behing the corresponding cladding dryout and heatup within the bundle.

Failures of the intrinsic-junction thermocouples inevitably occured at or prior to the structure melting. Early failures (regarded as occuring prior to structure dryout) noted on several of the TC's were attributable to thermally induced distorsions of the test section assembly caused by both the rapid bundle heatup during the flow coastdown and, additionally, by radial and azimuthal temperature variation brought about by pins "snaking" within the bundle. This severe bundle straining, which has also been noted from both TC and hodoscope data for other R and L-series LOF tests, results in premature TC failures by breaking one or both of the TC wires at their point of attachment, or by causing the wires to short to one another or to the sheath away from the intended junction location. Certain of these possible failure modes causes an upward or downward shift in the output, but still permits qualitative assessment of voiding and dryout occurances. Other TC failures, typically lower in the bundle, may reflect either a burn thru of the sheath higher in the bundle or a draining of molten steel material onto it from above.

In general, the R4 TC data was of good quality. Only two thermocouples, TCTS-8 and -9, appeared to fail prematurely in the sequence. However, the R5 data shows numerous ambiguities attributable to erratic TC performance, and the discussion of temperature data will principally involve the R4 data.

Thermocouple TCTS-1 (Fig. C10), located 30-cm above the top of the active fuel shows the initial system temperature to be about 339°C (620°F) prior to the start of reactor power. The preheat stage of the power operation increased the outlet temperature by about 110°C within 1.5 s of power startup. By the time the flow coastdown had started at 8.0 s, the outlet temperature had risen to 460°C (860°F). Thereafter the upper structure heated at about 56°C/s during the flow coastdown. At the time of initial channel voiding in the test section, 14.2 s, the upper structure was still subcooled, at about 748°C (1380°F). The interval of data from 15.3 s to 16.6 s appears to be anomolous. During this interval channel voiding had progressed upward past the location TCTS-1, and the convected sodium should have heated the wall to T_{sat}. By 16.6 s the TC appears to be properly functioning and has leveled off at approximately T_{sat}, indicating the presence of a liquid film on the inside surface of the structure. The structure cooled gradually from the time of the flowtube failure at 18 s.

The data from TCTS-2 (15-cm above the top of the active fuel) shows a very similar trend as TCTS-1, although it apparently malfunction from 14.8 to 16.2 s. TCTS-3 (7.5-cm above the active fuel top) functioned properly throughout the test duration. The wall temperature first reached T_{sat} at about 14.4 s, 0.2 s after the start of net channel voiding. There was no indication of structure dryout at this elevation. TCTS-4 (2.5 cm above active fuel top) appeared to function properly during both R4 and R5 throught the time of flowtube failure. In the R4 test, Fig. C13, the hex flat upon which TCTS-4 was located appeared to be consistently overcooled until the time of flow reversal at about 18.8 s. At that time, the TC indicated a sharp increase past T_{sat}, followed closely by a return to near T_{sat}. It is not clear whether this was a TC anomoly or indicated a sudden change in the positions of the pins inside the bundle, going from an overcooled to an undercooled condition at the TC hex flat. The R5 data, Fig. D13, approached T_{sat} smoothly, first reaching that plateau at about 14.4 s, 0.16 s prior to the time of flow reversal. The temperature data from both tests showed an oscillatory behavior about T_{sat} for about 2 sec, with the frequency of oscillation matching that of the inlet flowrate chugging. Film dryout was not indicated at this TC elevation.

The R4 TCTS-5 data (at the top of the active fuel) shows that T_{sat} was reached at about 14.8 s, 0.2 s earlier than at the TCTS-4 elevation. This data also exhibits the film temperature oscillations up to 17.4 s when a 200°C temperature spike was recorded. This spike does not appear to have been an anomoly. Indications are that it was caused by molten cladding motion within the test bundle. Thereafter, the wall heated up monotonically toward steel melting, typical of TC data recorded within the active fuel region. Similar behavior was evidenced by TCTS-7 located 7.5 cm down into the active fuel region. The saturation temperature was first reached momentarily at 14.4 s, and was sustained by 15.2 s. Again, the film "sloshing" oscillations were evident up to 17.3 s when a 180°C temperature spike was recorded. The spike occured 0.1 s earlier than at TCTS-5, 7.5 cm higher in the bundle. Following the temperature spike, there was indication of immediate dryout and structure heatup. The TCTS-7 data from test R5, Fig. D15, shows a downward offset in the TC output, but otherwise appears to be functioning qualitatively correctly from 14.8 to 17.3 s. This interval of data also shows the film "sloshing" oscillations and additionally shows a temperature spike at 170 s, about the same time as recorded in R4. Hence there appears to be very consistent temperature behavior measured during the two tests, and the temperature spike at about 17 s, shown by three TC's near the top of the active fuel region appears to be indicative of a physical occurance inside the test bundle; ie, molten cladding motion.

Figure C16 and D16 show data from TCTS-10, located at the active fuel midplane. Data from both tests shows cyclic temperature variations during the flow coastdown stage of the transient which were probably caused by fuel pin motion inside the flowtube. The data indicates that at the time of inlet flow reversal at 14.9 s, the coolant temperature at the fuel midplane was about 670°C. At 15.8 s the temperature abruptly increased to the saturation temperature as the downward voiding progressed past the midplane. The temperature oscillated about T_{sat} for an additional 2.0 s as the sodium film sloshed up and down on the flowtube inside wall. At 18.0 s, simultaneous with flowtube failure, the wall resumed heatup, indicating the sodium film had either dried out or been stripped from the surface. The measured wall heatup lasted for 1.0 s until TC failure occured at just slightly less than the wall melting temperature.

Temperature data at the entrance to the active fuel region is shown in Fig's. C17 and D17. The measured temperature was basically that of the sodium entering the pin bundle and was constant up to the time of inlet flow reversal. Upon flow reversal, sodium which had been heated in the active fuel region was expelled downward past the bundle entrance elevation. The downward chugging oscillations are evidenced in the test data by wall temperature oscillations.

3.4 Neutron Hodoscope Data[17]

Hodoscope film data from test R4 was lost due to improper development by the commercial photoprocessor. As a result of this incident, extensive steps were taken to augment hodoscope data acquisition and data processing procedures in order to avoid a future reoccurance.

The R5 hodoscope data showed that the bundle underwent a coherent "snaking" prior to scram. The coiling increased after scram, and the delayed-neutron data indicated that a final warped configuration was reached within a few seconds. As anticipated for this early termination test there was no evidence of fuel slumping within the 48 cm (19-in.) viewing area centered on the test fuel midplane.

3.5 Preliminary Posttest Examinations

Immediately following the tests, efforts were made to restore sodium flow through the test apparatus in order to assess the completeness of channel blockages. With the sodium flow valve initially closed, the supply tank was pressurized to 0.17 MPa (25 psid). The valve was reopened and flowrate data was recorded at the inlet and outlet of the test bundle. In both the R4 and R5 tests there was an initial surge of sodium flow toward the bundle as the gas trapped below the inlet blockage was compressed. In the R5 test, the volume of trapped gas was calculated to be about 280 cm^3. A small net flow of sodium through the bundle was eventually established for R5, indicating that neither the inlet nor outlet blockage was totally complete. However a simple pressure drop calculation suggests that the inlet blockage effectively plugged greater than 99% of the original flow area. In the R4 test, no net flow of sodium could be established through the bundle.

The system was cooled to room temperature and was partially disassembled to enable the test train to be relocated from the central core slot to the radiography position. Following radiography, the test sections were eventually cut into 61-cm lengths and sent to the ANL-W Analytical Laboratory for preliminary disassembly and inspections. In the R5 test, the test section was found to be filled with sodium which had entered during the reflow operation and had frozen during the cooldown stage. The sodium was melted out of the various segments prior to making the longitudinal cuts on the moly liner which barred the test remains. In the R4 test, there was no sodium in the test section between the lower and upper blockages. Additionally, there was no sodium in the segment above the upper blockage, indicating that surface tension effects prevented the sodium from returning downward through the upper fission-gas plenum regions of the pin bundle to cool the upper side of the upper blockage. Photographs of the R5 test debris and the upper cladding blockages found in both tests are shown in Figs. 31 through 33.

The neutron radiograph, Fig. 34, shows that negligible fuel or steel was relocated below the active fuel region in the early termination R5 test. Molten cladding drained downward and solidified among the intact fuel pins in the bottom 15 cm of the active fuel region forming a lower plug. Above this, region 4 in Fig. 34, the fuel pellets were completely jumbled for a height of about 13-cm. A photograph of the segment above this is shown in Fig. 31. This photo spans the upper two-thirds of the original active fuel region and shows long stacks of pellets which remained intact after the cladding had melted off. There is no indication of pellet center melting among the pellets visible in this photo. Nearly all the cladding originally in this region had relocated downward, and to a lesser extent upward, forming the upper and lower steel plugs. Figure 31 shows that the hex flowtube had also melted over nearly this entire length, forming a steel crust on the inside surface of the moly liner. A planar upper blockage was formed in the region of the upper insulator pellets and is shown in Fig. 32.

In the R4 test, with about 6 s longer time at full power, the radiograph shows that the lower cladding plug was very thick and extended well below the active fuel entrance into the reflector-rod region. It is also evident that a large amount of fuel melting occured during the extended power operation.

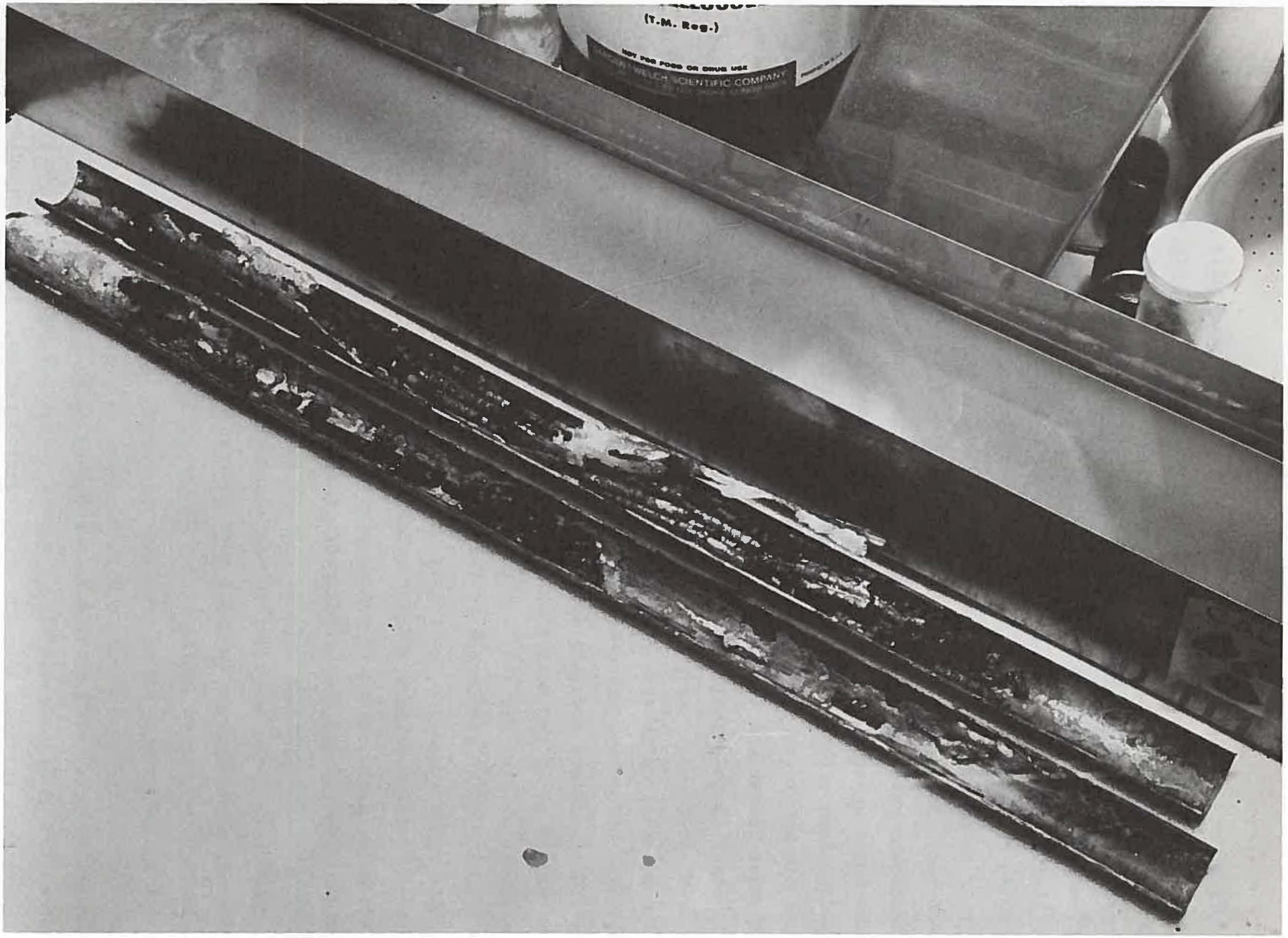

Fig. 31 Photograph of R5 Test Section Following Removal of Sodium.

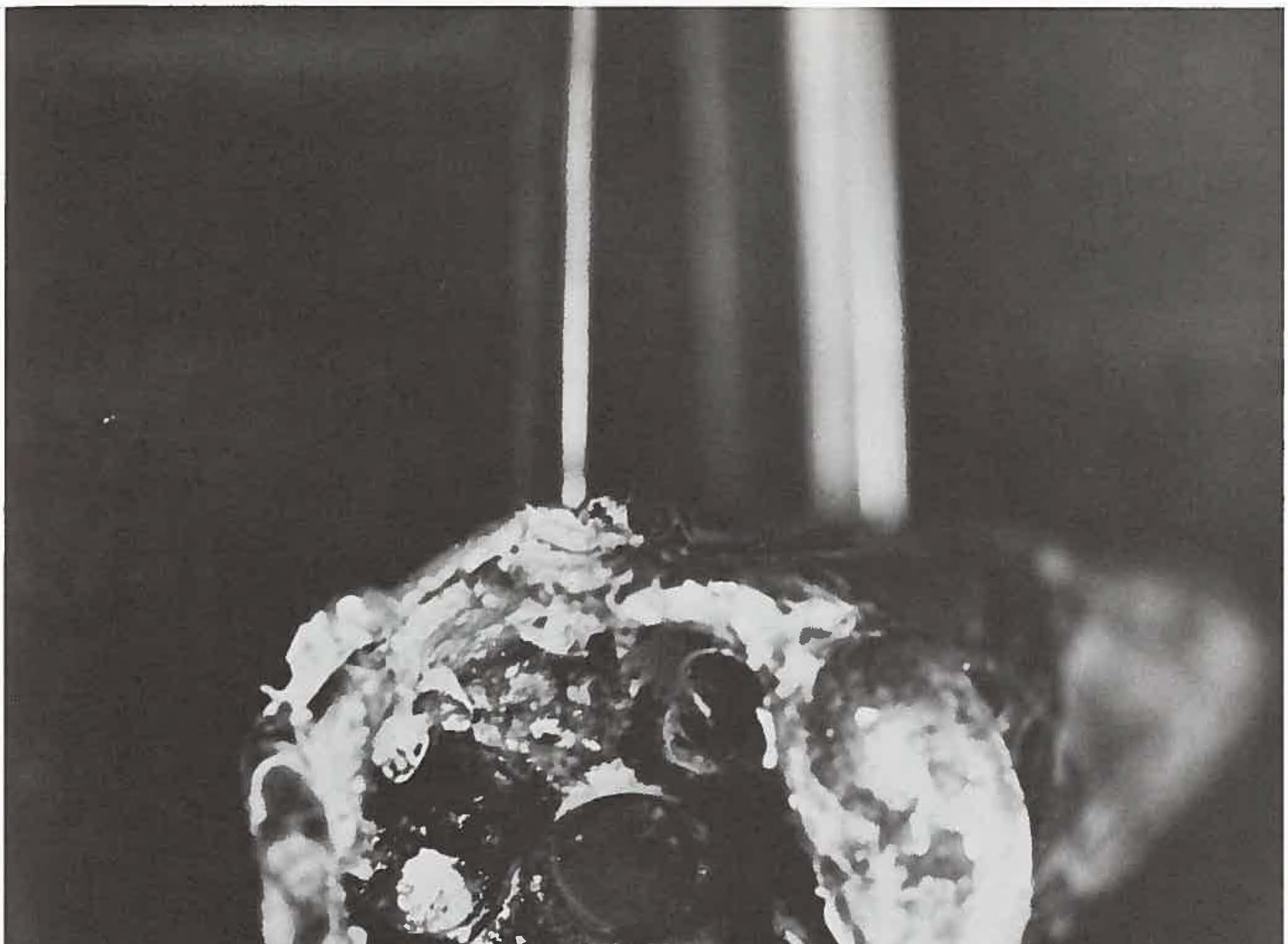

Fig. 32 Photograph of Region of R5 Upper Cladding Blockage as Viewed from Below.

Fig. 33 Photograph of R4 Upper Cladding Blockage as Viewed from Below.

1. SOLIDIFIED STEEL PLUG ON TOP OF UNHEATED INSULATOR PELLETS.
2. SOLIDIFIED STEEL BETWEEN INTACT FUEL ELEMENTS.
3. FUEL ELEMENT APPEARS INTACT OVER LOWER 6 IN. OF ACTIVE FUEL. THIS IS IN REGION OF CLAD PLUG FORMATION.
4. DISLOCATED ARRAY OF FUEL PELLETS ≈ 5 IN. HIGH.
5. SOLIDIFIED STEEL FILM ALONG REMAINS OF HEX CAN.
6. FUEL ELEMENTS (FUSED PELLETS) STANDING IN COLUMNS ≈ 15 IN.
7. EDGE OF HEX CAN SEVERED BY MELTTHROUGH AROUND FAIRLY EVEN BAND. AMOUNT OF STEEL PLUGGING; UNCERTAIN.

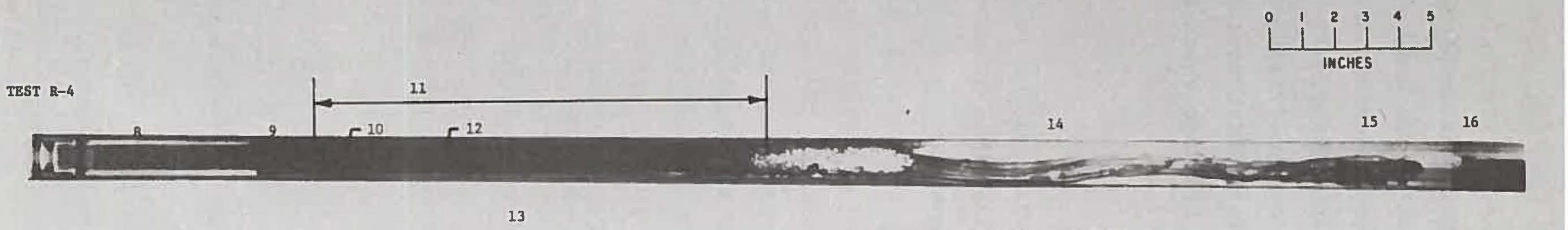

8. NO EVIDENCE OF MATERIAL PENETRATION BELOW STEEL PLUG.
9. SOLIDIFIED STEEL PLUG PENETRATES ≈ 4 IN. BELOW ACTIVE FUEL ZONE.
10. POSSIBLE INDICATION OF LOCAL BURN THROUGH OF MOLYBDENUM TUBE - ONLY SUCH INDICATION IN TEST RADIOGRAPHS.
11. REGION OF COMPACTED FUEL ≈ 15 IN.
12. COOLING FRACTURE IN COMPACTED FUEL.
13. REGION OF SOME EVIDENT POROSITY.
14. POSSIBLE TWISTED REMAINS OF HEX CAN.
15. SOME SOLID PELLETS (POSSIBLY INSULATOR PELLETS LEFT IN STEEL DEBRIS).
16. EDGE OF HEX CAN SEVERED BY MELTTHROUGH - EXTENT OF STEEL PLUGGING UNKNOWN.

Fig. 34 Posttest Neutron Radiographs of R4 and R5 Test Sections.

Molten fuel appears to have drained downward and collected atop the lower steel plug. Above this, in the region of the original active fuel midplane, the fuel appears to have been completely melted and relocated downward, leaving only a frozen crust on the inside surface of the moly liner. Region 14 in the radiograph shows twisted pellet stacks, where the pellets have undergone appreciable center melting. The amount of fuel melting appears to lessen toward the top of the original fuel column. At the top, there appear to be numerous unmelted pellets which have jumbled. Figure 33 shows a photograph of the R4 upper cladding blockage which formed in the region of the upper insulator pellets.

4.0 INTERPRETATION OF RESULTS

From the timing of key test events, Table 10, it is apparent that one is seeing nearly identical patterns in Tests R4 and R5 up to the R5 termination. This is evident in the similarities of times of the onset of boiling, net voiding, inlet flow reversal, fuel pin plenum gas release (cladding failures), and flow-tube failure. The similarity is particularly evident in the inlet flowmeter data shown superimposed in Fig. 28. Interpretation of the test sequence based upon test data is presented in this section.

4.1 Sodium Superheat

The indication from tests R4 and R5 is that initial liquid superheat prior to boiling was negligible. Flowmeter behavior at incipient boiling (point indicated in Fig. 35) suggests boiling was initiated at very low bulk superheat. Wall temperature measurements in the axial location of initial of void formation were generally 100°F below the local saturation temperature (see Fig. 36) for R4. Pressure temperature characteristics of 55 psia and 600°F prior to the transient would indicate the potential for incipient superheats at 2 atm (1760°F saturation) would be less than 300°F. Large incipient superheats have never been observed for sodium boiling above 1 atm, because of the evolution of dissolved or entrained gas in most large practical systems. Gas entrainment or gas evolution is distinctly possible in the R-series apparatus.

During the flow decay prior to boiling inception, several random temperature anomalies were observed (see Fig. 36). These anomalies are interpreted to be an indication of severe radial motion of the 7-pins within the test bundle during the heatup period.

4.2 Initial Boiling Characteristics

There are several interesting characteristics of the initial stages of boiling and flow regime development that are consistent with out-of-pile OPERA data under similar loss-of-flow conditions. Figure 37 illustrates the comparison of OPERA out-of-pile and R-4 inlet flowmeter signals in the region of boiling development. The similar results are encouraging.

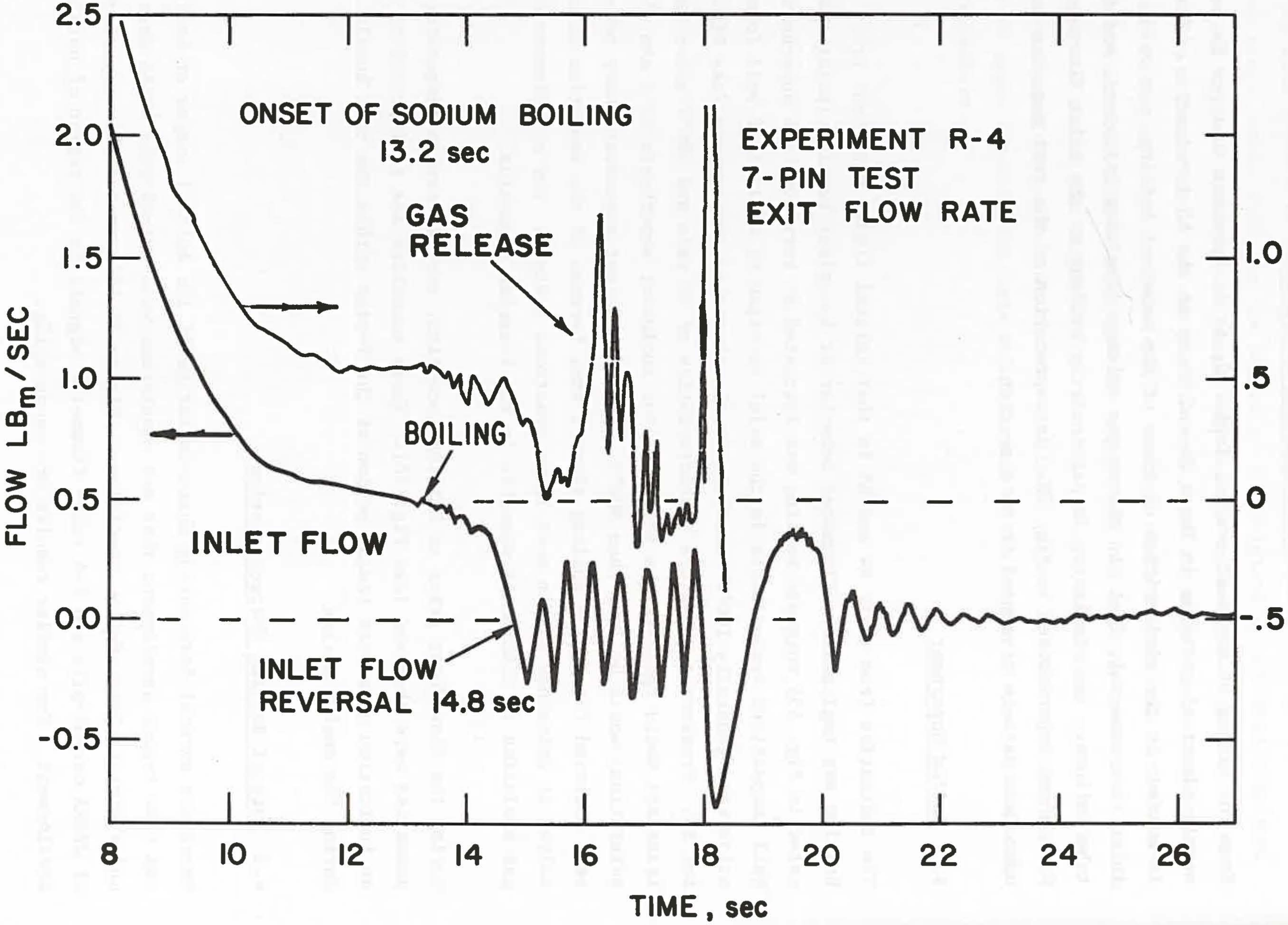

Fig. 35 Measured Inlet and Outlet Flowrate Behavior During Test R4.

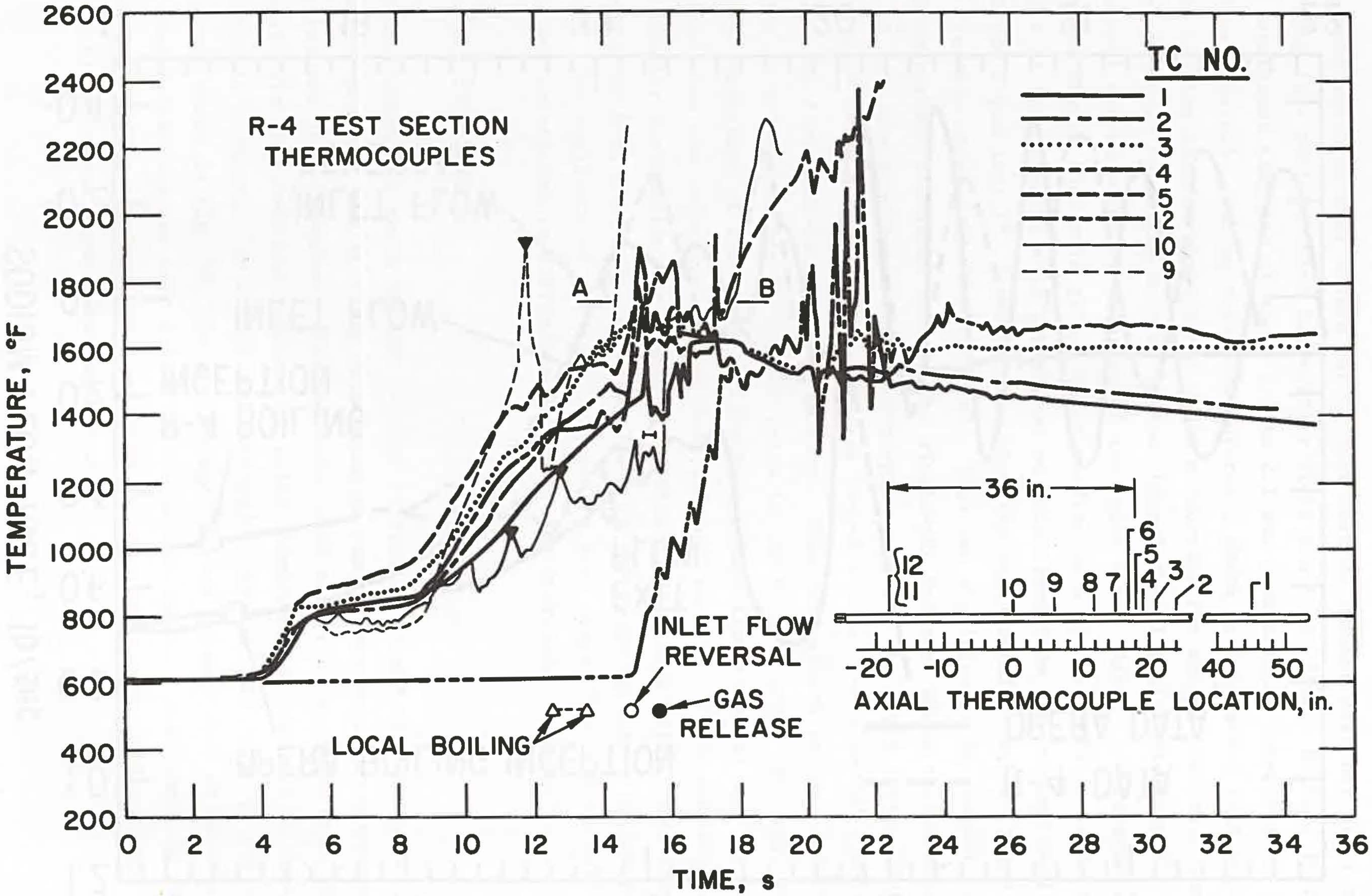

Fig. 36 Response of R4 Test Section Thermocouples.

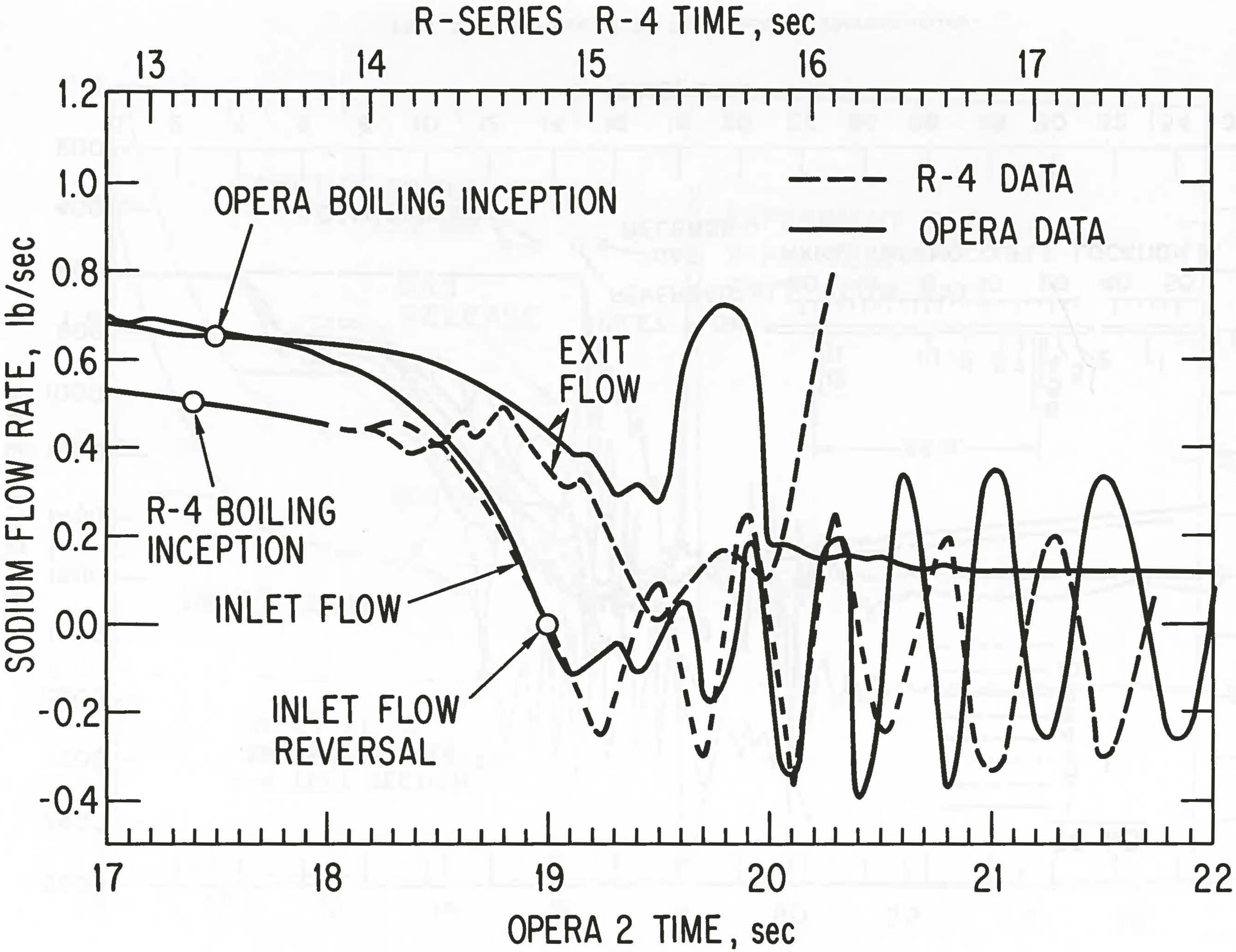

Fig. 37 Comparison of In-pile R4 and Out-of-pile OPERA Flow Rate Response at Boiling for Seven-pin Test Sections under Similar Loss-of-flow Conditions.

The consistent fact that stands out is that initial voiding does not start out as a slug flow pattern which immediately stops the inlet flow. Rather, there is a consistent time lag of about 1.7 to 2.1 sec from boiling inception to inlet flow reversal. During this time interval, there is indication that subcooled boiling occured without net vapor production for about 1 second. Thereafter, net void formation occured in the channel for slightly less than 1 additional second prior to reversal of the inlet flow. After flow reversal, it can be argued that void growth is proceeding as a slug interface. Refined details of this initial void growth can be determined from the voltage taps of the OPERA 7-pin test.[18] These details show the rapid axial growth of a low void fraction core until flow reversal. This has significance in respect to model comparison discussed later. The single-pin R-3 test shows characteristics of both the single-pin OPERA out-of-pile test and the 7-pin tests. The single-pin[4] OPERA test had a short-heated length ∿20 in. and produced a multi-bubble slug flow upon inception of voiding. This void growth is more nearly related to prior L-series in-reactor tests in the Mark-II loop. However, the relative variation of flowmeter oscillations before flow reversal for the R-3 test show the influence of heat loss and heat capacity of the unheated surface totally surrounding the single pin. Flow oscillations after inlet flow reversal for R-3, R-4, R-5, and OPERA-7 are in the range of 2 to 4 cycles per second. The amplitude of the oscillations are also comparible. Minor differences are attributed to differences in power and hydraulic resistance.

4.3 Void Development

Void development is shown for the R4 test in Fig. 38, based upon integrated flowmeter behavior and TC data; this would be similar for R-5. Integrations of inlet and exit flowmeters give the total void volume development with time. Analysis with SAS code and response of axial thermocouples was used to locate approximate boundaries of voided and unvoided regions. This leads to the development shown in Fig. 38. On the average, it was assumed that at least a 25% liquid fraction was left behind in the voided region. Also shown in Fig. 38 is the voiding envelope which would be calculated from the SAS analysis (Sect. 6) for these experiment conditions.

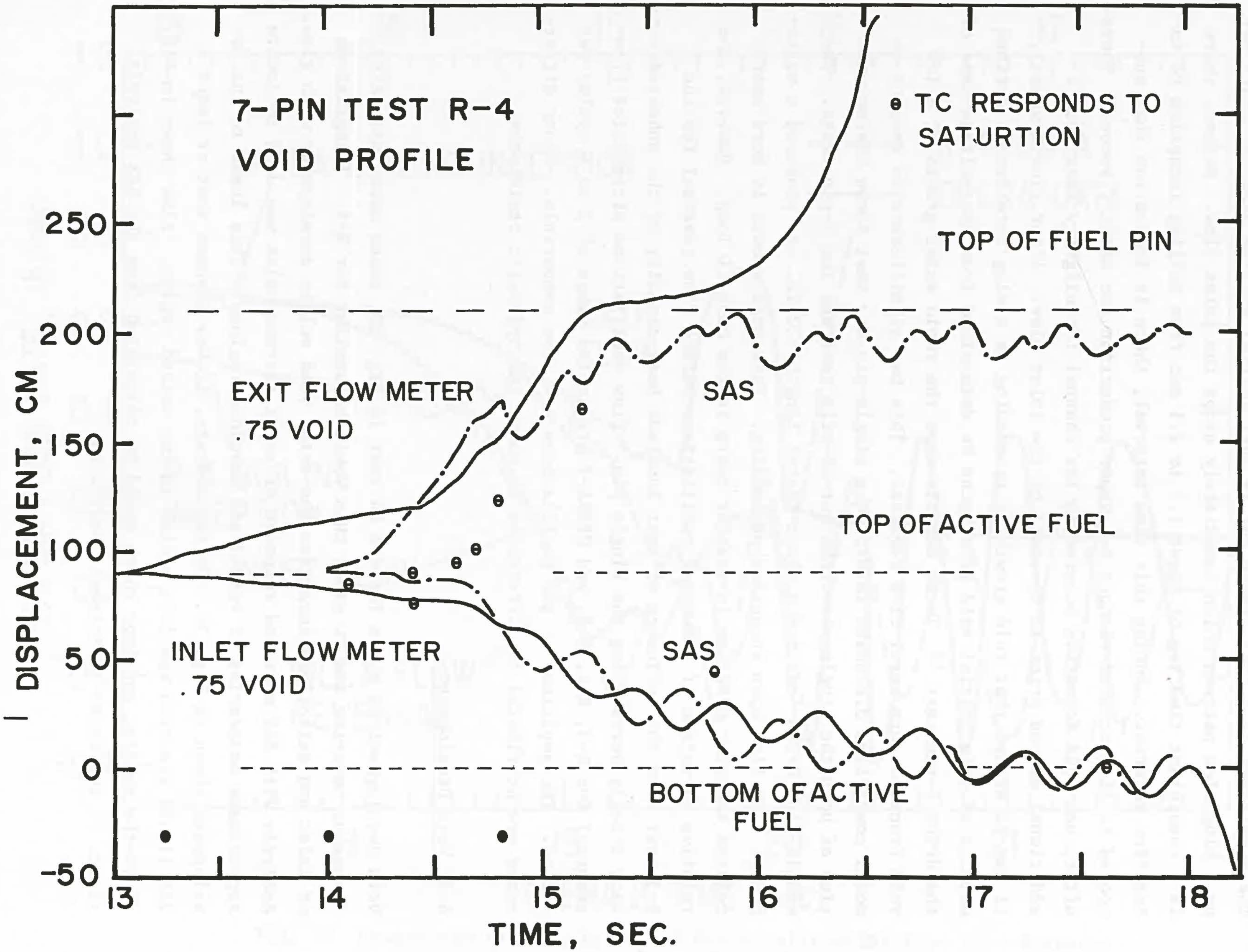

Fig. 38 Axial Void Displacement for Seven-pin R-4 Test and Comparison With SAS Analysis.

Figure 35 illustrates a comparison of inlet and exit flowmeters for Test R-4 in the region of void development. The initial decrease in exit flowmeter reading to near zero represents the slowing down of the upper interface growth near the top of the fuel pin plenum section. However, a new acceleration is seen in the upper flowmeter which cannot be related to boiling phenomena but can be related to gas release from the fuel pin plenums. This has significance in reactor applications and model development. Note that this gas release is not seen at the inlet flowmeter. The same effect is also illustrated in Fig. 38.

The observed effects are consistent with estimates of the maximum flow displacement which can be associated with the volume of the fuel pin gas plenum. The plenum volume consistent with as-built dimensions is $\approx$ 1.2 in.^{3}/pin which can be assumed to have been filled with helium at 14.7 psia and 75°F at the time of fabrication. The pressure in the fuel pin plenum prior to failure can be estimated at 40 psia on the basis of an average temperature of 1000°F. Test section pressure and temperature in the voided region can be taken as 16.5 psia and 1600°F. Gas release into these conditions would displace 20 in.^{3}. Integration of the exit flowmeter signal from 15.4 to 17.4 sec (see Fig. 35) yields 16.8 in.^{3} displacement under the above assumptions. The fact that no indication of this gas release is seen in the downward direction suggests that the channel was not significantly pressurized by the released plenum gas and that the chugging motion was thereby dominated by thermal effects for these tests with nominally unpressurized pins. The later R8 test[9] addressed the effects of pressurized pin failures in the otherwise identical accident sequence, which resulted in significant channel pressurization and downward expulsion of the inlet slug.

4.4 Clad Motion

Clad and fuel motion information is inferred from pre- and posttest analytical modeling, posttest radiographs, and test data where possible. Analysis of test section conditions at the onset of clad melting would indicate the sodium vapor velocities might well be as high as 250 to 300 ft/sec on the average. These velocities are much in excess of velocities required for "flooding"[19,20] or causing upward clad motion. Pretest analysis[21] would indicate the upward motion of molten cladding which would solidify to form a flow restriction cutting off vapor streaming. Vapor velocity will decrease drastically with the flooding transition itself as this transition leads to an increase in pressure drop or equivalent friction resistance by over an order of magnitude.[22] It is apparent from posttest radiographs that the clad has drained prior to fuel melting.

Figure 39 illustrates test data from R4 during the time interval of cladding melting and motion.[23] Two aspects of the thermocouple data are of special interest insofar as their implications about bundle events. First, with the onset of sodium voiding at about 14.4 sec, sodium vapor streaming becomes an important phenomenon within the bundle. Sodium vapor, produced in the lower region of the bundle, streams upward toward condensation sites in the pin plenum region. The estimated vapor velocity of up to 300 fps exceeds the flooding threshold for liquid sodium (wall film) or for molten stainless steel (cladding) by an appreciable margin. The vapor flow is oscillatory in nature due to the chugging behavior exhibited by the lower sodium slug (Fig. 39). As a consequence of the cyclic nature of the associated film motion and vapor condensation, the vapor streaming phenomenon is detectable by the wall thermocouples as a characteristic temperature oscillation. Hence, the occurrence of sodium vapor streaming is an event which is qualitatively detectable from the fast-response wall thermocouple. Secondly, at a time in the test sequence when SAS calculates the onset of cladding motion (about 1 sec after the cladding solidus temperature is reached), thermocouple TCTS-7, located 3 inches below the top of the fuel column, indicates a rapid transient heating event. This is interpreted as being caused by the motion of molten cladding material which accumulates and bridges to the flowtube wall. Additionally, thermocouple TCTS-5, at the top plane of the fuel column (not shown in Fig. 39), shows a similar heating event about 0.1 sec after the lower TC, suggesting a net upward motion of the molten material. However, thermocouple TCTS-4, located one inch above the heated zone in the colder insulator pellet region (Fig. 39), does not show such an event, suggesting that the molten material stopped its upward motion between these two measurement locations. This upper thermocouple indicates that at about this same time in the test sequence the cyclic wall temperature behavior is interrupted, suggesting that a cutoff of the vapor streaming has taken place. Hence, the thermocouple data provided indications of a) the time of molten cladding motion (first indication at 17.3 sec for R4 data), b) the initial progression of motion under the influence of sodium vapor

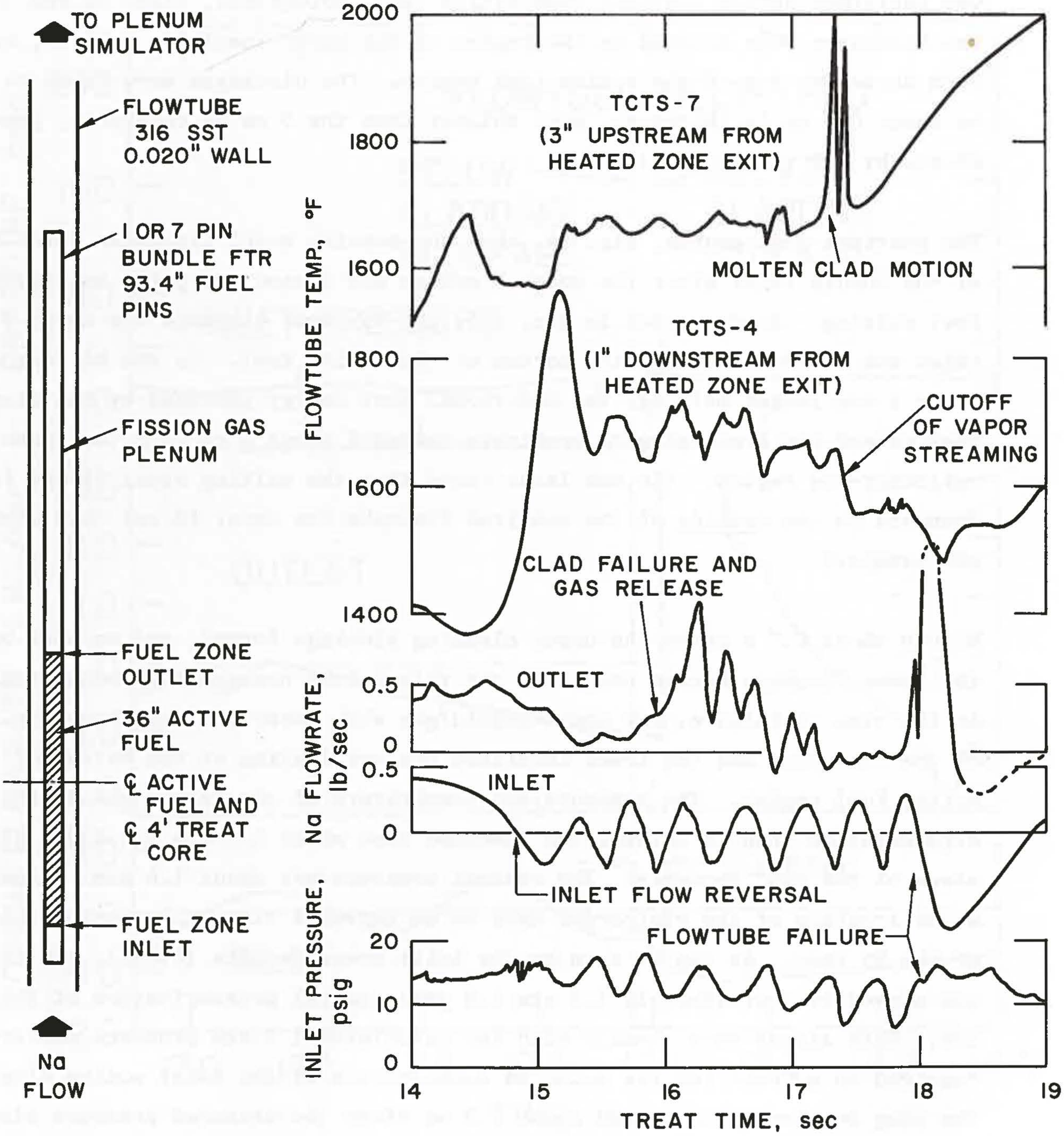

Fig. 39 Composite of R4 Test Data During Time Interval of Cladding Melting and Motion.

streaming (upward in direction from initially 3 to 4 inches below the top of the fuel column to less than 1 inch above the fuel column), and c) the influence of cladding relocation upon the bundle configuration (formation of a steel blockage at the top of the fuel). The presence of the upper cladding blockages was confirmed during posttest examination (see photographs, Figs. 32 and 33). The blockages were located in the region of the upper insulator pellets, within 2 cm above the top of the active fuel region. The blockages were found to be about 0.3 cm in thickness, much thinner than the 5 cm in thickness, predicted by SAS (Sect. 6.3.3).

The posttest radiographs, Fig. 34, show the massive steel blockages which formed at the bundle inlet after the upper blockage was formed and prior to significant fuel melting, As described in Sec. 3.5, the R5 lower blockage was about 8 cm thick and extended down to the bottom of the active fuel. In the R4 test with about 6 sec longer melting, the additional heat energy provided by the slumping fuel caused the steel plug to penetrate downward about 5 cm into the lower reflector-rod region. (It was later found that the melting steel flowed farther downward on the outside of the unmelted flowtube (to about 10 cm) than within the pin bundle.)

Within about 0.7 s after the upper cladding blockage formed, and seconds before the lower blockage became complete, the thin-walled hexagonal flowtube failed. At the time of failure, the upper liquid/gas slug interface was above the tops of the fuel pins and the lower interface was oscillating at the bottom of the active fuel region. The pressure and temperature of the helium gas in the instrumentation annulus outside the flowtube were about 2.4 atm and 430°C at this stage of the test sequence. The channel pressure was about 1.4 atm. Figure 40 shows tracings of the visicorder data on an expanded time scale during this stage of the R5 test. As can be seen by the inlet pressure data (PTK-1), the failure was marked by approximately 1.3 atm (18 psi) channel pressurization at the inlet. This agrees very closely with the calculated 1.2 atm pressure difference required to account for the measured deceleration of the inlet sodium slug. The slug deceleration started about 2.5 ms after the measured pressure rise, which is approximately the acoustic-wave transit time from PTK-1 to the inlet flowmeter. Note in the figure that the measured acceleration of the upper sodium slug was delayed by 50 ms from the pressure rise. This delay is too long to be

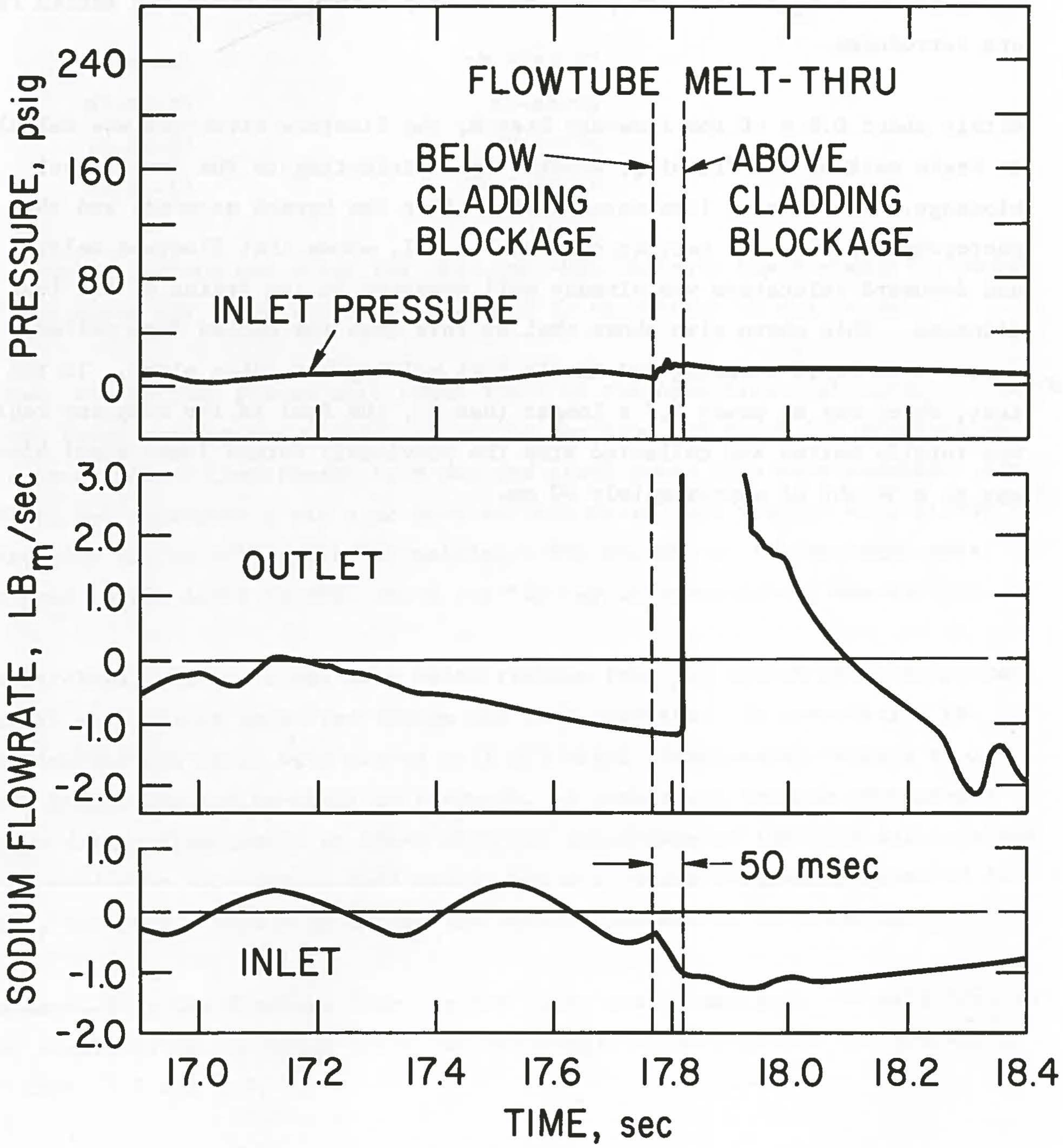

Fig. 40 Expanded View of R5 Visicorder Data Showing Flowrate and Pressure Behavior During Flowtube Failure.

attributed to the acoustic transit time, even taking into account the presence of gas and vapor. The delay is regarded as indicating the presence of a channel blockage, the upper cladding blockage, between the breech location in the active fuel region and the upper sodium slug. This data indicates that the upper blockage was complete by the time of the hexcan failure and that it was capable of being breeched by the 1.3 atm pressure buildup across it which the hexcan failure introduced.

Within about 0.6 s of the flowtube breech, the flowtube structure was calculated to begin melting and draining, eventually contributing to the lower steel blockage. The R5 test terminated 1.16 s after the breech occured, and the photograph of the test section debris, Fig. 31, shows that flowtube melting and downward relocation was already well advanced in the region of the fuel midplane. This photo also shows that at this time the declad fuel pellet stacks were still standing and little fuel melting had taken plane. In the R4 test, which was at power 5.7 s longer than R5, the fuel in the midplane region was totally melted and collected atop the previously formed lower steel blockage to a height of approximately 20 cm.

5.0 Metalographic Examinations

After the transient the test section, with the solidified sodium in place, was cut into four principal parts containing the remains of the elements. The four pieces were identified as follows:

113.5-R4-92	113.5-R5-87
92-R4-70	87-R5-60
70-R4-40	60-R5-36.5
40-R4-17	36.5-R5-17

The numbers before and after the -R4- and -R5- indicate the distance in inches of the upper and lower cut with reference to the bottom of the U-tube.

These test section pieces were taken apart at the Analytical Laboratory at ANL-W. Where found, sodium was melted out of the sections and saved for examination. The test section containment tube and the steel dewar tube were removed. Some additional disassembly was also done and all parts were treated with alchol to react the sodium not removed by melting. The remains of the sections were shipped to the AGHCF in MSD, ANL-E for further disassembly and examination.

As received, all parts had some white residue from the sodium-reaction process and in some pieces unreacted sodium was still present. In preparation for examination all parts were washed with 50% ethyl alchol-water mixture to remove sodium and sodium-reaction products. A comparison between photographs taken during disassembly at ANL-W with the appearance of the material received indicated that sections of fuel-pellet columns, which originally appeared intact, had partly broken up during the various procedures in disassembly.

In Sect. 5.1, the findings from the two tests are summarized. Details from the two examinations including X-ray and metalographic photographs are presented in Sect. 5.2 and 5.3.

5.1 Summary of Metalographic Examinations

The S-shaped configuration of the upper part of the fuel columns apparent on the R4 neutron radiograph, Fig. 34, was destroyed when the hexagonal flow tube dropped into that region during disassembly. The low density of fuel in that region was due to pellet center melting followed by a general downward flow of fuel, leaving behind stacks of hollow pellets. Some radial movement of melted fuel through cracks in the unmelted pellet annuli occurred on a local basis.

Since there was practically no material for several centimeters below the stacks of hollow pellets, the stacks were most likely supported by leaning against the molybdenum tube with at most only flimsy support from below. Most of the fuel which melted out of the pellets became part of the pool of melted fuel in the lower part of the fuel column. The 12.7-cm region devoid of almost all fuel was probably the region of highest fuel temperature. The fuel in this region also flowed downward among the fuel columns below.

Although internal pressure was generated inside of at least some pellets, the pellets did not disintegrate explosively. The obvious sources for pressure generation were solid-liquid expansion and as-fabricated absorbed gases with a possible assist from fuel vapor pressure.

The steel which melted earlier first formed a pool around the bottom of the fuel columns. Subsequently, other melted steel flowed downward and joined the pool. When the fuel melted and flowed downward in the central region, it displaced the melted steel both radially and upward because of the lesser steel density. Some mixing occured as melted steel rose upward and molten fuel settled downward. An ingot of steel centrally located on top of the mass of fuel may have flowed from above into an existing cavity late in the sequence of events. On the other hand the ingot may represent steel displaced from below by descending fuel. The evidence for one or the other process was not clear.

The extensive bottom blockage was initially formed by molten steel and was subsequently augmented by melted fuel filling in among the fuel columns. The top blockage consisted of stainless steel frozen in the flow channels in the region of the insulator pellets. The blockage thickness varied from about 5 mm around the central pin to about 1 mm around the outer pins. Both top and bottom blockages were complete.

The components inside the upper part of the fuel elements showed some tendency to move downward when the reflector rods lost support from below. This was probably a gravity effect although expanding gases in the plenum may have provided some assistance.

In the R5 test, fuel melting was found to be very small overall. Only about 9% of the total fuel melted although locally as much as 65% of one pellet was melted. The center element had more fuel melting than the peripheral pins at an equivalent axial location. The zone of fuel melting extended about 30 cm in length, centered slightly above the active fuel midplane.

A slight upward movement of molten steel was evident which resulted in an upper flow-channel blockage around the insulator pellets. Some holes were evident in the thin blockage layer, and the blockage definitely was not complete. The principal motion of molten steel was downward. A plug of steel 7 to 8 cm in depth formed around the lower protion of the fuel columns. The steel froze irregularly among the columns and open channels probably existed along the wall of the flow tube. The bottom blockage did not appear to be complete.

5.2 R4 Metalographic Examination

5.2.1 Distribution of Fuel

After removing the residual sodium-reaction products, the upper and lower parts of Section 40-R4-17 appeared as shown in Fig. 41. One-half of the split molybdenum tube remains fused to the upper part. The bottom part of the section contains the bottom end plugs, the reflector rods, insulator pellets and fuel. Gamma radiographs of the upper and lower parts of Section 40-R4-17 are shown in Fig. 42. The general distribution of fuel corresponds with that shown by the neutron radiograph, but more details are visible. The bottom of the fuel column for 5.7 cm (2 1/4 in.) (10-12 pellets) is relatively undisturbed.

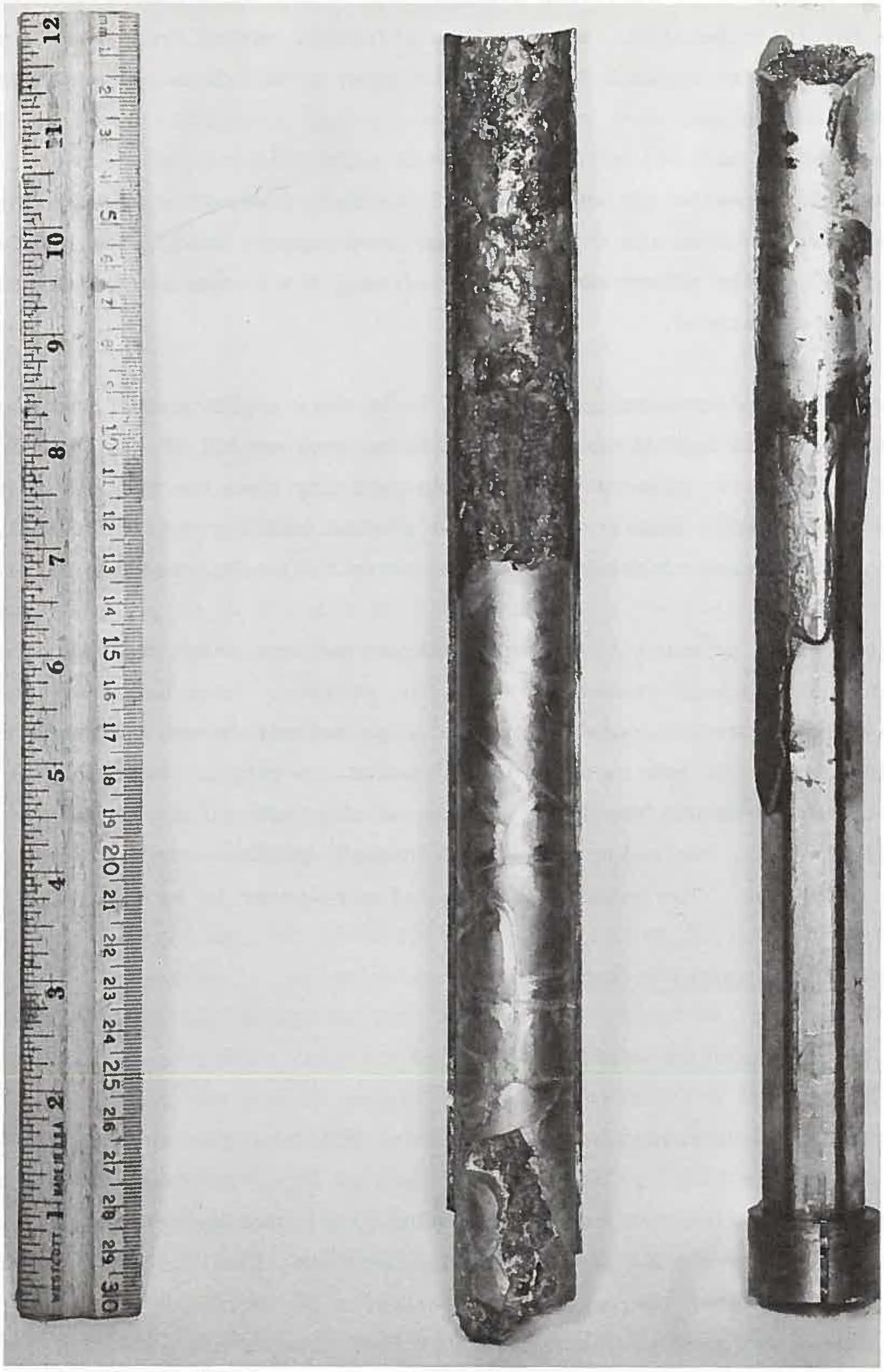

Fig. 41. Upper (left) and Lower (right) Segments of Section 40-R4-17 After Cleaning. Neg. No. MSD-183789.

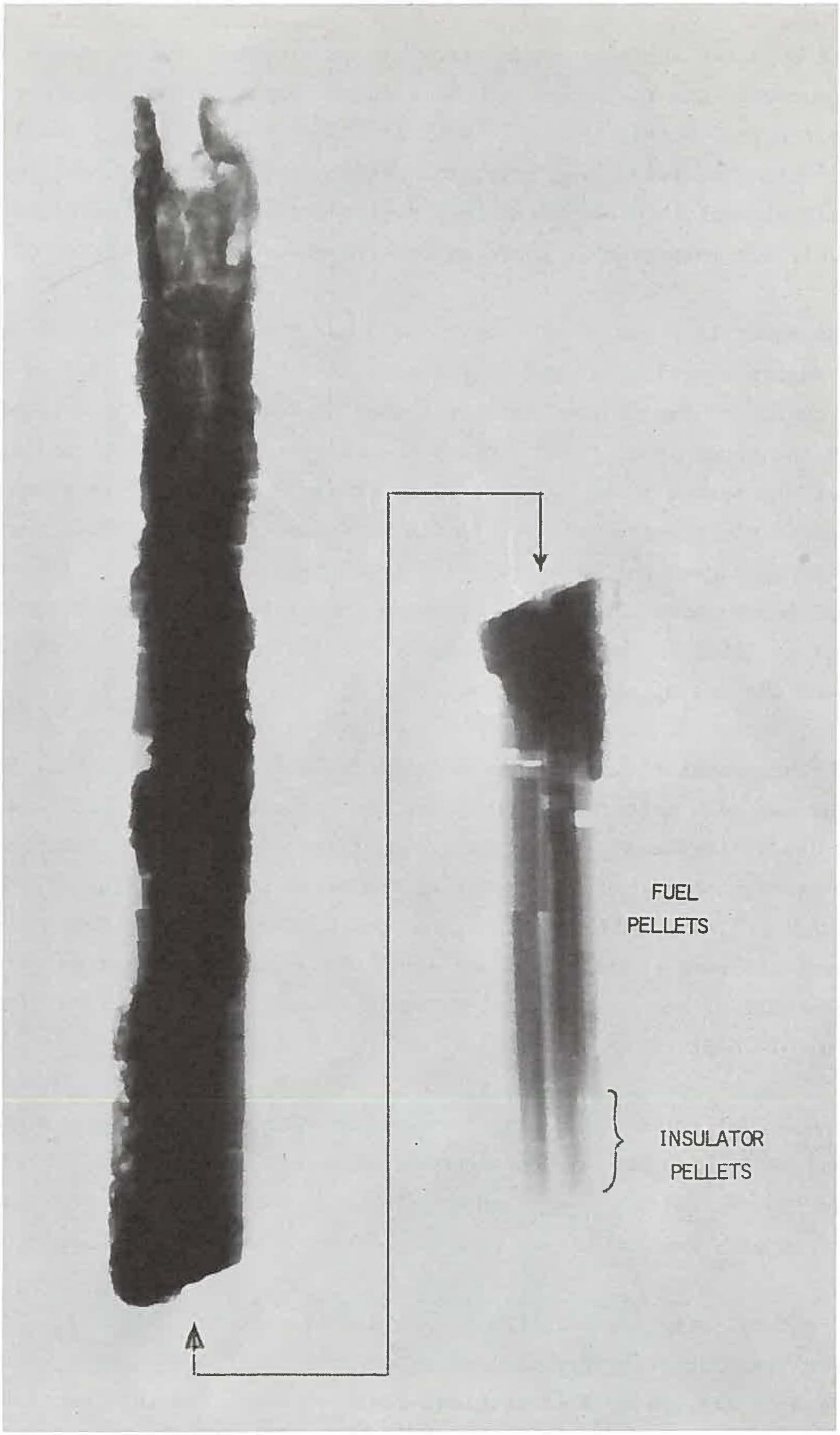

Fig. 42 Gamma Radiograph of Fuel in Upper and Lower Parts of Section 40-R4-17. Neg. No. MSD-185672. ∿1X.

The columnar arrangement persists but some radial displacements of pellets have occurred. The fuel columns show a slight gap at a location just below where melted fuel begins to show. This is probably a posttest thermal contraction effect. The two bottom insulator pellets are in their normal positions in each element. In the dense fuel region in this section there is much melted fuel, but intact pellets are quite evident toward the outside of the fuel mass.

For about 12.7 cm (5 in.) above the dense fuel the neutron radiograph showed a region practically devoid of fuel. Then for the next 43.8 cm (17 1/4 in.), a region of low density fuel in a shallow S-shaped configuration was present. In the upper 10 cm (4 in.) of this latter region some practically intact fuel pellets seemed to be humg up. This debris configuration was not preserved intact since sodium had not reentered and solidified in this region. It was destroyed when the hexagonal flow tube dropped about 23 cm (9 in.) inside the molybdenum heat shield tube when the flow tube was freed from support by the cut at 113.5 in. during disassembly. A further drop of 2.5 cm (1 in.) occurred when the cut at 92 in. was made.

The hexagonal flow tube from Section 70-R4-40 is shown in Fig. 43. The bottom end has been melted off. This section contains the insulator pellets, reflector rods, springs and part of the plenum spacer tubes of the seven elements. An X-radiograph of the lower part of the hexagonal tube (Fig. 44) shows the insulator pellets, reflector rods and part of the springs. Some relative displacement of these components is evident. Subsequent examination revealed about one-half of an unmelted fuel pellet remained with the central fuel element in this section.

Loose fuel recovered during disassembly amounted to 366 g from Section 70-R4-40 and 59.5 g from the top of Section 40-R4-17. An additional 27.3 g was obtained during the cutting operation at 40 in. Pieces of melted steel and thermocouple wires were removed before weighing. The total weight of loose fuel was 452.8 g.

The total original quantity of oxide fuel was 1215 g or 13.3 g/cm of length for the cluster of seven elements. The 452.8 g was present in about the upper 56.5 cm (22 1/4 in.) of original fuel columns. For this section an average of 8.0 g/cm was calculated compared to the original 13.3 g/cm. The displaced

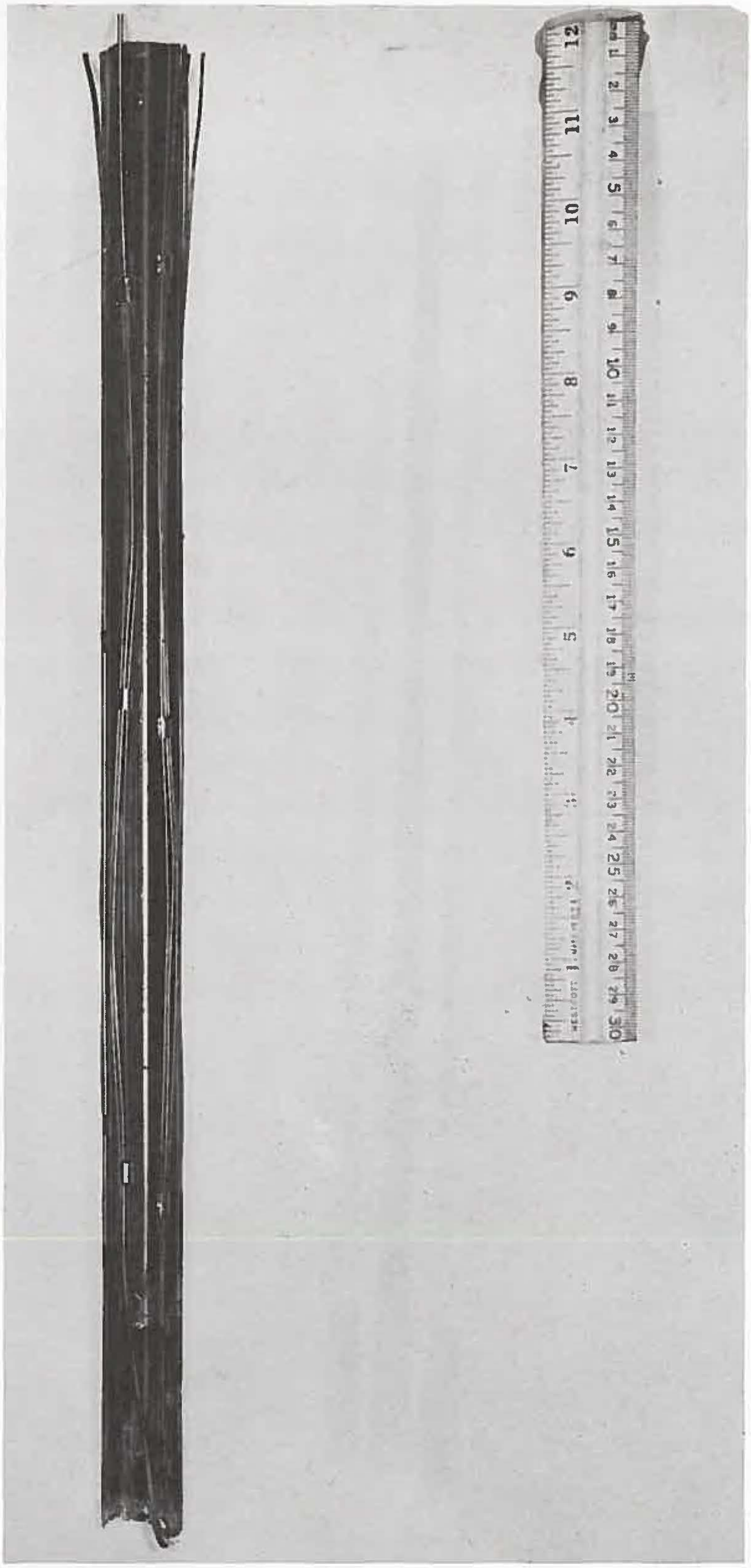

Fig. 43. The Hexagonal Flow Tube from Section 70-R4-40 with Lower End Melted off. Neg. No. MSD-183792.

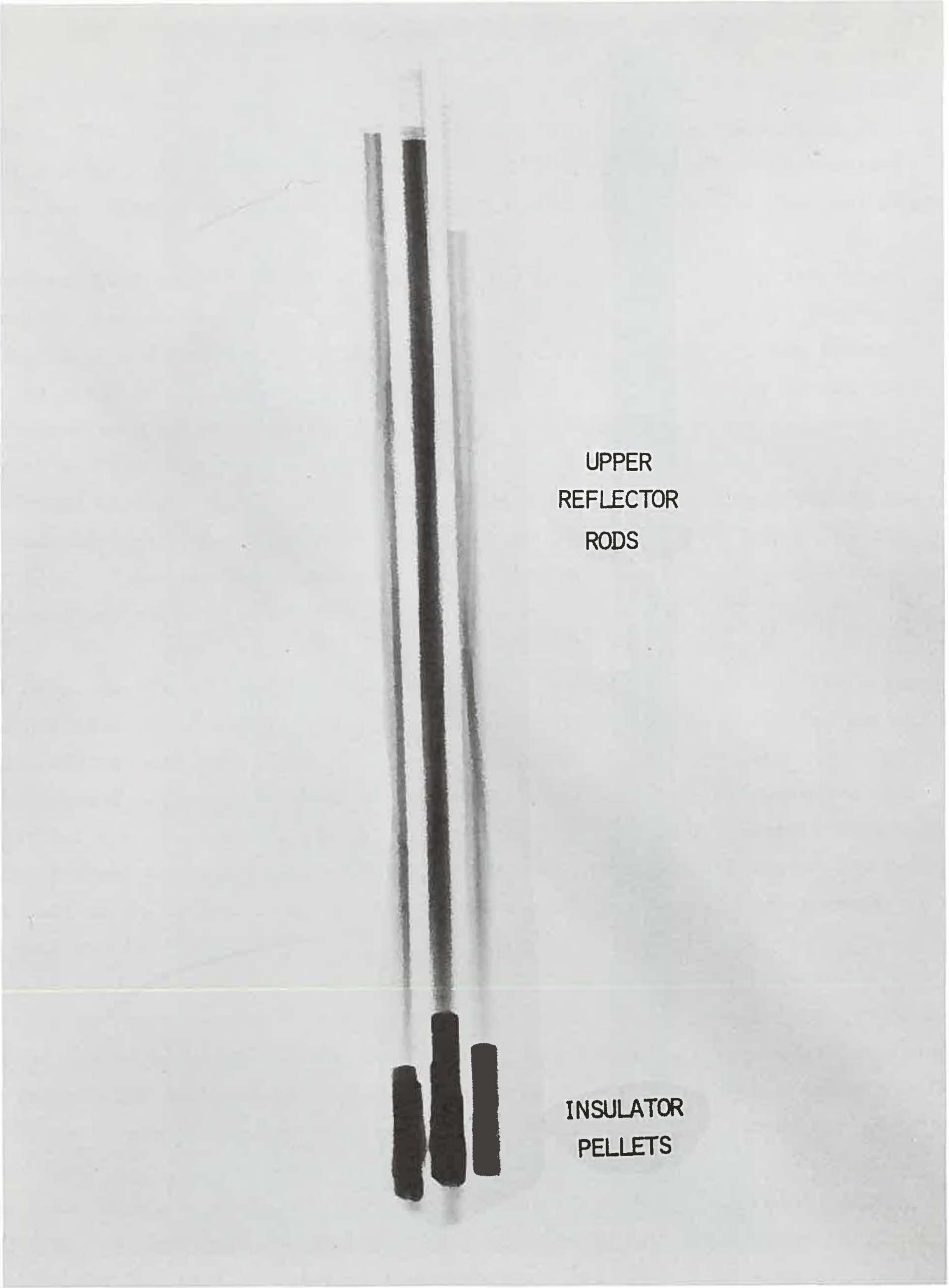

Fig. 44 X-radiograph of the Lower Part of Section 70-R4-40 Showing Insulator Pellets at the Melt-off. Neg. No. MSD-185673. ~1X.

fuel (298.7 g) was presumed to be in the lower region of the fuel columns (34.9 cm) of Section 40-R4-17.

Transverse cuts were made through Section 40-R4-17 at several locations. Typical cut surfaces are shown in Fig. 45. These specimens were subsequently used to calculate the amount of additional fuel and the melted fuel on the cut surfaces.

Section A (Fig. 45) was 4.7 cm (1 7/8 in.) below the bottom of the fuel column and contained no fuel. Section B, 0.6 cm (1/4 in.) above the bottom of the fuel column shows seven practically intact fuel pellets with no evidence of melting. The original arrangement of pellets still exists.

Section C was from ∿5.7 cm (2 1/4 in.) above the bottom of the fuel column. Some of the pellets in Section C are cracked but are generally intact. The regular hexagonal pattern of the pellets has been disrupted and they are closer together on one side. Metallic filaments can be seen penetrating into pellets from the steel-pellet interface (center and bottom pellet). In addition, a considerable amount of melted fuel has flowed down into this section. This melted fuel is quite dense. It is off to one side and appears to have touched the molybdenum heat shield tube. One of the original pellets in this section (lower left) appears to have partly melted on the side in contact with melted fuel.

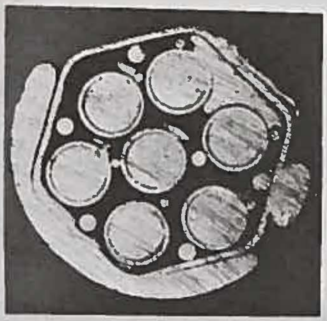

SECTION A. 4.8 CM BELOW
BOTTOM OF FUEL COLUMN.
REFLECTOR RODS IN ELEMENTS,
SOME MELTED STEEL.

SECTION B. 0.6 CM ABOVE
BOTTOM OF FUEL COLUMN.
UNMELTED FUEL PELLETS IN
MATRIX OF STAINLESS STEEL.

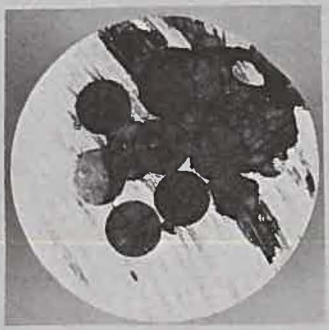

SECTION C. 5.7 CM ABOVE
BOTTOM OF FUEL COLUMN.
MELTED FUEL AROUND
PELLETS IN STEEL MATRIX

SECTION D. 10.8 CM ABOVE
BOTTOM OF FUEL COLUMN.
MELTED FUEL, FUEL PELLETS
IN STEEL MATRIX.

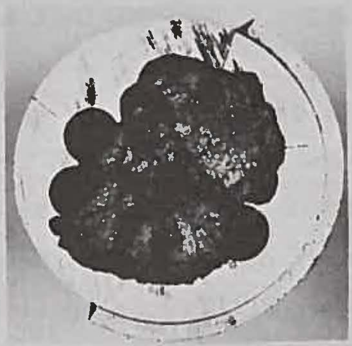

SECTION E. 18.1 CM ABOVE
BOTTOM OF FUEL COLUMN.
MELTED FUEL, PARTS OF
PELLETS IN STEEL MATRIX.

SECTION F. 22.9 CM ABOVE
BOTTOM OF FUEL COLUMN.
MELTED FUEL, PARTS OF
PELLETS IN STEEL MATRIX

Fig. 45 Transverse Sections Through Section 40-R4-17. Neg. No. MSD-187470.

In Section D, from 10.8 cm (4 1/4 in.) above the bottom of the fuel column, the original fuel pellets are still prominent but disintegration by melting has progressed. Of the sections examined this one had the most new fuel. While the melted fuel seemed quite dense, some large voids were present.

Only parts of pellets of the original fuel are evident on the periphery of the fuel mass in Section E, 18.1 cm (7 1/8 in.) above the bottom of the fuel column. Most of the fuel has melted. The central void in the melted fuel is probably a shrinkage cavity.

Section F was located 22.9 cm (9 in.) above the bottom of the fuel column. Portions of some of the original pellets are evident on the outside of the mass of fuel. Most of the fuel had melted and looked quite dense as solidified. The prominent void in the center of the fuel appears to be a shrinkage cavity.

In Sections B, C, D, E, and F, the fuel tended to be centrally located and surrounded by stainless steel. The top 5 cm (2 in.) of the fuel region remaining in Section 40-R4-17 (Fig. 42), showed a reverse situation. An ingot of steel occupied the center and was surrounded by melted fuel and parts of pellets. This ingot will be described later. The fuel from around the steel ingot broke away on handling. It was collected and weighed (128 g).

Areal fractions occupied by fuel (melted and unmelted), steel and voids, as bounded by the molybdenum heat shield tube in the sections of Fig. 45, were measured. With the fuel of Section B at 0.63 cm (1/4 in.) from the bottom of the fuel columns as a reference for the areal fraction of fuel originally on the cross section, the relative amounts of additional fuel (melted) and of melted original fuel were determined. These data are shown in Table 11. A maximum in the amount of fuel on the cross section appears to exist about 10.8 cm above the bottom of the fuel columns.

TABLE 11 Fuel and Steel on Transverse Sections at Various Axial Locations of Segment 40-R4-17 (Fig. 45)(a)

Section	Location(b)	% Fuel	% Fuel Added(c)	% Original Fuel Melted(d)	% Steel	% Void(e)
A	-4.8 cm ($1\frac{7}{8}$ in.)	0	0	-	53	47
B	+0.6 cm ($\frac{1}{4}$ in.)	23	0	0	75	2
C	+5.7 cm ($2\frac{1}{4}$ in.)	42	19	5	59	0
D	+10.8 cm ($4\frac{1}{4}$ in.)	62	39	5	35	3
E	+18.1 cm ($7\frac{1}{8}$ in.)	53	30	69	46	1
F	+22.9 cm (9 in.)	46	23	43	50	4

(a)Sections bounded by molybdenum heat shield tube.

(b)Location referred to bottom of fuel columns; -, below; +, above.

(c)All fuel added to section had melted.

(d)Actual % of original fuel assumed to be on cross section.

(e)Visible to the eye and readily measured.

Note: The procedure involved cutting out the respective areas from a photographic enlargement of the section and weighing.

An attempt was made to establish a mass balance between the 298.7 g of fuel which had been displaced from the upper part of the fuel section and the fuel added to the lower 34.9 cm of the fuel section. This effort was not very successful. The relatively few cross sections examined, and various assumptions as to amount of admixed steel in fuel, and porosity led to results sometimes as much as 25% over the quantity of displaced fuel.

5.2.2 Characterization of the Fuel

The loose fuel material collected from the upper part of the fuel column consisted of pellet pieces and cinder-like pieces of melted fuel as shown in Fig. 46. The pellet pieces ranged from relatively intact pellets to small pieces; only a very small amount of powder was associated with this fuel. Almost all of the pellet pieces showed various degrees of center melting. Stainless steel was present only occasionally as small metallic globules on the surface of the fuel. Pieces of thermocouple wire and thermocouple insulation were also present.

Melting in fuel pellets is shown in Fig. 47. In the single pellet on the left the melt zone amounts to slightly more than 50% of the cross section of the pellet. Much of the melted fuel flowed away leaving a large central void in the distorted pellet. The stack of three pellets in the center of the figure also shows evidence of extensive central melting. The internal pressure in the middle pellet was relieved by the expulsion of melted fuel through a crack, resulting in the two projections shown. The two upper pellets on the right appear to either have melted on the ourside or have been eroded by melted fuel from elsewhere. Center melting was also evidenced in these pellets.

Figure 48 shows a transverse section through a pellet with extensive center melting (56%) in which part of the melted fuel has been pushed out beyond the original pellet surface. The large central void indicates that some of the melted fuel ran off. Large radial cracks are present in the unmelted fuel. In general, fuel pellets intact enough for measurement of the melt zone gave values in the range of 28 to 56% areal. However, the appearance of other pellet pieces implied even greater melting. The concentration of bubbles in the melted fuel at the interface with the unmelted fuel was a frequent observation.

Fig. 46 Pellets and Pellet Fragments from Section 70-R4-40. Neg. No. MSD-183616.

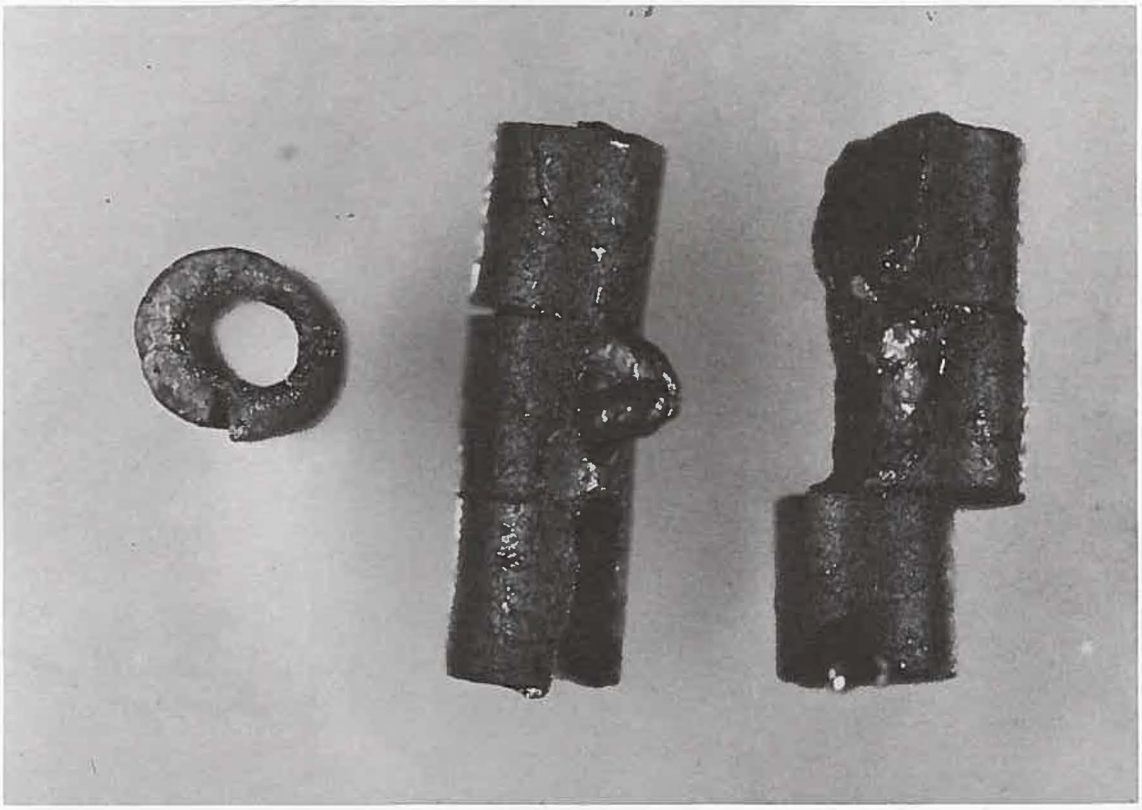

Fig. 47 Center Melting in Fuel Pellets from Section 70-R4-40. Neg No. MSD-183604.

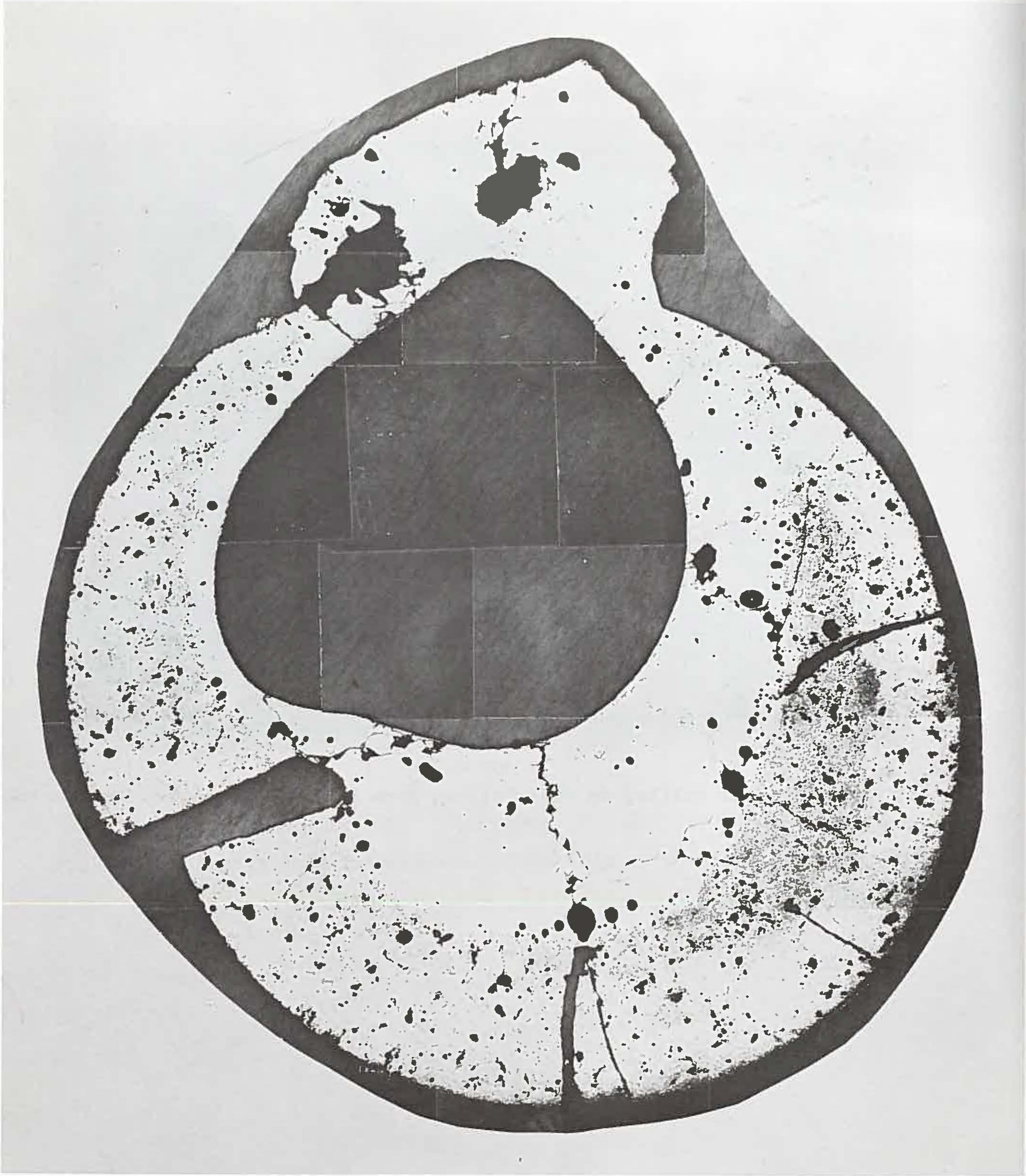

Fig. 48 Transverse Section Through a Fuel Pellet with Extensive Center Melting and a Central Void. Neg. No. MSD-184395.

A longitudinal section through a vertical plane of a pellet is shown in Fig. 49. Part of the unmelted crust has been pushed out by pressure generated internally. The pressure appeared to be due to the volume expansion of the fuel on melting and the release of as-fabricated absorbed gases. Fuel vapor pressure may have been involved in conjunction with as-fabricated absorbed gas pressure. However, bubbles from fuel vapor pressure alone would have collapsed as the molten fuel cooled to the freezing temperature of the fuel. By way of example, gas evolved from some unirradiated UO_2 fuel pellets heated to 1600°C was 0.02 cc/pellet at NTP. At the melting temperature of fuel this amount of gas would have expanded about ten times to a volume about twice the volume of a pellet.

Unmelted fuel from a peripheral location on the fuel column at a position about 23 cm above the bottom of the fuel column is shown in Fig. 50. In Fig. 50(a) the grain size is close to that of the as-fabricated pellet (4 μm dia.). In Fig. 50(b) grain growth has occurred and the grain diameter is about 40 μm.

Melted fuel from a location 18 cm from the bottom of the fuel column is shown in Fig. 51. View (a) shows very large columnar grains in contact with melted steel. The grains are radially oriented to the steel. The fuel has no steel intermixed with it. View (b) at the same axial location also shows large columnar grains of fuel but many small globules of steel are intermixed and some grain boundaries are outlined by beading of the globules.

A scanning electron microscopic examination of a fuel particle with some central void surface resulted in the following three photographs. Figure 52(a) is a picture of the particle. Figure 52(b) shows a part of the surface of the central void with numerous crystalline projections on the surface. Figure 52(c) shows a highly magnified view of one of the projections of fuel which appears to have come through the surface. Some of these projections appeared to be hollow. Other fuel particles showed similar projections of fuel.

5.2.3 Distribution of Melted Steel; Blockages

The steel components inside of the molybdenum shield tube melted from just below the upper insulator pellets all the way down to the bottom of the fuel columns. These components were the hexagonal flow tube, cladding and wire

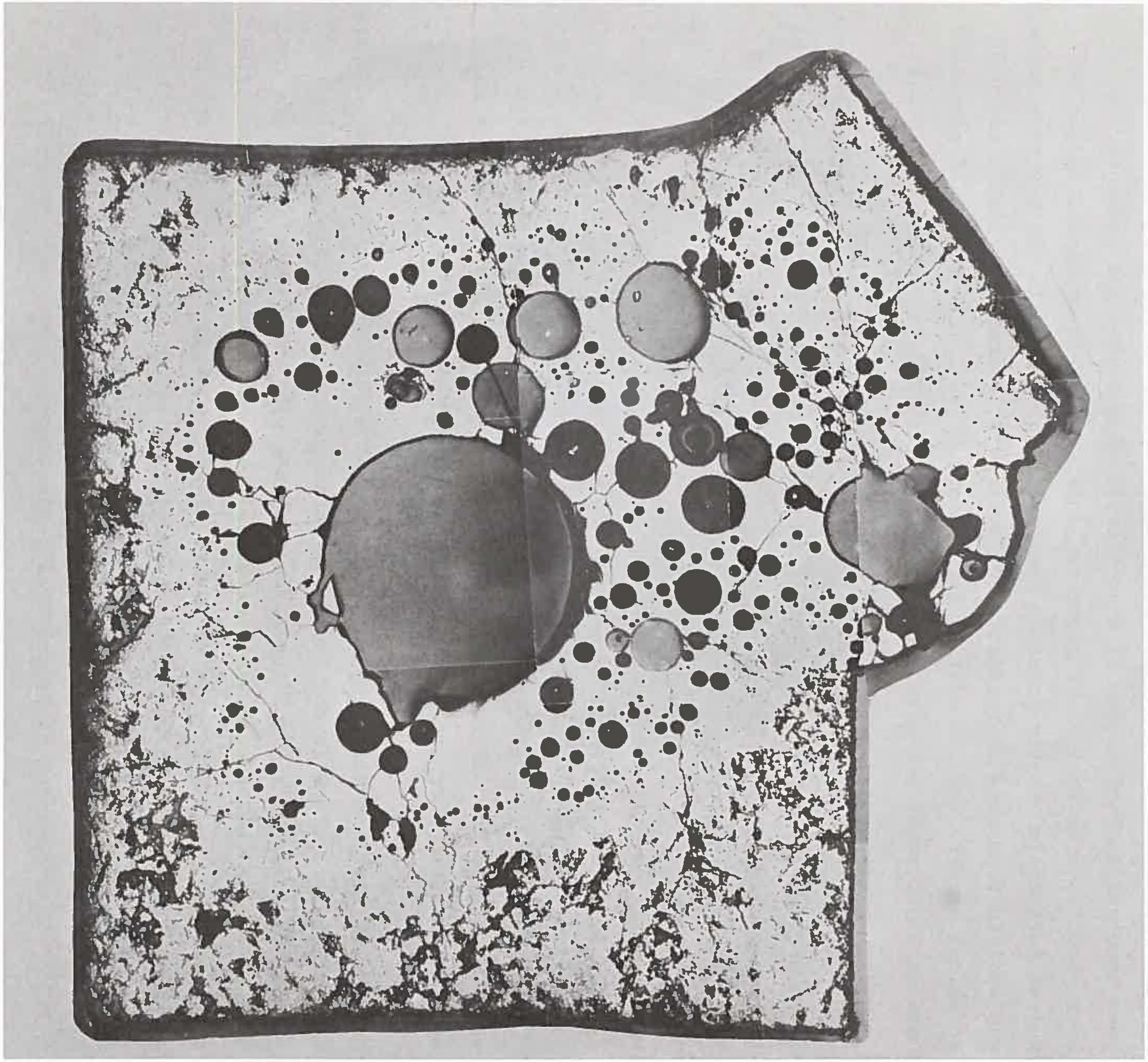

Fig. 49 Section through Vertical Axis of a Pellet Showing Center Melting and Gas Bubbles. Neg. No. MSD-184393.

Fig. 50(a) Small Grains in Unmelted Fuel. Neg. No. MSD-185241.

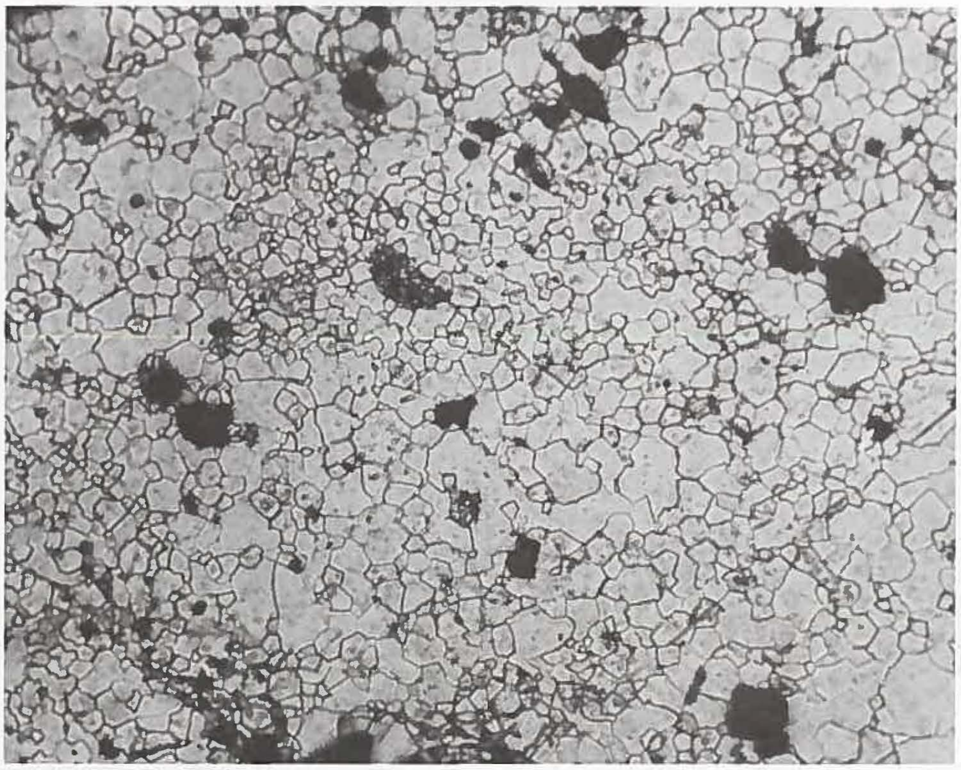

Fig. 50(b) Large Grains from Grain Growth in Unmelted Fuel. Neg. No. MSD-185242.

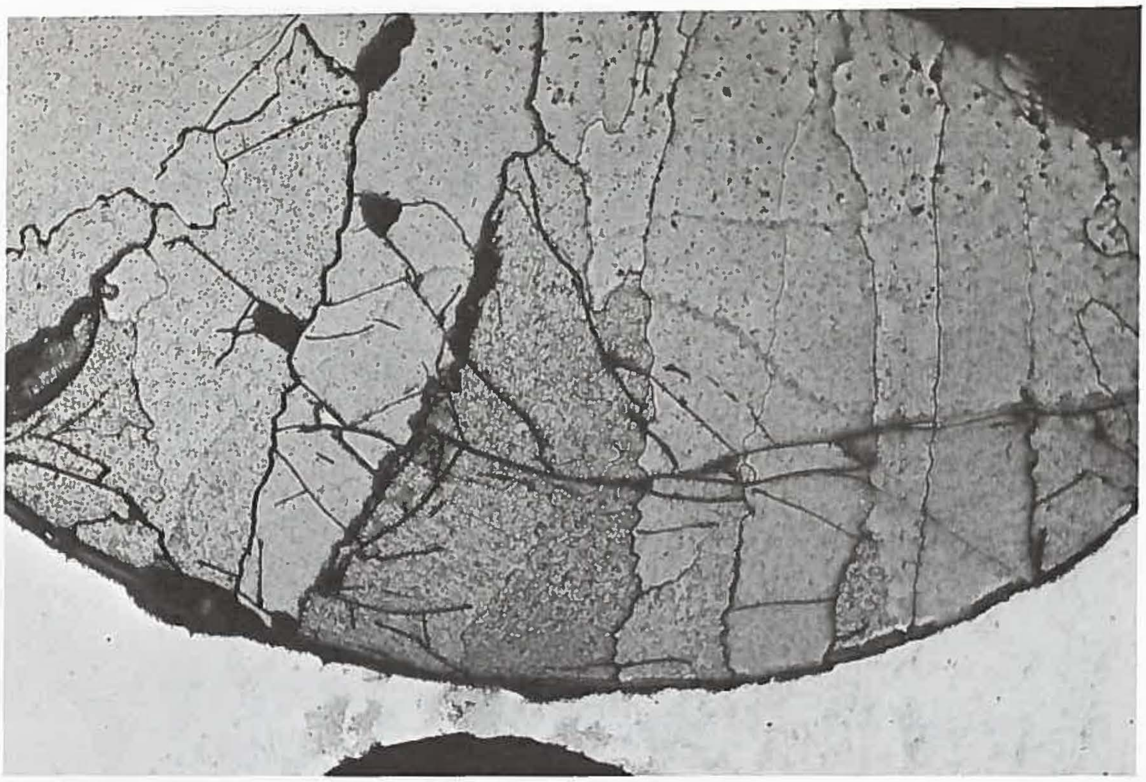

Fig. 51(a) Columnar Grains of Melted Fuel. Neg. No. MSD-185238.

Fig. 51(b) Columnar Grains of Melted Fuel with Globules of Steel. Neg. No. MSD-185239

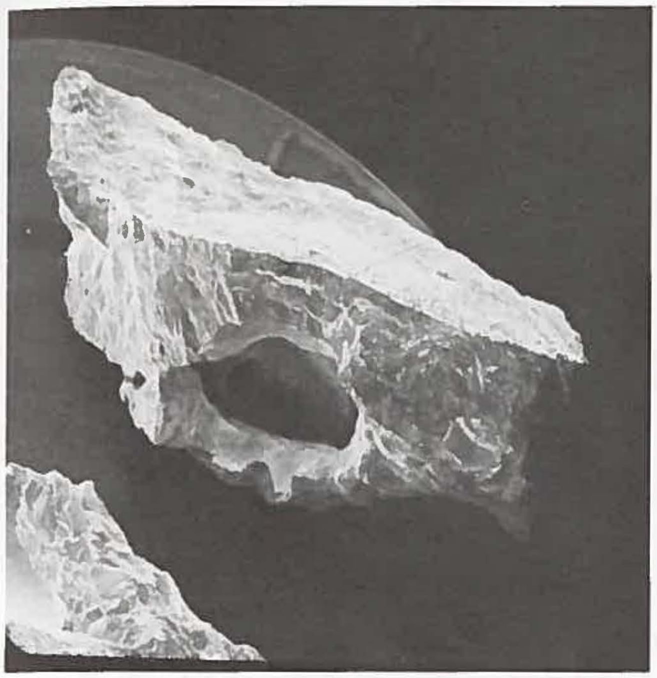

Fig. 52(a). Fuel Particle with Central Void Surface. Neg. No. MSD-200550.

Fig. 52(b). Crystalline Projections on Surface of Central Void. Neg. No. MSD-200552.

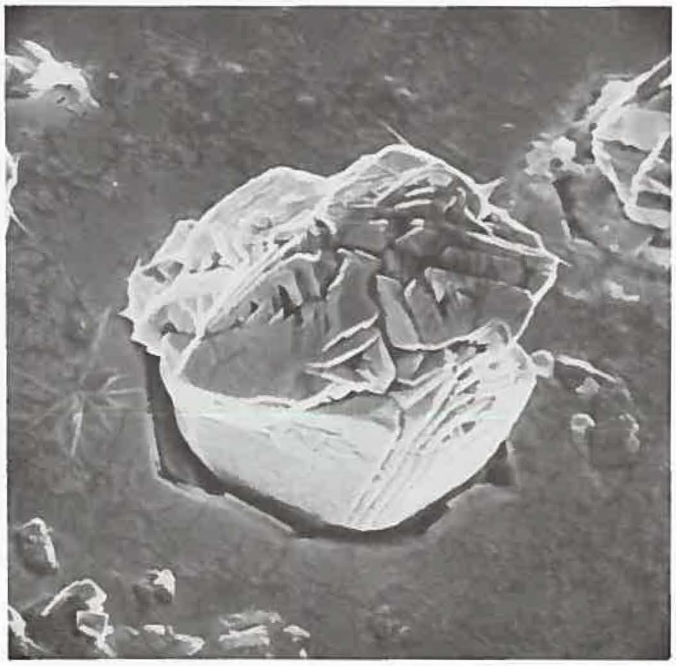

Fig. 52(c). Crystalline Projection on Surface of Fuel. Neg. No. MSD-200564.

wrap on the elements. Near the top of the bottom reflector rod a part of the flow tube was melted by contact with melted steel. In the same manner, a small amount of cladding was melted in this region (Fig. 45, Section A).

Practically all of the melted steel flowed downward and ended up around the lower part of the fuel columns in Section 40-R4-17. This pool of melted steel was contained on the bottom by a plug of steel that was frozen by contact with a relatively cold heat sink just below the fuel column, and on the side by the molybdenum shield tube. The pool of melted steel probably acted as a heat sink for heat generated in the lower part of the fuel column and as a quenching medium for the melted fuel that came from higher up the fuel columns.

The steel constituted a blockage in great depth to the flow of sodium coolant. Details of this steel blockage are shown in Fig. 45. Section A in the figure, about 4.8 cm ($1\frac{7}{8}$ in.) below the bottom of the fuel column, shows the beginning of the accumulation of melted steel near the tops of the reflector rods. In Section B the seven fuel pellets are completely surrounded by melted steel. The cladding, wire wrap and flow tube have been melted. The molybdenum tube confined the melted steel. This section was 0.6 cm (1/4 in.) above the bottom of the fuel columns. The quantity of steel tends to diminish on going up the fuel column (to Section D) as more fuel occupies space on the cross sections. The steel in these sections, B through F, occurs mainly as an annulus between the fuel and the molybdenum tube. Some radial cracks in the steel are probably due to thermal stresses on cooling. Areal percentages of steel on these cross sections are given in Table 11.

Approximately 30 cm from the bottom of the fuel column a 5 cm long steel ingot was located. The top of the ingot was $\sim 8\frac{1}{2}$ cm down from the top of Section 40-R4-17. The appearance of the ingot as removed from the section is shown in Fig. 53(a). The fuel in direct contact with the ingot appears to have been melted. Fuel farther removed in the radial direction has the remains of pellets. The fuel on the ingot was brittle and most of it came off during handling. The ingot with most of the fuel removed is shown in Fig. 53(b). The maximum corss section dimension was about 1.25 cm. In contrast to the situation lower down the fuel column, this ingot of steel occupied a central position in the fuel. The bottom of the ingot rested on melted fuel in a depression fitting

Fig. 53(a) Steel Ingot with Fuel Attached from Upper Part of Section 40-R4-17. Neg. No. MSD-183799.

Fig. 53(b) Steel Ingot with Fuel Removed. Neg. No. MSD-183801.

the bottom of the ingot. This ingot was completely separated from the pool of melted steel just below it as an annulus around the fuel.

A transverse section was made 1.25 cm from the bottom of the ingot. This section is shown in Fig. 54. The ingot is practically all steel. The beginning of a shrinkage cavity is apparent near the center of the section. At a higher magnification, the polished and etched section showed the steel to have a dendritic structure. Various shapes of fuel particles were observed scattered throughout but more concentrated near the surface. The fuel shapes were spheriods, star-bursts and elongated discontinuous streaks as can be seen in Fig. 55(a). Fuel at the surface of the ingot in some cases gave the appearance of having penetrated into the steel while still liquid [Fig. 55(b)].

Because of the lower melting temperature of the steel and its lower density compared to fuel, it is probable that the ingot was formed late in the sequence of events either by molten steel flowing from above into an existing void or by molten steel displaced upward by melted fuel moving downward.

The upper blockage consisted of steel frozen in the flow channels in the region of the insulator pellets just above the melt-off of the hexagonal flow tube. A cross section through the cluster of elements in this region is shown in Fig. 56(a). The specimen was mounted in clear plastic. The center element contained fuel as determined by autoradiography. Five of the peripheral elements contained insulator pellets and the sixth peripheral element has an Inconel reflector rod in this section. The claddings appeared to be intact on the peripheral elements but the cladding on the central element showed considerable melting. The light-colored material in the flow channels is melted steel which was pushed up from below. Appreciable areas in the flow channels are not filled with steel in this section and the top surface of the steel blockage is quite irregular. The cut to produce this section was very close to the top of the total blockage. Perhaps about 0.5 cm ($\frac{3}{16}$ in.) of steel was present along one side of the center element above the cut. No fuel was detected above the section with blockage.

As viewed from below before mounting [Fig. 56(b)], all flow channels were blocked with steel.

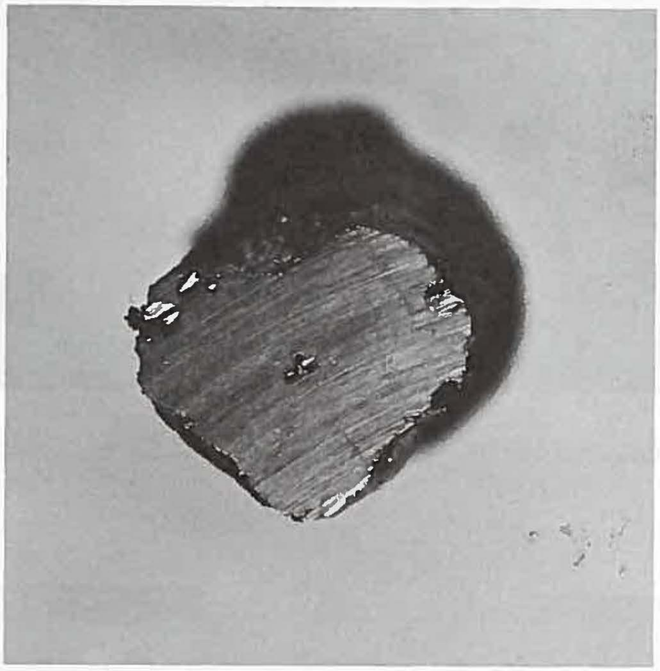

Fig. 54 Transverse Section through Steel Ingot. Neg. No. MSD-185349.

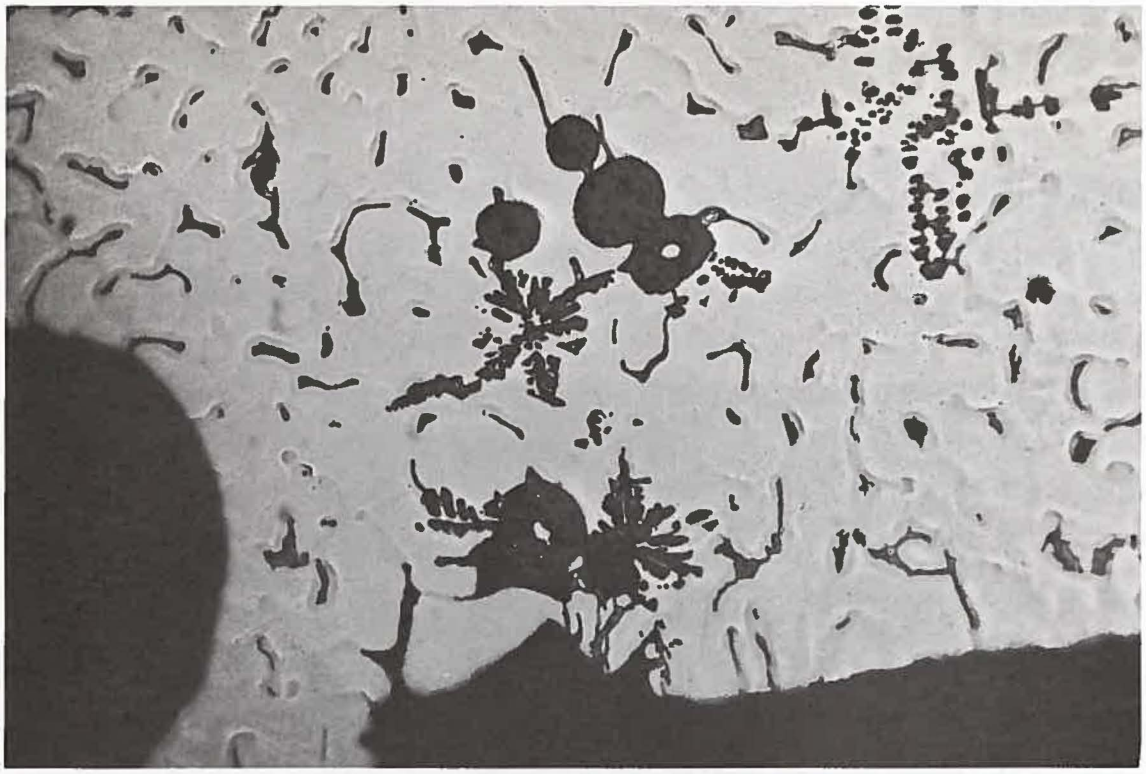

Fig. 55(a) Fuel Particles within the Steel Ingot. Neg. No. MSD-184192.

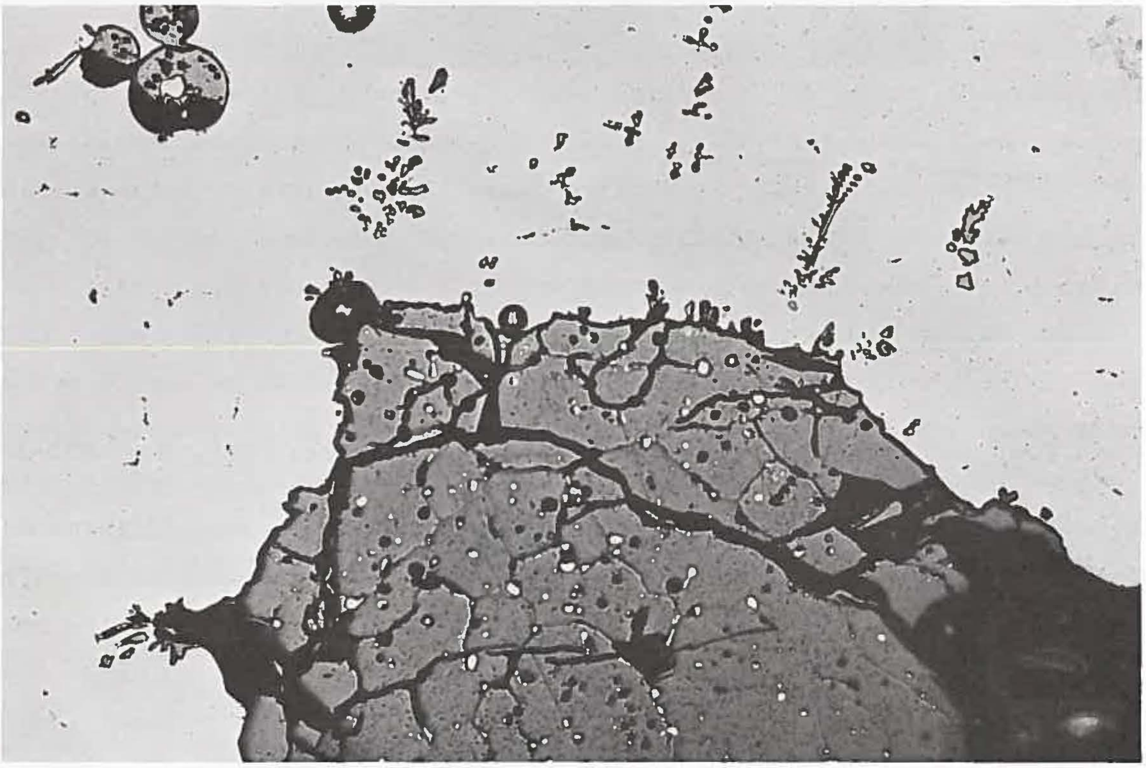

Fig. 55(b) Fuel on Surface of Steel Ingot.
Neg. No. MSD-184195. 250X Etched.

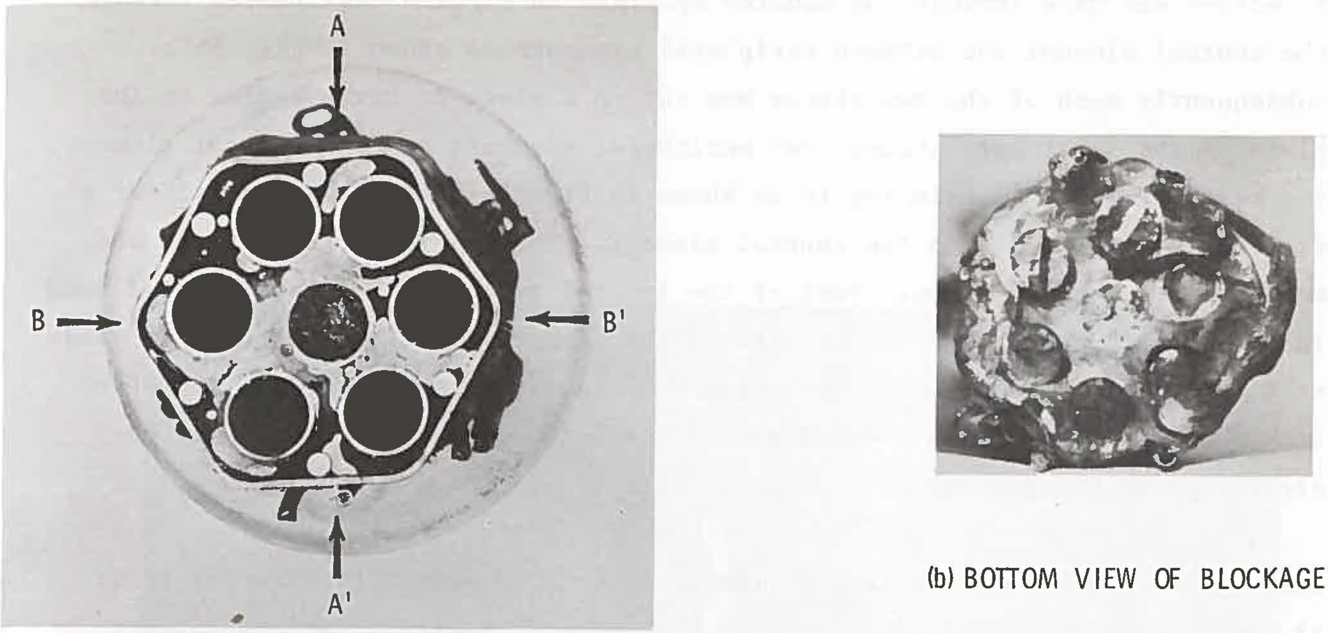

(a) TOP VIEW OF BLOCKAGE

(b) BOTTOM VIEW OF BLOCKAGE

(c) SECTION A-A' THROUGH BLOCKAGE

(d) SECTION B-B' THROUGH BLOCKAGE

Fig. 56 Views of Blockage at Top of Fuel Columns. Neg. No. MSD-187469. ∿3X.

A section was made through the mounted specimen in a plane that passed through the central element and between peripheral elements as shown in Fig. 56(c). Subsequently each of the two pieces was cut on a plane at right angles to the plane of the first cut, through two peripheral elements and the central element. The results of this sectioning is as shown in Fig. 56(d). About one half of a fuel pellet remained with the central element. The light-colored regions are metal, melted and unmelted. Part of the Inconel reflector rod is evident. Some insulator pellet material can be seen in the first section because the cut wandered from the desired plane. The steel blockage is thickest and most coherent around the central element. Elsewhere thickness of 0.1 cm ($\frac{1}{32}$ in.) were observed in the blocking steel.

There is not much steel in this blockage. But since sodium did not get by it at the conclusion of the test, it must have been a tight blockage in conformance with the observations made here.

The reflector rod in this section must correspond in position with the plenum tube which had moved downward 1.3 cm. The two insulator pellets in this element must have ended up with the jumble of fuel pellet parts but they were not detected.

5.2.4 Fuel-steel Interfaces

Interfaces between fuel and steel occur in many forms as the following illustrations will show. In Fig. 57 a stringer of steel from an external pool penetrates a crack in an unmelted fuel pellet. This location is ∿1.25 cm from the bottom of the fuel column. Mixing of steel and fuel on a macroscale is shown in Fig. 58 for a location ∿6.5 cm from the bottom of the fuel column.

Small pieces of fuel pellets were examined with the scanning-electron microscope (SEM). One such piece is shown in Fig. 59(a). A piece of fuel is in intimate contact with a base of steel. There is a hole into the piece of fuel. This hole is shown at higher magnification in Fig. 59(b). Small globules of steel can be seen on the surface outside the hole. The particles on the surface inside the hole appear to be fuel. In a recess at the intersection between the steel and the fuel, projections of stainless steel are

Fig. 57 Stringer of Steel Extending from Pool of Steel into Unmelted Fuel. Neg. No. MSD-185647. 75X.

Fig. 58 Mixture of Steel and Fuel.
Neg. No. MSD-185264. 100X Etched.

Fig. 59(a). Particle of Fuel on a Metallic Substratum. Neg. No. MSD-200705. 40X SEM.

Fig. 59(b). Hole in Fuel Particle. Neg. No. MSD-200707. 400X SEM.

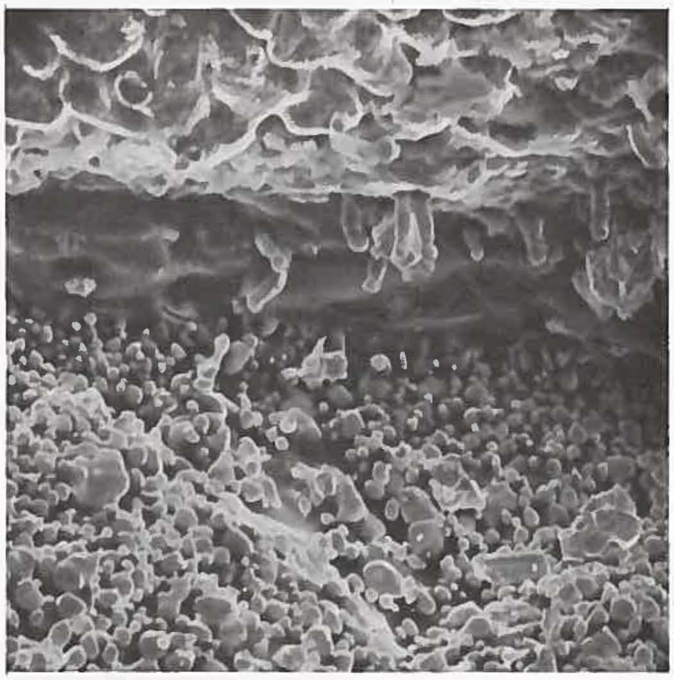

Fig. 59(c). Projections of Steel in Crevice at Intersection of Fuel and Steel. Neg. No. MSD-200729. 1000X SEM.

suspended from a base of dendritic steel toward the fuel surface which has a covering of irregular globules of fuel [Fig. 59(c)].

A third SEM specimen again consisted of fuel embedded on a metal base. The fuel has both a fractured surface and a solidified-from-melt surface. The surface of the metal is a fracture. This specimen is shown in Fig. 60(a). The metal is basically stainless steel with a large component of molybdenum as shown in the X-ray spectra of Fig. 60(b). A field of metallic globules on the solidified fuel surface is shown in Fig. 61(a). Some of these globules are seen at higher magnification in Fig. 61(b). The size of these metallic globules ranges from 5 to 40 μm. Many of these particles lie on grain boundaries. According to one hypothesis these globules are formed by being squeezed out of the fuel when it solidified and cooled while the steel was still molten and trapped within. It has also been suggested that the globules formed by vapor condensation. The manner in which the globules relate to the fuel surface does not however seem to imply a condensation process. They are essentially stainless steel as shown by the X-ray spectra of Fig. 61(c).

In another area on the same specimen similar but less rounded globules of metal project from the surface of fuel [Fig. 62(a)]. The projections from the surface are steel [Fig. 62(b)] and the material encrusting the globules is fuel as shown by the X-ray spectra in Fig. 62(c). The steel appears to have broken through a crust of fuel from below.

Figure 63 shows a dispersal of steel on a fine scale in fuel. The globules of steel occur both in grain boundaries and within grains. This specimen was about 23.5 cm ($9\frac{1}{4}$ in.) above the bottom of the fuel column and about 2.5 cm (1 in.) below the steel ingot previously described. The steel globules occupy ∿3% of the surface in this view.

5.2.5 Upper Parts of the Fuel Elements

Externally, the upper parts of the fuel elements above the flow blockage were visually unchanged. There appeared to be slight differences in the relative positions of the tops of the elements with reference to the cut at 92 in. as shown in Fig. 64 (X-radiograph). The identy of the elements was not maintained

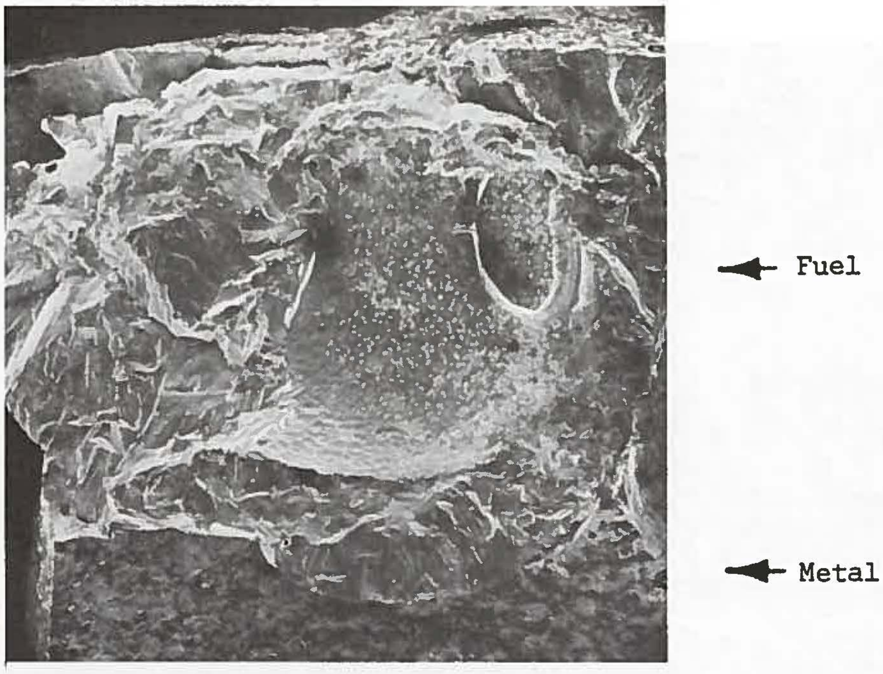

Fig. 60(a) Fuel on a Metallic Substratum.
Neg. No. MSD-200589. 20X.

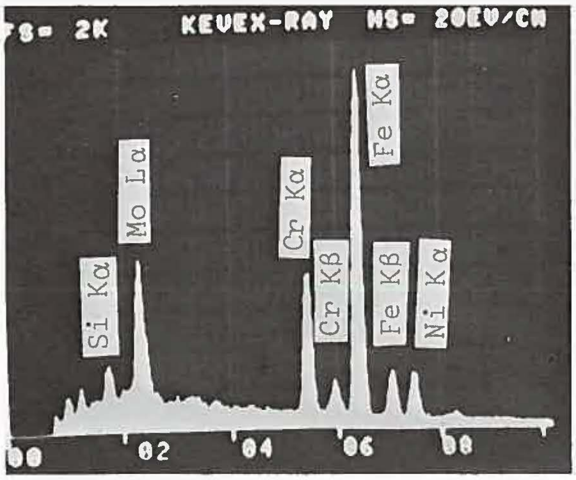

Fig. 60(b) X-ray Spectra of Metallic Substratum.
Neg. No. MSD-187445.

Fig. 61(a). Colony of Metallic Globules on Surface of Melted Fuel. Neg. No. MSD-200700. 200X SEM.

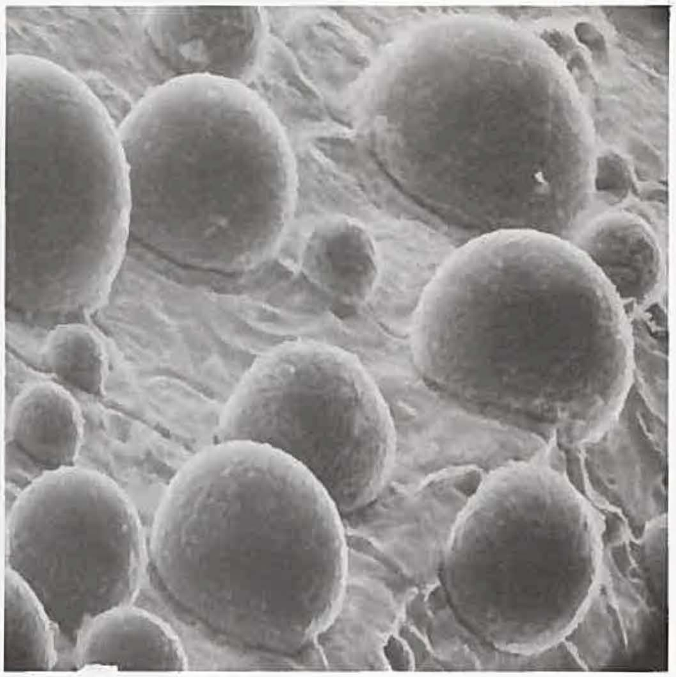

Fig. 61(b). Steel Globules on Surface of Melted Fuel. Neg. No. MSD-200701. 1000X SEM.

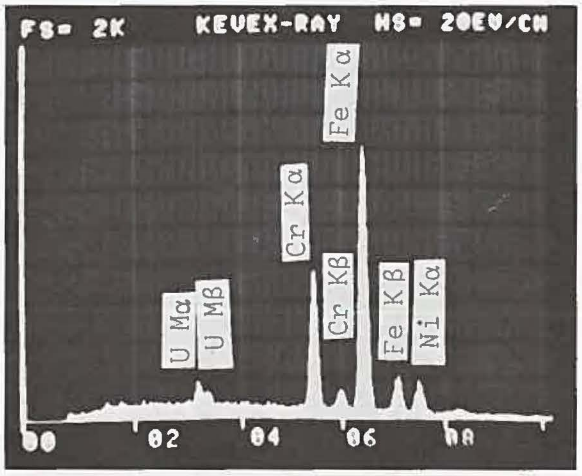

Fig. 61(c). X-ray Spectra of Metallic Globules. Neg. No. MSD-187446.

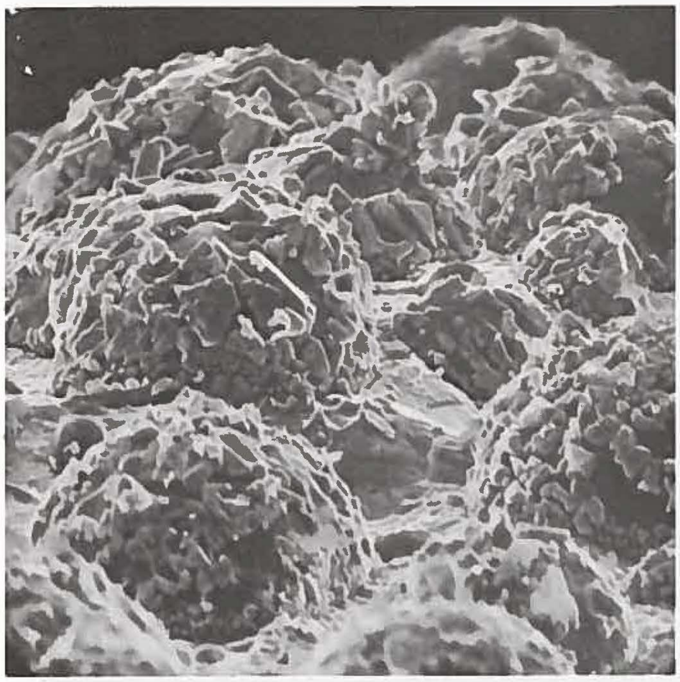

Fig. 62(a). Encrusted Globules on Surface of Fuel [Fig. 21(a)]. Neg. No. MSD-200678. 1000X.

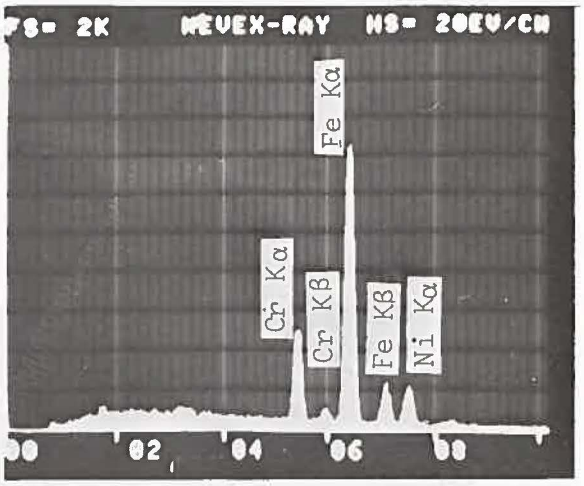

Fig. 62(b). X-ray Spectra of Globules Beneath the Encrustation. Neg. No. MSD-187444.

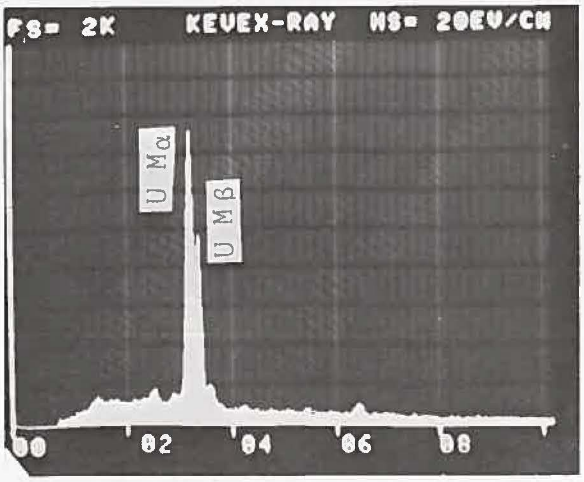

Fig. 62(c). X-ray Spectra of Encrusting Material on Globules. Neg. No. MSD-187443.

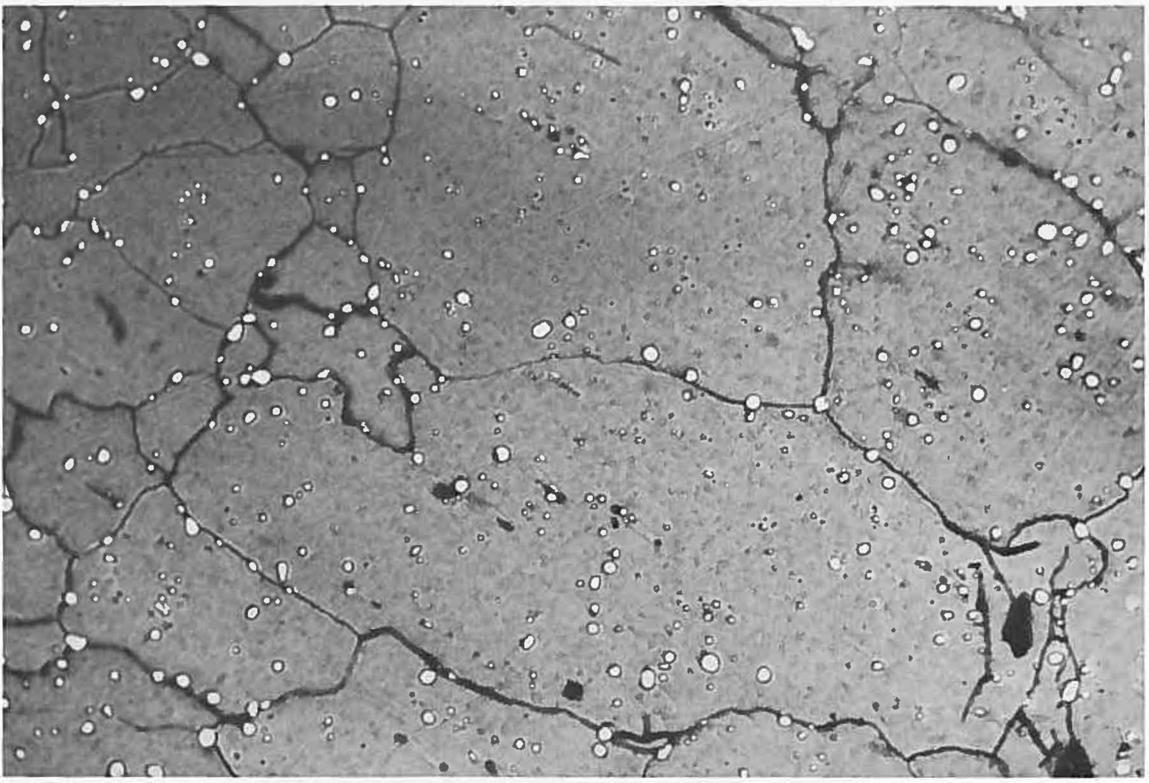

Fig. 63 Melted Fuel with Globules of Stainless Steel Dispersed Throughout. Neg. No. MSD-185244. 250X Etched.

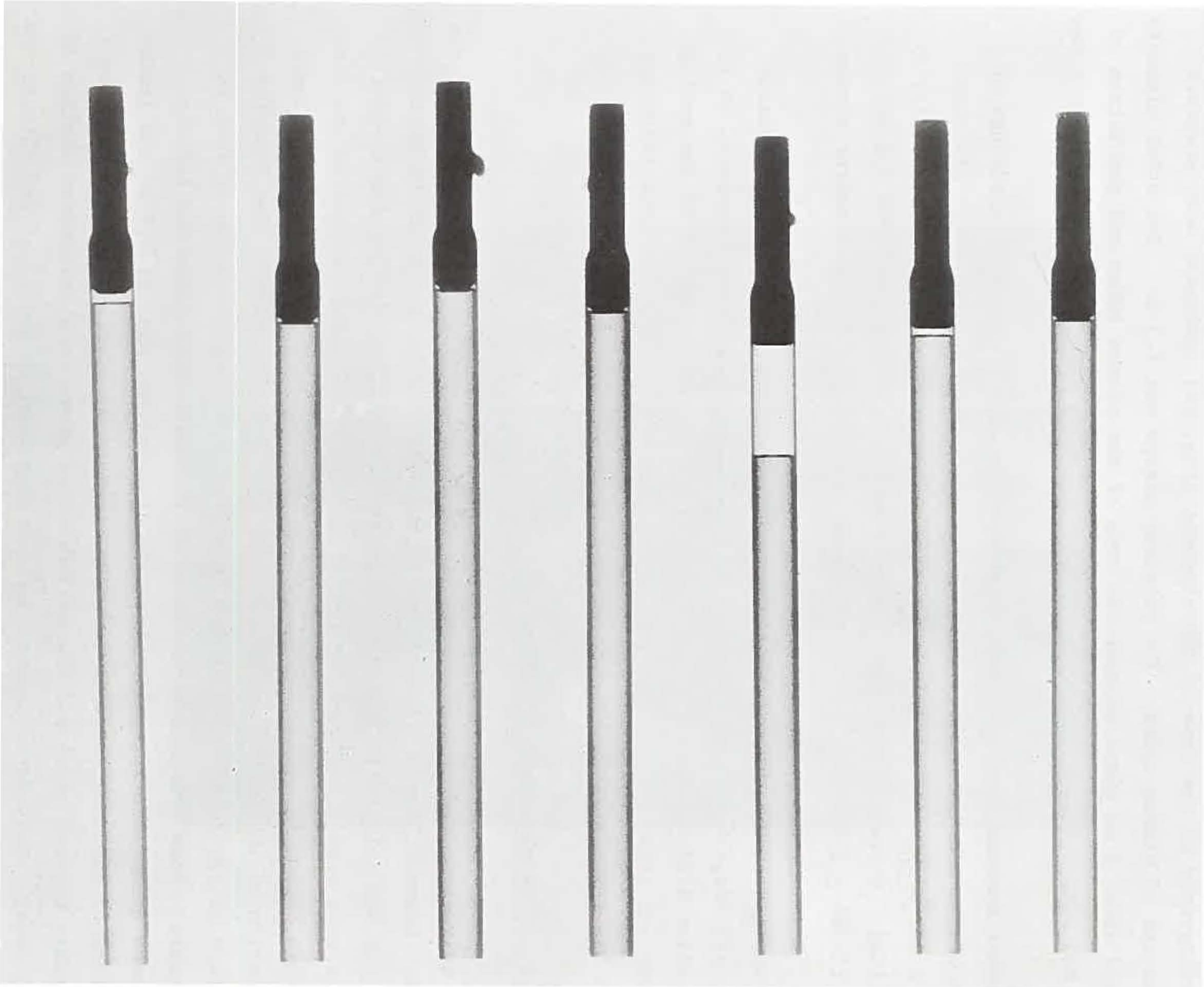

Fig. 64 X-radiographs Showing Location of Spacer Tubes and Relative Positions of the Tops of the Elements. Neg. No. MSD-185671. $\sim 1\frac{1}{4}$X.

during disassembly so only relative changes are noted.

X-radiography of the tops of the elements (Fig. 64) indicated some downward movements of plenum tubes. The greatest change was 1.3 cm. Two other elements showed about 1 mm space between the tops of the plenum tubes and the bottom of the end plug. Sodium was found in a few elements even up into the plenum tubes.

Diameter measurements were made at several locations along the claddings of each of the elements. The average of all diameters for the seven elements was $0.582^{+0.002}_{-0.001}$ cm ($0.2293^{+0.0007}_{-0.0003}$ in.). There was no evidence of ovality or swelling. Since the specified diameter of the cladding was 0.230 ± 0.001 in. (0.584 ± 0.002 cm), the measurements do not indicate any diameter change.

The springs from three of the elements were examined. The spring constants were 693 N/m,634 N/m and 609 N/m (3.65, 3.62 and 3.84 lb/in.) compared to that specified 3.27 ± 0.16 lb/in. (573 ± 28 N/m). The free lengths of the springs before and after compression were essentially unchanged. The test transient does not seem to have significantly affected the springs.

5.2.6 Molybdenum Heat Shield Tube

The molybdenum heat shield tube appeared to be intact at the conclusion of the test. However, during disassembly the molybdenum tube proved to be quite brittle and relatively easy to break toward the top of the Section 40-R4-17. There were some visual indications of cracks on the outer surface of the tube in this region (upward from about 10 cm above the bottom of the fuel column). A section of the broken molybdenum tube is shown in Fig. 65. The interior surface of the tube has reacted with molten steel and a section of fuel is attached. Some thinning of the wall of the tube ($\sim$10%) occurred locally. In some areas thin irregular platelets of metal had spalled off of the inside surface of the tube where it had been attacked by steel. The nature of the boundary between steel and the molybdenum is shown in a transverse section in Fig. 66(a). Molybdenum appears to have dissolved in the steel and altered the character of the steel. The molybdenum itself has completely recrystallized to equiaxed grains as can be seen in the right side of the figure. For comparison a transverse section of the molybdenum tube from the top of section 92-R4-70 is shown in Fig. 66(b). The grain structure at this location does not

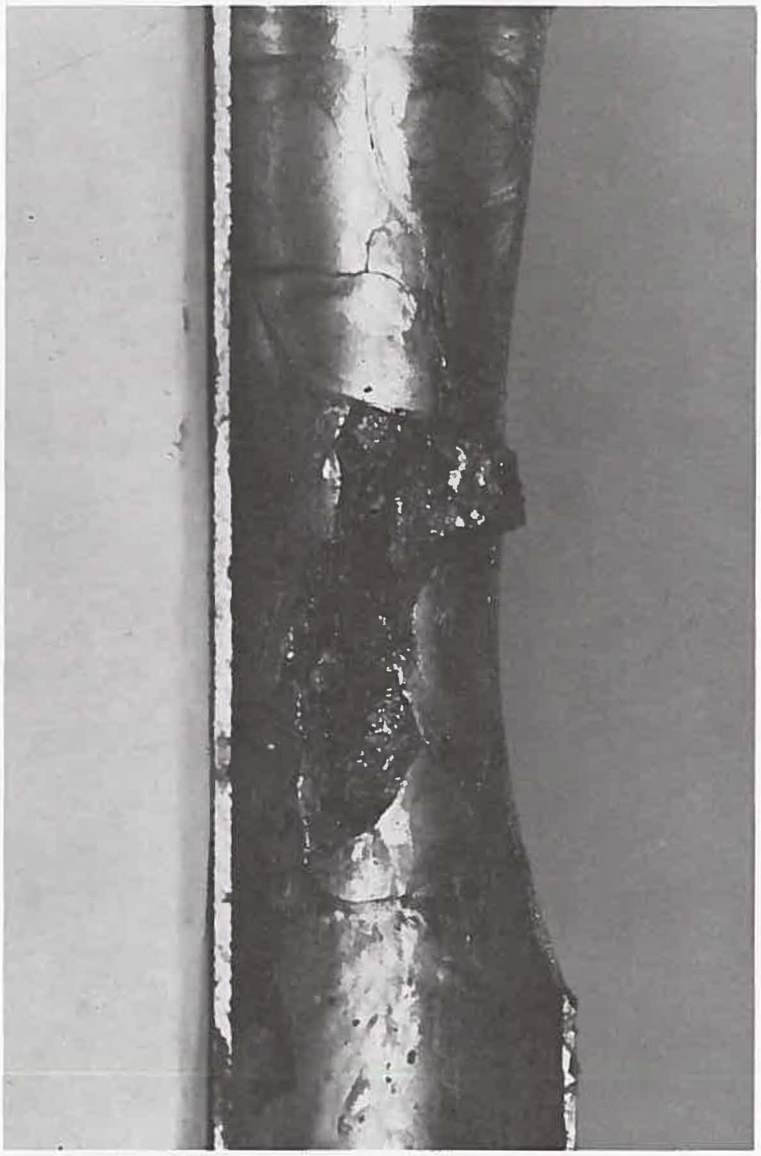

Fig. 65 Inner Surface of Molybdenum Tube from Section 40-R4-17 Showing Fuel and Steel. Neg. No. MSD-183806. $1\frac{1}{2}$X.

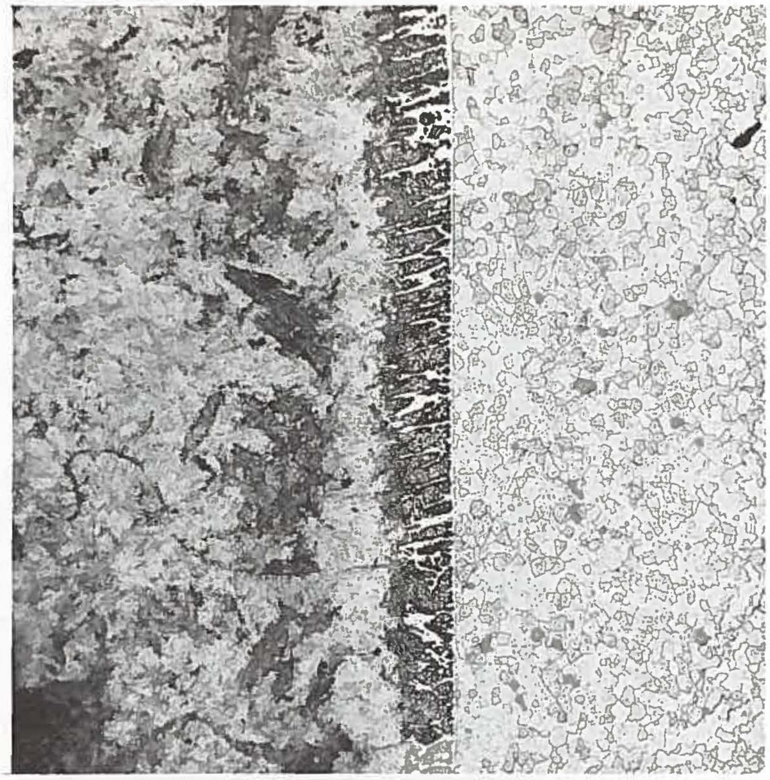

Fig. 66(a). Interface between Molybdenum Tube and Melted Steel. Neg. No. MSD-184762. 50X Etched.

Fig. 66(b). Microstructure of Molybdenum Tube from Top of Section 92-R4-70. Neg. No. MSD-184778. 150X Etched.

seem to have been affected by the transient.

Although visual appearance of the molybdenum tube did not indicate any simple melting, a small globule of molybdenum in contact with melted fuel is shown in Fig. 67(a). The material of the globule was essentially molybdenum as shown by the X-ray spectra [Fig. 67(b)] but some uranium was also present. The broken-egg-shell-like objects behind they molybdenum globule are an unusual formation of fuel material.

5.3 R5 Metalographic Examination

5.3.1 Distribution of Fuel

Measurements made on the neutron radiograph, Fig. 34, along the length of the test section of R5 indicated the following distribution of fuel from the top to the bottom of the original fuel column.

Length	
9.0 cm (3.56 in.)	Void, no fuel
13.4 cm (5.28 in.)	A jumble of pellets, mostly individual but some fused end-to-end in pairs, supported on stacks below.
37.5 cm (14.78 in.)	Partly intact stacks of pellets
16.8 cm (6.60 in.)	A jumble of individual pellets
14.4 cm (5.68 in.)	Stacks of pellets embedded in melted steel
91.1 cm (35.90 in.)	Nominal overall length 36 in. or 91.4 cm

During the initial sectioning two cuts were made through the fuel-column region at a nominal 36.5 in. (92.7 cm) and 60 in. (152.4 cm) distance from the bottom of the U-tube. The cut at 36.5 in. went through the top of the 16.8 cm length of the jumble of individual pellets. The cut at 60 in. went through the region void of fuel about 1 in. (2.5 cm) below the upper insulator pellets.

Section 36.5-R5-17 had been further cut into four pieces which have been designated from bottom to top as #1, 2, 3 and 4. These pieces are shown in

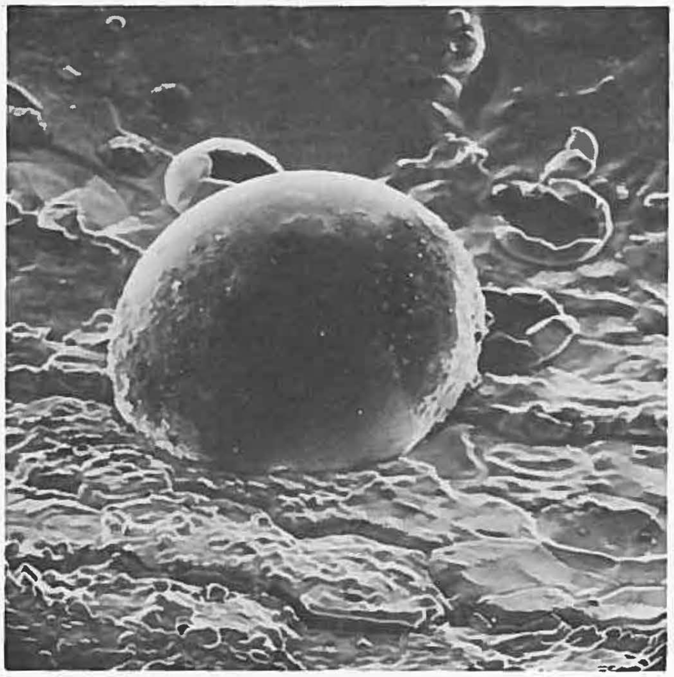

Fig. 67(a) Globule of Molybdenum on Surface of Melted Fuel. Neg. No. MSD-200658. 400X SEM.

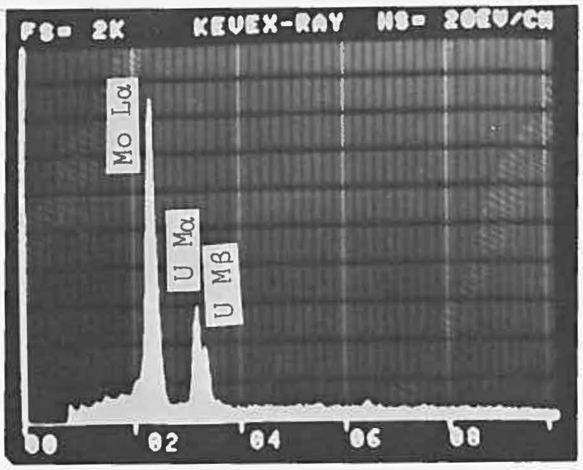

Fig. 67(b) X-ray Spectra of Globule Showing Molybdenum with Some Uranium. Neg. No. MSD-187442.

Fig. 68 after cleaning in the AGHCF to remove sodium residues. Piece #1 contained the bottom part of the end plugs; piec #2 contained part of the end plugs, the bottom reflector rods, the insulator pellets and about 7.8 cm (3 in.) of pellets. Piece #3, before the sodium was melted out, had stacks of fuel pellets; piece #4 had the topmost part of the pellet stacks (in section 36.5-R5-17) and most of the 16.8 cm long region of the jumble of individual pellets. The top of section 36.5-R5-17 was 31.2 cm above the bottom of the fuel columns. As received at the AGHCF, the upper part of the section (piece #4) contained no fuel pellets. Piece #3 contained some pellet stacks held in by melted steel, but many of the pellets had fallen out. In piece #2 the hexagonal flow tube had been removed from around the bottom of the elements. The top piece #2 was about 7.8 cm above the bottom of the fuel columns. The seven fuel pellet stacks in this latter piece were supported by the melted steel which had flowed around them. The X-radiographs of Fig. 69 shows the location of fuel in pieces 2 thru 4 of section 36.5-R5-17 as received.

The split molybdenum heat-shield tube from section 60-R5-36.5, along with the melted steel associated with it, is shown in Fig. 70. This section, which in the posttest neutron radiograph contained partial stacks of pellets, had no fuel as received at ANL-E. The bottom of section 87-R5-60, which would have contained the tops of the fuel columns before the test, had no fuel in it after the test. From the neutron radiograph the fuel originally in the bottom of section 87-R5-60 had relocated farther down the test section in the top of 60-R5-36.5. The absence of fuel in section 87-R5-60 was noted during disassembly at ANL-W.

The five lots of fuel which were received in plastic vials were weighed separately as shown below with their "as received" identification.

87-R5-60		111.7 g
60-R5-36.5,	#1	293.8
	#2	276.2
	#3	148.7
36.5-R5-17		96.1
		926.5 g

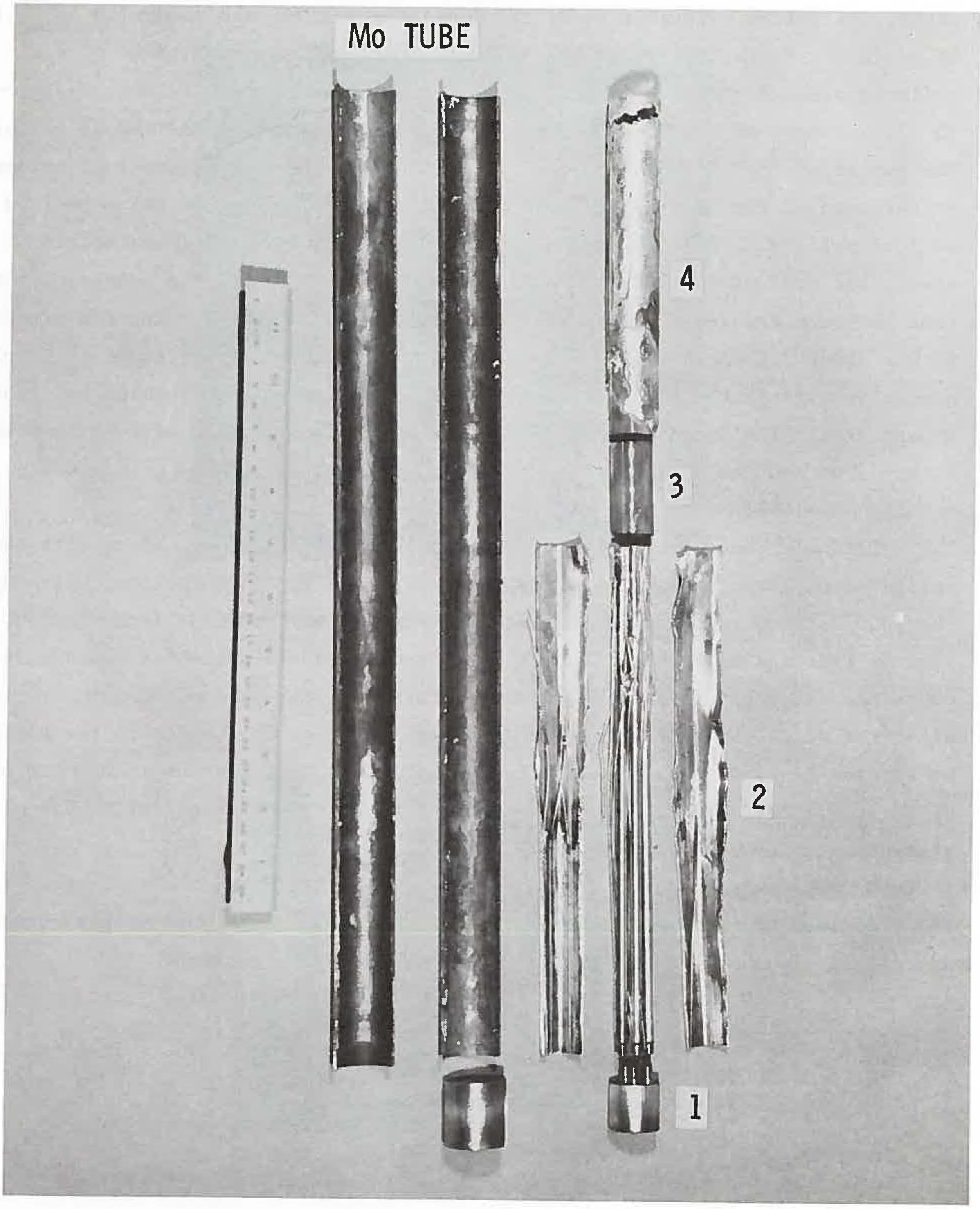

Fig. 68 Section 36.5-R5-17 Partly Disassembled.
Neg. No. MSD-185607.

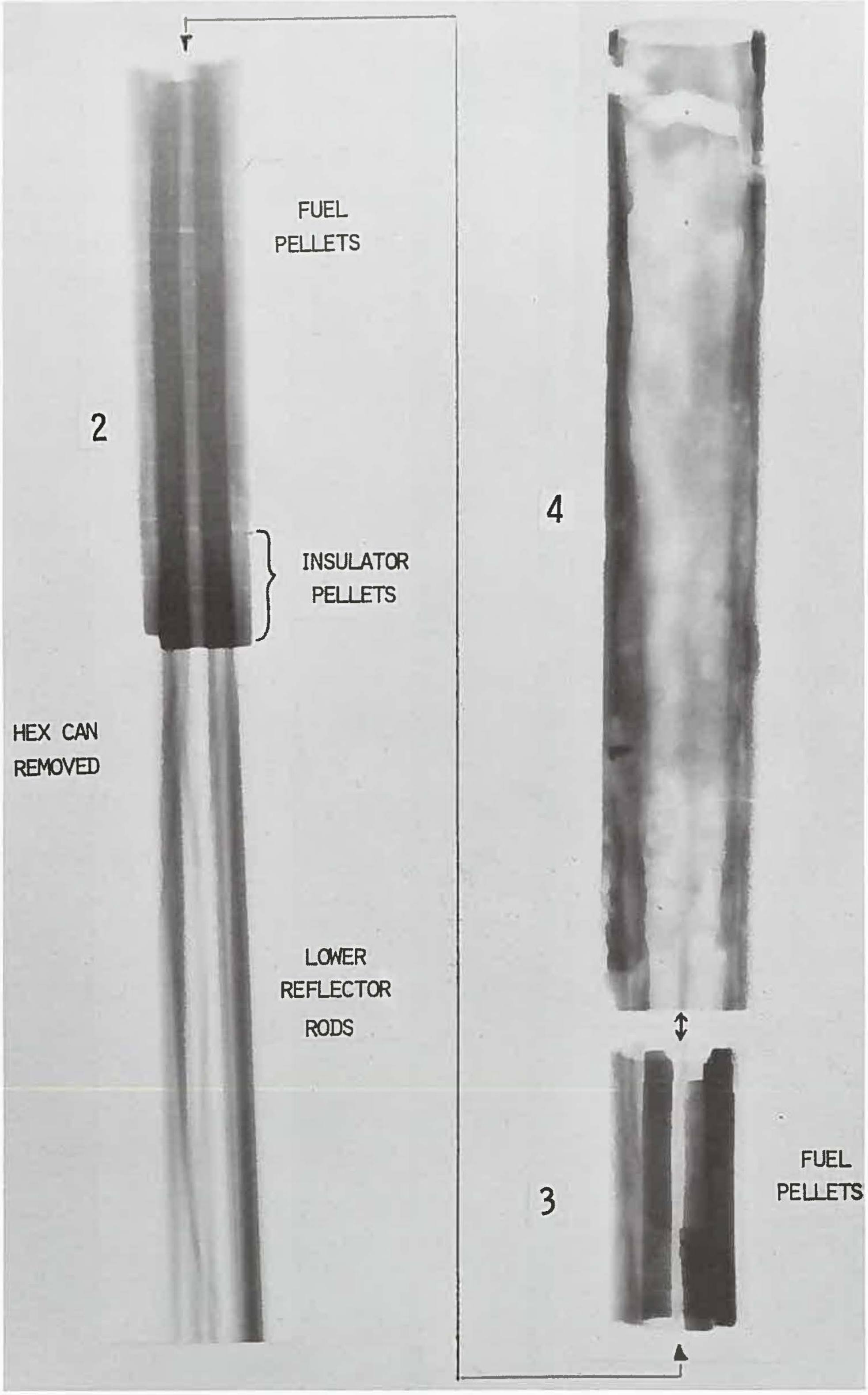

Fig. 69 X-ray Radiograph of Section 36.5-R5-17 Showing Fuel Pellets and Insulator Pellets. Neg. No. MSD-185676.

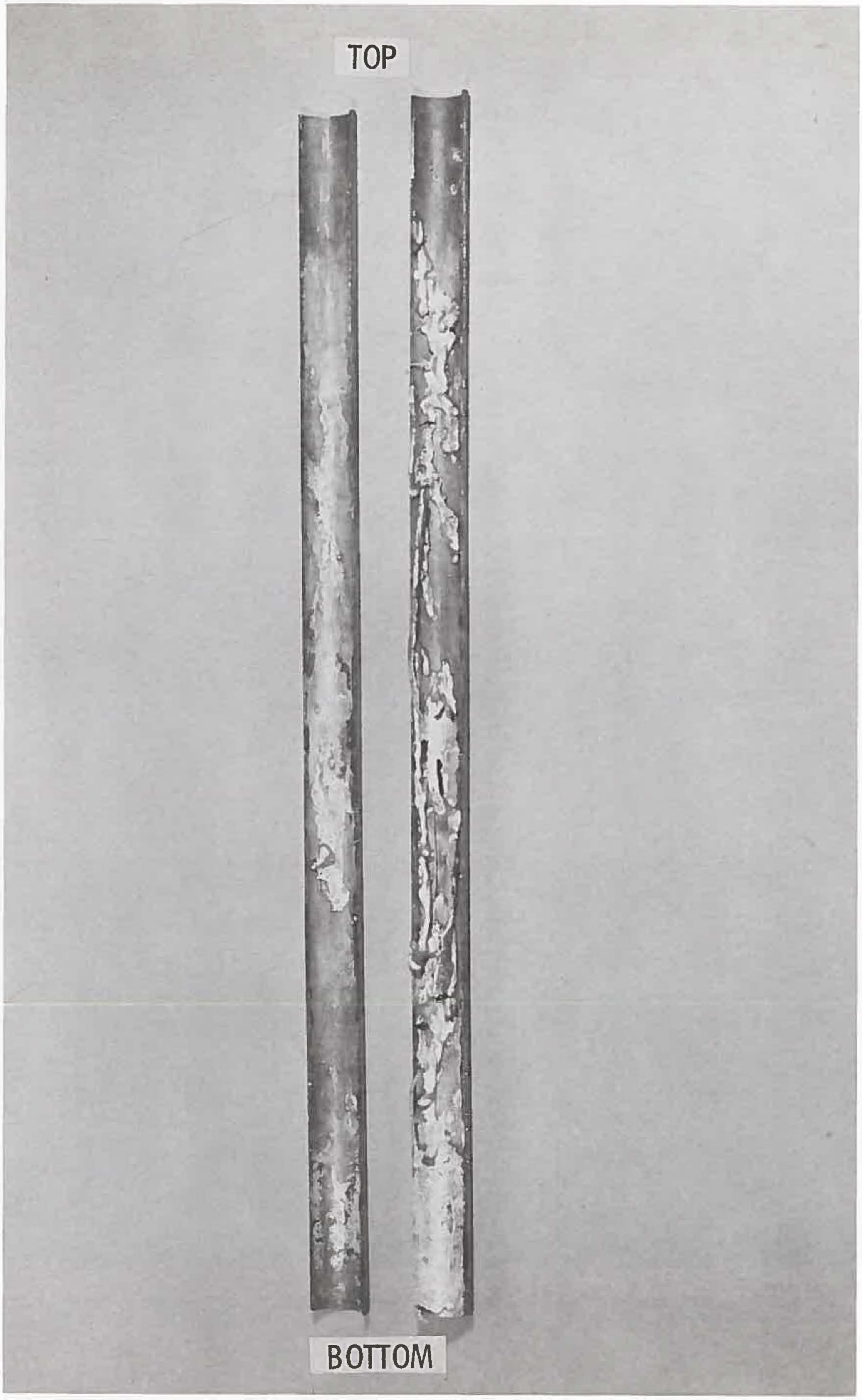

Fig. 70 Split Molybdenum Tube with Melted Stainless Steel on Inside Surface. Section 60-R5-36.5. Neg. No. MSD-185605.

Thirty pellets were counted in the 4.4-cm (1 3/4 in.) long segment (piece #3 of 36.5-R5-17) with the aid of X-radiography and visual observation. Since each fuel pellet weighs about 1 g, the estimated mass of fuel in piece #3 was about 30 g. Similarly the pellets in the stacks in piece #2 of 36.5-R5-17 were counted at 119 and their weight would be ∿119 g. At this point the total fuel accounted for is 1075 g out of a total of 1214 g. The remaining pellets were found by X-radiography in the cans of sodium collected from each section at ANL-W as follows:

87-R5-60	2 pellets
60-R5-36.5	83
36.5-R5-17	59
	144 pellets or ∿144 g

The total fuel accounted for is 1219.5 g which compares favorably with the 1214 g charged.

The original 36-in. (91.4 cm) long fuel columns had 13.28 g of oxide fuel per cm of length as fabricated. The weight of fuel originally in each section was calculated and is compared with the fuel in the sections after the test, as follows:

Section	Original Weight of fuel, g	Posttest Weight of fuel, g	Change, g
87-R5-60	33.7	2.0*	-31.7
60-R5-36.5	800.8	801.7	+ 0.9
36.5-R5-17	379.5	415.8	+36.3
	1214.0	1219.5	

---

*Found in sodium recovered from section 87-R5-60.

A weight of pellets equivalent to that lost from section 87-R5-60 was found as an addition to the pellets originally in section 36.5-R5-17, in piece #4.

5.3.2 Characterization of fuel

In this test, the cylindrical fuel pellets tended to maintain their external geometry although some pellets had center melting. The only fuel pellets remaining in their original locations were those in pieces #2 and #3 of section

36.5-R5-17 (Fig. 68). In piece #2 stacks of pellets from all seven elements were intact and embedded in melted steel. In piece #3 some stacks of pellets were complete, some incomplete and some missing. None of the pellets in either #2 or #3 that were still in place showed evidence of melting. Some pellets had cracks however. Typical cross sections through these pellets are shown in Fig. 71. A cross section of a single unmelted pellet is shown in Fig. 72 at a higher magnification.

The loose fuel pellets had been identified as coming from the upper part of section 36.5-R5-17, principally piece #4, and from section 60-R5-36.5. The loose pellets from section 36.5-R5-17 were generally intact. These were individual pellets with no evidence of melting. Some roughening of the ends and sides had occurred. The roughening appeared to be either from local movement on the surface or possibly a nonuniform loss of material from the surface. Broken pellets were present, and these pieces showed a discoloration of the material toward the center of the pellet. The discoloration may have been associated with a high temperature reduction from the original oxygen-to-metal ratio of ∿2.00. Only one small piece of melted fuel was observed among these pellets. Small globules of stainless steel had attached themselves to the end and side surfaces of some pellets without significant penetration beyond the surface.

The three vials of pellets from section 60-R5-26.5 were not separately identified as received. For the purpose of examination they were arbitratily identified as #1, #2, and #3.

In lot #1 many pellets were fused together end-to-end (Fig. 73). Some pellets were stuck together on their sides or were held together by melted steel. Central melting was very much in evidence but many pellets showed no evidence of melting. Some globules of steel (Fig. 74) were included in this lot. The breaking of some of the pellets had resulted in the generation of a small cmount of powder.

Lot #2 was very much like #1 but was judged to have more center melting in the pellets. Some globules of melted steel and some powdered fuel were associated with this batch.

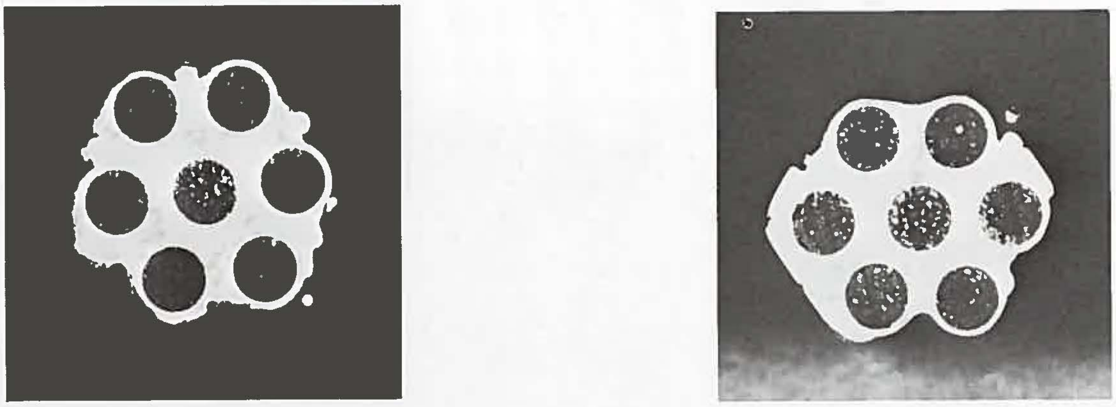

(a) 4.8 cm. above bottom of fuel column

(b) 1.8 cm. above bottom of fuel column.

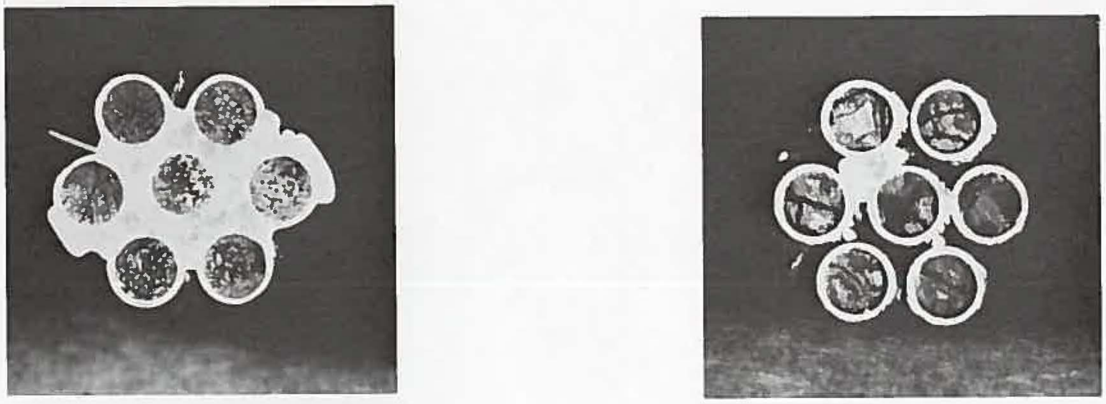

(c) 0.3 cm. above bottom of fuel column.

(d) 1.2 cm. below bottom of fuel column.

Fig. 71 Transverse Sections Through Piece #2 of Section 36.5-R5-17. Neg. No. MSD-187529.

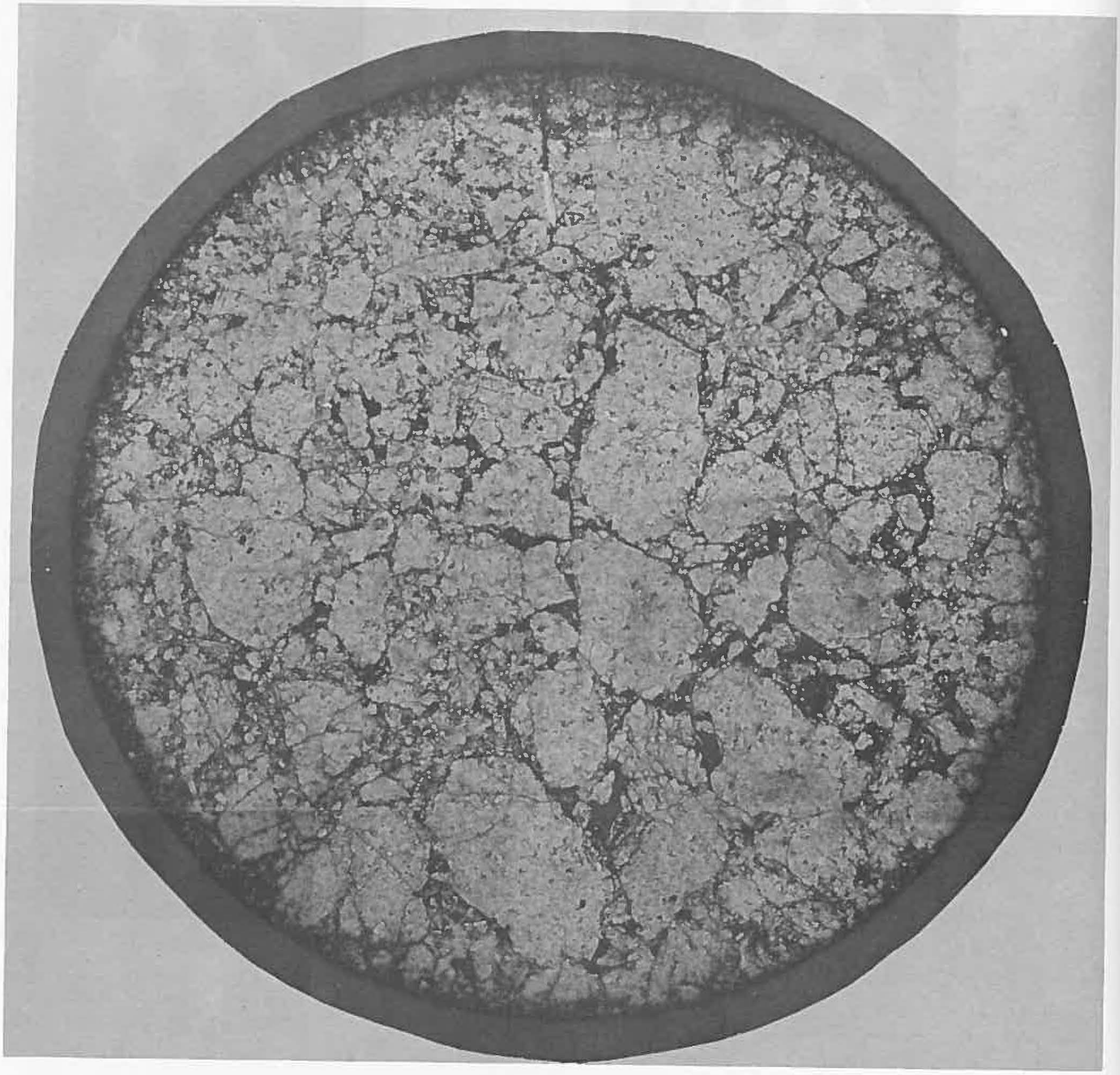

Fig. 72 Cross Section of Unmelted Fuel Pellet with Metallic Intrusion. Neg. No. MSD-186449. ∿30X.

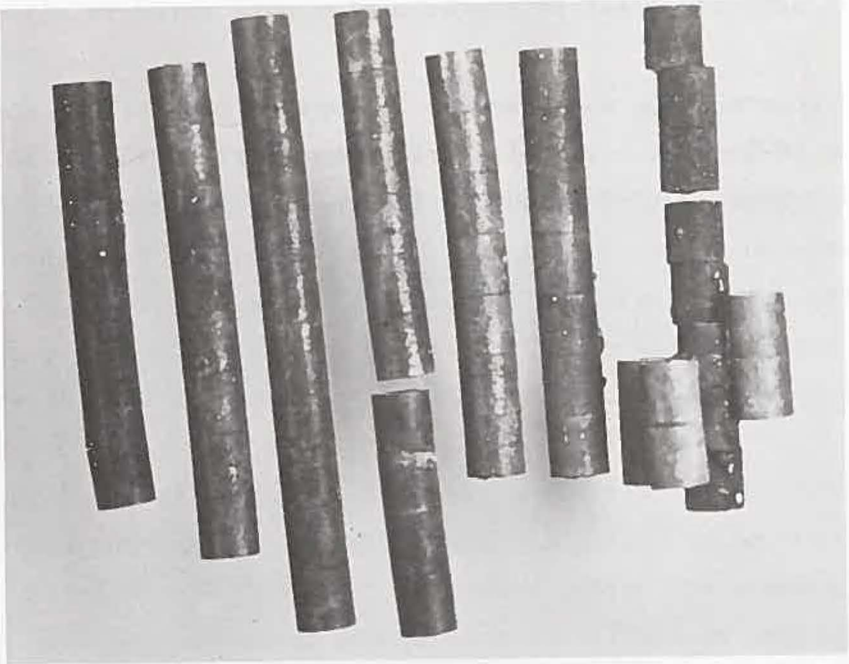

Fig. 73 Fuel Pellets Fused Together.
Section 60-R5-36.5
Neg. No. MSD-185609. ~1-1/2X.

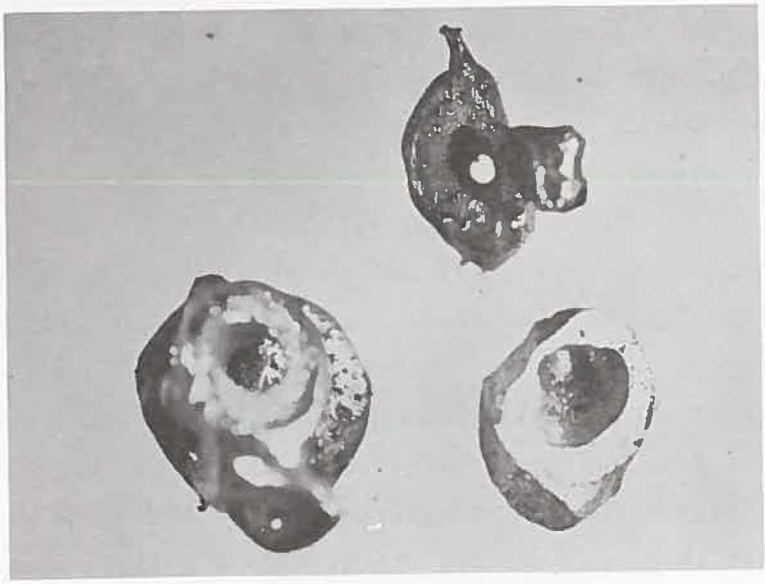

Fig. 74 Globules of Melted Steel
from Section 60-R5-36.5.
Neg. No. MSD-185638. 5X.

In lot #3, the pellets were present mostly as individuals and without obvious center melting. Some melted steel particles and fuel particles were also present. Occasional pieces of thermocouples were noted in all three lots.

Extensive center melting was observed in some of the pellets and pellet pieces from section 60-R5-36.5. Examples are shown in Figs. 75 and 76. Figure 75 shows a transverse section through a fuel pellet in which much of the large, dense grains around the central void. The percent of fuel melted was 65% areal and the central void was 40% areal. Unrestructured fuel is present around the melted region with a small transition zone where some grain growth occurred. A number of spherical bubbles are randomly present in the melted fuel zone.

A longitudinal section through a piece of a fuel pellet is shown in Fig. 76. In this section melted fuel has formed a bridge across the central void with a large void above and below the bridge (the "up" direction is not known). The general structure is similar to that of the transverse section of Fig. 75. However, a noticeable number of bubbles are present in the melted fuel at the boundary between melted and unmelted fuel. The percent of fuel melted on a cross section of this pellet was calculated to be 55% and the largest void was 37% of the cross section area.

Melting, without the development of a central void, also occurred as shown in Figs. 77 and 78. In these two transverse sections about 22% areal of the fuel pellets has melted. In one case, Fig. 77, the pellet appears to have begun to crack open from the internal pressure. In the other (Fig. 78), melting has occurred locally out to the surface of the pellet. The pressure appears to result from a combination of the volume change on melting of the fuel and the presence of a gas in the "as-fabricated" fuel pellets. The measure of the void area in the melted fuel of Fig. 77 and in an unmelted pellet of Fig. 72 with the Quantimet gave 21% and 14% respectively.

The center element was calculated to have the highest fuel temperature. However, melting of fuel was not restricted to the center element as shown in Fig. 79. This figure shows a transverse section through a group of three stacks of almost three pellets per stack. These pellets appear to be in their original relative position with respect to one another so one of them must have been a central element pellet. One pellet has melted appreciably more than the

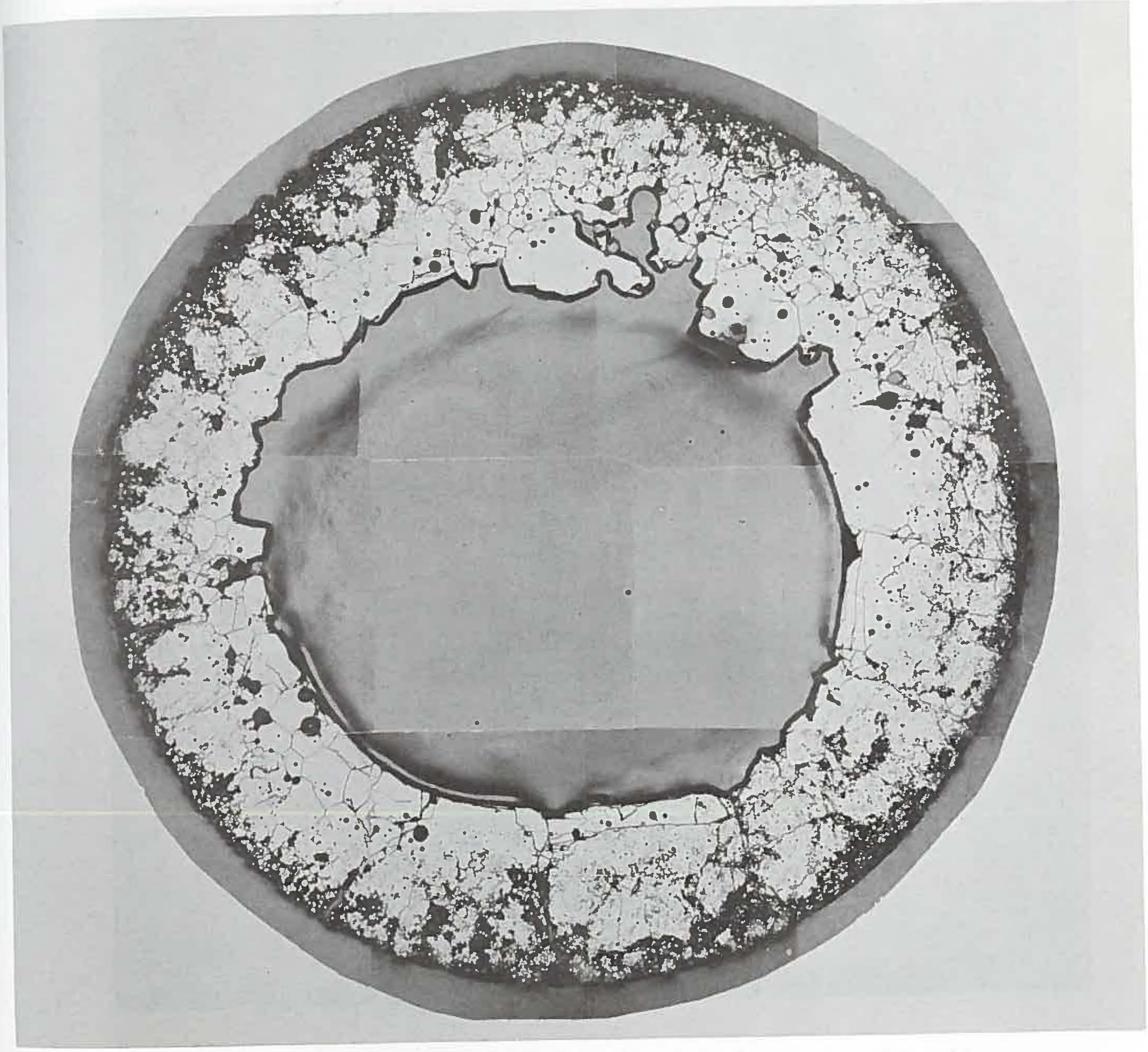

Fig. 75 Transverse Section of Fuel Pellet with Center Melting and Central Void. Neg. No. MSD-186350. ∿30 X.

Fig. 76 Longitudinal Section of Fuel Pellet Showing Bridge of Melted Fuel Across Central Void. Neg. No. MSD-186349. ~30X.

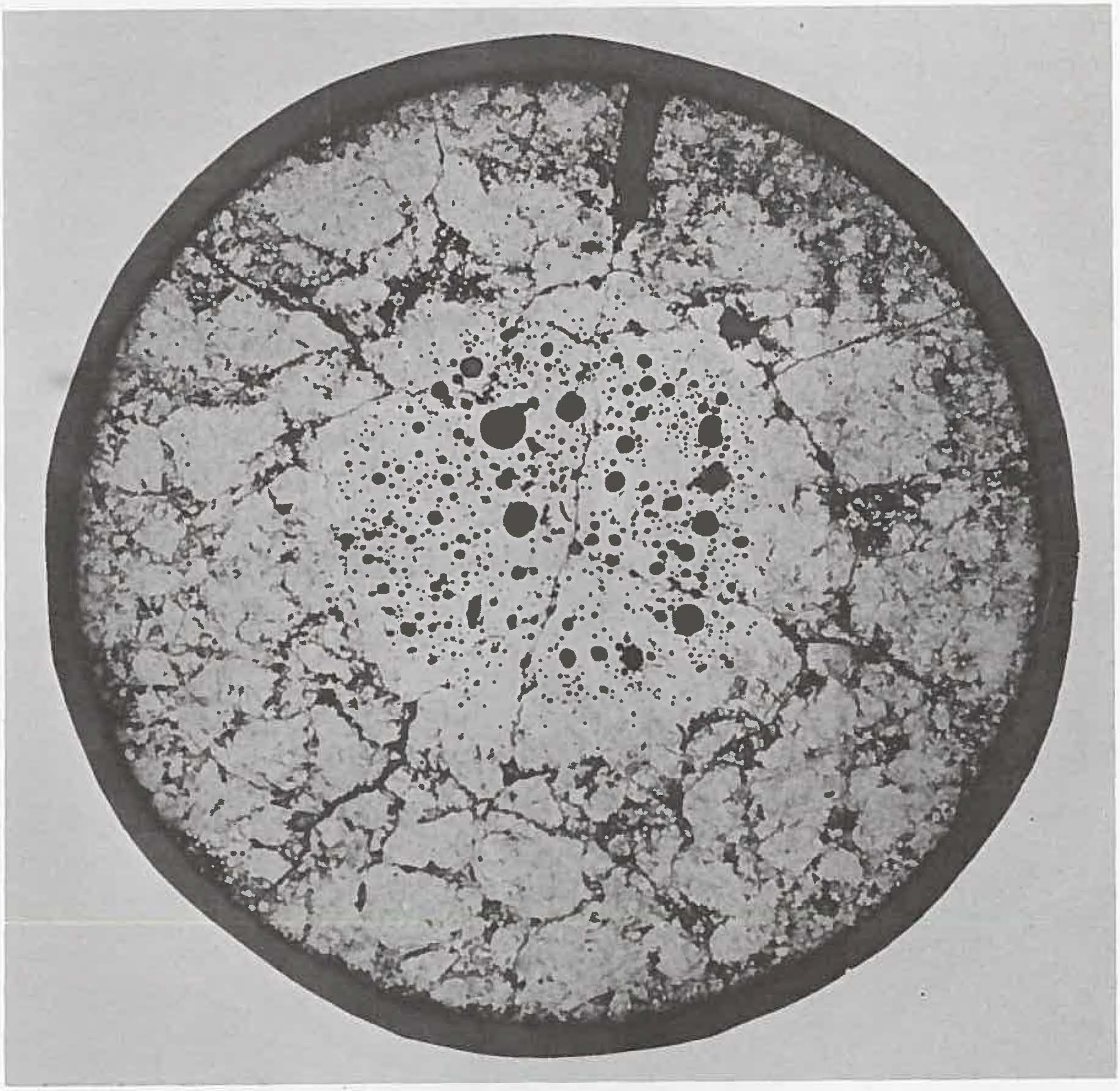

Fig. 77 Bubbles in Melted Fuel Contained Inside of Pellet. Neg. No. MSD-186451. 26X.

Fig. 78 Melted Fuel Locally Extended to Surface of Pellet. Neg. No. MSD-186448. 26X.

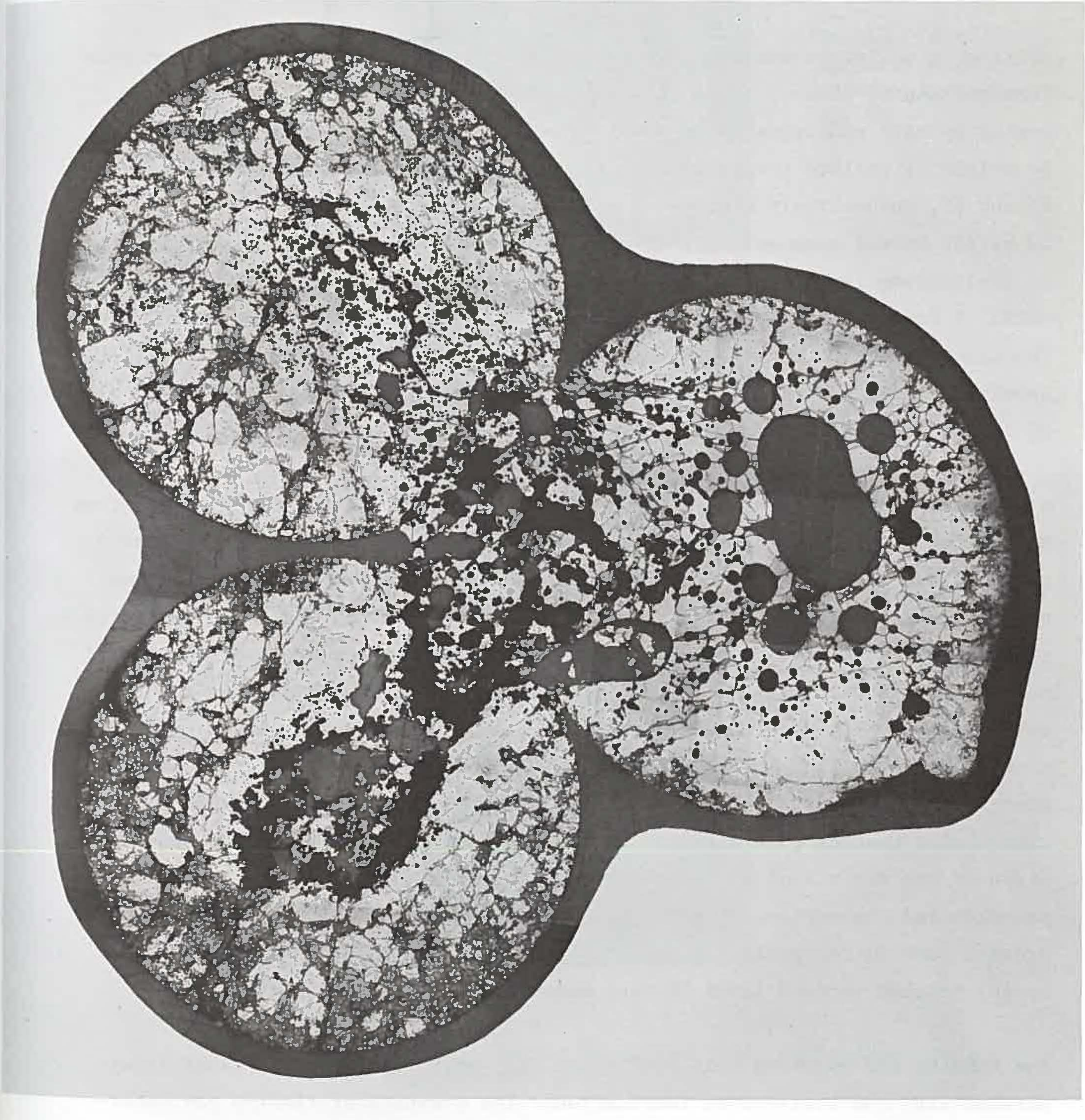

Fig. 79 Pellets Fused Together on the Side. Center Pellet Appears on the Right. Neg. No. MSD-186852. 16X.

other two and is assumed to be the central element. The extension of the melt zone from the center to the surface of the other two pellets in the direction of the third pellet is in agreement with the argument that the third pellet is from a hotter central element.

Melting in pellets occured significantly only in two of the batches of pellets from section 60-R5-36.5. The pellets showing evidence of melting were separated by hand employing a low power binocular microscope. The percentage by weight of pellets that showed melting were 0.6%, 55% and 82% for lots #3, #1 and #2, respectively from section 60-R5-36.5. In total, 33% of the pellets by weight showed some evidence of melting or approximately 30.5 cm (12 in.) of fuel-column length. Most of the pellets appeared to have areal melting of ∿22%. A few pellets had areal melting of 55% and probably represent fuel from the central element. Applying these two percentages to the percent of pellets showing melting and to the total fuel, it appears that approximately 9% of all of the fuel melted.

A piece of a pellet with a central void was examined with the Scanning Electron Microscope (SEM). The surface of the central void and the adjacent fractured surfaces are shown in Fig. 80. This particular central void appears to have a bridge across it (at right in figure) similar to that in Fig. 76. The surface of the void is generally smooth but one hole can be seen in the surface toward the bottom right in Fig. 80(a). Fairly large bubbles are present in the fractured surface of the melted fuel. A view of the bubbles at higher magnification is shown in Fig. 80(b). The larger bubbles seem to be closer to the central void. The inside surfaces of the bubbles are generally smooth but sometimes holes connect with adjacent bubbles. Figure 80(c) is an SEM photograph of the surface of one of the large bubbles at high magnification. The boundary and the surface of a grain are shown in which small holes (vents) are present both in the grain boundary and within the grain. In addition a thin, rough, cracked surface layer of fuel seems to exist on most grains.

The bubbles and vents in this fuel could only have resulted from gases incorporated into the fuel during fabrication. The quantity of fission gas generated during the test would have been very small, and fuel vapor bubbles would neither be likely to persist nor to have the morphology of the bubbles encountered here. Since intimate mixing of melted steel and melted fuel did not occur,

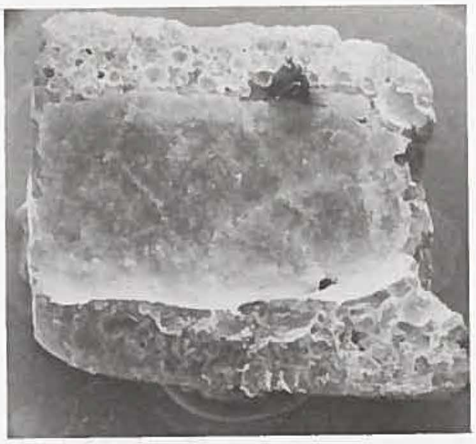

(a) Piece of a pellet showing surface of central void and bubbles on fractured surface Mag. 12X

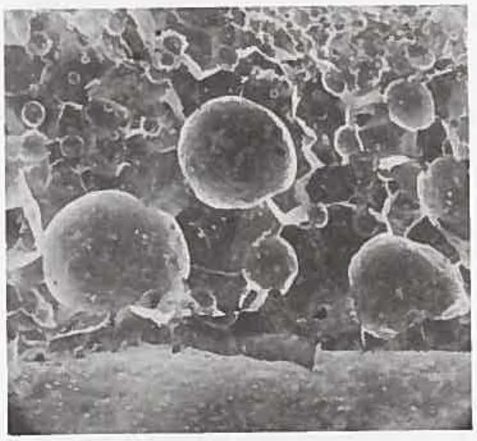

(b) Bubbles on fractured surface of fuel pellet. Mag. 46X

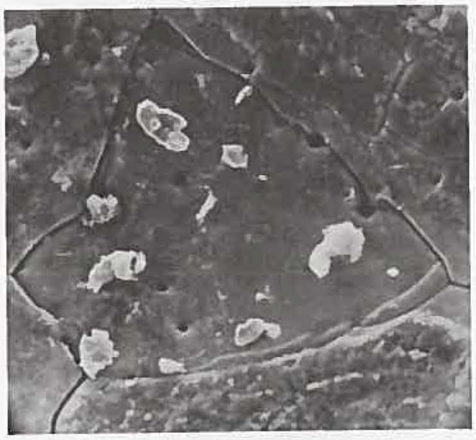

(c) Surface of a bubble in fuel showing "vent" holes. Mag. 1300X

Fig. 80 Bubbles in Melted Fuel, and Central Void. Neg. No. MSD-187528.

the presence of steel vapor was unlikely.

5.3.3 Distribution and Characterization of Melted Steel

The hexagonal flow tube was mostly intact around the upper insulator pellets although some melting had occurred (Fig. 81). Below this, from a location just below the upper insulator pellet the hexagonal flow tube had melted completely all around the circumference down to a location about 29 cm from the bottom of the fuel column (near the top of piece #4, section 36.5-R5-17). Below this location the flow tube was melted on most of four sides and was relatively intact only on two sides for about 15 cm (to about 14 cm from the bottom of the fuel column). From this point downward the flow tube was intact externally but some internal melting occurred from contact with molten steel (Fig. 82) in the region from 8.5 to 14 cm above the bottom of the fuel column. The remainder of the flow tube downward was intact both inside and out.

The cladding and spacer wires of the fuel elements were partly melted in the region of the upper insulator pellets as shown in Fig. 83. Below the top insulator pellets these two stainless steel components had completely melted down to the bottom end of piece #4, section 36.5-R5-17 (about 14 cm above bottom of the fuel column). At both the top and bottom of piece #3, remnants of the cladding of the peripheral elements were present on the outside of the cluster. Farther down the fuel column where melted steel filled the spaces between elements (Fig. 71), sections of cladding were still present on the peripheral elements on the outside of the cluster. Around the bottom insulator pellets the cladding on all elements appeared to be intact, although some melted steel had lodged in the region.

It appears that the stainless steel from the hexagonal flow tube and the cladding and spacer wires of the elements completely melted over the upper two-thirds of the fuel columns and flowed downward, finally freezing around the lower portion of the fuel columns within the hexagonal tube. A plug of steel to a depth of 7 or 8 cm resulted from the flow of melted metal. Although the spaces between fuel columns are filled with melted steel at this location, the irregularities of the outline indicated that flow channels probably existed along the wall of the flow tube. The bottom blockage does not seem to have been complete.

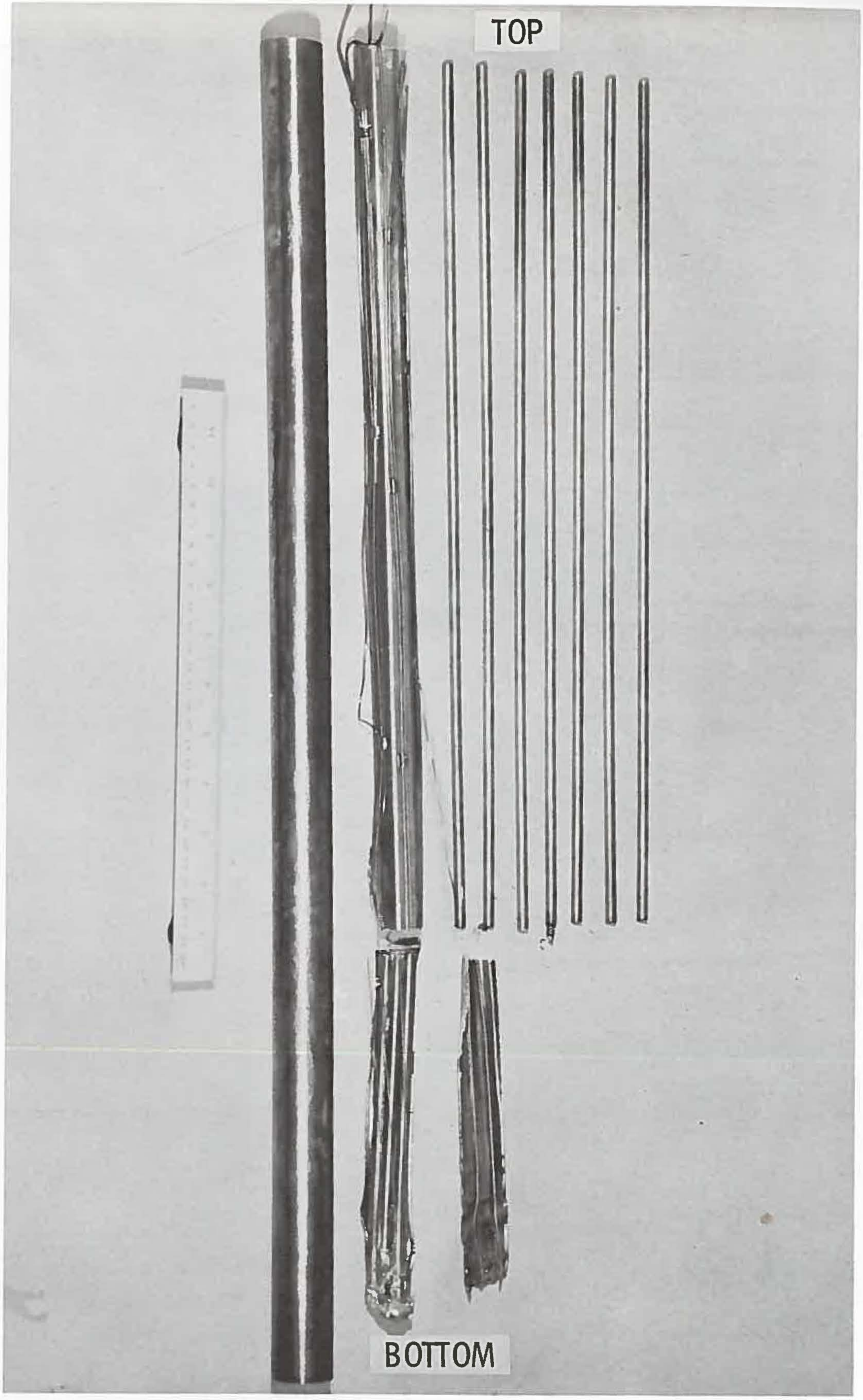

Fig. 81 Section 87-R5-60 Partly Disassembled.
Neg. No. MSD-185603.

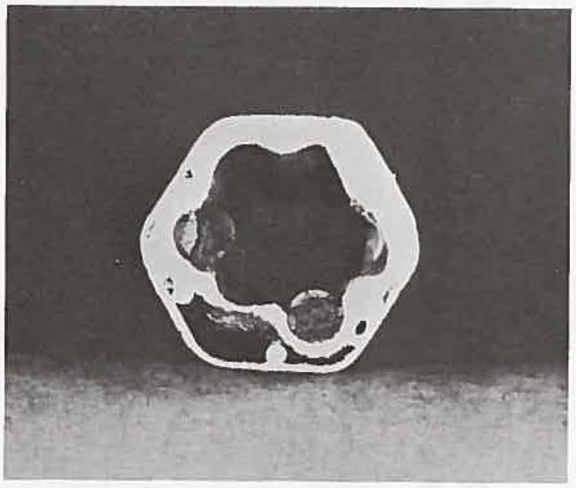

Fig. 82 Top View of Piece #3 of Section 36.5-R5-17, 12.2 cm above Bottom of Fuel Column. Neg. No. MSD-185663.

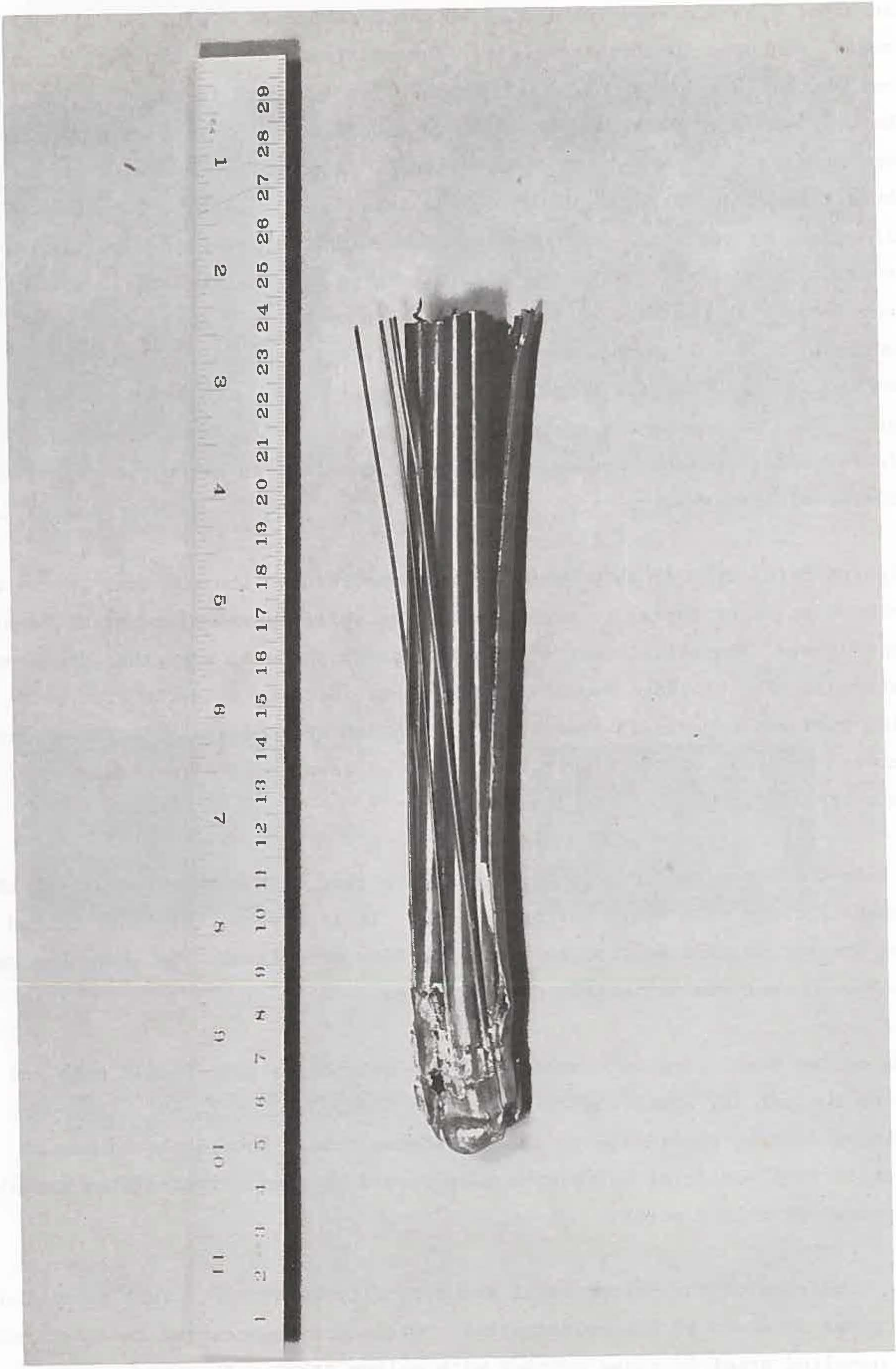

Fig. 83 Section 87-R5-60. Half of hexagonal flow tube removed to show region of melt-off. Neg. No. MSD-185604.

The upper flow blockage resulted from the presence of a plug of melted steel around the upper insulator pellets. The underside of the blockage occurred just above the melt-off of the hexagonal flow tube and is shown in Fig. 84(a). The uranium oxide insulator pellets are embedded in a matrix of melted steel. Some holes are evident in the melted steel. A transverse section about 1 cm above the bottom of the blockage can be seen in Fig. 84(b). The pellets are all insulator pellets. No fuel was detected in this section either visually or by autoradiography. The melted steel, judging by quantity and location came from below. The portion of the flow tube shown in Fig. 84(b) generally intact, but it does show some evidence of melting. The half of the flow tube removed from the section during disassembly at ANL-W also appeared to be intact. Much of the spacer wire and cladding material is also unmelted. The flow blockage does not appear to have been complete on the periphery of the cluster of elements.

Figures 84(c) and (d) show vertical sections through the specimen in two directions at right angles to each other. The white-appearing material is stainless steel. The pellets are a somewhat darker shade of gray than the mounting material. The blockage appears to have been incomplete on the side where the flow tube was removed in section AA'. Section BB' shows a definite opening between the wall of the flow tube and the adjacent pellet (B' side of BB'). This opening is ∿0.3 cm in diameter.

A 1-cm-thick section from just above the section with the major part of the upper blockage fell apart during cutting. It is obvious that less melted steel was present in this section to block the flow of sodium. The upper blockage in the R5 test was definitely not complete.

The molten steel came in contact with the molybdenum heat-shield tube and froze against it, particularly in section 60-R5-31.5 (Fig. 70). However, nowhere did the steel fuse to the molybdenum tube. Toward the bottom of section 60-R5-36.5 the molybdenum tube served as a mold restraining radial movement of molten steel.

The structure of the melted steel was typically dendritic. Fuel particles were not observed in the melted steel. Grain growth occurred in some areas of unmelted steel in close contact with molten steel. In other areas

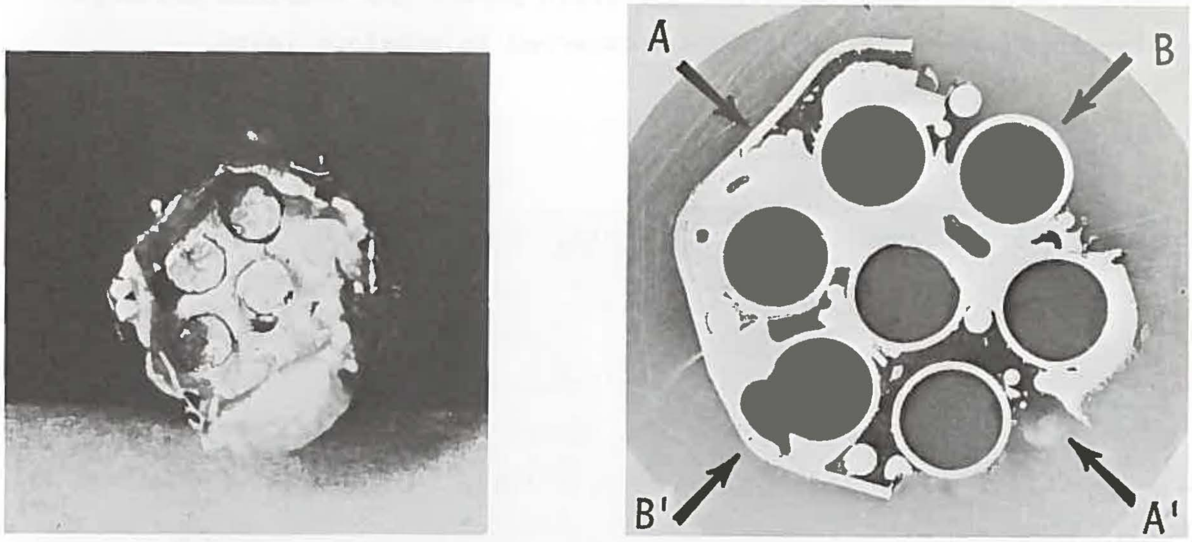

(a) Bottom view of upper blockage. 1 X.

(b) Top view of upper blockage. 2.5 X.

(c) Section A-A' through upper blockage. 1 X.

(d) Section B-B' through upper blockage. 1 X.

Fig. 84 Views of the Upper Blockage Around the Insulator Pellets. Neg. No. MSD-187530.

incipient grain boundary melting occurred in steel where the temperature was intermediate between those required for grain growth and complete melting. These structures were typical of those observed in previous tests.

5.3.4 Fuel-Melted Steel Interfaces

Interfaces between melted steel and unmelted fuel occurred in several ways. Figure 71 shows an interface in which a mass flow of melted steel froze around stacks of fuel pellets. The melted steel is usually in intimate contact with the fuel pellets, but there is little evidence that melted steel has penetrated into cracks or crevices in the pellets. One instance of penetration of melted steel into an unmelted pellet can be seen in Fig. 72. Wetting of the fuel by the melted steel is implied in this case. Droplets of steel occurred on the surface of some pellets and at the interface between pellets (Fig. 85(a)). The spherical nature of these particles results in a contact angle indicative of nonwetting. On the other hand, in Fig. 85(b) the pellet surface shows a degree of wetting by melted steel and some steel seems to have penetrated the interface between pellets and perhaps somewhat into surface cracks.

The relatively small amount of fuel melting in this test preclude an opportunity for mixing of melted steel and melted fuel as was observed in Test R4. No evidence of such mixing was observed here.

5.3.5 The Upper Parts of the Fuel Element

The parts of the fuel elements above the upper flow blockage are shown in Figs. 81 and 86. These parts of the fuel elements do not seem to have been affected by the transient. Diameter measurements (32 per element) of the cladding along the lengths of the elements in sections 113.5-R5-87 and 87-R5-60 resulted in the following values for all seven elements: 0.583 ± 0.001 cm ($0.2294^{+0.0003}_{-0.0004}$ in.). This average can be compared with the specification 0.230 ± 0.001 in. (0.584 ± 0.002 cm). No diameter change or ovality of the cladding resulted from the transient.

Spring constants in compression were determined on sections of springs slightly shorter than the full length. About 1 cm was cut from the length of the springs during disassembly as indicated in Fig. 81. The spring constants measured on three of the springs were: 6.35 N/cm (3.63 lb/in.), 6.34 N/cm

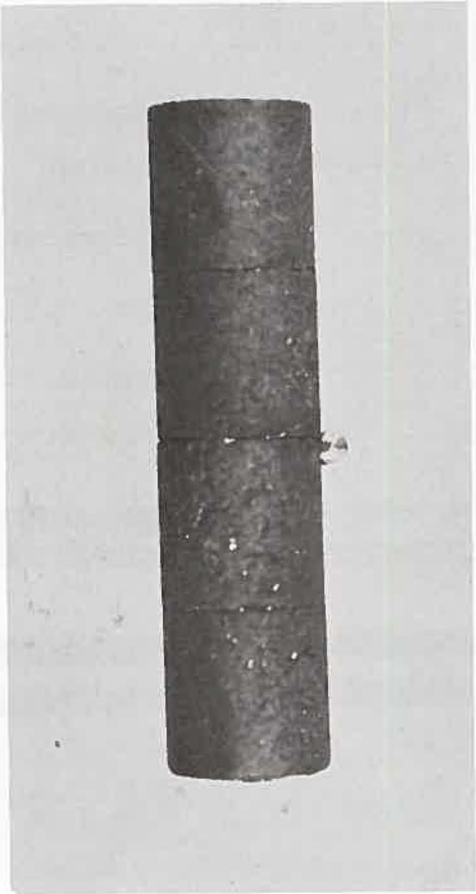

Fig. 85(a) Nonwetting Globule of Melted Steel on Fuel Surface. Neg. No. MSD-185666. 4.5X.

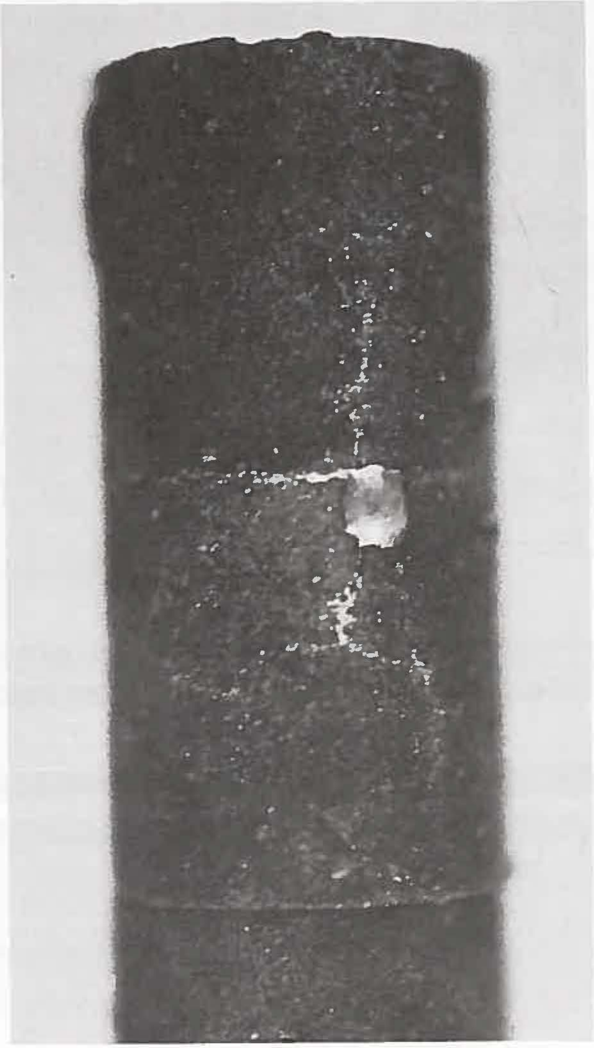

Fig. 85(b) Some Degree of Wetting by Globule of Melted Steel on Fuel Surface. Neg. No. MSD-185670. 11X.

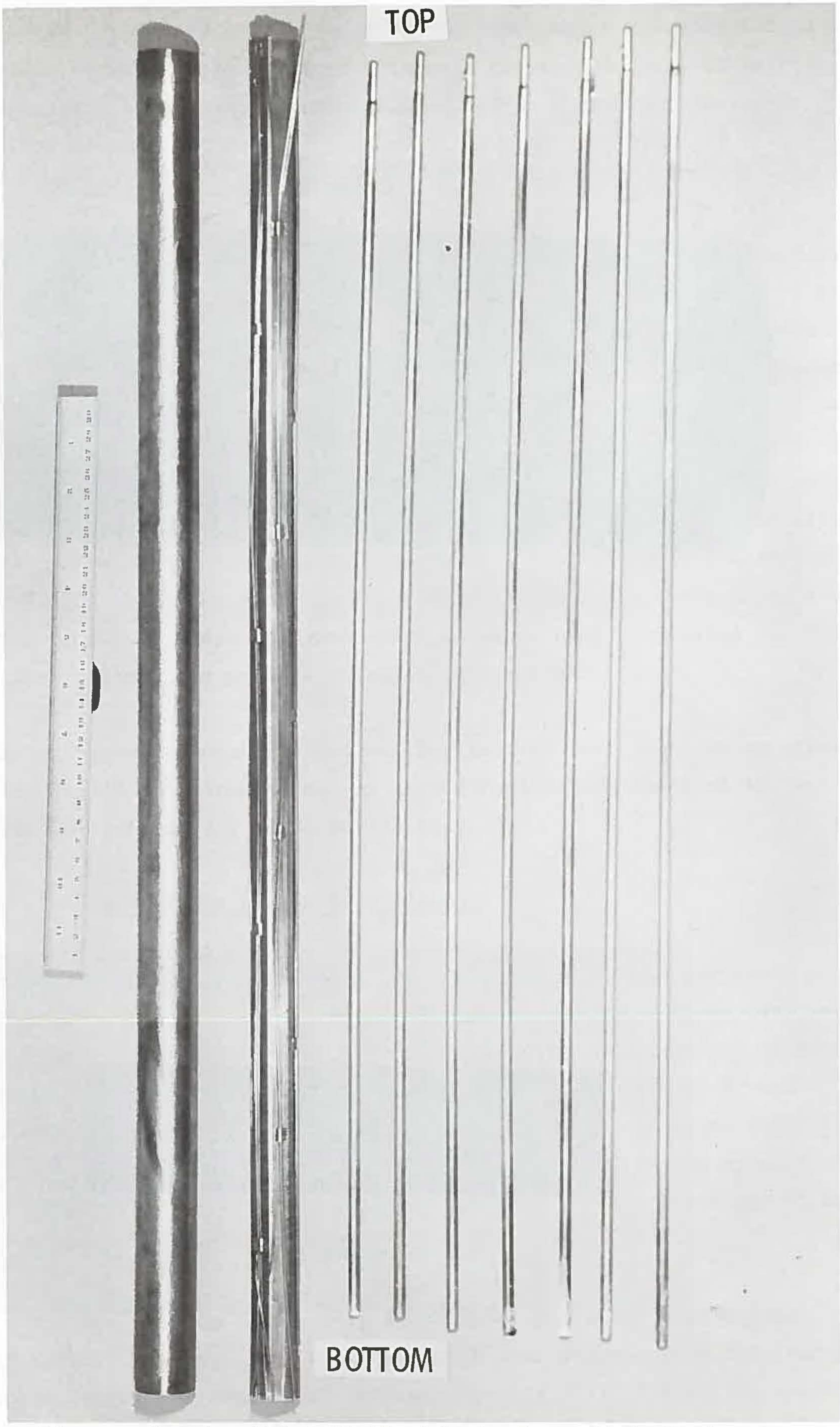

Fig. 86 Section 113.5-R5-87 with the Tops of the Fuel Elements. Neg. No. MSD-185602.

(3.62 lb/in.) and 6.37 N/cm (3.64 lb/in.). The specified spring constant was 3.27 ± 0.16 lb/in. or 5.37 ± 0.28 N/cm. Although the posttest spring constants are somewhat higher than the specification value, it is doubtful that an increase in the spring constant has occurred. The free length of the spring was unchanged after the compression test.

An X-radiograph of the tops of the elements (Fig. 87) shows that the plenum tubes have moved away from the end cap by a maximum of 0.58 cm (0.23 in.). These displacements are matched in part by the relative displacement of insulator pellets and reflector rods in Fig. 88. Some sodium was found within the pins up around the reflector rods and in some cases around the springs. This sodium probably entered the pins during the cooldown stage after the test.

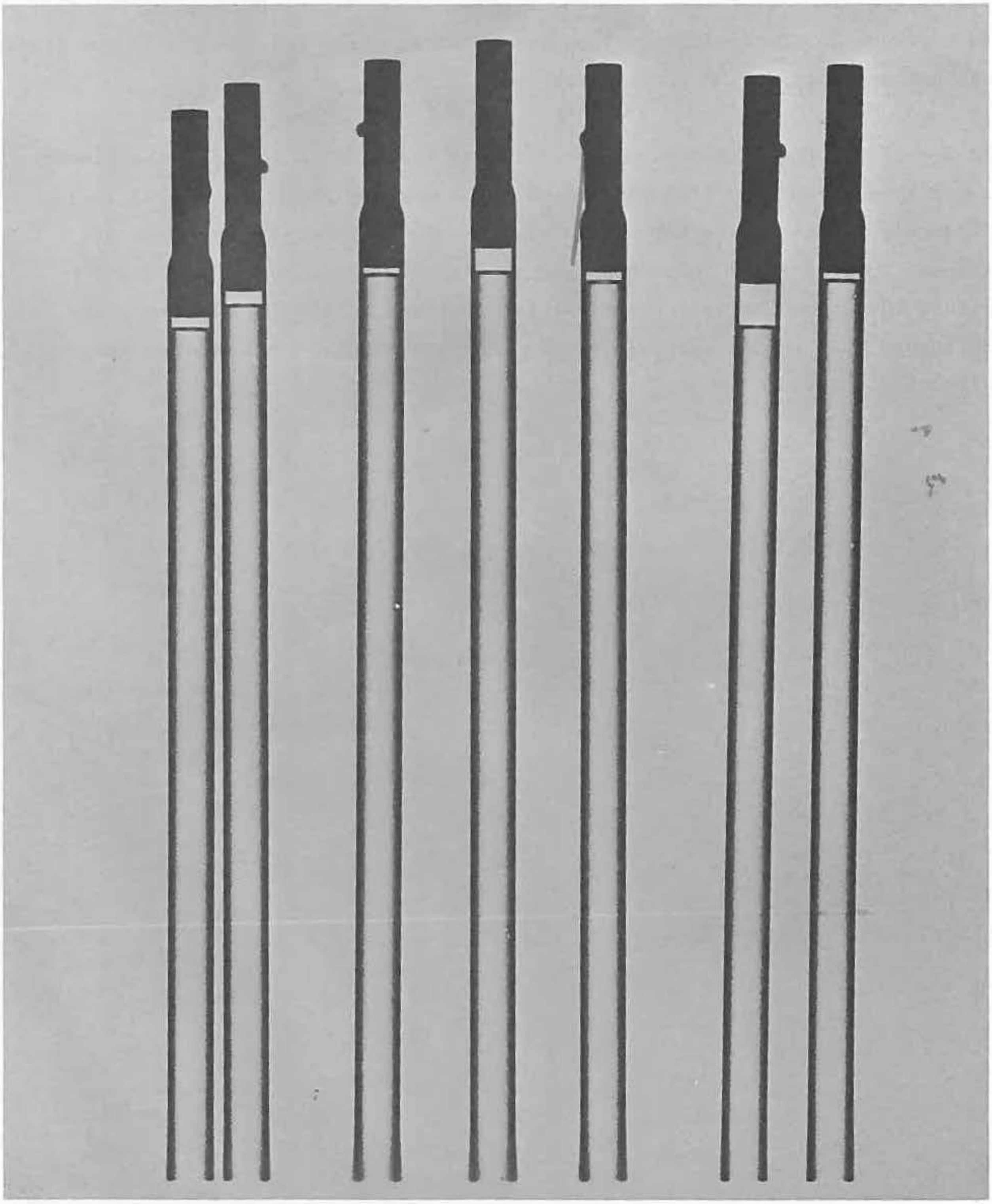

Fig. 87 X-ray Radiograph of the Tops of the Fuel Elements

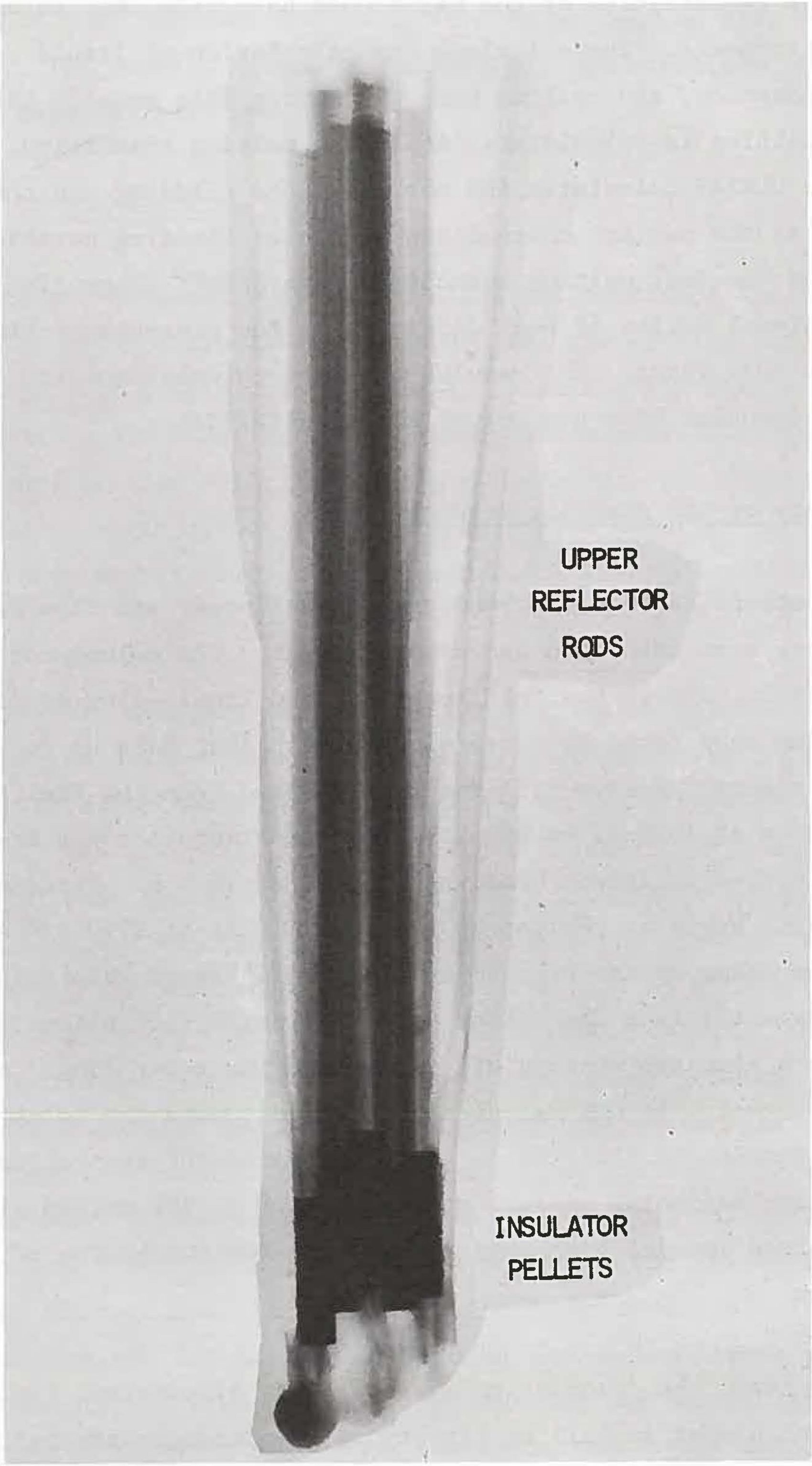

Fig. 88 X-radiograph Showing Relative Displacements of the Top Insulator Pellets. Neg. No. MSD-185674.

6.0 ANALYSIS

The current capabilities of the SAS3A code have been used to analyze the R-series experiments. These include the calculation of liquid sodium heatup, boiling inception, and boiling with the moving film model. Later in time, cladding melting is calculated. After the melting transition, the clad motion subroutine CLAZAS calculates the motion of the cladding and the development of blockages in the coolant channel due to frozen cladding material. After fuel melting and the fuel melting transition, the SLUMPY subroutine calculates the one-dimensional motion of fuel particles in the presence of fission gas, steel vapor, and fuel vapor. The results of these calculations for the R4 and R5 tests are compared with the actual experimental data.

6.1 Summary of SAS Analysis Results

For the posttest SAS calculations, the actual power and flow data from the R4 and R5 tests were tabulated and used as input. the calculated single-phase coolant heatup, sodium boiling inception, and liquid-slug oscillations after core voiding were found to agree closely with that data up to the time of cladding failure. Helium fill gas was released from the fuel pins upon cladding failures at 16.0 s, an aspect of the test sequence not modeled by SAS. SAS3A calculated incipient cladding melting at 16.2 s. Cladding motion was calculated to begin at the top of the active fuel at 17.0 s. According to the models, the shear stress exerted by high sodium-vapor velocities forced the cladding material into the colder upper reflector rod region. There it froze and formed a blockage cutting off further sodium vapor flow. As cladding continued to melt, it was calculated to drain toward the inlet under gravity, forming a semi-solid blockage in the lower reflector-rod region by 21.9 s. Hence, by the beginning of fuel motion at 22.8 s, the molten cladding had already formed channel blockages at both the top and bottom of the active fuel region.

For the R4 test, the calculation was continued at constant fuel power. The fuel was calculated to fall by gravity as permitted by the melting progression. The calculated fuel collapse may have been somewhat faster than in the test due to the SAS approximating treatment of the radial test sink. The maximum fuel temperature was calculated to be 3688 K. The corresponding fuel vapor pressure was not capable of dispersing fuel upward so that, by the time of power shutdown at 25.0 s, the fuel was calculated to be resting atop the lower cladding blockage. The overall agreement between the SAS calculated scenario and the R4 and R5 data was very good.

6.2 SAS-Modeling of the R-series Tests

The integrated accident-analysis code system SAS3A was developed for a deterministic calculation of both transient overpower and loss-of-flow unprotected accidents in LMFBRs. The models are designed to calculate the complete sequence of accident events starting from a steady state condition through liquid sodium heatup, boiling with liquid film motion, fuel pin dryout, cladding melting, cladding motion, and fuel motion up to the point of subassembly disruption. All these models were used in the present R-series posttest analysis.

A SAS channel explicitly models a single fuel pin and its associated coolant and structure. For the seven-pin R4 and R5 tests, a characteristic fuel pin and characteristic data for the coolant channel and the structure were chosen. The pretest analysis had given an indication of the incoherence to be expected for the various fuel pins and subchannels (Sect. 2.5.1). The thermal-hydraulic properties of six isolated subchannels within the seven-pin assembly were used for SAS calculations. All subchannels reached sodium boiling within 1.8 s of one another. This was due to the flat power and flow profiles designed into the subassembly. The expected incoherence with respect to onset of boiling, i.e., the time lag between local boiling and gross boiling, was therefore less than 1.8 sec. Thermal mixing effects would certainly reduce the boiling incoherence. It was therefore considered appropriate to model an average pin, calculate an average coolant volume fraction, and an average structure for the R4 and R5 tests. The radial dimensions of the fuel pin were input directly. The volume fraction of the coolant was calculated by dividing the coolant cross section by the cross section of fuel plus clad plus coolant for the hex can arrangement. Structure-to-clad surface area ratio was calculated by dividing the structural perimeter including wrapper and filler wires by the total clad perimeter. The equivalent thickness of the structure was calculated in such a way that the total thermal capacity of the structure was conserved. The actual values used for the structural thicknesses include additional structural mass provided by the thermocouples affixed to the hex can.

The SAS channel structure is shown in Fig. 89. Beginning at axial location zero, there are two blanket nodes of 7.24 cm length each, representing the stainless steel pin. A third blanket node of 2.03 cm represents the lower insulator pellet. Next there is a small active fuel node of 0.72 cm followed by 12 active fuel nodes of 7.5 cm each. The top of the active fuel pin is modeled by a small node of 0.72 cm length, followed by a 2.03 cm insulator pellet blanket node. The next two blanket nodes of 7.24 cm length represent the upper stainless steel pin. Below axial location zero are two lower reflector nodes. The length and the hydraulic diameter of the lower reflector were calculated so as to model the frictional resistance and the inertia provided by the downcomer section of the R-series vehicle. Above the fuel pin as described there is a gas plenum of 106.7 cm length which is modeled by six axial nodes. Following them are two upper reflector nodes. The length and the hydraulic diameter of the upper reflector were calculated to model the frictional resistance and the inertia accurately. Thermophysical properties and heat transfer correlations are identical to the input data used for the FTR-LOF analysis. The fuel properties were input for fresh UO_2. For all tests, normalized power versus time tables were derived from the test data. Normalized flow versus time was also input-supplied in table form. Iterations were used to obtain these tables in the form of normalized driving pressure versus time from the measured flow versus time data. A direct use of measured pressure versus time data led to slightly higher flow rates in SAS during the approach to boiling than were actually measured. Other important input data are listed in Table 12. Figures 90 and 91 show the power versus time forcing functions as used by SAS for R4 and R5.

6.3 SAS Calculations and Comparisons with Test Results

The R4 experiment has been used to present a sensitivity study of SAS input. First it is shown how various uncertainties in the input affect the time of boiling inception. Further on, one case with minimal heat loss to the structure and a second case with maximal heat loss to the structure will be

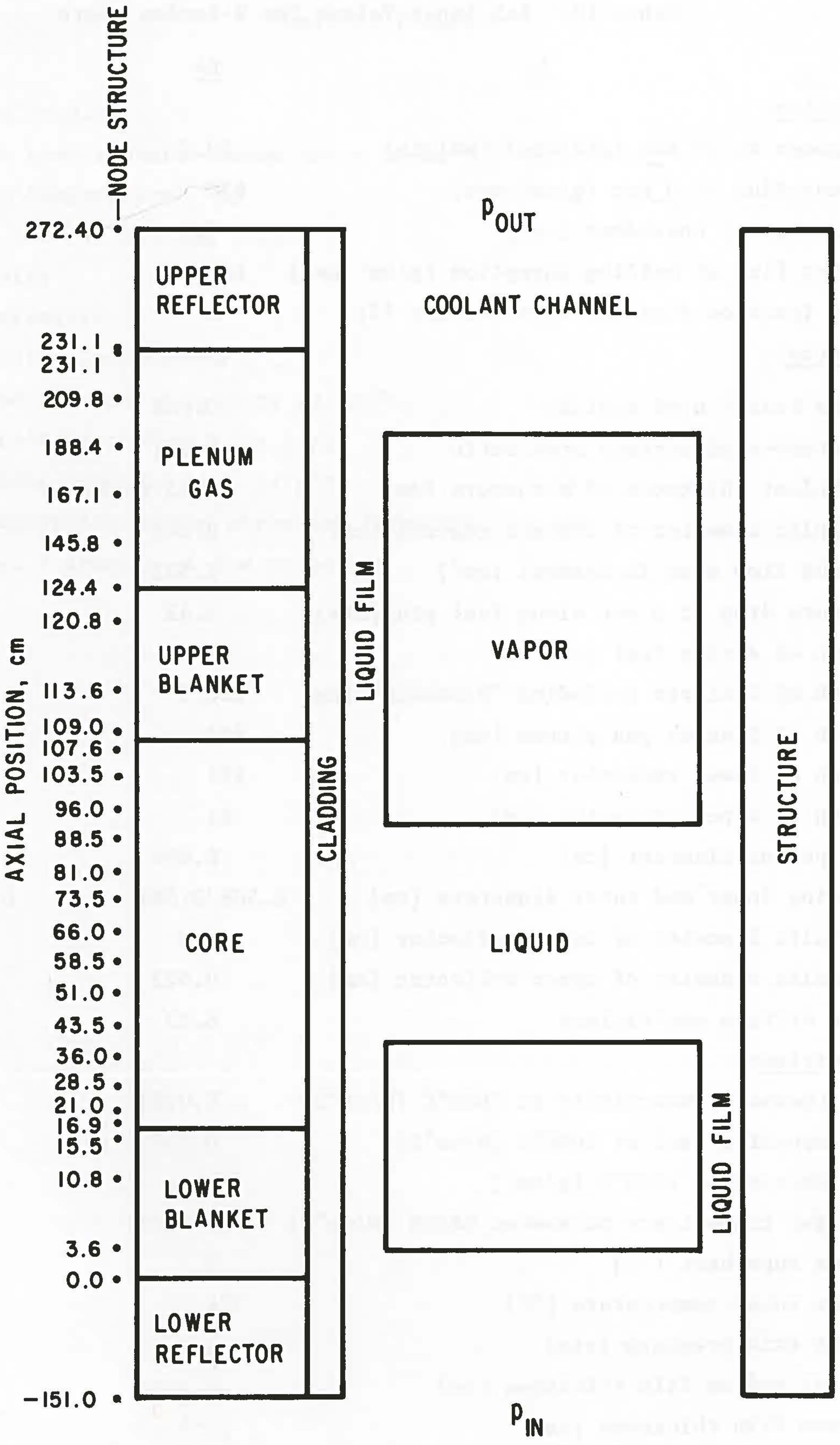

Fig. 89 SAS Nodal Structure Used for R-series Calculations

Table 12. SAS Input Values for R-Series Tests

	R4	R5
Operation:		
Pin power at 15 sec (plateau) [kW/pin]	29.5	29.6
Coolant flux at 0 sec [g/cm^2 sec]	650	620
Initiation of coastdown [sec]	7.9	7.9
Coolant flux at boiling inception [g/cm^2 sec]	148	148
Power fraction directly in structure [%]	3	0
Geometry:		
Volume fraction of coolant	0.448	0.448
Structure-clad surface area ratio	0.932	0.932
Equivalent thickness of structure [cm]	0.05 (0.15)	0.1
Hydraulic diameter of coolant channel [cm]	0.245	0.245
Coolant flow area in channel [cm^2]	1.523	1.523
Pressure drop at 0 sec along fuel pin [atm]	5.42	5.05
Length of active fuel [cm]	91.4	91.4
Length of fuel pin including "blankets" [cm]	126.5	126.5
Length of fission gas plenum [cm]	107	107
Length of lower reflector [cm]	151	151
Length of upper reflector [cm]	41	41
Fuel pellet diameter [cm]	0.494	0.494
Cladding inner and outer diameters [cm]	0.508/0.584	0.508/0.584
Hydraulic diameter of lower reflector [cm]	2.0	2.0
Hydraulic diameter of upper reflector [cm]	0.623	0.623
Inlet orifice coefficient	8.23	10.96
Properties:		
Fuel thermal conductivity at 1600°C [W/cm°C]	0.0207	0.0207
Fuel specific heat at 1600°C [W/cm°C]	0.350	0.350
Fuel density at 1600°C [g/cm^3]	9.38	9.38
Bond gap conductance parameter HBPAR [W/cm°C]	0.0028	0.0028
Sodium superheat [°C]	5	5
Sodium inlet temperature [°C]	324	327
Sodium exit pressure [atm]	0.966	0.966
Initial sodium film thickness [cm]	0.0111	0.0111
Minimum film thickness [cm]	10^{-5}	10^{-5}

Table 12 (Contd.)

	R4	R5
Properties (Contd.):		
Condensation heat transfer conductance [W/cm^2°C]	6.3	6.3
Fuel melting temperature [°C]	2767	2767
Fuel latent heat of melting [J/g]	280	280
Fuel emissivity	0.5	0.5
Structure emissivity	0.1	0.1
Cladding melting temperature [°C]	1371	1371
Cladding specific heat * density [J/cm^3°C]	4.23	4.23
Cladding latent heat of melting [J/g]	283	283
Molten cladding specific heat [J/g°C]	0.59	0.59
Thermal conductivity of the structure [W/cm°C]	0.196	0.196
Specific heat * density of the structure [J/cm^3°C]	4.6	4.6

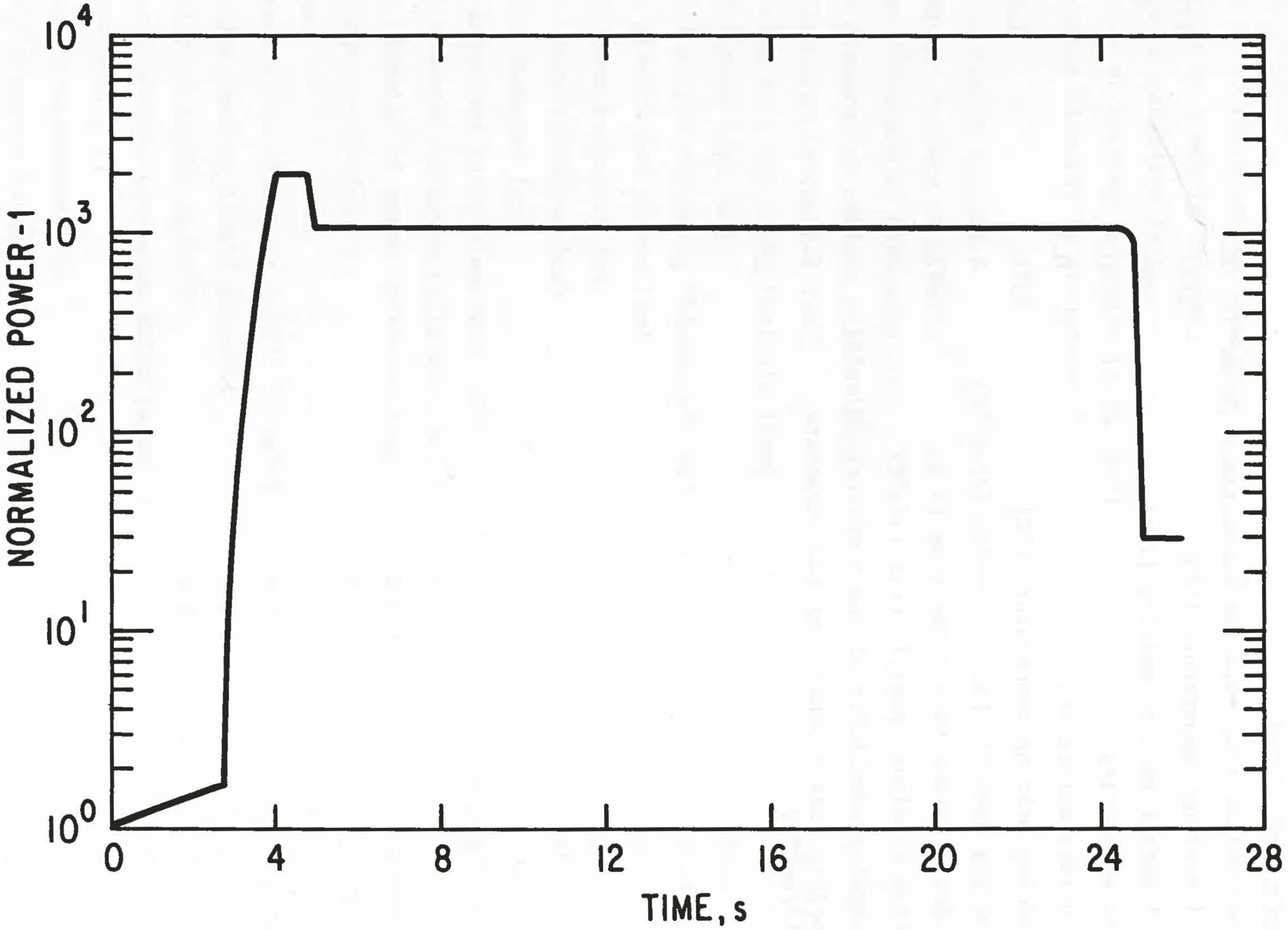

Fig. 90 SAS Input for R4 Power-time History

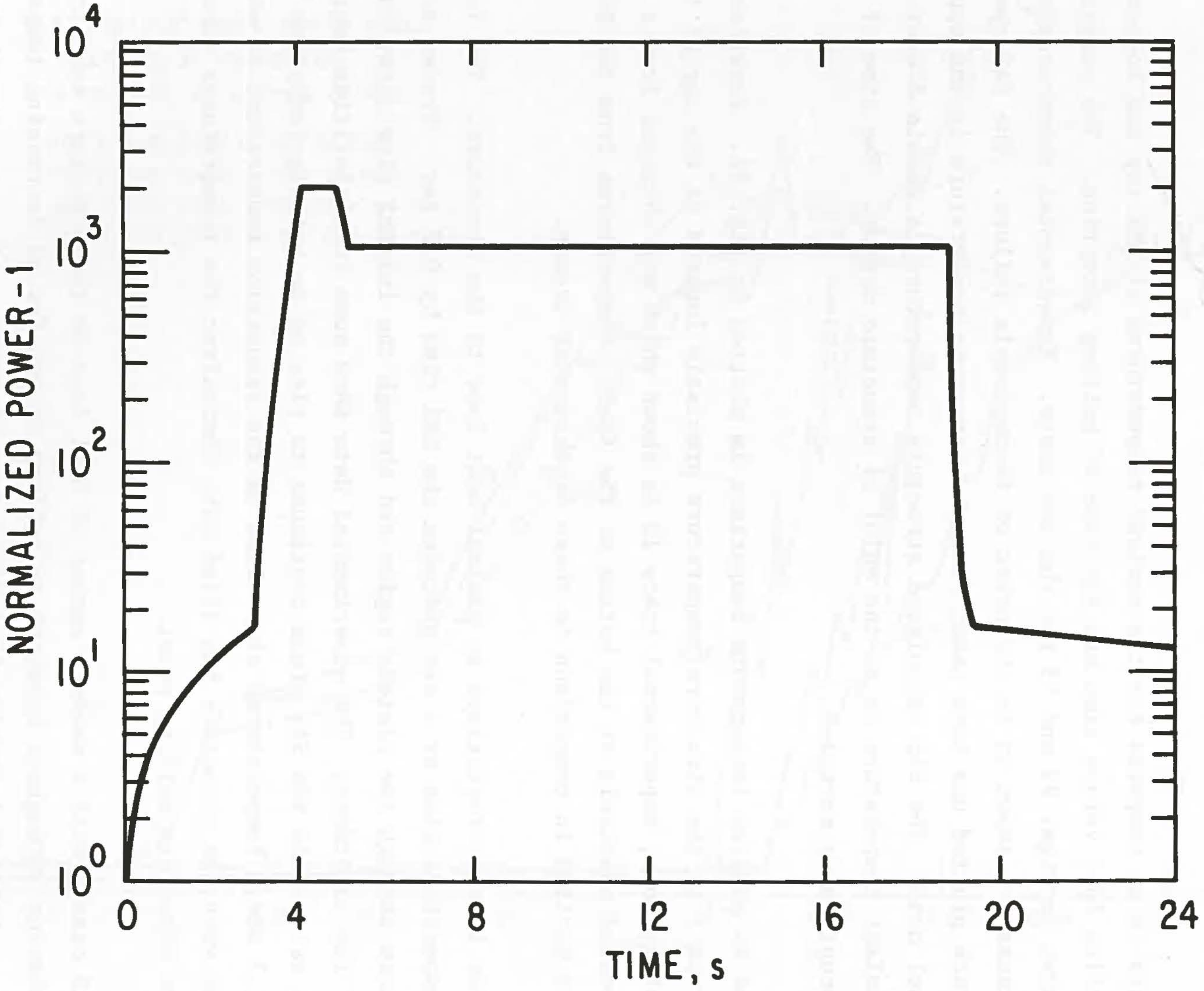

Fig. 91 SAS Input for R5 Power-time History

presented. Both cases are compared with the test results in order to achieve an understanding for the uncertainties and the ranges of results involved in SAS calculations.

6.3.1 Preboiling and Boiling Inception

Data to be compared are the coolant temperatures at the top and bottom of active fuel versus time and the time of boiling inception. The comparison is shown in Figs. 92 and 93 for the two tests. Experimental thermocouple traces are shown up to the point of thermocouple failure. The SAS temperature trace plotted has been taken from the structure temperature in the uppermost fuel node. The SAS calculated structure temperature is within 5°C of the coolant temperature up to the point of structure dryout. The time of boiling inception is marked B.

The R4 coolant temperature comparison is plotted in Fig. 92. Experimental trace 5 is the structure temperature precisely located at the top of the fuel. Furthermore, experimental trace 12 is shown which was obtained from a sensor located precisely at the bottom of the fuel. Temperatures from two SAS runs are plotted in comparison to these experimental traces.

Case 1 is characterized by minimal heat loss to the structure. The initial temperature rise at 4 sec precedes the SAS rise by 0.2 sec. Traces are fairly close through the plateau region and through the initial rise after initiation of the coastdown. The experimental data show some irregularities beginning at 11 sec, while the SAS trace continues to rise up to boiling inception near 13.3 sec. Temperatures stay close to the saturation temperature to about 17.5 sec when the structure has dried out; thereafter the temperatures rise toward the structure melting point.

SAS case 2 with a maximum amount of heat loss to the structure exhibits similar behavior throughout approach to boiling except for an increasing temperature lag. Boiling inception is indicated at 14.1 sec. After passing through the saturation temperature plateau, the structure temperature starts rising at 17.5 sec at a much slower rate than in case 1. The comparison of the coolant inlet temperatures indicate strongly the bounding character of cases 1 and 2.

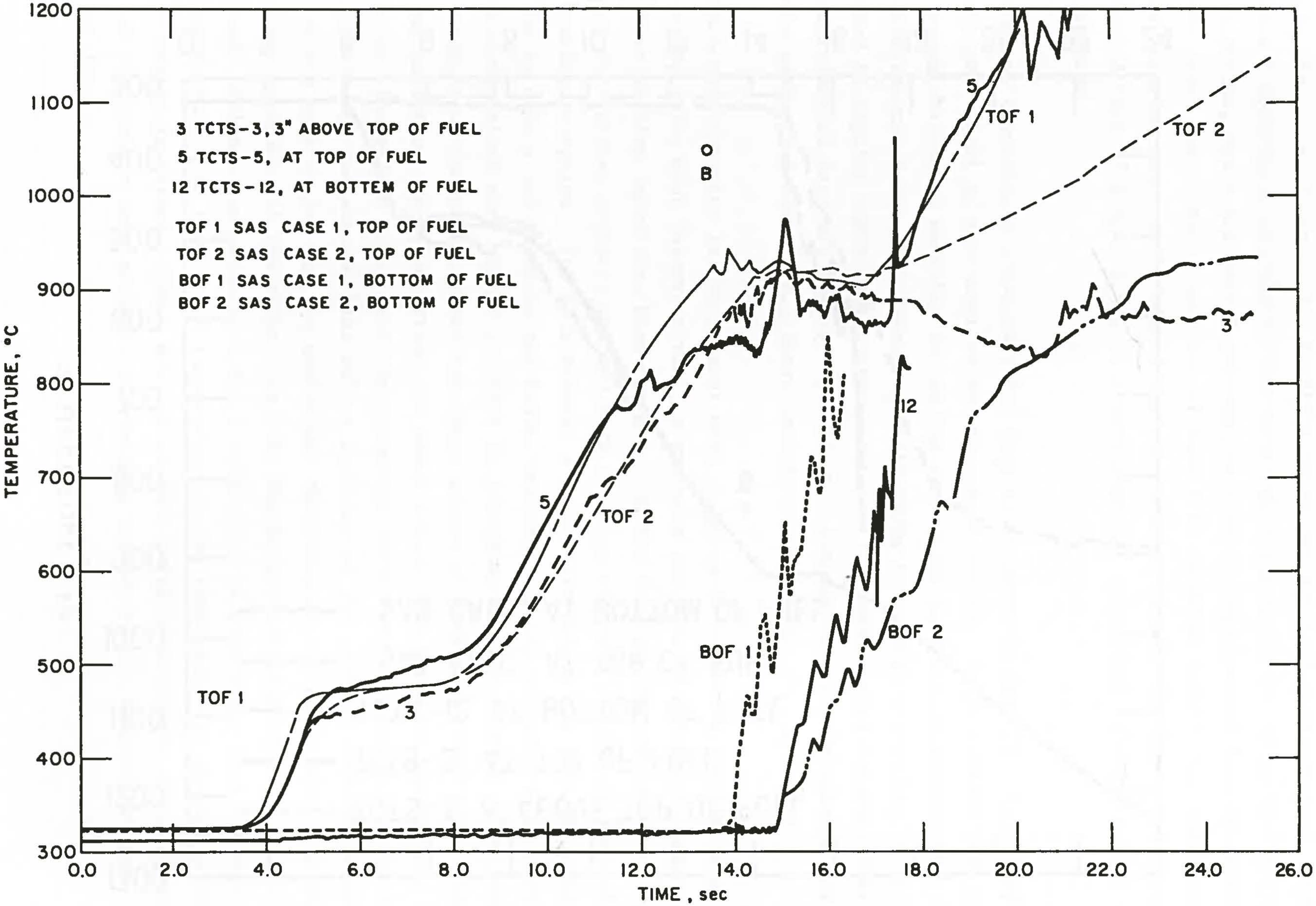

Fig. 92 R4 Coolant Temperature Comparison

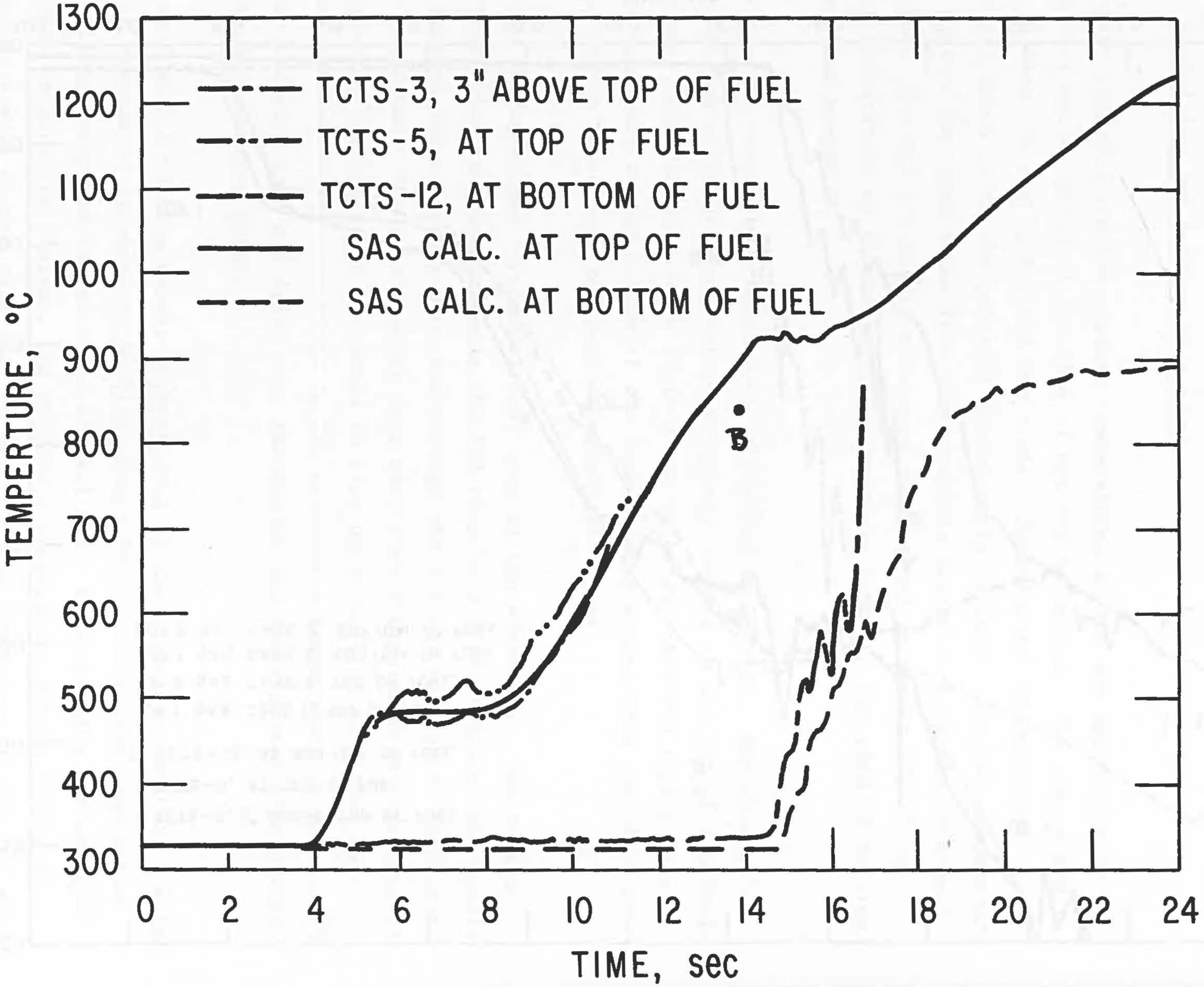

Fig. 93 R5 Coolant Temperature Comparison

All the temperatures remain at 315°C up to the point of flow reversal. SAS case 1 apparently calculates flow reversal 1 sec early due to earlier boiling inception, while SAS case 2 matches the time of experimental flow reversal. The inlet temperature rise rate of case 1 is somewhat larger than the experimental rise rate, while case 2 has the opposite trend. The inlet thermocouple failed near 17.8 sec, i.e., at a time when SAS calculated cladding motion well advanced.

Coolant temperature comparison for test R5 is given in Fig. 93. It exhibits the same level of agreement as was discussed for R4. It is evident that the thermal-hydraulic modeling in the SAS code gives good agreement with the experimental data. The remaining differences to a large degree can be attributed to regular experimental uncertainties. One should also consider that experimental data are pointwise, while SAS temperatures are an average for the respective mesh, i.e., large amounts of material.

Much consideration in the present work is given to comparing the timing of events. The most important time is probably the time of boiling inception. After boiling inception, heat removal from the fuel pin is reduced drastically and the further scenario unfolds with a timing strongly related to time of boiling inception. For this reason, a sensitivity study has been performed. The R4 case 1 was taken as the basis, and eight of the parameters considered most important were varied in order to determine the sensitivity to boiling inception. Generally, there are three groups of parameters that affect boiling inception. Most important are power versus time and flow versus time data. The second group involves geometric parameters expressing the thermal capacity of the system, like volume fraction of the coolant, structure-to-clad surface area ratio, and the equivalent thickness of the structure. The third group includes all the properties like thermophysical properties of fuel, clad, coolant, and structure, and a collection of properties that express the temperature rise from inlet temperature to the temperature at which the first Na bubble is formed. These are the coolant inlet temperature, the superheat, and the coolant exit pressure determining the saturation temperature for boiling.

These uncertainties were found to result in the following differences with respect to boiling inception time of the R4 test: 5% power causes 0.55 sec difference in boiling time, 5% flow during approach to boiling causes 0.38 sec, 20°C uncertainty at which the first bubble forms causes 0.33 sec, uncertainties in the geometry cause 0.33 sec, and uncertainties in thermal properties cause 0.4 sec. Combining these independent uncertainties, one obtains the boiling inception time uncertainty as 0.9 sec. All the SAS runs calculated the time of boiling inception well within 0.9 sec of the times established in the experiment sequence.

6.3.2 Boiling, Dryout, and Cladding Melting

The SAS calculations for both tests indicate that it takes approximately 3 sec from boiling inception to inception of cladding melting. The first Na-vapor bubbles form at the top of the active fuel section, where the coolant temperature is highest, and the coolant pressure, i.e., the corresponding saturation temperature, is lowest. The single channel representation of the early boiling is that these bubbles are swept downstream until they collapse due to condensation in the cold upper blanket and gas plenum regions. The presence of sodium vapor in the channel increases the frictional resistance, thereby causing further flow decay. The liquid coolant continues to heat up along the fuel pin so that vapor bubbles originate further upstream. The buildup of pressure in the vapor region together with the increased channel friction eventually lead to a complete reversal of the sodium flow. Interconnected or parallel channel effects in the experiment lead to flow reversal due to pressure buildup in the vapor region on a slightly longer time scale and with further upstream voiding than SAS analysis. The flow reversal is very quickly followed by cladding dryout near the top of the active fuel. In the SAS model, the bubbles originating before flow reversal always carry a small liquid slug upward in the channel, thereby rewetting the dried out fuel pin surface. At flow reversal, the situation shows a single vapor region with considerable axial pressure drop and high sodium vapor velocities. The shear stress generated by the sodium vapor on the liquid film leads to film dryout within 10 ms. The coolant temperatures during this period are calculated as the saturation temperatures corresponding to the sodium vapor pressures. The structure temperature closely follows the coolant temperature. Figures 92 and 93 show reasonably good comparison of the experimental and calculated temperatures. The SAS calculated coolant and structure temperatures for one axial position are also plotted in Figs. 94 through 96. They all exhibit the saturation temperature plateau during the 3 sec period after boiling inception.

Other experimental data that can be compared during this period are the readings for the upper and lower flowmeters. This comparison is made in Figs. 97 through 100. The SAS calculated times for boiling, dryout, flow reversal, clad motion, and moving clad are also marked in these figures. Flow rates during the approach to boiling agree by virtue of SAS input. The inlet flowmeter shows small, early disturbances which might be interpreted as local boiling in a generally subcooled environment. In the SAS calculation, it takes slightly over 1 sec from boiling to the coincidental dryout and flow reversal. During this period, the SAS calculated flow rate trace is considerably smoother than the experimental trace. This might be expected considering the averaging and lumping done in the SAS models and the present inability to calculate parallel flow effects prior to inlet flow reversal which accounts for the observation that SAS calculated times between boiling and flow reversal are often shorter than experimentally observed times. However, the differences are only minor, and one can be very well satisfied with the general agreement of experiment and SAS calculated coolant dynamics after inlet flow reversal. Table 13 compares the timing of R-series events.

Near the time of cladding melting, helium fill gas was expelled from the gas plenum region of the fuel pins at the time of cladding failures, which for three fresh fuel tests is very close to the time of incipient cladding melting. This caused an excursion of the upper liquid sodium slug. Remarkable agreement is observed for calculated cladding melting times and the experimental flow trace excursion in both tests. This is indication that SAS calculates the time of clad melting correctly. The helium gas contained in the fuel pins acts as an unintentional instrumentation indicating cladding failure. The negative aspect of the discrepancies of flow traces near cladding melting is that SAS presently cannot handle the simultaneous presence of sodium vapor and fission gas. In the R4 test, the effect of the gas disappears after about 0.5 sec and flow traces very nearly agree again.

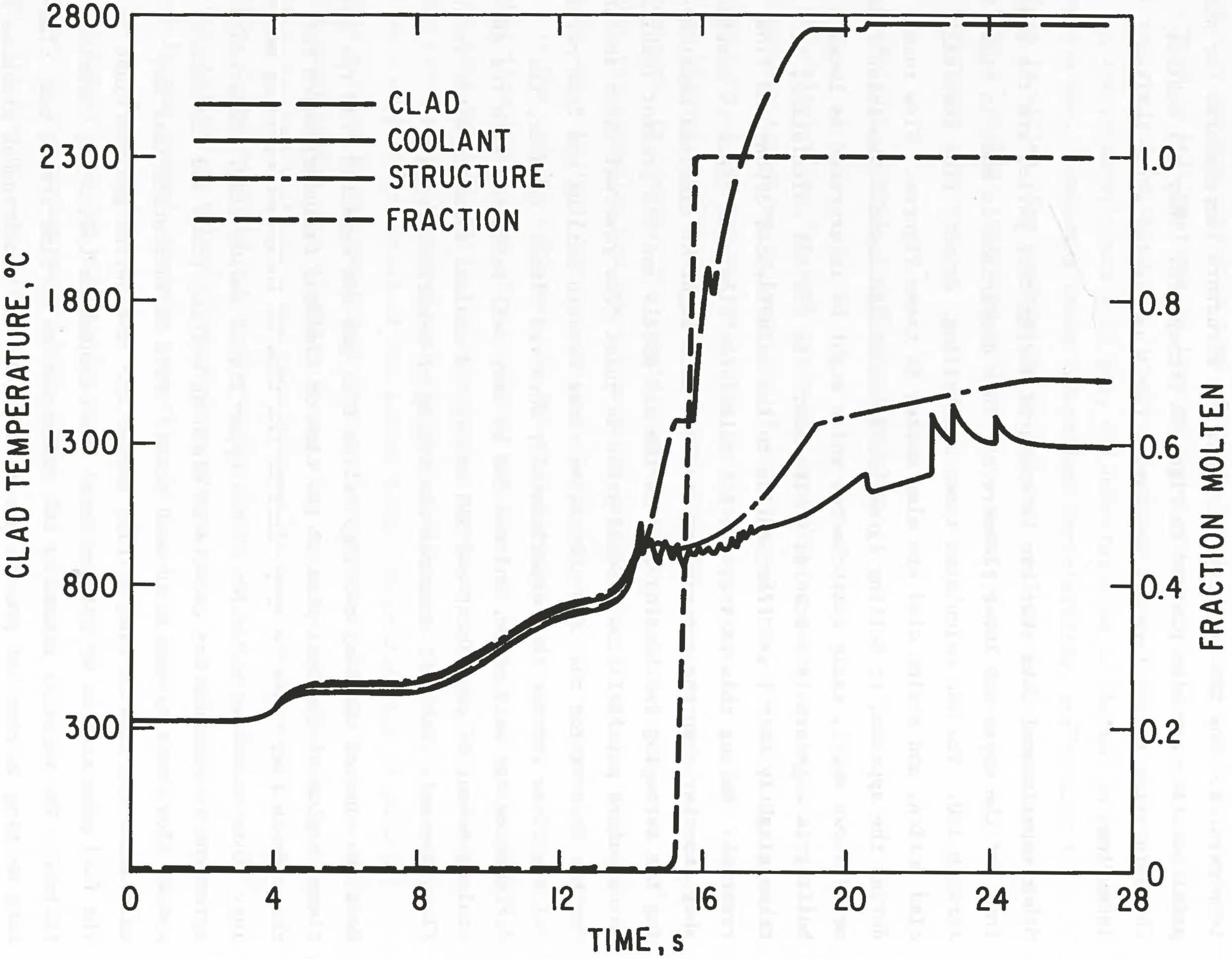

Fig. 94 R4 Temperature Conditions at 74.6 cm for SAS Case 1 (Low Heat Loss)

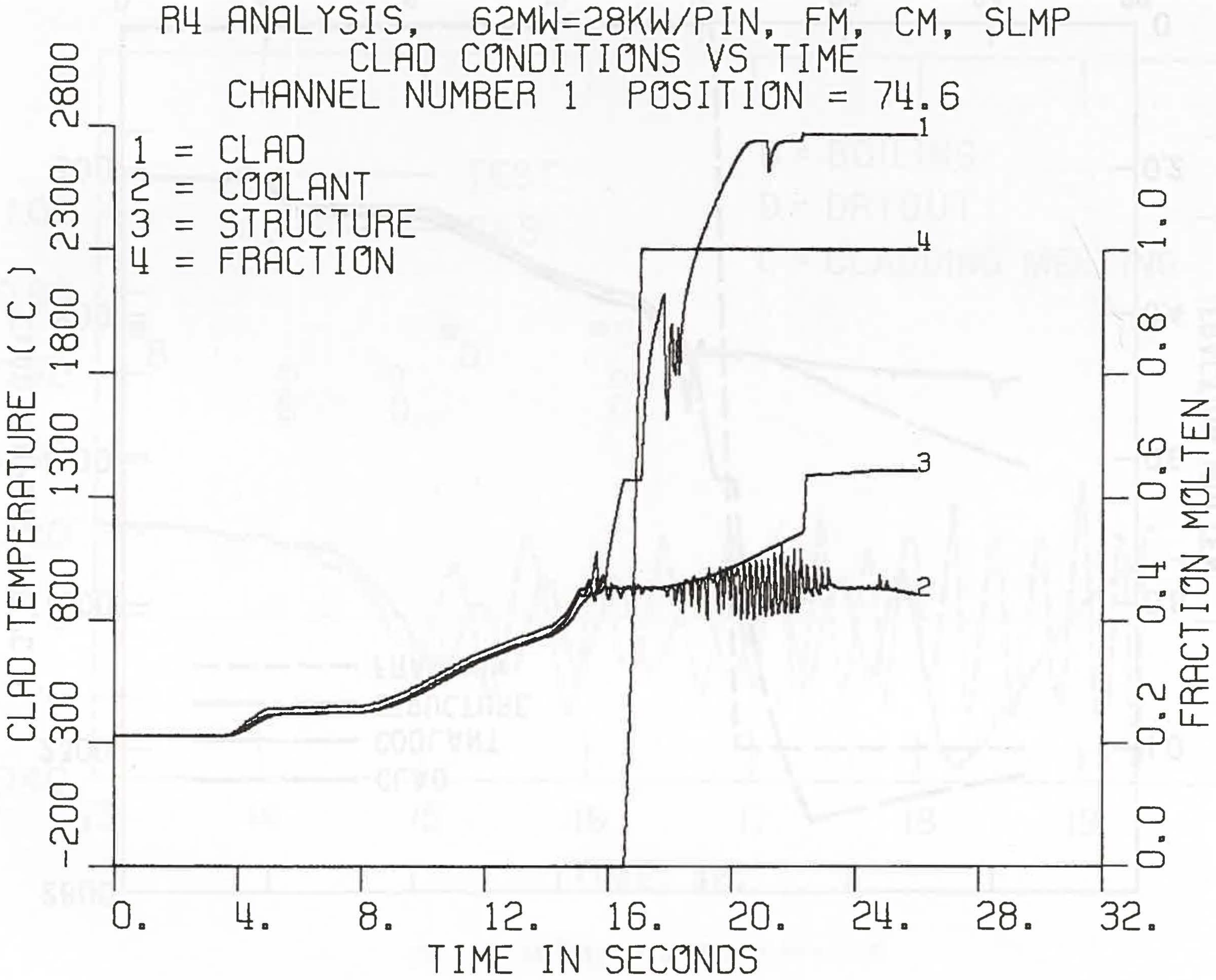

Fig. 95 R4 Temperature Conditions at 74.6 cm for SAS Case 2 (High Heat Loss)

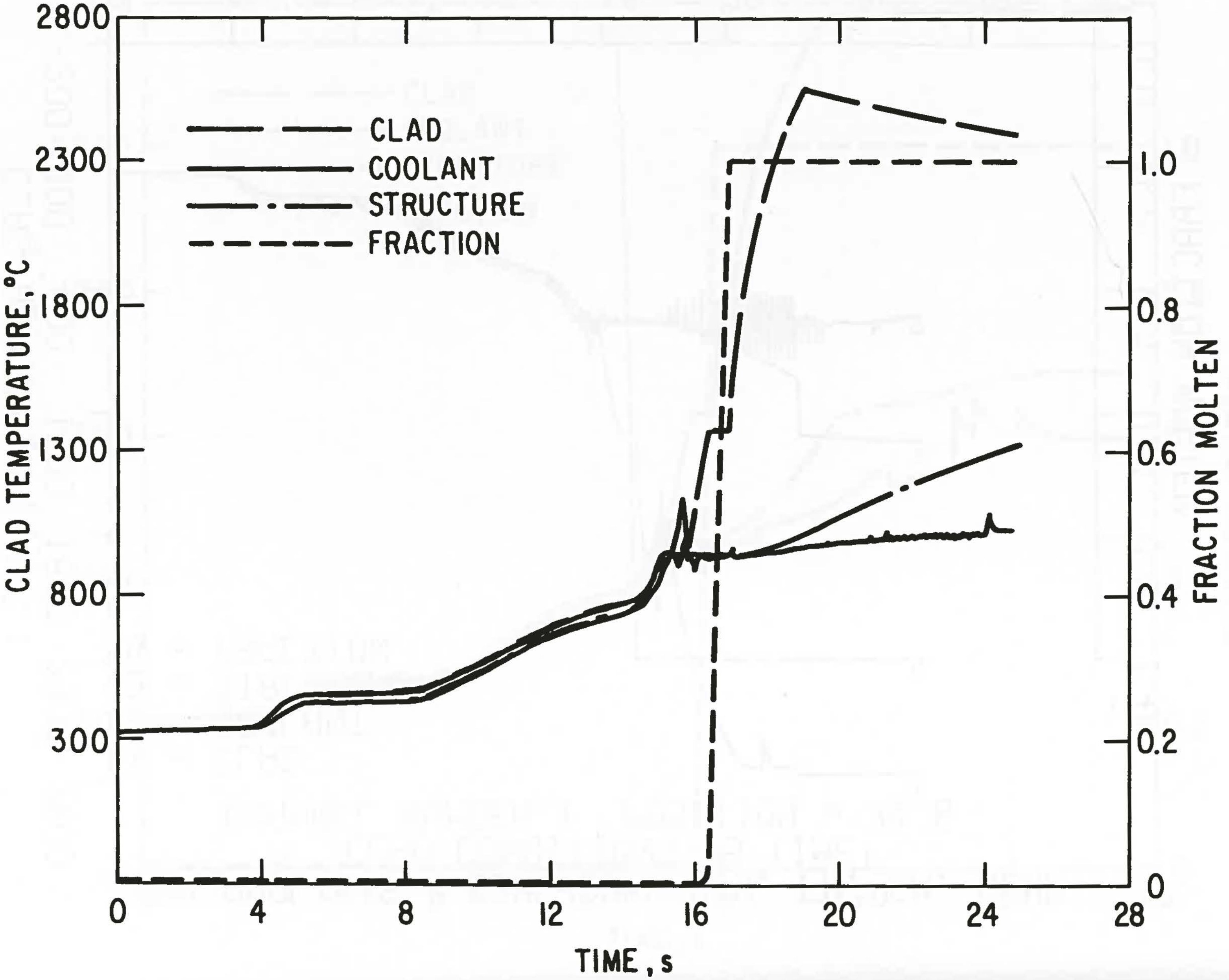

Fig. 96 R5 Temperature Conditions at 76.4 cm

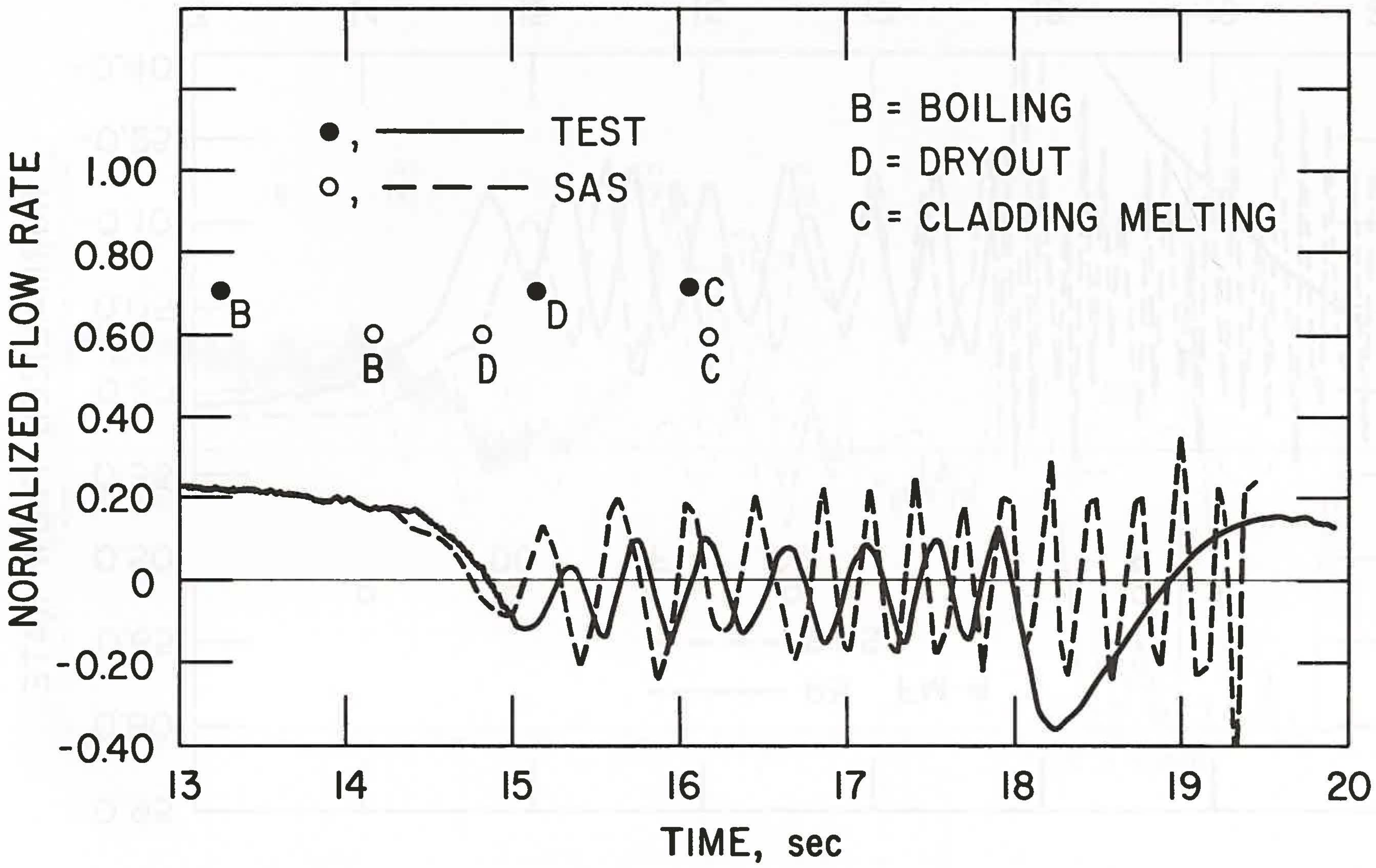

Fig. 97 R4 Inlet Flow Rate Comparison

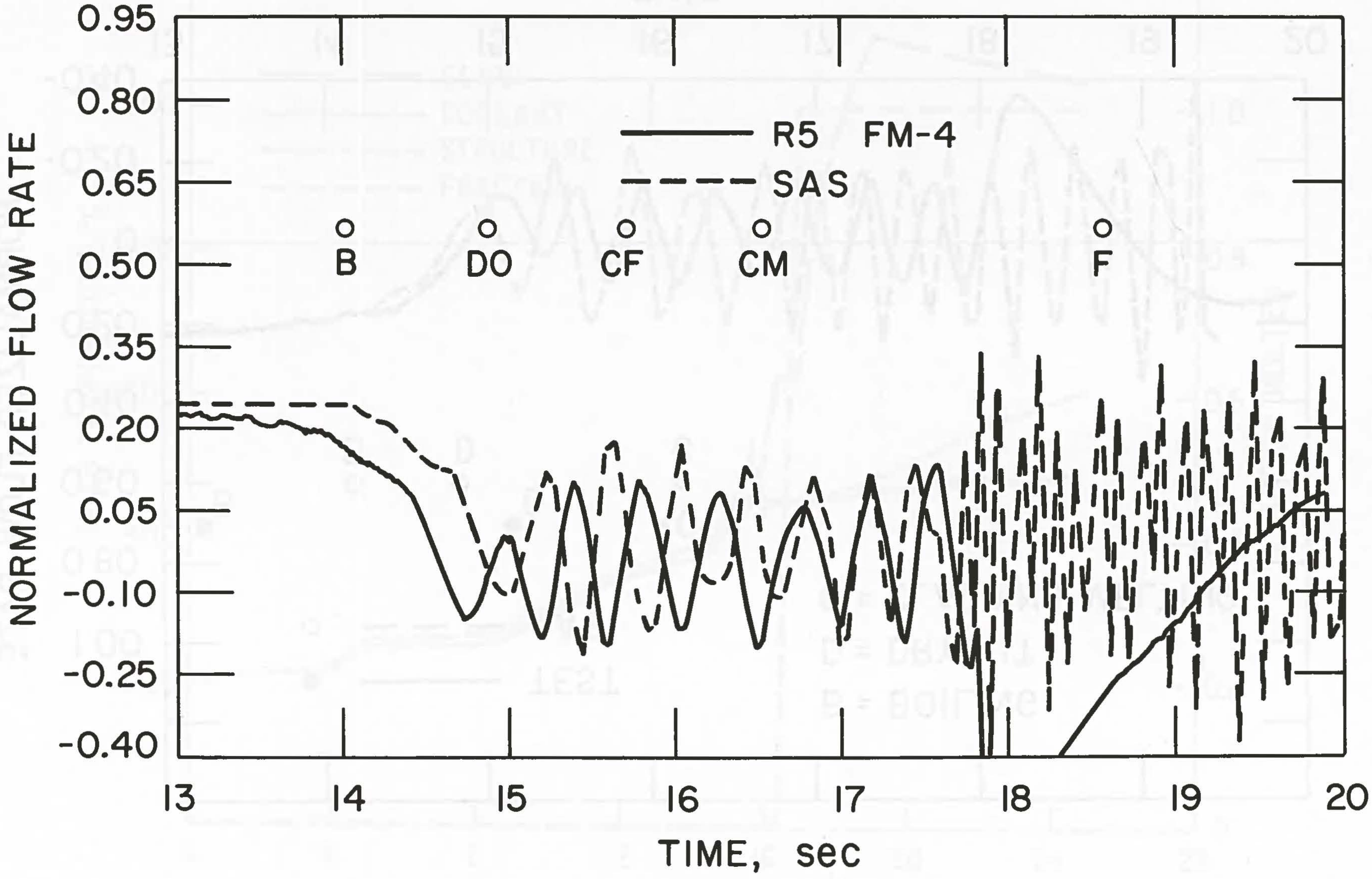

Fig. 98 R5 Inlet Flow Rate Comparison

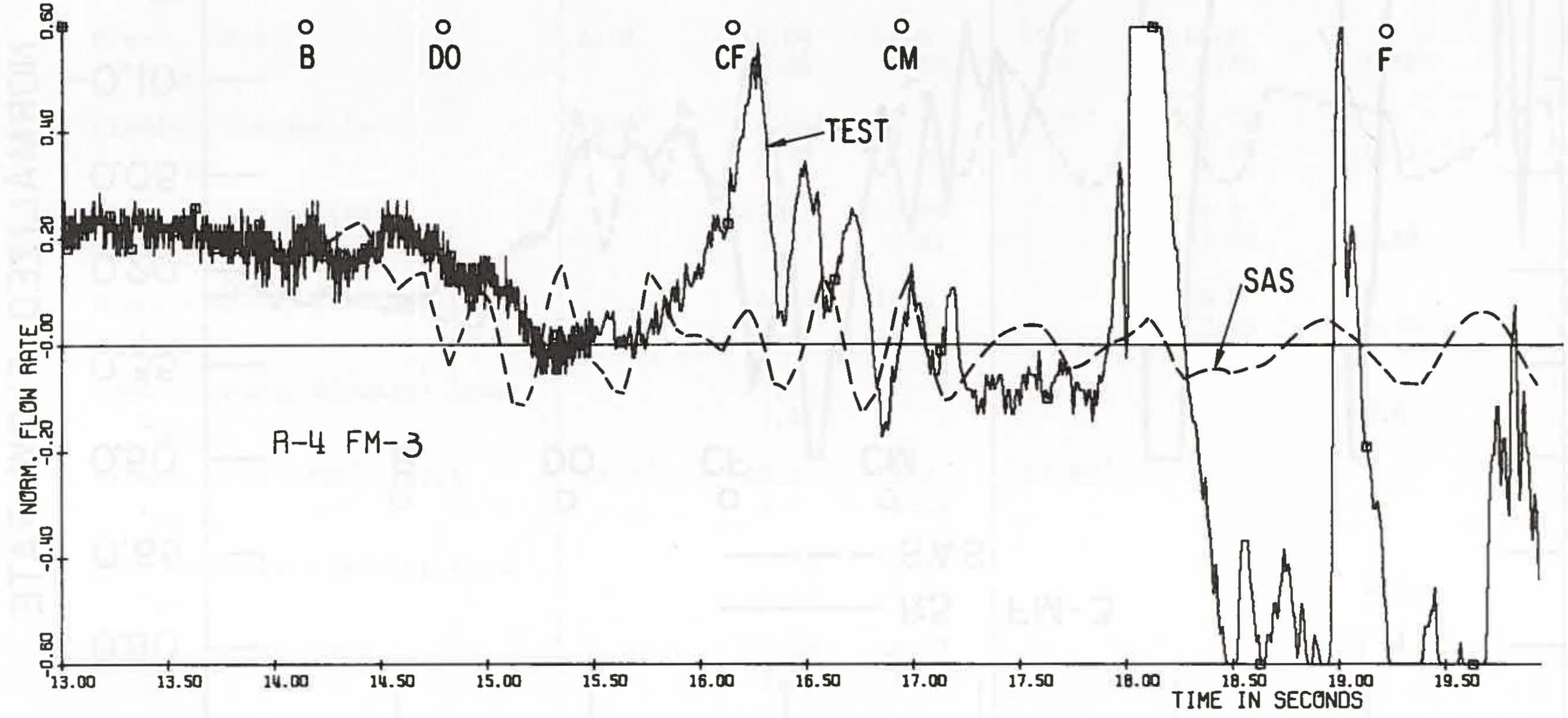

Fig. 99 R4 Exit Flow Rate Comparison

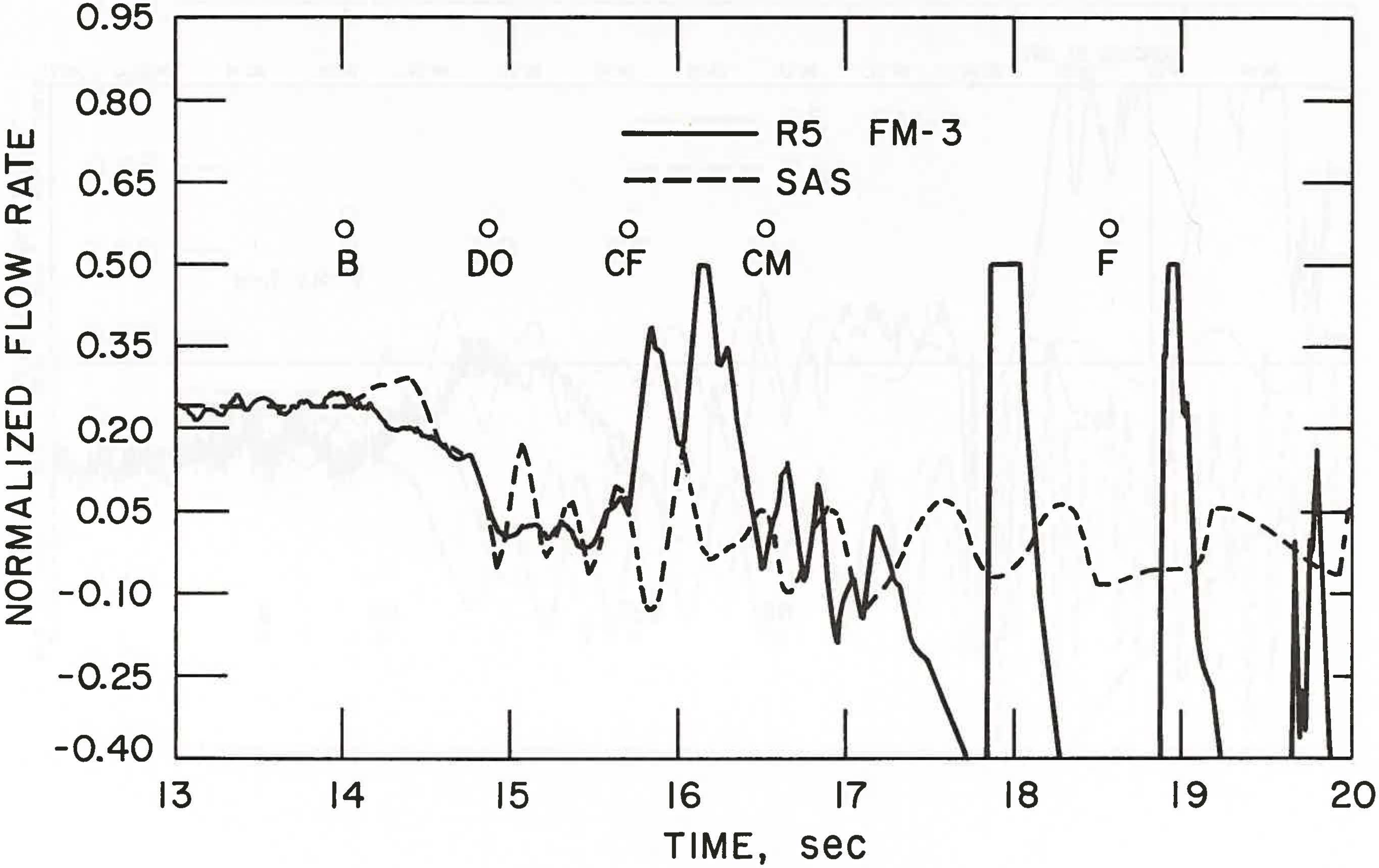

Fig. 100 R5 Exit Flow Rate Comparison

Table 13. Comparison in Timing of Events in R-Series Tests

		R4			R5	SAS
	Test	SAS_1	SAS_2	Test	SAS	Pretest
Boiling [sec]	13.25[1]	13.30	14.15	13.5[1]	14.01	11.0
t_{BOIL}		0.	0.		0.	0.
Flow Reversal [sec]	14.87	13.88	14.8	14.56	14.8	
t_{BOIL}		0.58	0.65		0.79	0.80
Dryout [sec]	15.2	14.04	14.8	14.8	14.8	
t_{BOIL}		0.74	0.65		0.79	0.92
Cladding Melting [sec]	16.0[2]	14.96	16.2	15.7[2]	15.76	
t_{BOIL}		1.66	2.05		1.75	1.61
Cladding Motion [sec]		15.77	16.96		16.5	
t_{BOIL}		2.47	2.81		2.49	2.48
Upper Cladding Blockage [sec]		16.08	18.3		16.9	
t_{BOIL}		2.78	4.15		2.89	2.75
Lower Cladding Blockage [sec]		17.54			17.4	
t_{BOIL}		4.24			3.39	6.0
Structure at 1000°C [sec]	18.0[3]	18.0	21.0	17.85[3]	20.0	
t_{BOIL}		4.7	6.85		5.99	
Fuel Centerline Melting [sec]		18.03	19.25		18.64	
t_{BOIL}		4.73	5.10		4.63	4.56
Fuel Slumping [sec]		20.55	22.77			
t_{BOIL}		7.25	8.17			
Reactor Shutdown [sec]	25.	25.	25.	19.0	19.0	
t_{BOIL}		11.7	10.85		4.99	3.3

---

[1] First indication of local boiling.

[2] Fill gas release from fuel pin.

[3] Hex can failure.

The cladding melting transition for the R-series tests takes place in approximately 0.8 sec. This is characteristic of the 30 kW per pin average pin power. Once cladding melting starts, the channel geometry is disturbed and the comparison moves into the next stage. Voiding, dryout and clad melting envelopes are given in Figs. 101 to 103.

6.3.3 Cladding Motion and Blockage Formations

The analysis of cladding motion in hypothetical fast-reactor accidents is important for three reasons. First, removing the cladding has important implications with respect to the thermal behavior of the melting subassembly. The cladding essentially acts as a heat sink. The molten cladding also transfers energy to cold sections of the subassembly. Secondly, removal of the cladding from the center of the core removes a neutron sink and increases reactivity. Thirdly, the behavior of the molten cladding strongly influences the fuel motion later in the accident sequence. Molten cladding moves under the influence of sodium vapor drag and gravity to the colder regions of the channel, whereupon the material freezes and forms a blockage. This blockage affects fuel motion and dispersal and therefore may impede accident progression to a permanently subcritical configuration. For these reasons, the CLAZAS subroutine of SAS was developed. The physical model pictures cladding segments defined by the SAS axial fuel pin mesh structure. These segments pass the melting transition whereupon they are calculated to move under the influence of gravity, vapor drag, wall friction, and axial pressure gradients.

It is important to note that in the physical model the cladding segments essentially retain their original shape except when they have overlapped another molten segment and are allowed to combine. The coolant-channel hydraulic diameter is changed accordingly. A number of overlapping segments can form a blockage, and if the blockage has been carried into a cold section of the channel, it can freeze and plug the coolant channel. The flow of sodium vapor is thereby cut off along the pin, so that melting segments subsequently can drain to the bottom under the influence of gravity.

The purpose and motivation of the R5 experiment was to study cladding motion explicitly. The knowledge gained from the experiment allows an assessment of

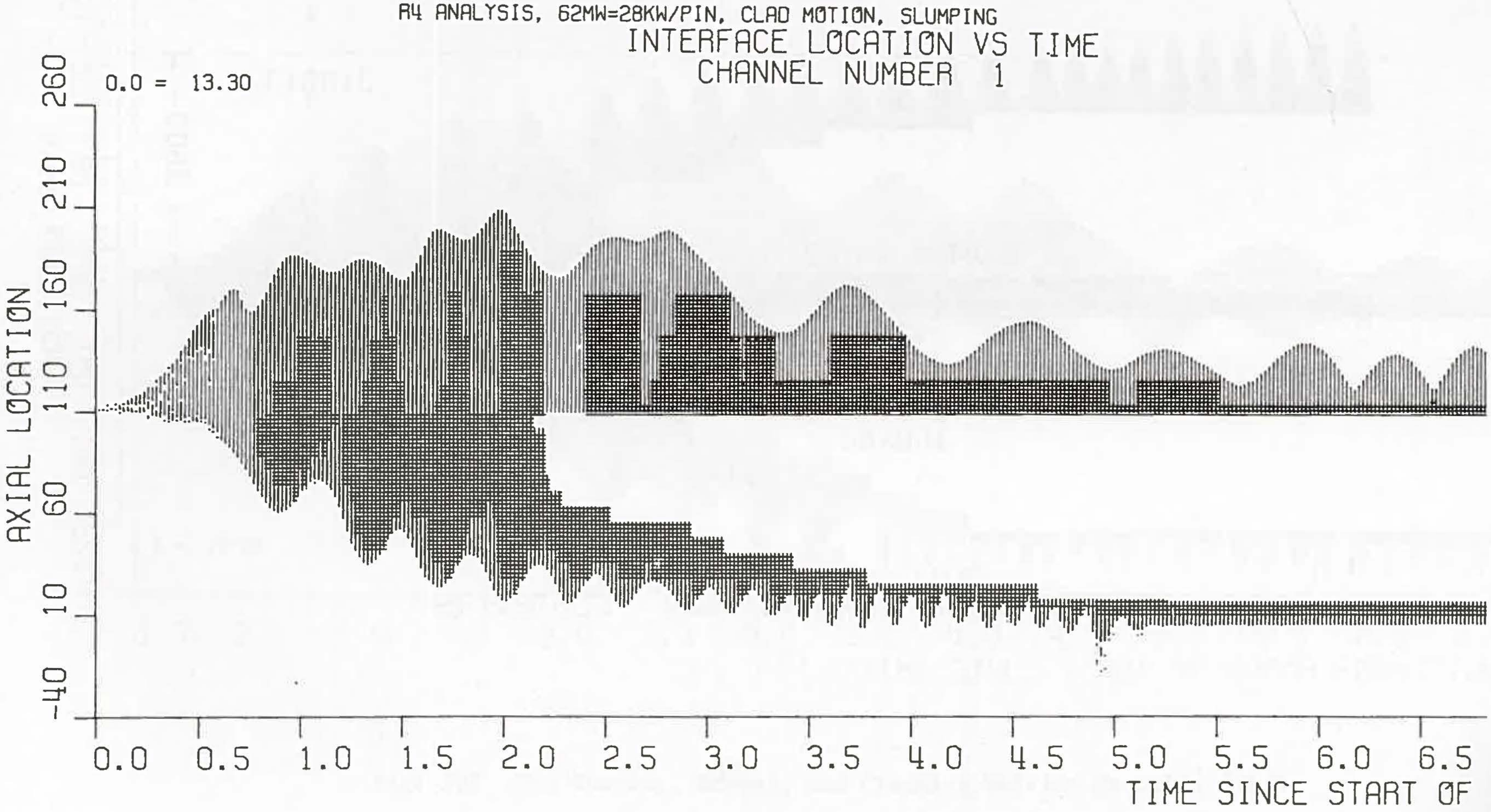

Fig. 101 SAS Voiding, Dryout, and Cladding Melting Profiles for R4; Case I

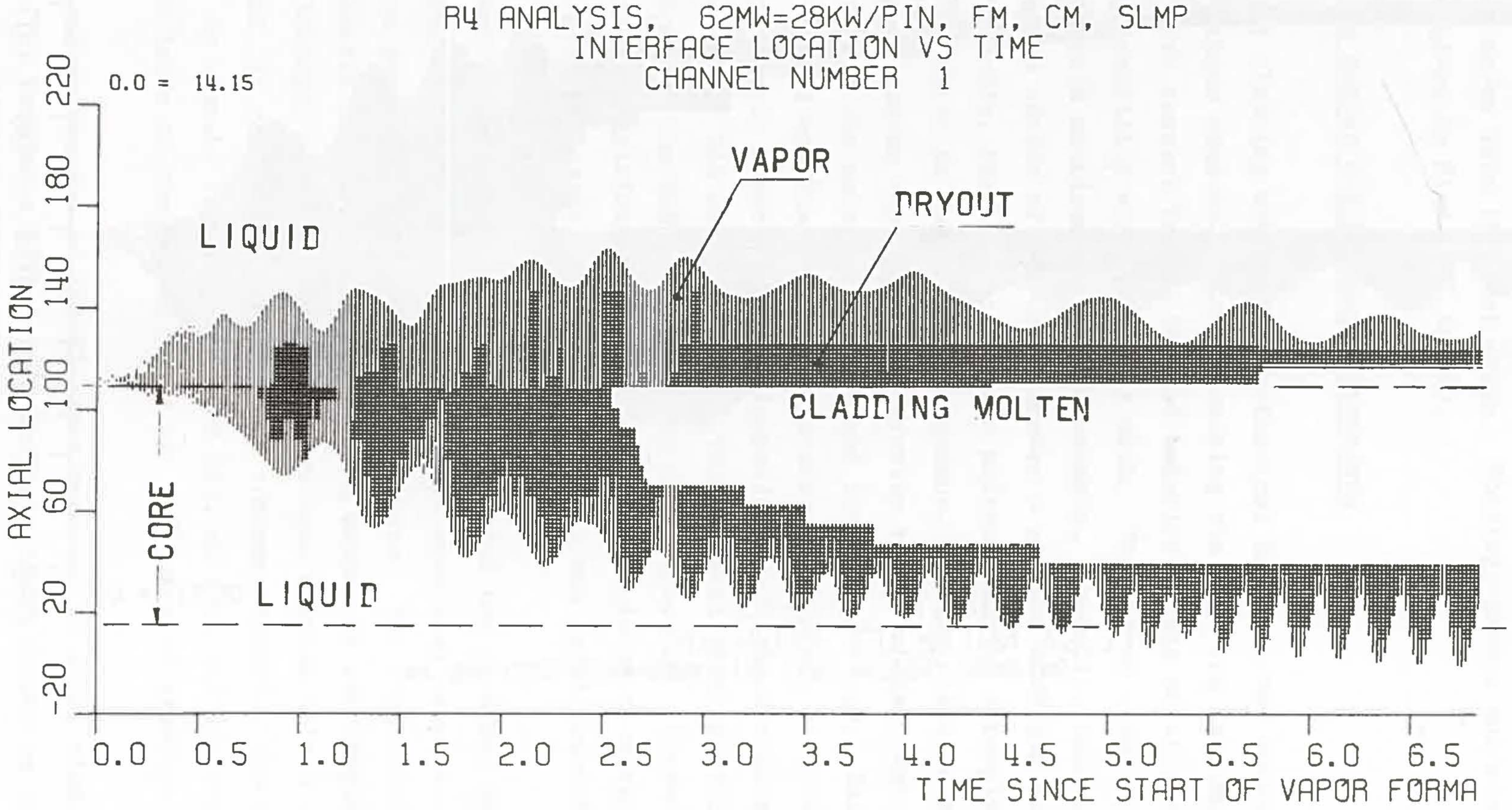

Fig. 102 SAS Voiding, Dryout, and Cladding Melting Profiles for R4, Case II

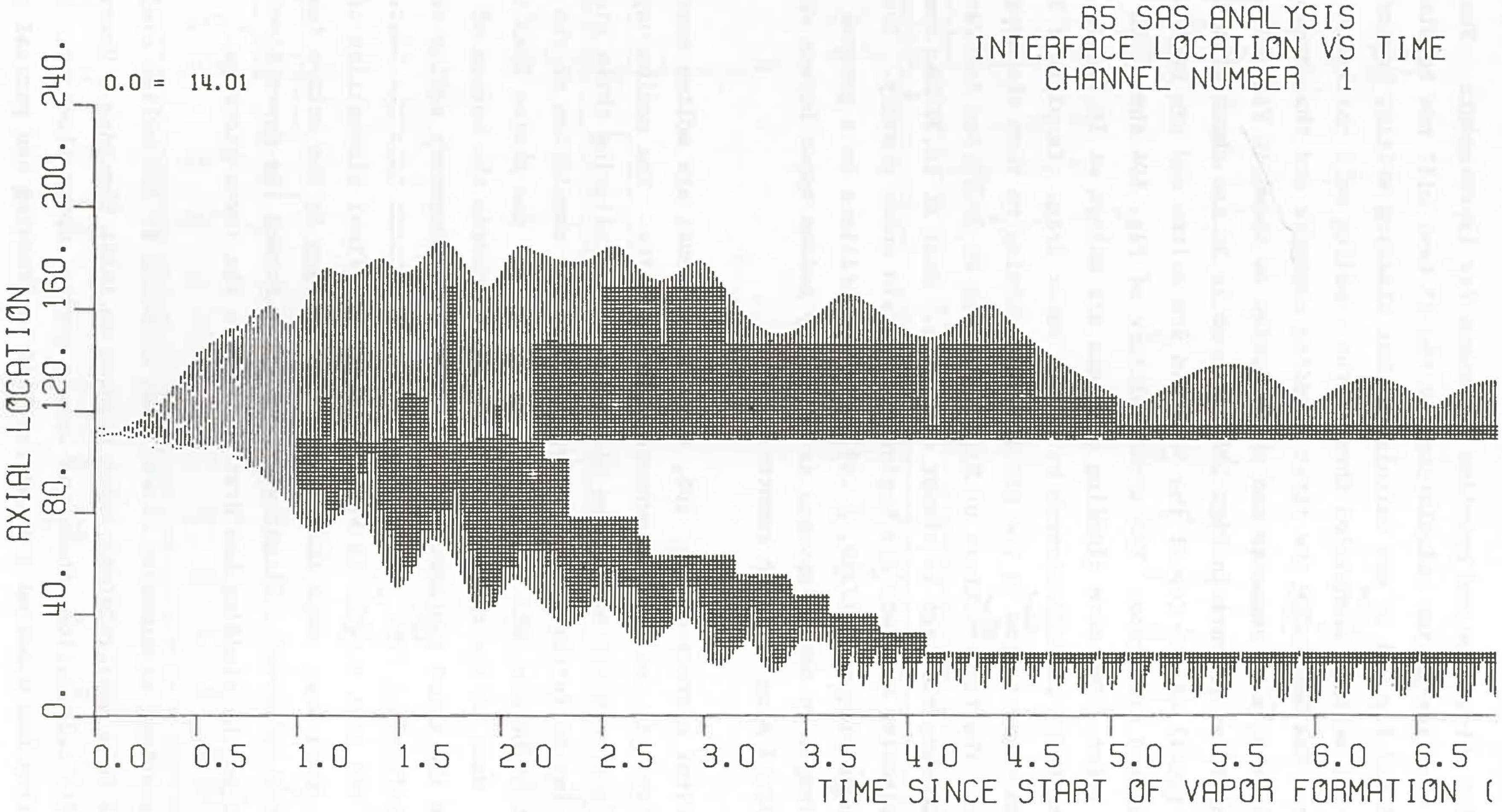

Fig. 103 SAS Voiding, Dryout, and Cladding Melting Profiles for R5

the CLAZAS subroutine and provides the basis for improvements. The results of the SAS cladding motion calculation for the R5 test will now be discussed. In Table 13 and Fig. 96 it was calculated that cladding melting begins at 15.8 sec and the melting transition through the cladding wall thickness lasts to 16.5 sec. The motion of the first cladding segments and the successive melting of further clad segments and their motion is shown in Figs. 104 through 106. The first picture in Fig. 104 taken at 16.50 sec shows that two nodes (8.3 cm total) at the top of the fuel pin are molten and are beginning to move in the upward direction. The second picture of Fig. 104 shows the situation 20 msec later. Two more cladding segments are molten at 16.66 sec in picture 3 and are being carried upwards by sodium vapor drag. In picture 4 at 16.71 sec three segments are in the process of combining to form the upper cladding blockage. The first picture of Fig. 105 taken at 16.76 sec indicates that the upper cladding blockage is almost completed. Next at 16.99 sec some of the molten cladding segments are beginning to drain under gravity. They combine in the next pictures (17.18, 17.37 sec) and oscillate on a general downward path. Temporary motion upwards is caused by sodium vapor bursts when the lower liquid slug tries to reenter.

In the first picture of Fig. 106, two more segments are molten near the center of the fuel pin and moving downwards under gravity. The sodium vapor flow has been effectively cut off by the blockages. The following three pictures show the melting of further cladding segments and the completion of the lower blockage. At 18.08 sec, all except the lower 16 cm of the active fuel cladding has melted. Most of the material is moving down towards the bottom of the fuel pin. In the third picture, taken at 19.60 sec, temporary sodium rewetting has caused sufficient flow to drag some cladding upwards into the heated section again. The last picture in Fig. 106 shows the final disposition of the cladding at 20.01 sec. More than 80% of the cladding in the active fuel region has melted and moved. Slightly over 20% has formed the upper blockage while the rest of the cladding has drained to form the lower blockage.

The R5 posttest examination showed that draining of the molten cladding had resulted in a massive steel ingot forming an inlet blockage. However, contrary to the SAS calculation, there was only a partial upper blockage. Upward cladding motion had occurred and had resulted in freezing and partial plug

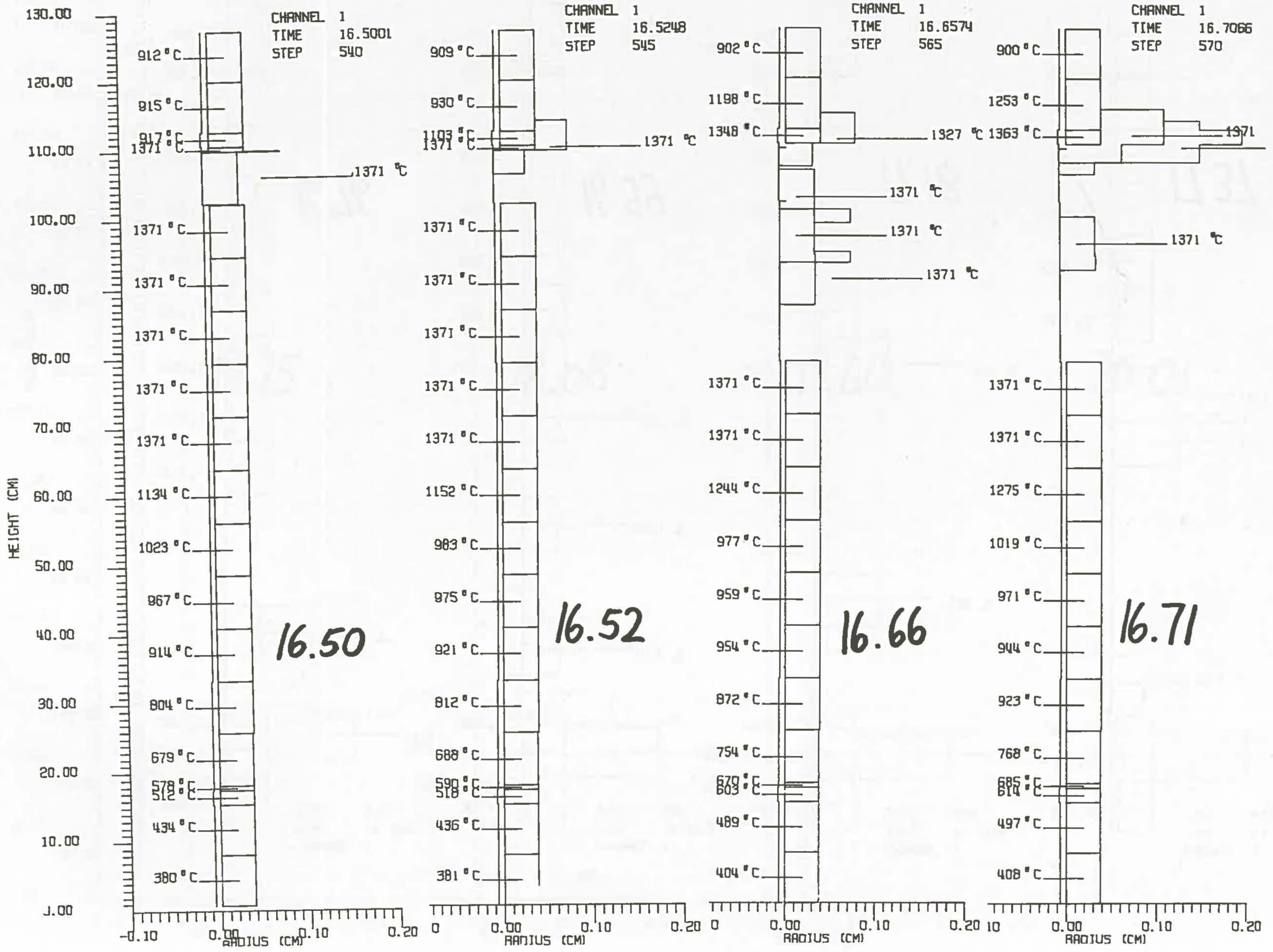

Fig. 104 R5 Cladding Motion Sequence, Initiation.

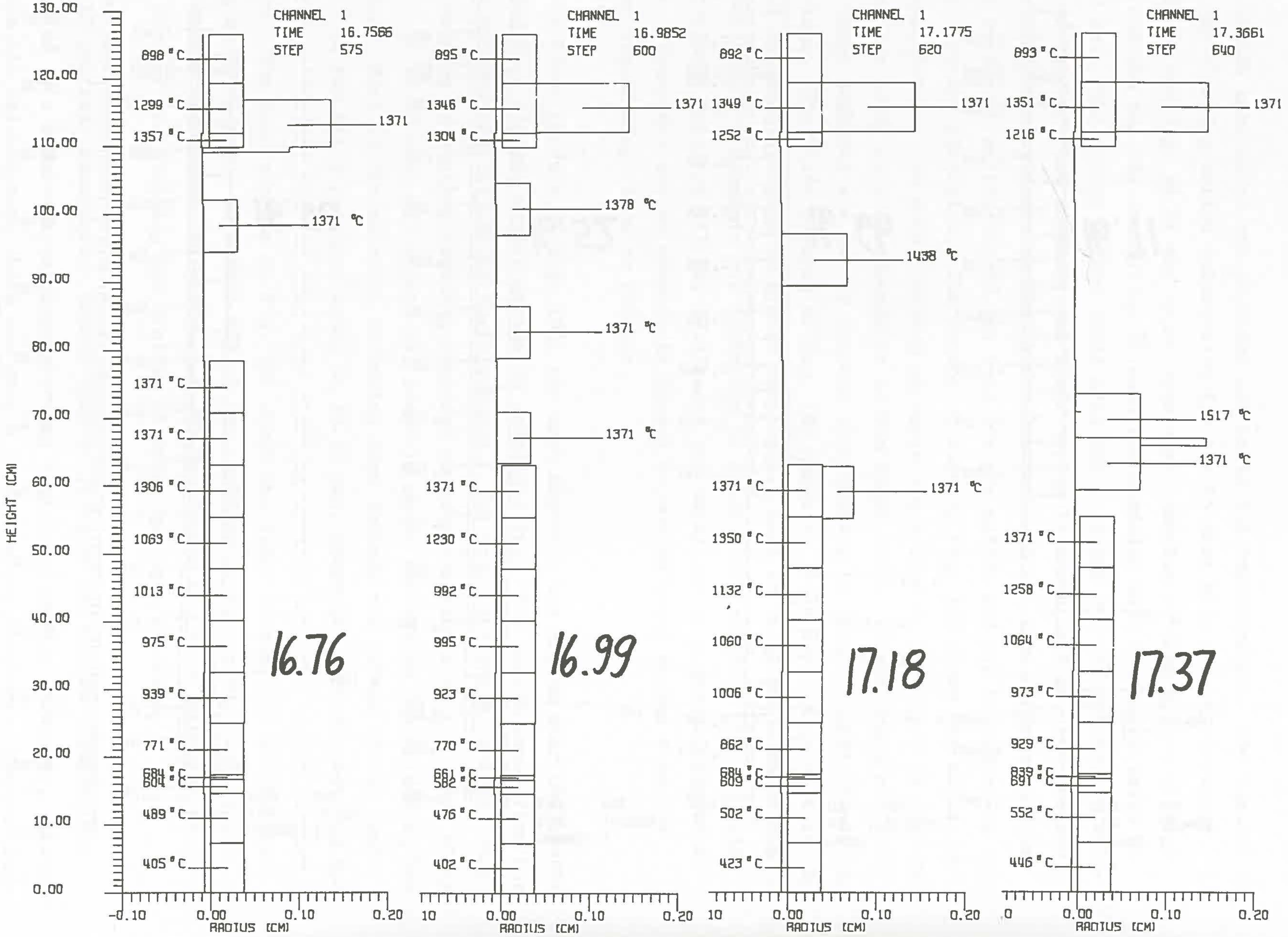

Fig. 105 R5 Cladding Motion Sequence, Upper Blockage and Draining.

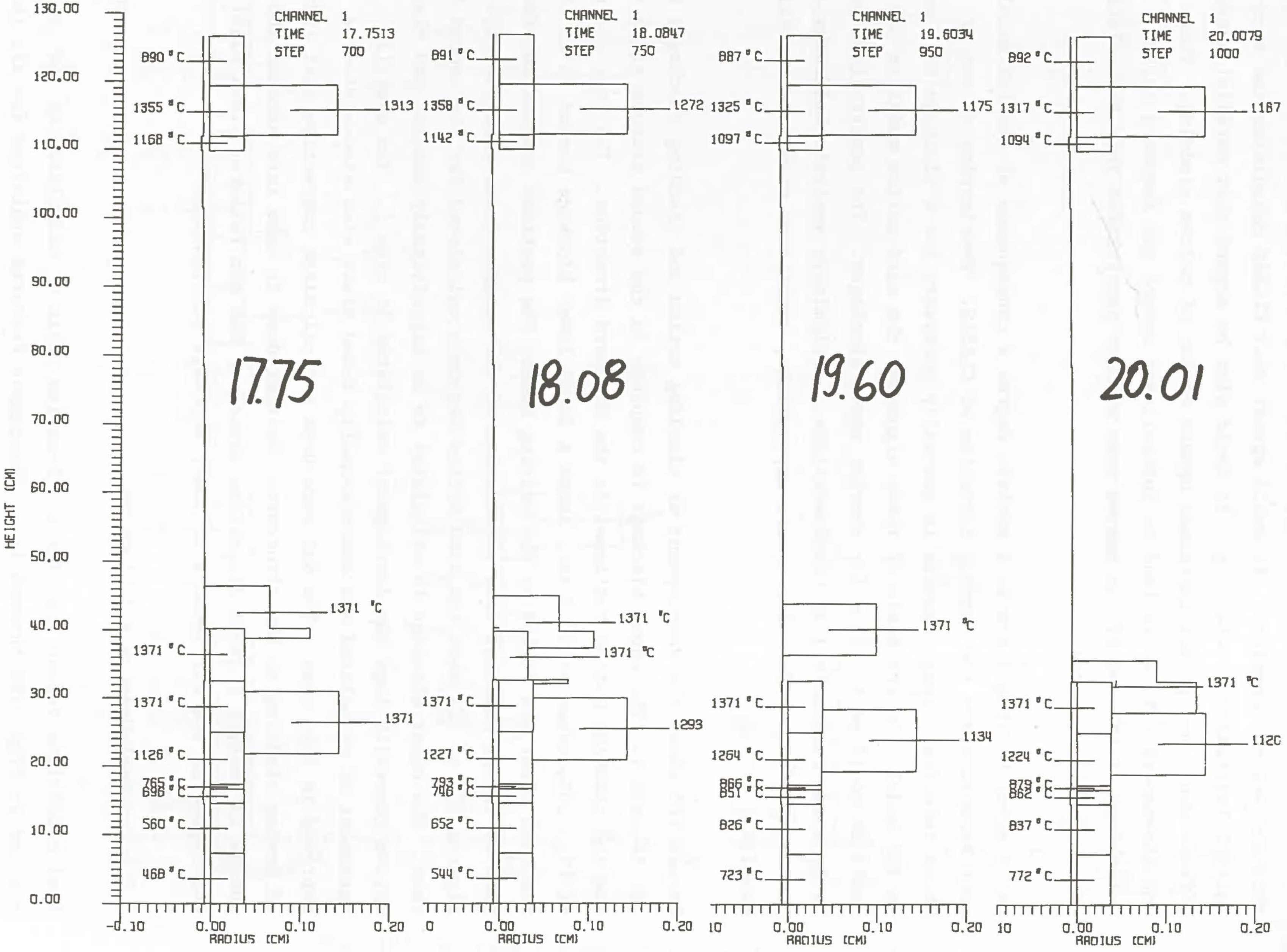

Fig. 106 R5 Cladding Motopm Sequence, Lower Blockage.

formation in the region of the upper insulator pellets, but the blockage was thin and was not complete. It would appear that CLAZAS calculates too much initial levitation of cladding. It could also be argued that parallel channel effects would not permit sustained upward motion of molten cladding. These incoherence effects would lead to intermittent upward and downward motion (sloshing) at the end of the heated zone without penetration into the colder unheated reflector region.

Large upper blockages are to a certain degree a consequence of the SAS axial node structure and the segment formalism of CLAZAS. Overlapping of two or three relatively long segments is generally necessary for a blockage to form in the model. On the basis of these arguments the clad motion model in SAS could be modified to allow for shorter upper blockages. The penetration could be derived from analytical considerations. Preliminary analysis indicates that blockages of the order of 1 cm are appropriate, consistent with experimental results.

Figure 107 shows the development of cladding motion and cladding blockages for the R4 case 1. The upper blockage is complete in the second picture at 16.4 sec and cladding motion continues in the downward direction. The last picture of Fig. 107, taken at 22.9 sec, shows a large lower blockage pushed 15 cm into the cold lower pin region by the melting fuel. The posttest examination for test R4 showed somewhat less penetration of the massive lower clad blockage. Figures 108 to 111 show the clad motion sequence calculated for the second SAS case. The upper blockage is calculated to be significantly smaller and clad motion generally lags the development calculated in case 1. The overall agreement of calculated and experimentally found final clad disposition is improved in this case. The SAS code does not calculate convective heat transfer of moving cladding to the structure. Neither does it take into account the change in coolant channel dimensions caused by hex can failure. This might contribute to the differences in lower blockage penetration.

6.3.4 Fuel Melting and Slumping

Fuel conditions versus time for the R-series tests as calculated by SAS are plotted in Figs. 112 through 114. The common features exhibited for all three tests are the following:

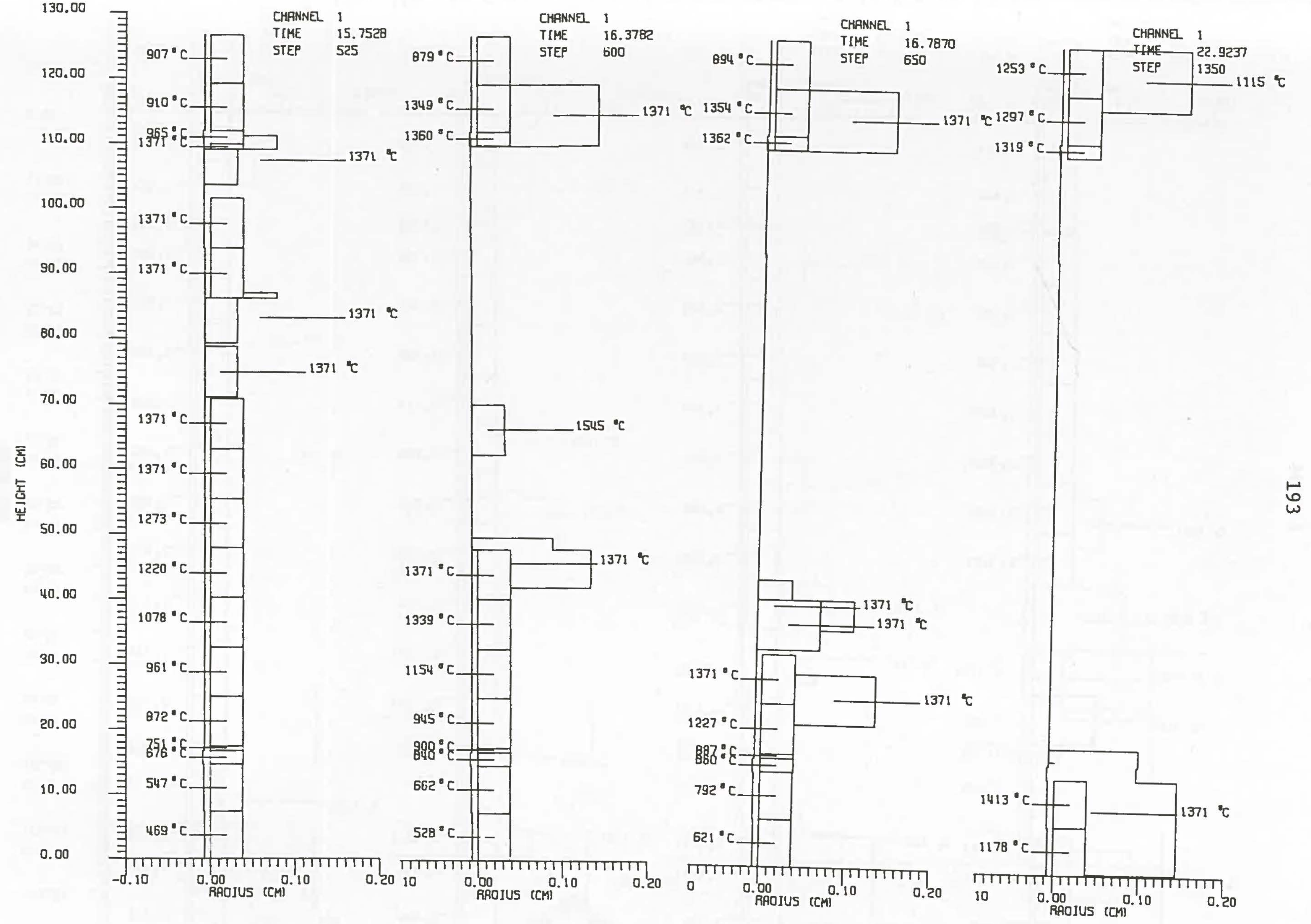

Fig. 107 R4 Case 1 Cladding Motion Sequence; 15.8 s to 22.9 s.

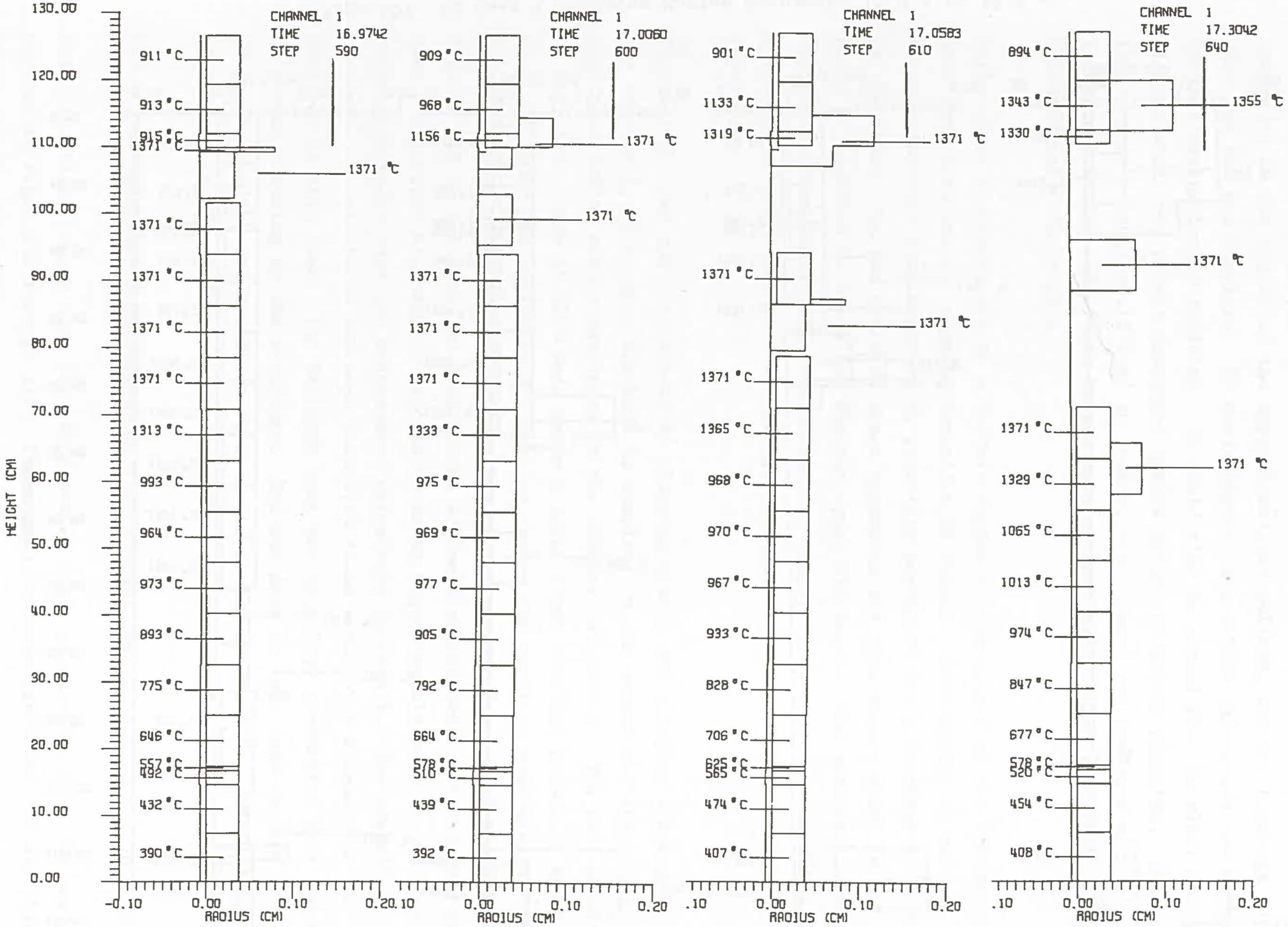

Fig. 108 R4 Case 2 Cladding Motion Sequence; 17.0 s to 17.3 s.

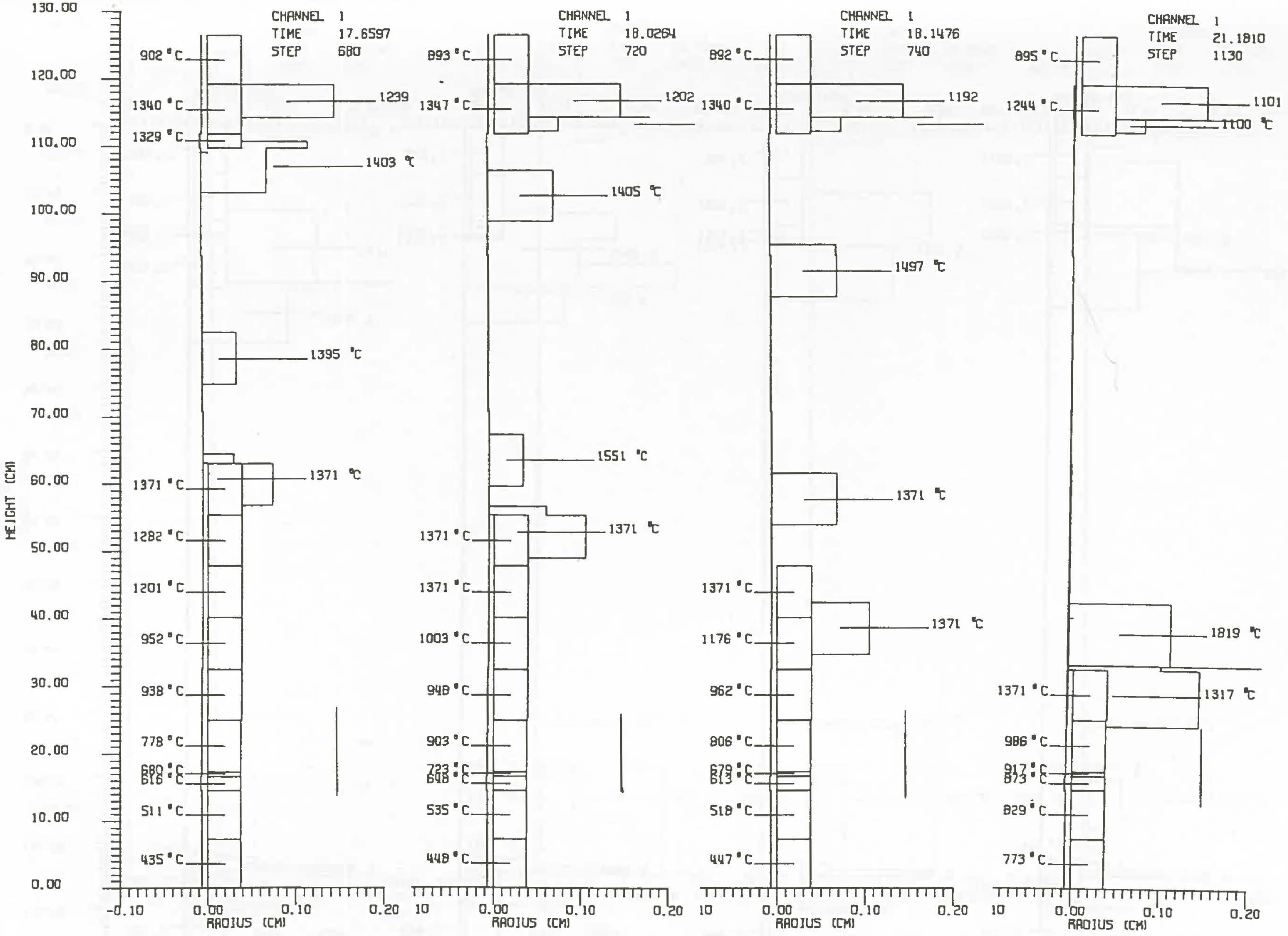

Fig. 109 R4 Case 2 Cladding Motion Sequence; 17.7 s to 21.2 s.

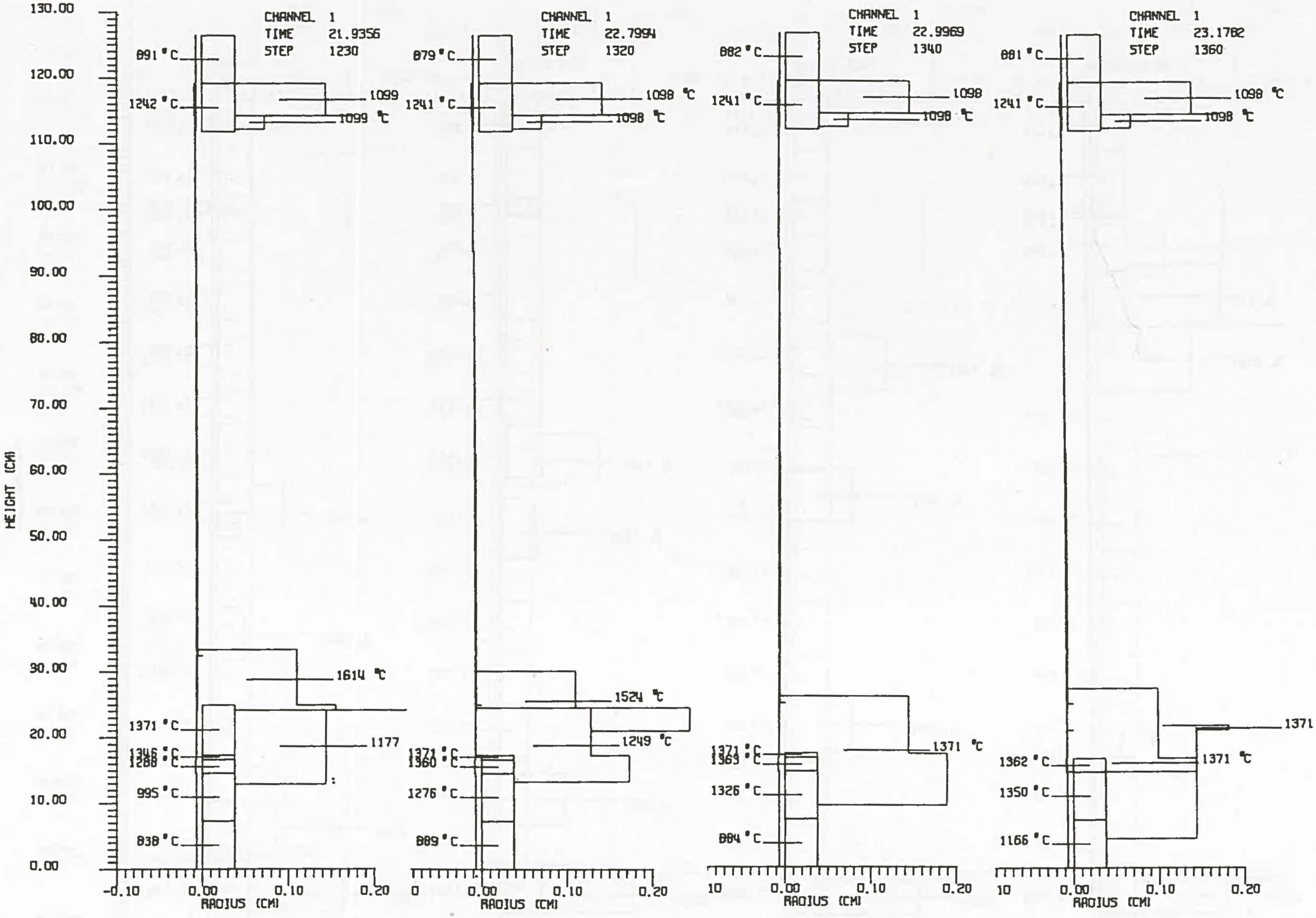

Fig. 110 R4 Case 2 Cladding Motion Seqeunce; 21.9 s to 23.2 s.

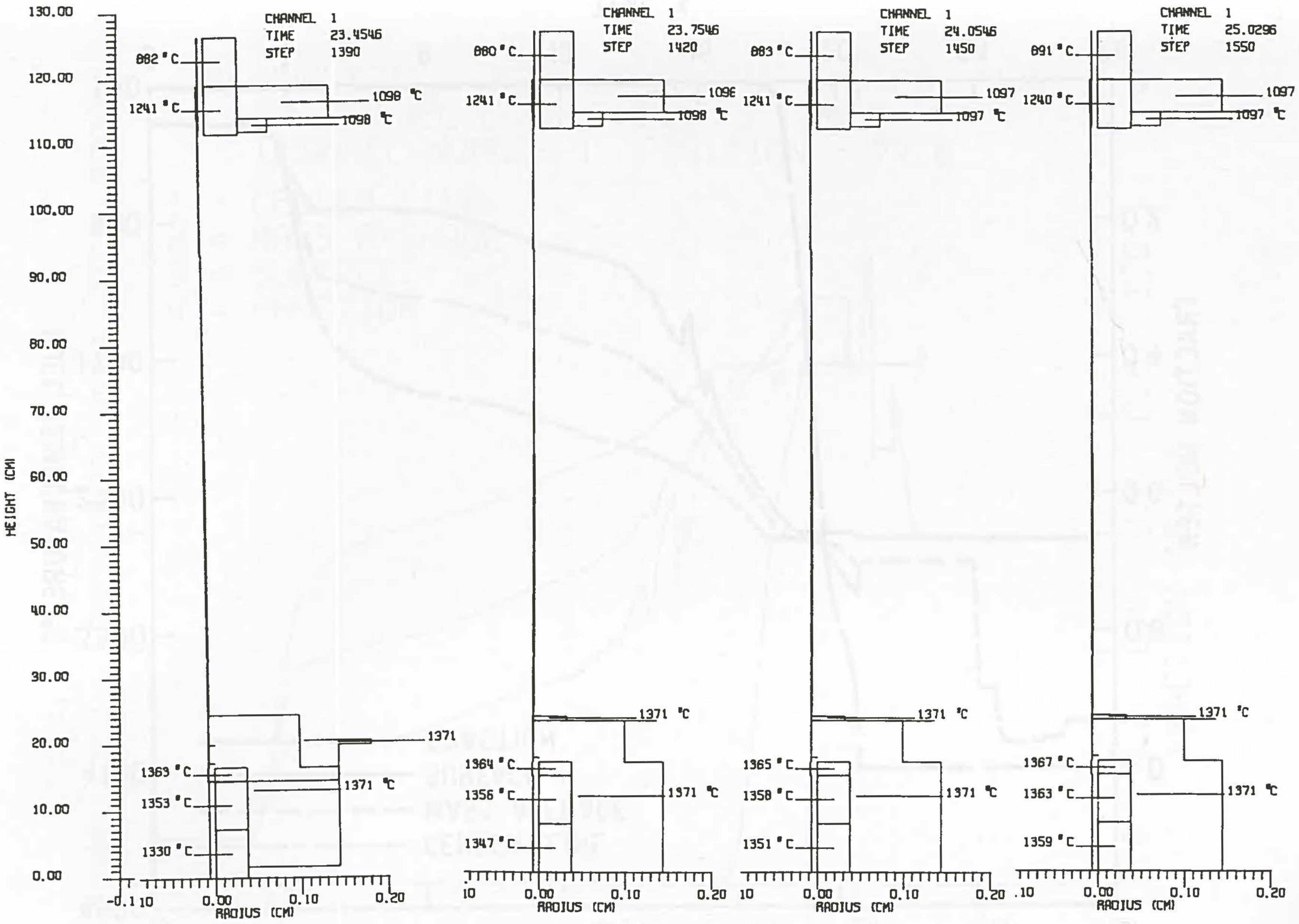

Fig. 111 R4 Case 2 Cladding Motion Sequence; 23.5 s to 25.0 s.

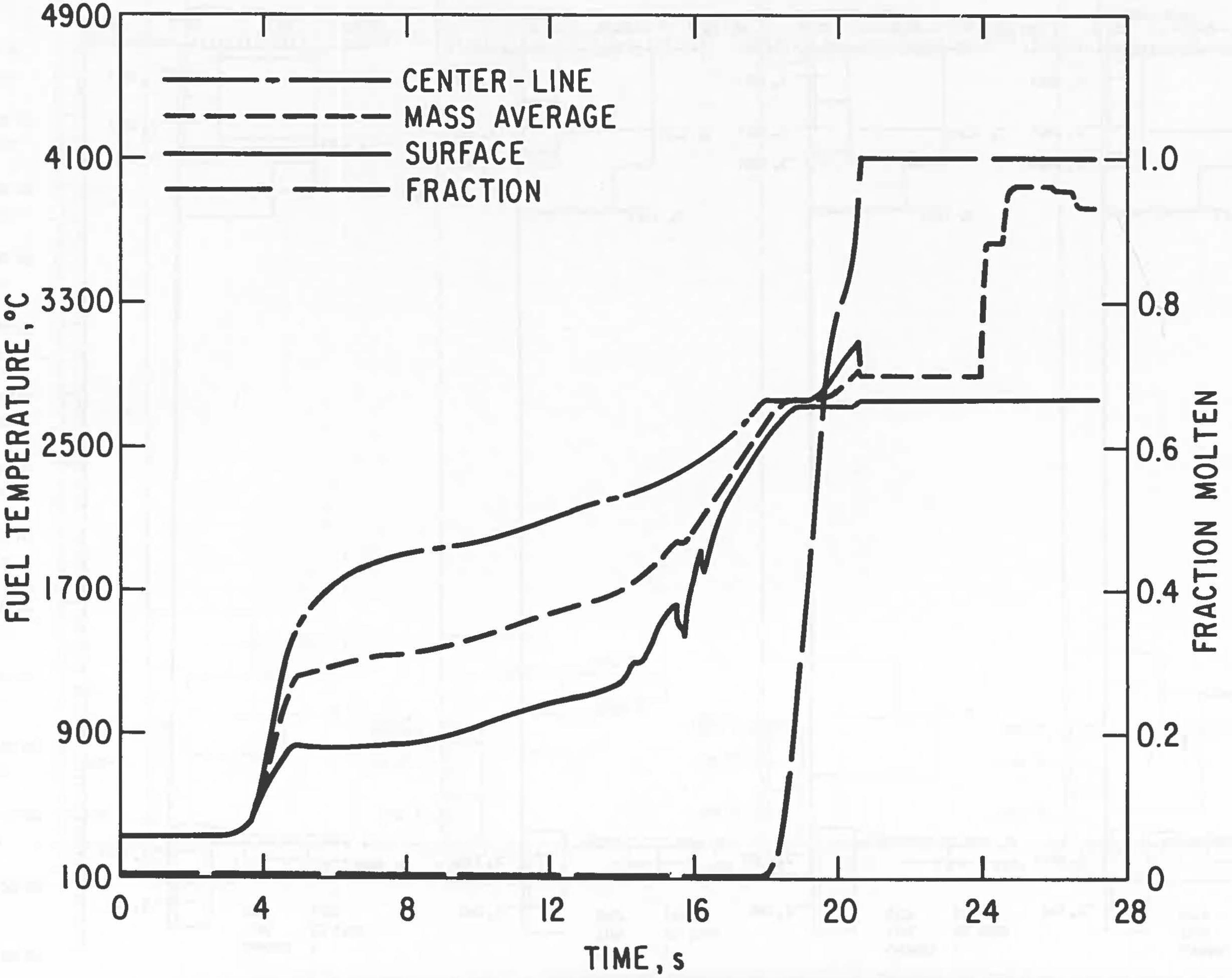

Fig. 112 R4 Fuel Temperature Conditions at 74.6 cm for SAS Case 1 (Low Heat Loss).

(Low Heat Loss).

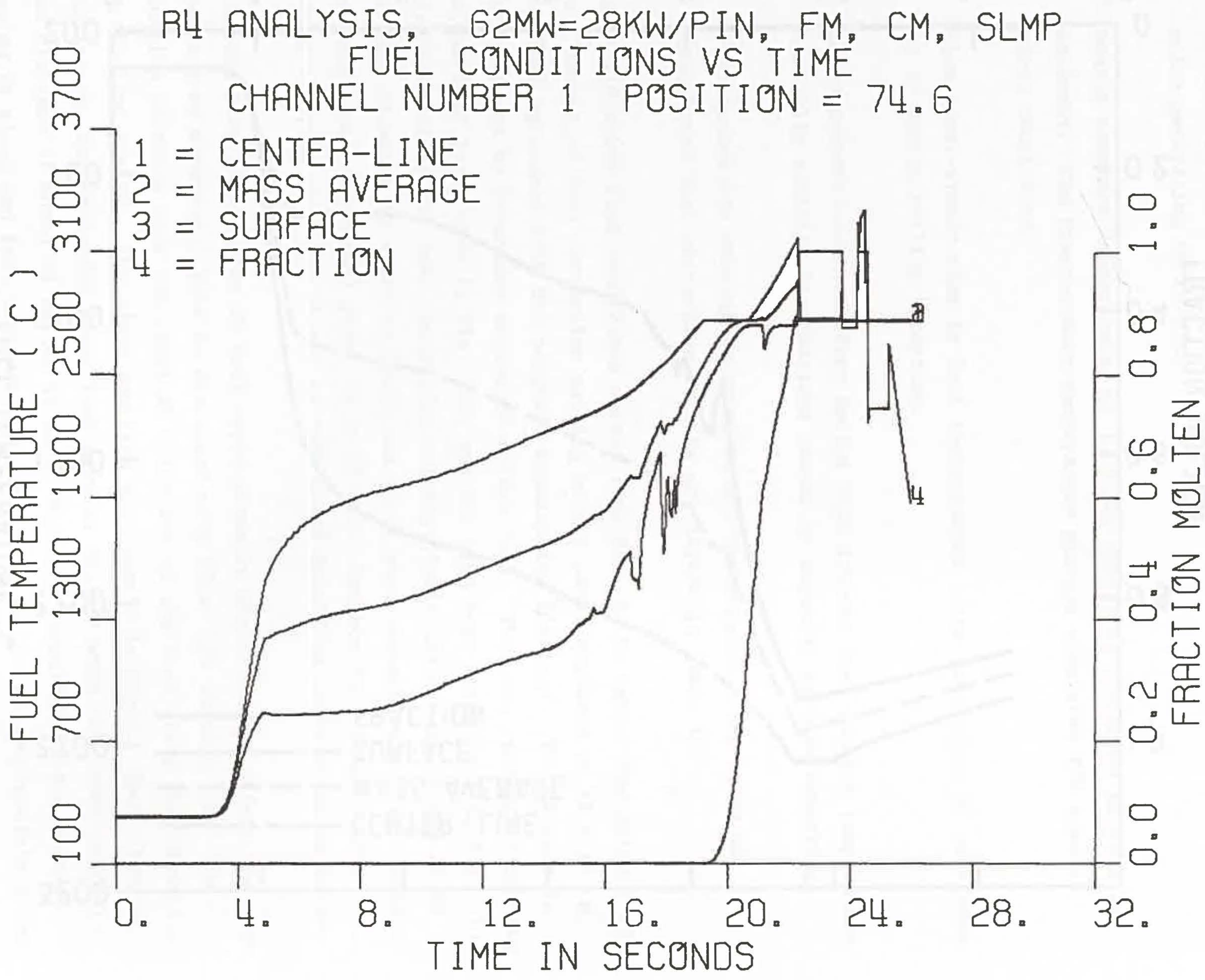

Fig. 113 R4 Fuel Temperature Conditions at 74.6 cm for SAS Case 2 (High Heat Loss)

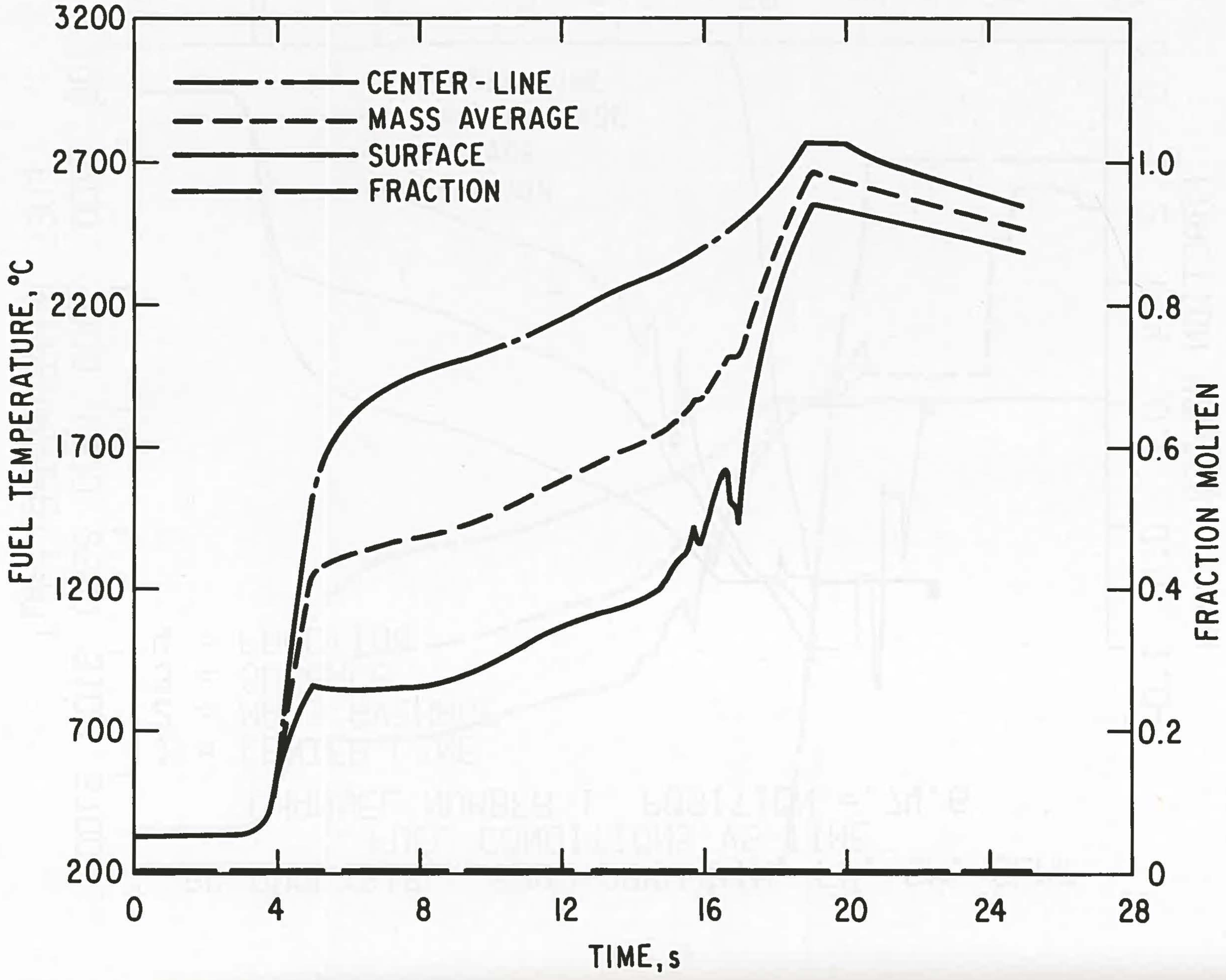

Fig. 114 R5 Fuel Temperature Conditions at 74.6 cm.

1. Constant initial temperatures up to 3.5 sec.

2. Sharp temperature rise during the next second due to the reactor power spike generating 60 kW/pin.

3. Nearly constant temperatures up to 9 sec when flow coastdown effects are apparent. The precoastdown temperature plateau simulated FTR steady-state conditions.

4. Slow quasi-steady rise in fuel temperatures after initiation of coastdown up to sodium boiling inception.

5. Steep temperature rise after sodium film dryout; fuel surface temperature initially exhibits fluctuations caused by repeated coolant rewetting.

6. Fuel centerline melting occurred in all three cases. The times of calculated fuel centerline melting are listed in Table 13.

Figure 114 shows fuel conditions versus time for the R5 test. The calculated small amount of fuel centerline melting before power shutdown at 19 s is in excellent agreement with the posttest examination findings. The R4 test is characterized by extensive motion of molten fuel. This was calculated in both the low heat loss, case 1, Fig. 112, and the high heat loss, case 2, Fig. 113. Calculated times for fuel centerline melting (Table 13) are 18.03 and 19.25 sec with slumping to start at 20.55 and 22.77 sec, respectively. The reactor was maintained at nominal power up to 25 sec. Maximum fuel temperatures during slumping were calculated as 3950°C and 3420°C in these bounding cases.

The resulting differences in fuel vapor pressure significantly affect the progression of slumping. This is discussed with Figs. 115 through 119. The slumping pictures show the physical situation of the fuel along the channel at the time listed. The lower unmolten pin segment is shown. Upon slumping initiation, the decladded upper fuel segment falls toward the lower segment. The distance it moved is listed as SAG. The mesh structure of the slumped region is given and fuel temperatures and pressures in the compressible nodes are listed. Fuel density is illustrated by the shading, also listed in the pictures.

Slumping for case 1 is initiated at 20.55 sec. The first picture in Fig. 115 depicts the fuel situation at 21.28 sec. The slumped fuel amounts to 38 cm (five SAS nodes) of the original fuel pin extending from axial location 56 to 94 cm. It has slowly fallen under gravity and heated up to 3083°C. The upper pin segment has fallen 37 cm. In the second picture of Fig. 115, taken at 22.47 sec, the upper pin segment and two additional nodes (15 cm) of the lower segment have slumped. The picture has the appearance of an uneventful gravity collapse, except for fuel temperatures rising up to 3341°C. In Fig. 116, picture 1, taken at 23.98 sec, the fuel has heated up to 3791°C, and the fuel vapor pressure is able to disperse some fuel upwards. The last picture at 26.98 sec (2 sec after reactor shutdown) shows the upwards dispersed fuel stopped by the upper cladding blockage. This fuel is likely to fall towards the bottom as the test section cools off.

Figures 117, 118, and 119 illustrate the progression of slumping in the second SAS calculation (high heat loss) of the R4 test. Significantly, this case does not exhibit an upward dispersal of fuel, since fuel temperatures do not exceed 3420°C. Figure 120 shows the gravity collapse of the fuel, as well as the cladding disposition, in comparison with the post-transient radiograph.

The SAS calculations of fuel slumping exhibit a general gravity collapse with possible but unlikely upward fuel dispersal driven by fuel vapor pressure. The amount of dispersal is dependent on the magnitude of radial heat loss to the structure and is therefore somewhat uncertain.

6.4 Evaluation

The SAS posttest calculations of the R4 and R5 experiments have demonstrated that the SAS3A code is an adequate tool for the analysis of LMFBR loss-of-flow accidents, provided incoherent or parallel channel effects are not strong enough to change the time sequence. The timing of events can be closely calculated with SAS, beginning at any steady-state condition, evolving through coolant heatup, boiling incipience, voiding progression, flow reversal, cladding dryout, cladding heatup and melting, cladding motion, development of upper and lower cladding blockages, and fuel slumping. The timing uncertainty at boiling incipience was shown to be about 1 sec for the R-series tests. The

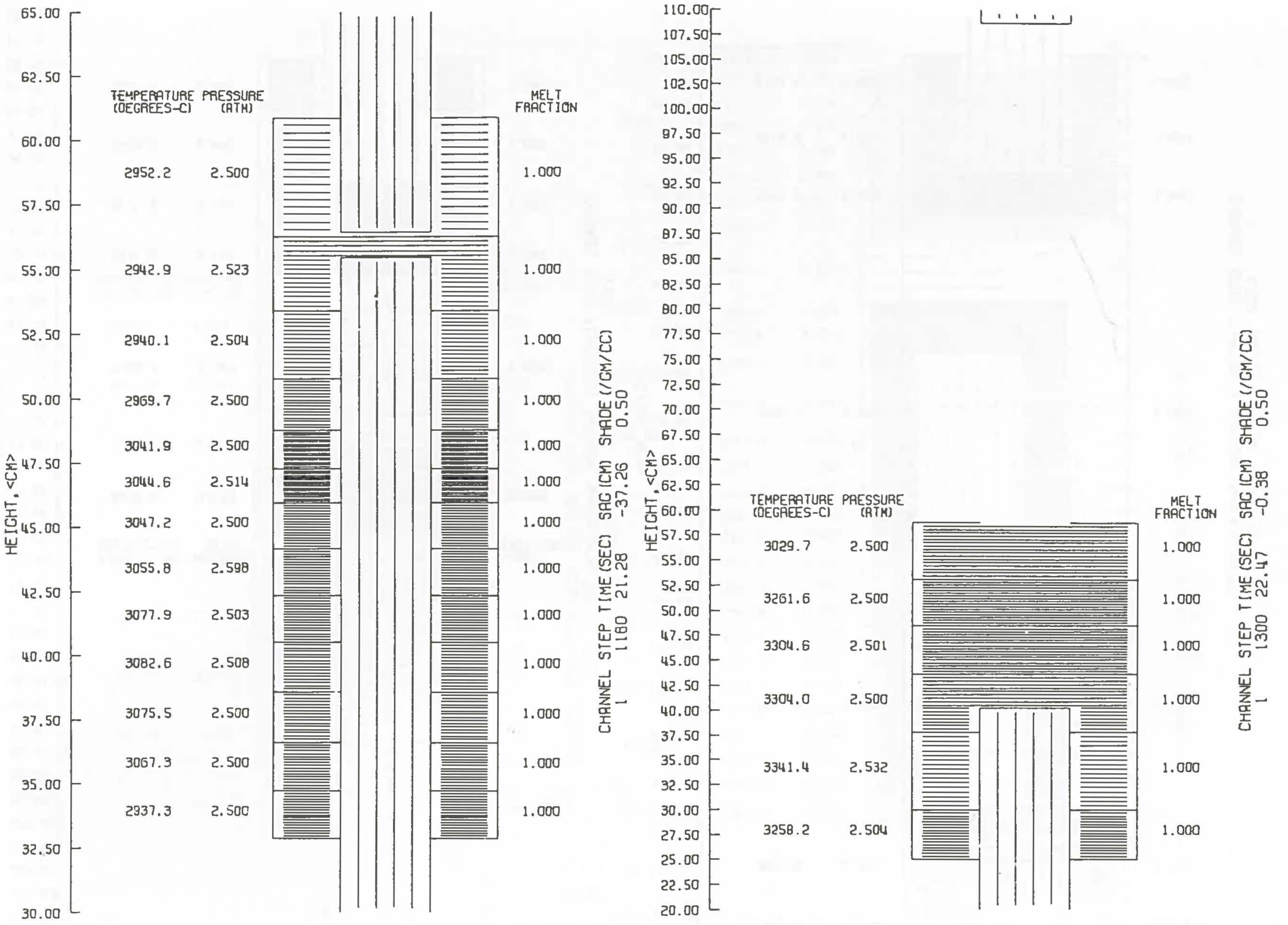

Fig. 115 R4 Case 1 Fuel Conditions at 21.3 and 22.5 s.

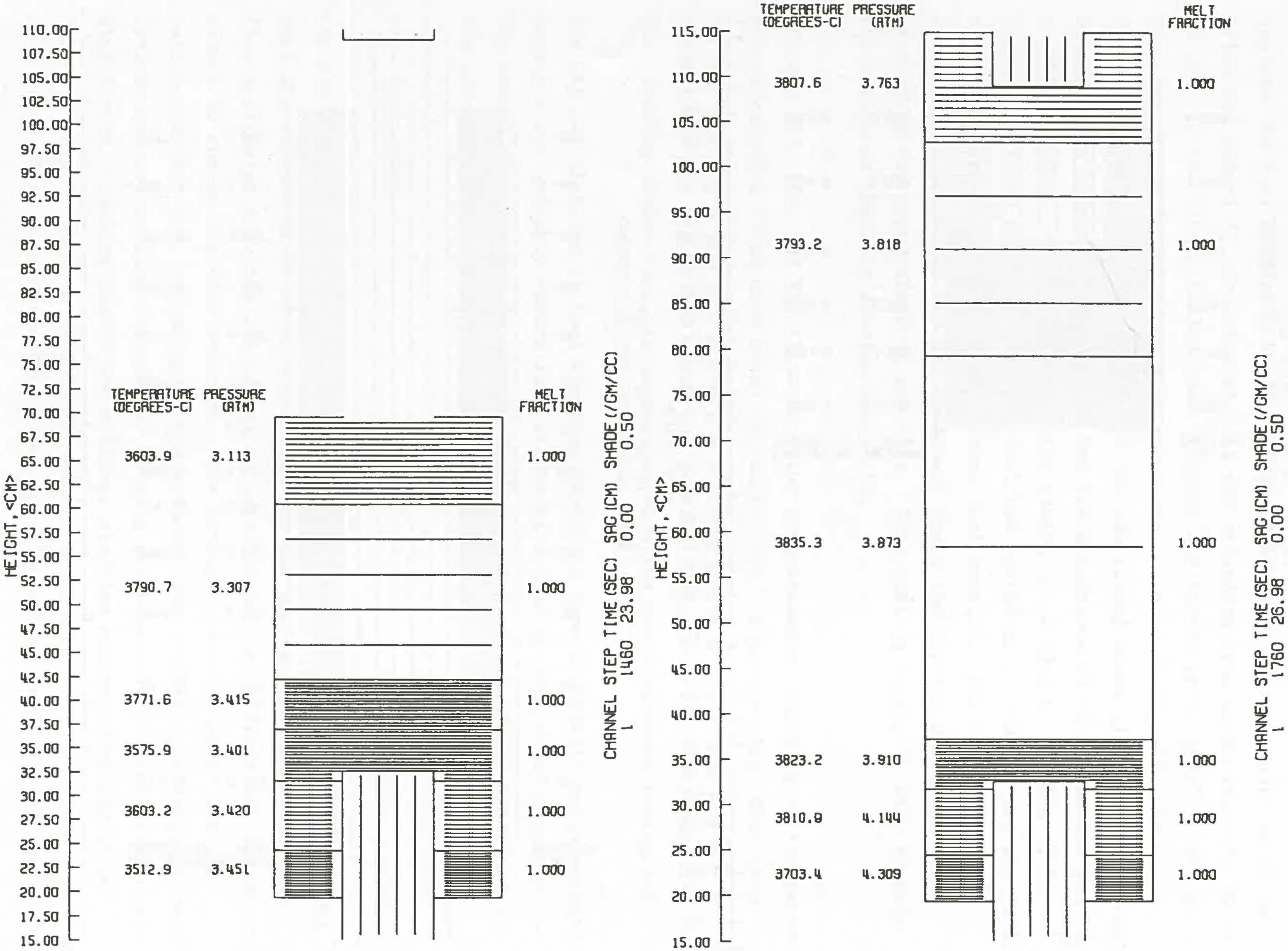

Fig. 116 R4 Case 1 Fuel Conditions at 24.0 and 27.0 s.

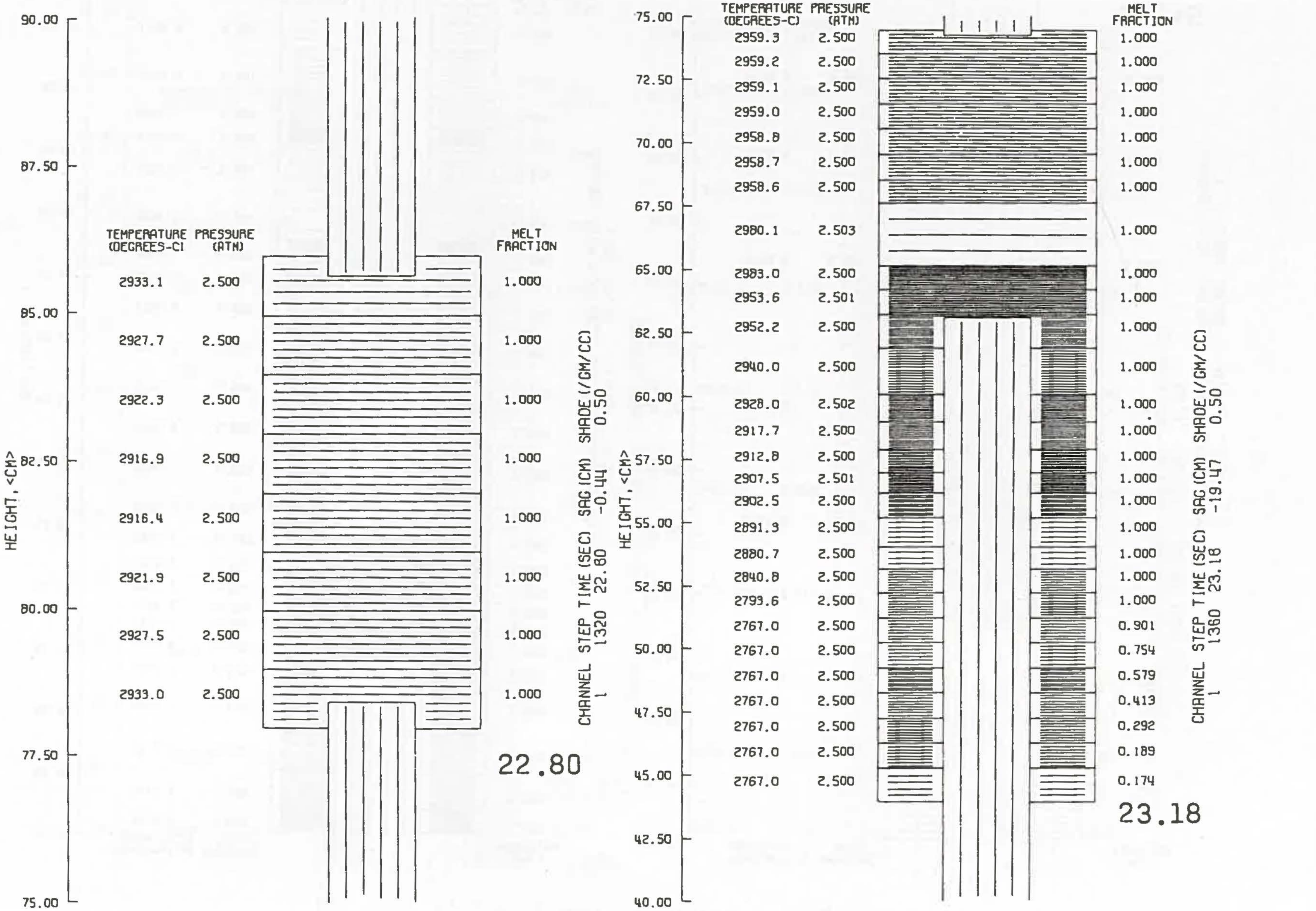

Fig. 117 R4 Case 2 Fuel Conditions at 22.8 and 23.2 s.

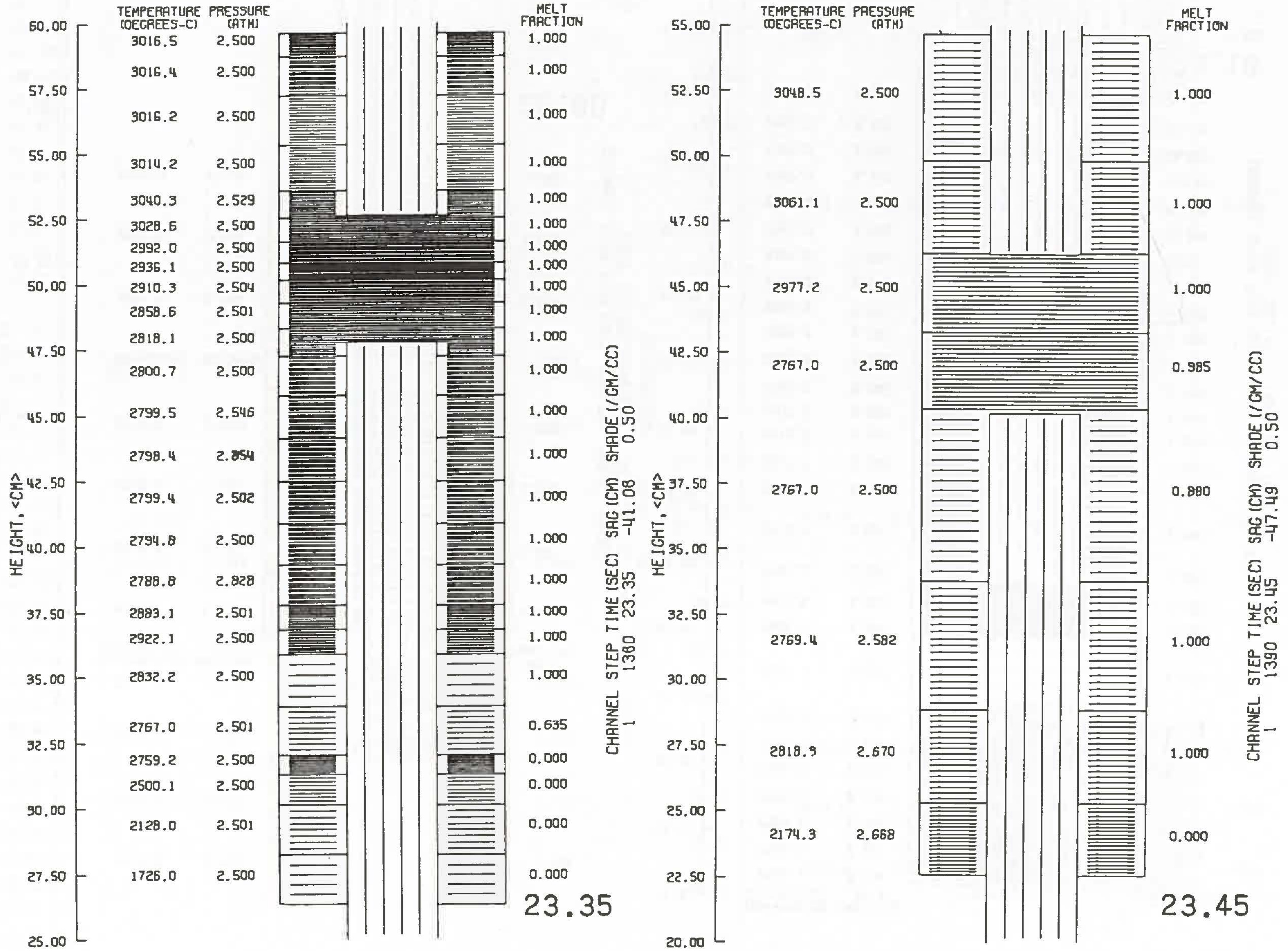

Fig. 118 R4 Case 2 Fuel Conditions at 23.35 and 23.45 s.

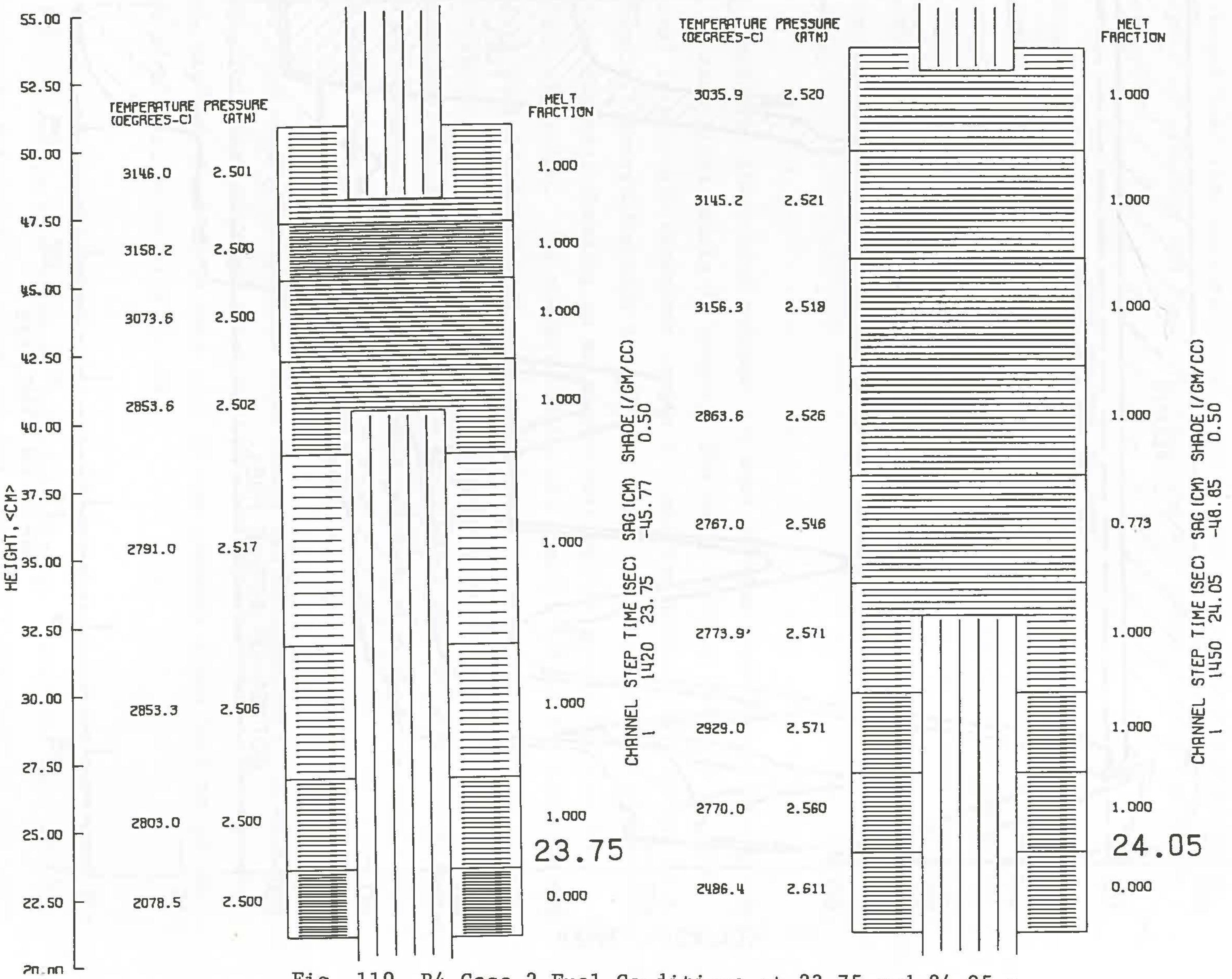

Fig. 119 R4 Case 2 Fuel Conditions at 23.75 and 24.05 s.

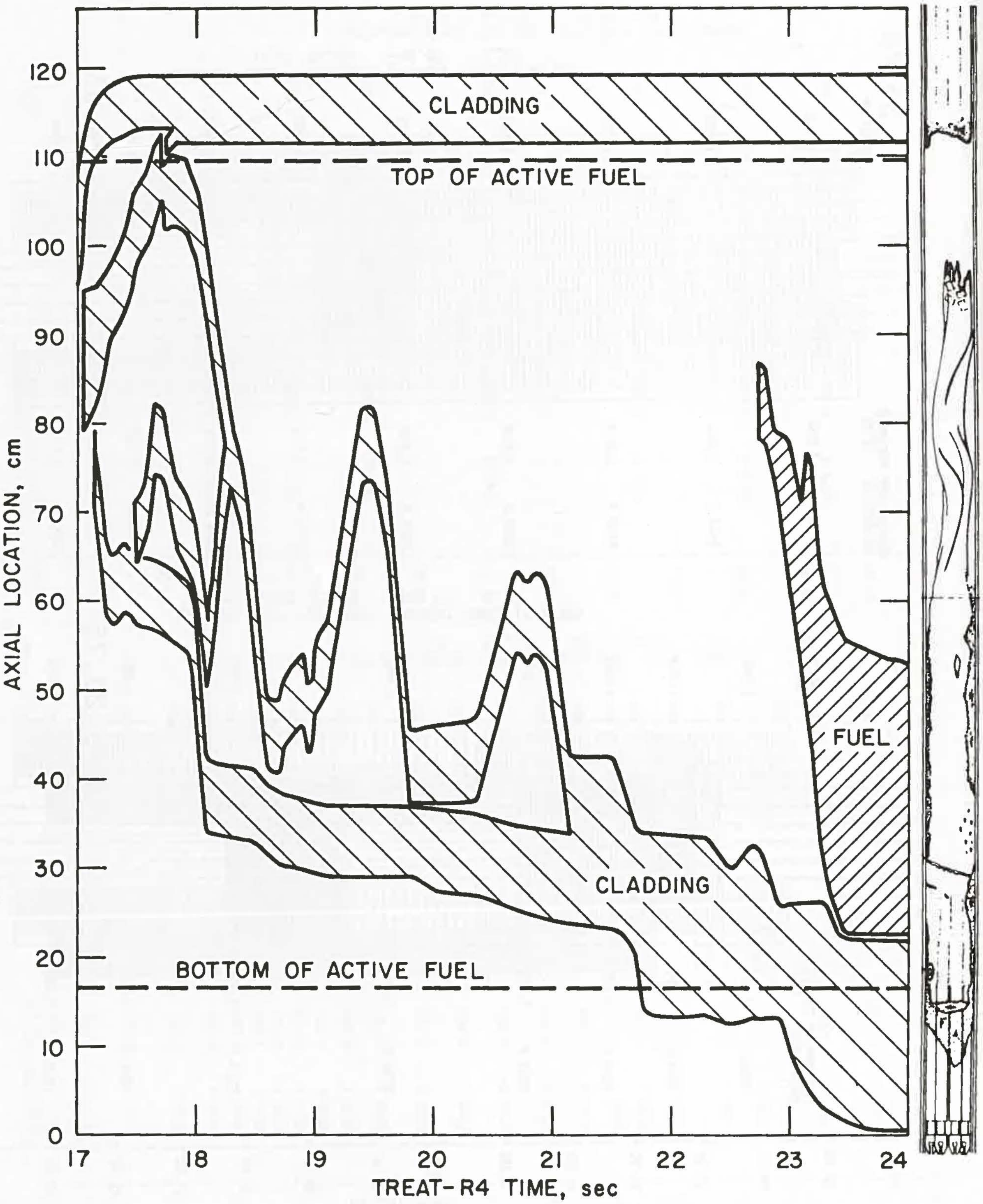

Fig. 120 R4 Case 2 Cladding and Fuel Motion Boundaries.

timing uncertainty grows to nearly 3 sec at beginning of fuel slumping. Since the R-series tests are essentially constant power tests (no reactivity feedback), the timing uncertainties result from energy input, thermal capacity, and radial heat loss uncertainties. The latter include convective energy transport of cladding and fuel after melting and emissivity of radiation transport.

The final disposition of the R-series test section as calculated by SAS was confirmed by posttest examinations (Section 4). The agreement is especially encouraging for the R5 test since it is most sensitive to total energy input. Experiment and SAS calculation agree that the fuel was at melting incipience when the reactor was shut down. The primary test objective, study of cladding relocation without fuel motion, was achieved with the help of the SAS pretest analysis.

This comparison study also pointed out some problem areas where more development of analytical models is needed. The early voiding phase up to flow reversal is strongly dependent on the thermal incoherence that exists in a pin bundle. Everything else being equal, the time between boiling inception and flow reversal (leading to extensive voiding) is longer for the less coherent situation. The characteristic pin concept of the SAS code implies complete radial coherence in a subassembly. The accuracy of SAS calculations is therefore expected to be higher for the more coherent physical situation. Nevertheless, sodium voiding in large pin bundles with sizable radial temperature gradients is likely to be even more coherent than 7-pin or single pin experiments show.[24]

On the other hand, the R-series experiments can be interpreted to mark points in time for local boiling, gross boiling, and flow reversal. The agreement of the SAS calculations is very good if one compares gross boiling in the tests with onset of boiling in SAS.

The comparison between experiments and SAS calculations looks very good for the period between flow reversal and clad melting. Inlet and exit coolant temperatures were shown to agree and the oscillatory character of the upper and lower liquid slugs were well represented by the SAS results. Clad failure in the tests appears as a flow excursion on the upper flowmeter caused by gas release from the pins. Failure of the flow tube (hex can) leads to a second flow excursion when the gas pressure in the outer annulus is relieved. SAS cannot presently handle the simultaneous presence of sodium vapor and non-condensible gas in a single bubble.

The actual presence of gas and the failure of the flow tube establish a situation that is physically different from the one modeled by SAS. The resulting discrepancies in sodium flow, coolant channel geometry, and radial heat loss propagate into the domain of cladding motion and fuel slumping. More basically, there exists an uncertainty with respect to the exact motion of molten cladding and fuel. It appears that the SAS cladding motion model calculates too much initial levitation and too big an upper blockage. In contrast, the posttest examination of the R5 experiment shows very little cladding material above the active fuel region.

The fuel motion (slumping) model of SAS is governed by a number of physical phenomena that strongly demand a series of calibrating experiments: criterion for slumping initiation, fuel particle sizes, shear stress acting on fuel particles due to fission gas, the relative importance of fission gas, sodium vapor, steel vapor and fuel vapor, radial heat transport (conduction, convection, and radiation are important) determining fuel vapor pressures and dispersal. All these phenomena are impossible to model from first principles.

Overall, the comparison of the posttest examinations for R4 and R5 with SAS calculated states at reactor shutdown is quite satisfactory.

7.0 DISCUSSION AND CONCLUSIONS

One significant outcome of the R4, R5, and OPERA tests is that most results are in quite good agreement with SAS code analysis of the test conditions. Features of SAS related to overall voiding, cladding motion, and to some extent fuel motion are substantiated in these results.

One aspect of the anticipated LMFBR behavior not simulated in these tests is the reactivity coupling to the experiment sequence. For the FTR case, incipient fuel motion would lead to significant power increase and not to the apparent slow melting and slumping observed in Test R4. However, for R4 test conditions, SAS predicts slumping collapse. In reactors larger than FTR (CRBR) sodium voiding and cladding motion would also lead to significant reactivity-feedback effects which influence the reactor-power behavior. For irradiated fuel, fission-product gases in fuel and plena would also play a role in development of the accident.

Some areas of required further examination were brought out by these test results.[25] The first is the early stages of voiding which show a different flow regime development (annular) than presently modeled in SAS (slug). The 7-pin data indicate that early void growth at low incipient superheat is best characterized as unidirectional annular flow. A transition from this flow regime to bi-directional annular flow occurs with inlet flow reversal, as a result of pressure increase in the voided region. The first flow regime is not described in present sodium boiling analysis. This flow regime was observed for ∿1 1/2 sec prior to inlet flow reversal with considerable voiding (∿20 cm) into the heated zone. In the recent SLSF 37-pin P3 Test,[27] this flow regime was observed for about 1 s. Upon inlet flow reversal, a bi-directional annular flow pattern developed which is that flow pattern described by SAS. This noted difference in initial flow regime did not affect the overall comparison between experiment and analysis in the integrated sequence of loss-of-flow events.

Boiling at low superheat and the existence of significant radial temperature gradients within the subassembly permit annular void growth with net positive flow. Increased voiding into the heated zone causes pressure increase leading to inlet flow reversal. The question whether inlet flow reversal would occur earlier or later with respect to the onset of boiling in a large subassembly when compared with the 7-pin test data has been examined.[24]

Figure 121 illustrates the large increase in void fraction that must take place with incremental voiding into the heated zone. This liquid flow diversion cannot be accomplished without pressure increase in the two-phase zone. Under such conditions, liquid could not be diverted from the two-phase region beyond the slug flow limit indicated in Fig. 121. This limit provides the minimum liquid film which must be left behind in the expanding two-phase zone. Figure 121 shows that this limit would be exceeded after only 5 cm of upstream voiding in a 217-pin subassembly. It is also indicated that this limit is not exceeded until ∿16 cm upstream voiding in a 7-pin test assembly. Thus, for loss-of-flow conditions, flow reversal should take place more rapidly in a large subassembly than the reference 7-pin test data, and present accident analysis codes should provide adequate description of the voiding sequence.

Another area requiring attention is the handling of plenum fission-gas release during the early voiding sequence.[9,26] The R8 test, which was later performed with pressurized pins, demonstrated that channel pressurization upon initial cladding failures substantially accelerated sodium voiding and altered the subsequent motion of molten cladding compared to SAS predictions, in which noncondensable gas effects in the channel were not handled. In that test, the inlet sodium slug was accelerated downward out of the core, and the sodium film dried out, cutting off sodium vapor streaming at the time of initial molten cladding motion. Under these test conditions the cladding drained; the planar upper cladding blockage of the type formed in R4 and R5 was not found, and the lower cladding blockage formed about 3s earlier.

With regard to molten cladding motion, the significance of R4 and R5 is the fact that vapor streaming caused molten cladding flooding which in turn resulted in formation of an upper cladding plug, in agreement with SAS analysis applied to the test conditions. Quantitative comparison with test results shows differences in the exact location and thickness of the plugs. They were found in the blanket pellet region and were about 3 mm thick, whereas the SAS calculations predicted the upper blockage would form higher in the

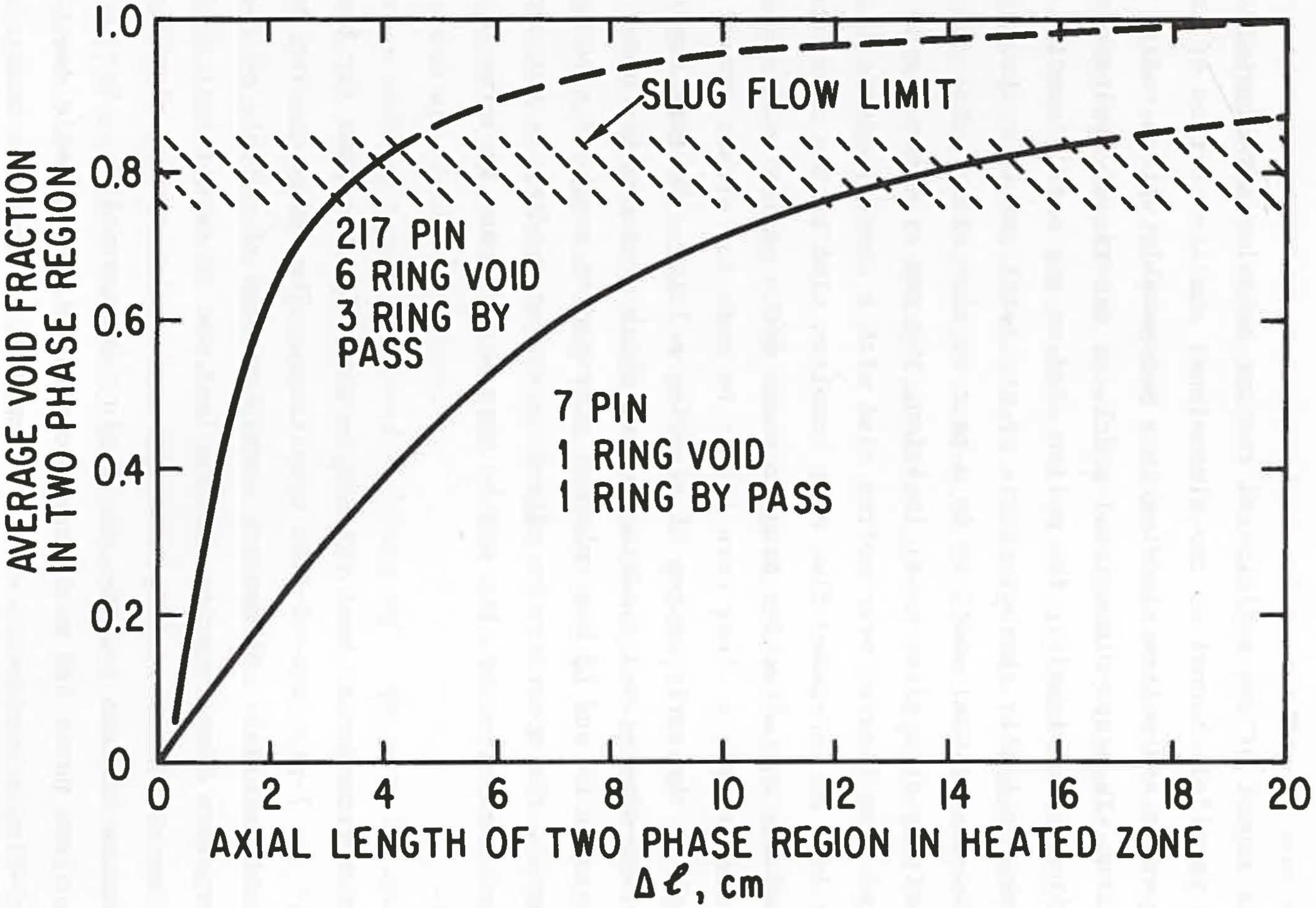

Fig. 121 Two-phase Void Fraction Required for Equal Pressure Gradient in Parallel Two-phase Flow with Liquid Bypass.

reflector-rod region with a thickness of about 7.5 cm (1 SAS node). The large calculated plug thickness was to a certain degree the consequence of the SAS axial node structure and the segment formalism of CLAZAS. This is currently being modified to allow for shorter upper blockages.

Another aspect of the anticipated reactor behavior not simulated in the tests is the parallel channel or two-dimensional characteristics of the behavior of sodium vapor and molten cladding in a subassembly with a radial power-to-flow variation. In a one-dimensional model, or experiment designed to behave nominally one-dimensionally, the molten clad at any axial location is influenced by a vapor velocity characteristic of the total gas flow through the channel. In a two-dimensional model or in a test section with radial nonuniformity in clad melting at a given axial location, the gas or vapor can be partially diverted from flowing over molten clad with a characteristic high friction factor into an increased flow over unmolten clad at the same axial location. This reduces the effective drag or shear force on the molten clad. Under these conditions, a clear case cannot be made for either upward relocation or draining in the early stages of cladding melting. In this regard, the nominally one-dimensional cladding motion which produced the upper cladding blockages in R4 and R5 was enhanced compared to expected subassembly conditions. In general, the noncoherence effect on sodium voiding is not expected to be large at nominal power, but may be more significant in terms of cladding motion.

The interpretation of test results is generally the same for both the single-pin R3[6] and 7-pin loss-of-flow conditions. The early voiding development is remarkably similar. Elementary considerations of effects of radial heat loss and structure heat capacity effects lead one to expect that differences between one and 7-pin test results (if any) would be more significant than differences between 7-, 19-, or 37-pin test assemblies. For large-pin bundles with uniform power SAS would seem to provide a reasonable description of loss-of-flow consequences with the previously mentioned exceptions.

It is recalled that one of the original test objectives was related to sodium reentry (hence, R-series) and potential fuel sodium interaction under loss-of-flow conditions. Again, voiding model development has shown sodium reentry to be unlikely under loss-of-flow conditions. Also, recent development in understanding fuel sodium interactions has led to the understanding that fuel and sodium are not likely to come in contact under these kind of test conditions and, that even limited contact will not lead to a coherent vapor explosion. Test R4 produced large quantities of molten fuel and molten steel, and no interaction was anticipated or observed.

In conclusion, this test series produced results consistent with both out-of-pile sodium voiding experiments and overall predictions of integrated accident analysis codes. The tests showed no major difficulties or differences in interpretation of 1- and 7-pin test data. Voiding data substantiated areas for analysis improvement in the early voiding flow pattern and subsequent effects of gas release upon cladding failure which may be significant in analysis of advanced reactors.

To summarize, the major findings from the R4 and R5 tests include the following:

1. Initial sodium superheat prior to boiling inception was negligible.
2. The initial stages of voiding showed a co-current annular flow regime rather than the slug flow modeled by SAS.
3. There was a consistent time lag of about 1 1/2 to 2 s from boiling inception to inlet flow reversal. After flow reversal, void growth proceeded as a slug interface.
4. Upstream voiding behavior showed a "chugging" type oscillation at about 3 Hz. The average void progression could be predicted by a simple heat-capacity model.
5. The cladding failures occurred after film dryout when the channels contained sodium vapor. Plenum gas release was benign for these tests which used nominally unpressurized pins. The oscillating inlet slug was not affected by gas release under these conditions; the gas was merely swept downstream.
6. The predicted upper cladding blockages were found in both R4 and R5. The blockage was complete for R4 but was incomplete for the early termination R5 test. In both tests, the blockages were located in the insulator pellet region, were thinner than predicted (∿3 mm), and were easily breeched by a 1.4 atm pressure differential.

7. Cladding draining followed formation of the upper blockage resulting in formation of a massive lower cladding blockage at the bottom of the active fuel region. Both the upper and lower blockages had formed prior to significant fuel melting for these test conditions.
8. With continued heating, declad stacks of fused pellets underwent melting. Downward motion of the melting fuel occurred due to both pellet stack buckling and draining of molten material from within the pellets. The draining occurred for a melt fraction greater than about 0.5.
9. Despite evidence of inter-mixing of molten fuel and steel, there was no indication of a fuel/steel thermal interaction.
10. No MFCI's occurred; sodium was prevented from reentring the core region initially by the escaping gas and vapor, and later by the blockage formations.
11. The general agreement between the R-series results and the SAS predictions was good. Areas of discripancy were relatively minor and resulted in further analytical study of such features as initial void growth, plenum gas release, molten cladding freezing, bundle coherency effects, and bundle size effects.

APPENDIX A
FUEL PIN DESIGN PARAMETERS

Fuel	UO_2
Uranium Enrichment	6 pins: 14% ± 1% ^{235}U in U (36.00 ± 0.15 inches) 1 pin: 20% ± 1% ^{235}U in U with last pellet at each end of column 14% ± 1% ^{235}U in U (36.00 ± 0.15 inches)
Fuel Pellet Diameter	0.1945 in. ± 0.0015 in.
Fuel Pellet Geometry	Dished Ends
Dish Depth	0.0035 in. ± 0.0015 in.
Fuel Column Length	36.00 in. ± 0.0015 in.
Fuel Pellet Density	14% ^{235}U in U: 9.945 g/cm^3 (nominal) 20% ^{235}U in U: 9.94 g/cm^3 (nominal)
Fuel Planar Smear Density	14% ^{235}U in U: 9.40 g/cm^3 ± 0.27 g/cm^3 20% ^{235}U in U: 9.39 g/cm^3 ± 0.27 g/cm^3
Fuel Weight	6 pins 14% ^{235}U in U: 172.7 g ± 3.2 g 1 pin 20% ^{235}U in U with 2 pellets 14% ^{235}U in U: 172.7 g ± 3.2 g
Natural UO_2-Column Total Length	1.60 in. ± 0.08 in.
Reflector Material	Inconel 600
Reflector Diameter	0.1895 in. ± 0.005 in.
Upper Reflector Length	5.700 in. ± 0.005 in.
Lower Reflector Length	5.700 in. ± 0.005 in.
Total Reflector Volume	5.27 cm^3 (nominal)
Cladding Material	316 SS
Cladding Condition	20% ± 5% cold work
Cladding Dimensions	0.230 in. ± 0.001 in. OD x 0.200 in. ± 0.001 in. ID

APPENDIX A (Contd.)

End Cap Material	316 SS
End Cap Condition	20% ± 5% cold work
Wire Wrap Material	316 SS
Wire Wrap Condition	0-40% cold work
Wire Wrap Diameter	0.032 in. ± 0.0005 in. on 14% enriched pins 0.054 in. ± 0.0005 in. on 20% enriched pins
Plenum Spring Material	302 SS
Gas Plenum Volume	18.67 cm^3

APPENDIX B

SEVEN-PIN BUNDLE DESIGN PARAMETERS

Length of Hexagonal Can	8 ft x 11 5/16 in.
Wall Thickness of Hexagonal Can	0.020 in.
Hexagonal Cross Section Across Inside Flats	0.796 in.
Hexagonal Cross Section Across Inside Sharps	0.922 in.
Total Cross Section Area (Inside Can)	0.552 in.^{2}
Total Cross Section Area (Fuel Pins)	0.291 in.^{2}
Total Cross Section Area (Wire Wrap)	0.0071 in.^{2}
Total Cross Section Area (Filler Wire)	0.018 in.^{2}
Coolant Flow Area	0.236 in.^{2}
Wetted Perimeter - Can	2.766 in.
Wetted Perimeter - Pins	5.058 in.
Wetted Perimeter - Wire Wrap	0.773 in.
Wetted Perimeter - Filler Wire	1.169 in.
Hydraulic Diameter	0.097 in.
Coolant/Bundle Area Ratio	0.428
Coolant/Pin Area Ratio	0.811
Coolant/(Coolant and Pin) Area Ratio	0.448
Fuel-coolant Mass Ratio (Mass Fuel/Mass Coolant)	11.8
Fuel-coolant Volume Ratio (Volume Fuel)/(Volume Coolant)	0.95
Structural Material	Type 316 SS
Gas in Tanks	He
Gas in Secondary Housing	N_2
Valve Operating Gas	N_2
Volume of Sodium	7 ft^3

APPENDIX C

R4 DATA PLOTS

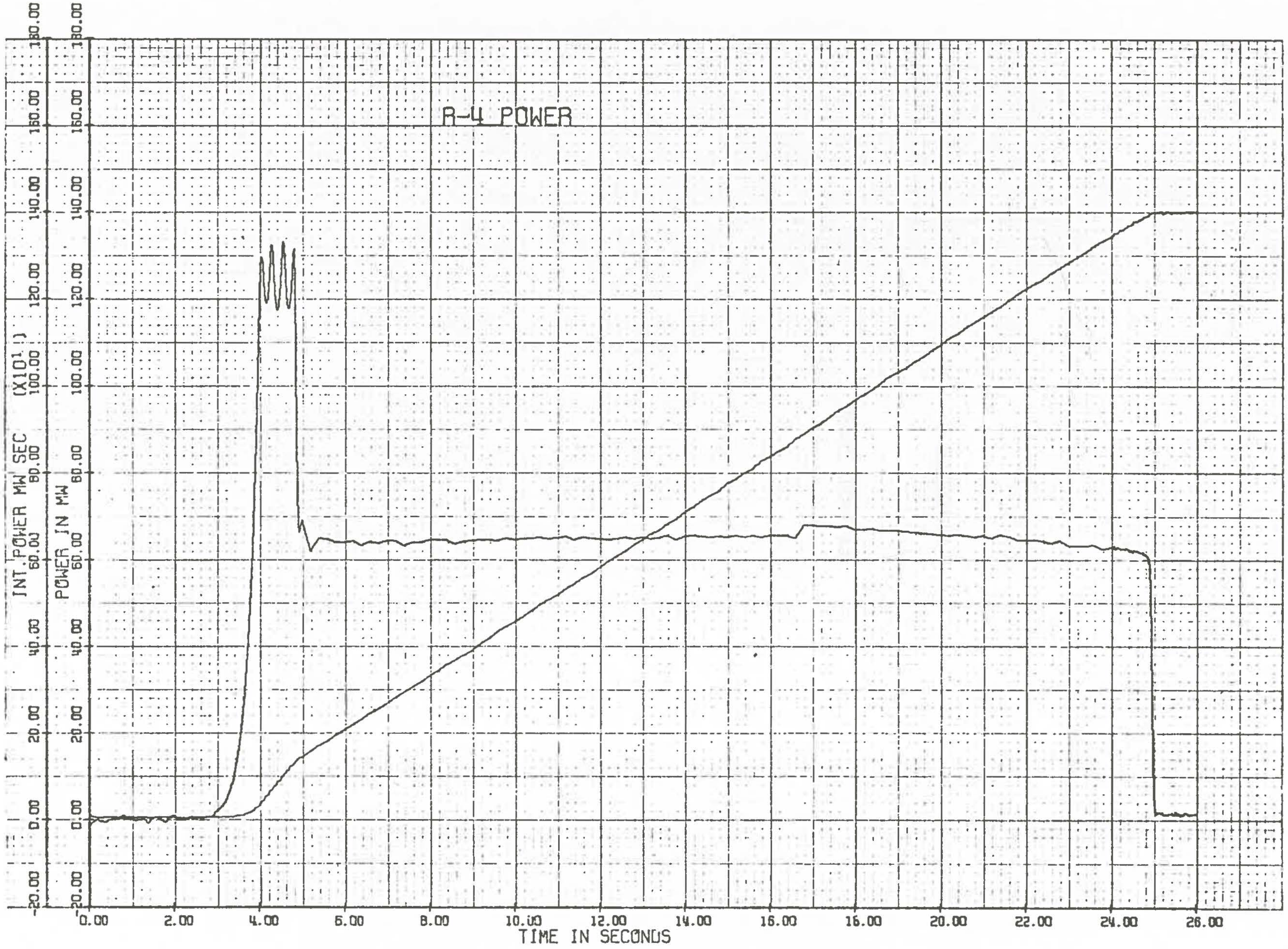

Fig. C1 R4 TREAT Power and Integrated Power.

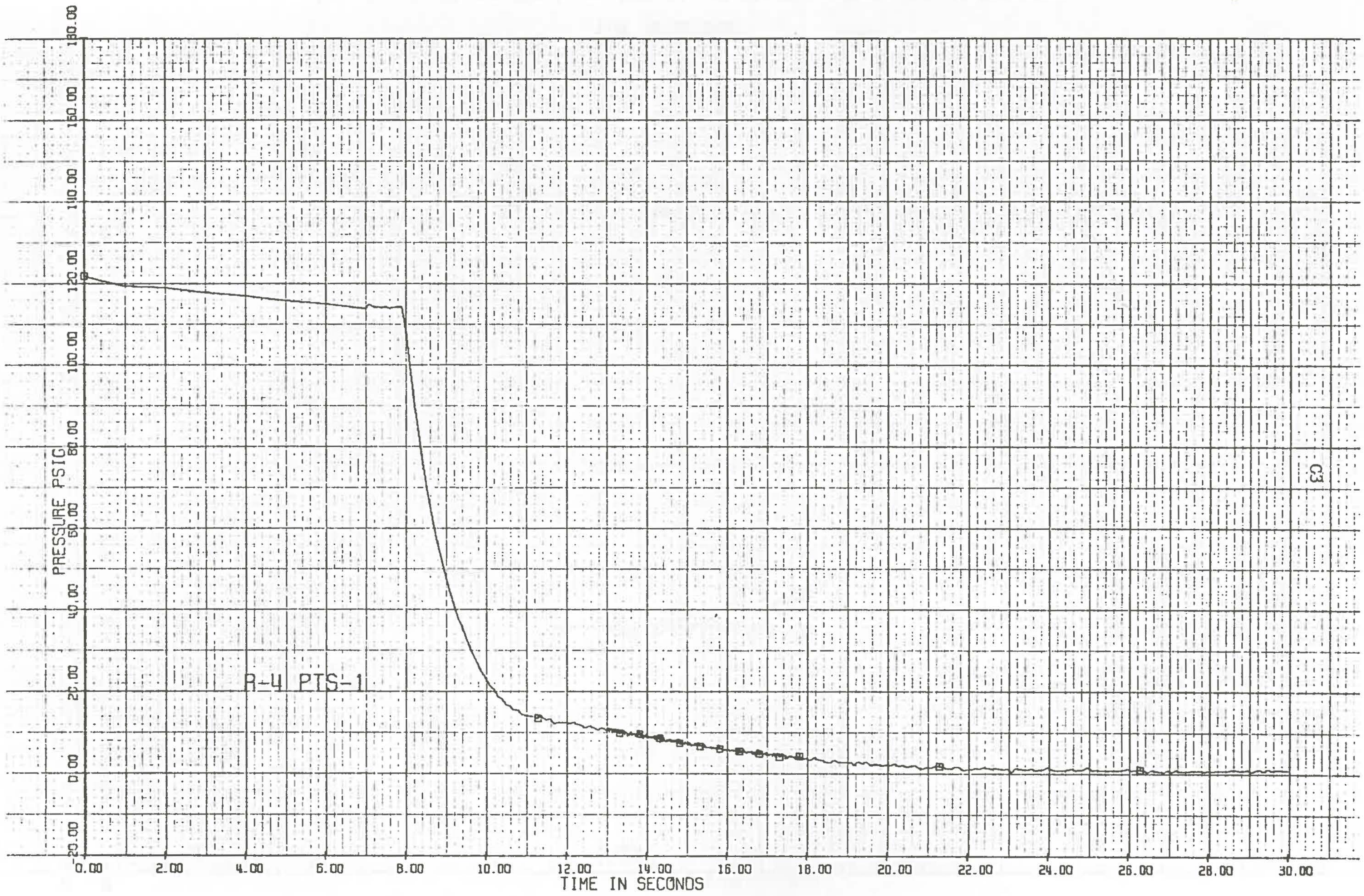

Fig. C2 R4 Supply Tank Pressure.

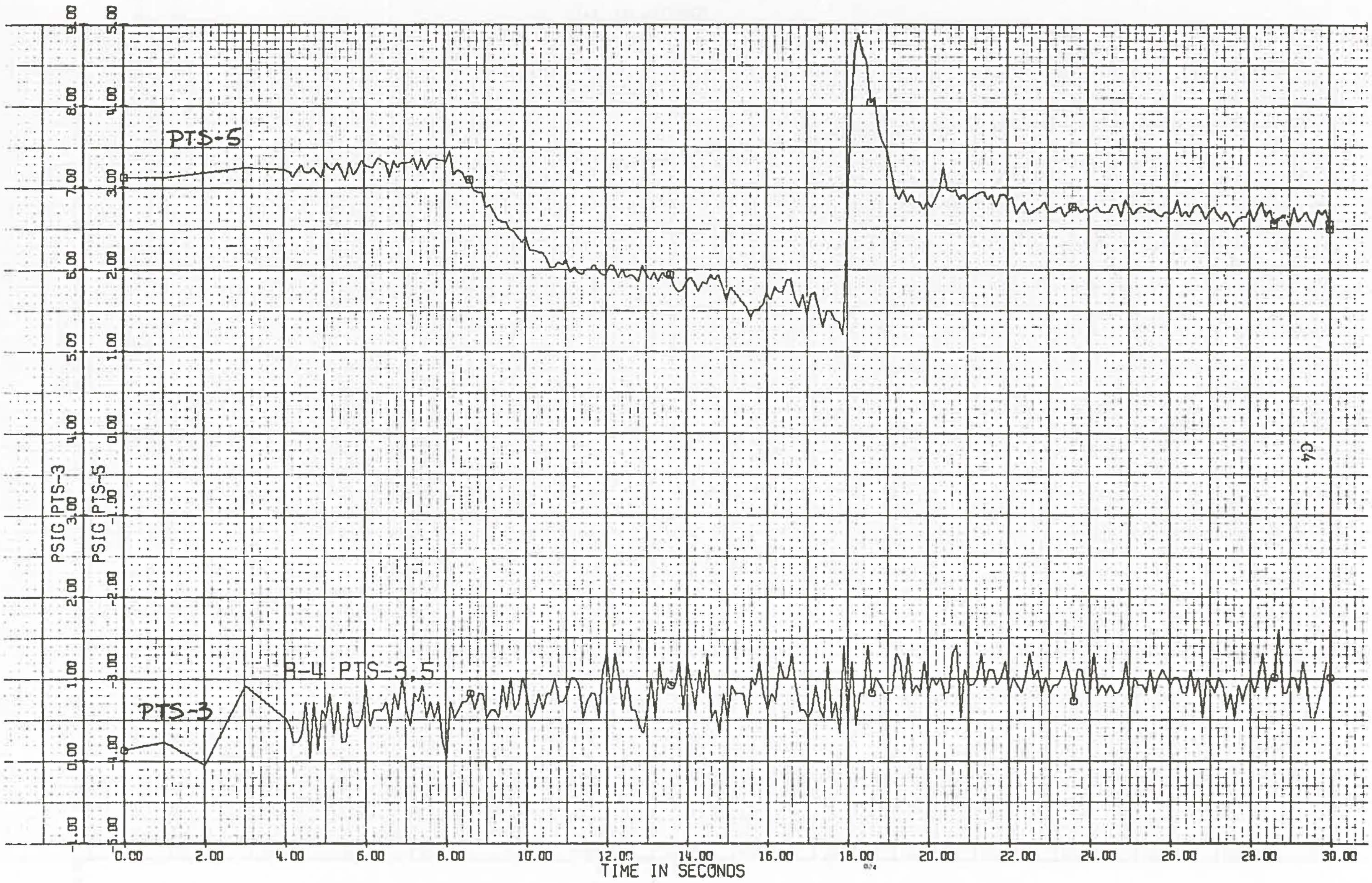

Fig. C3 R4 Plenum Simulator (PTS-5) and Discharge Tank (PTS-3) Pressure.

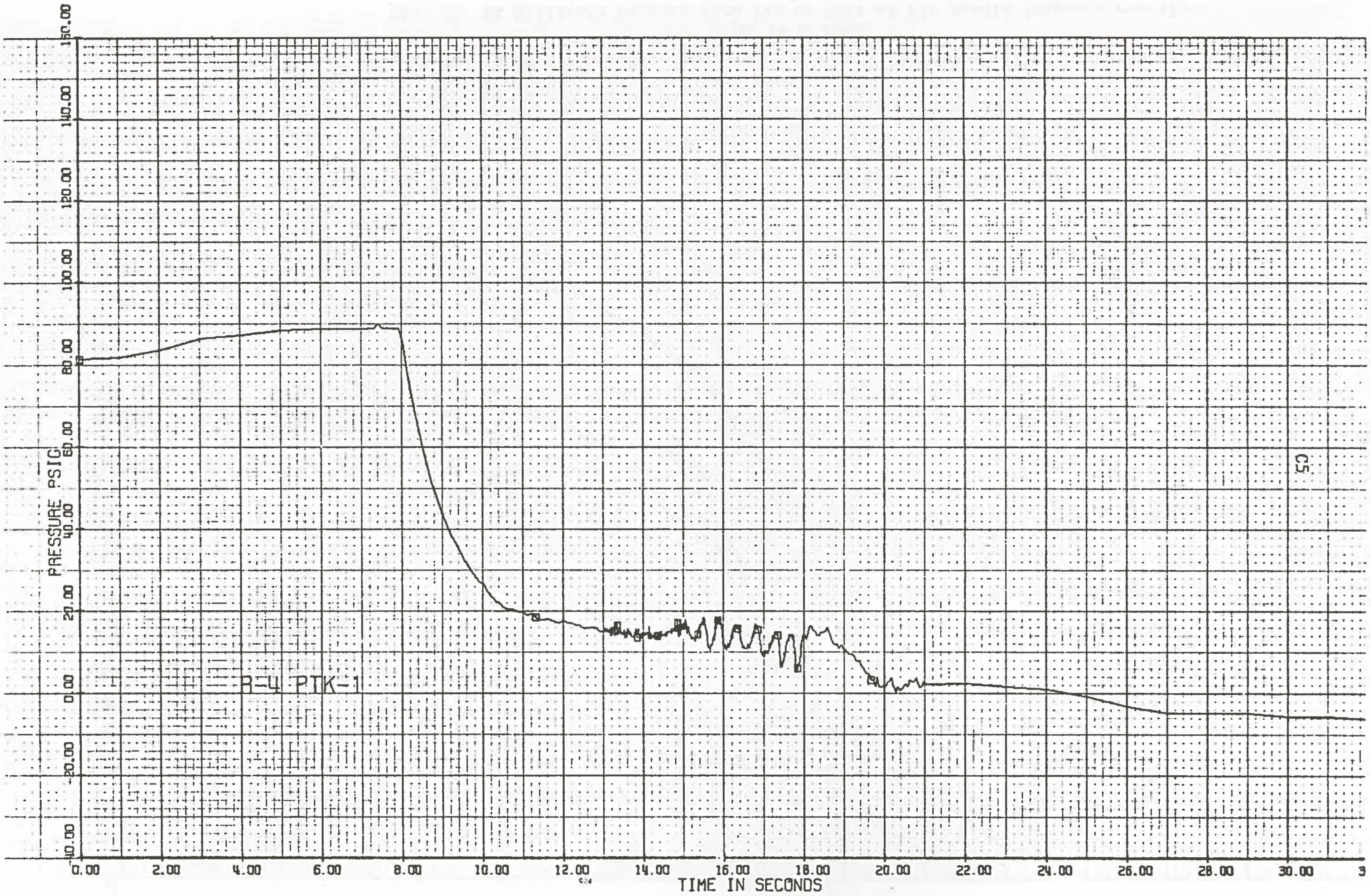

Fig. C4 R4 Pressure at Entrance to Pin Bundle.

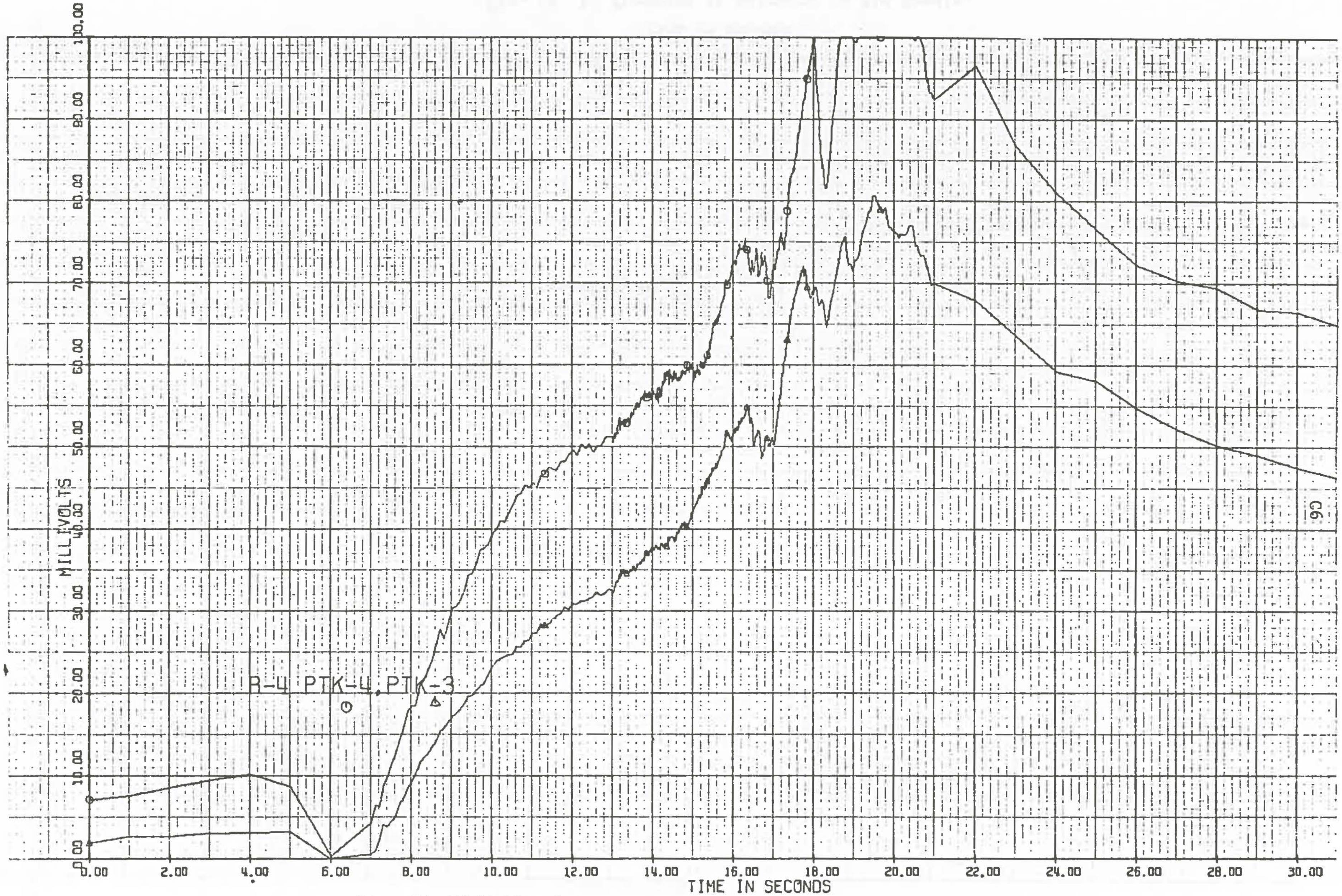

Fig. C5 R4 Millivolt Signals from PTs at Exit of Pin Bundle (Signals contain large transient temperature effect).

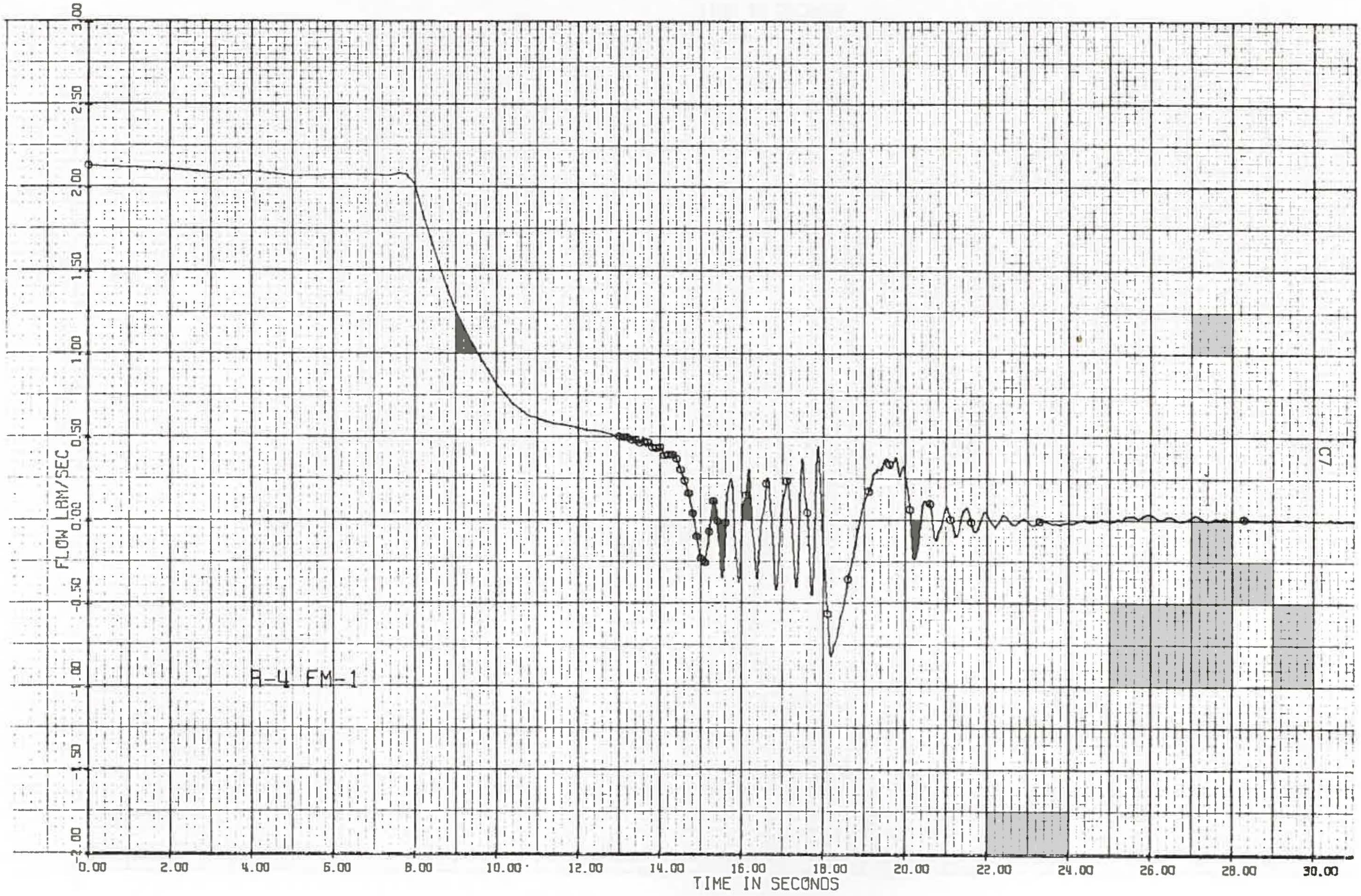

Fig. C6 R4 Sodium Inlet Flow Rate.

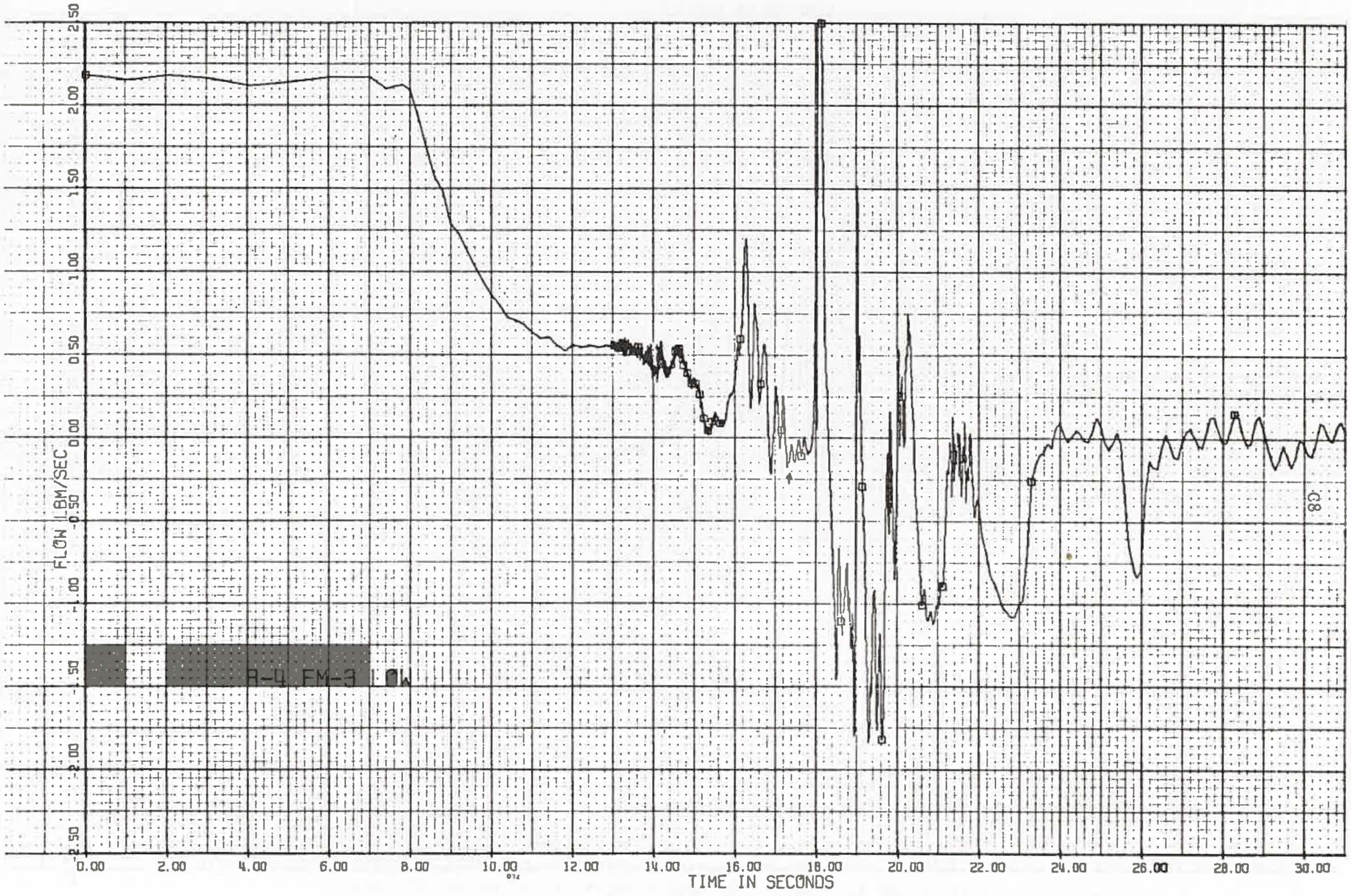

Fig. C7 R4 Sodium Exit Flow Rate.

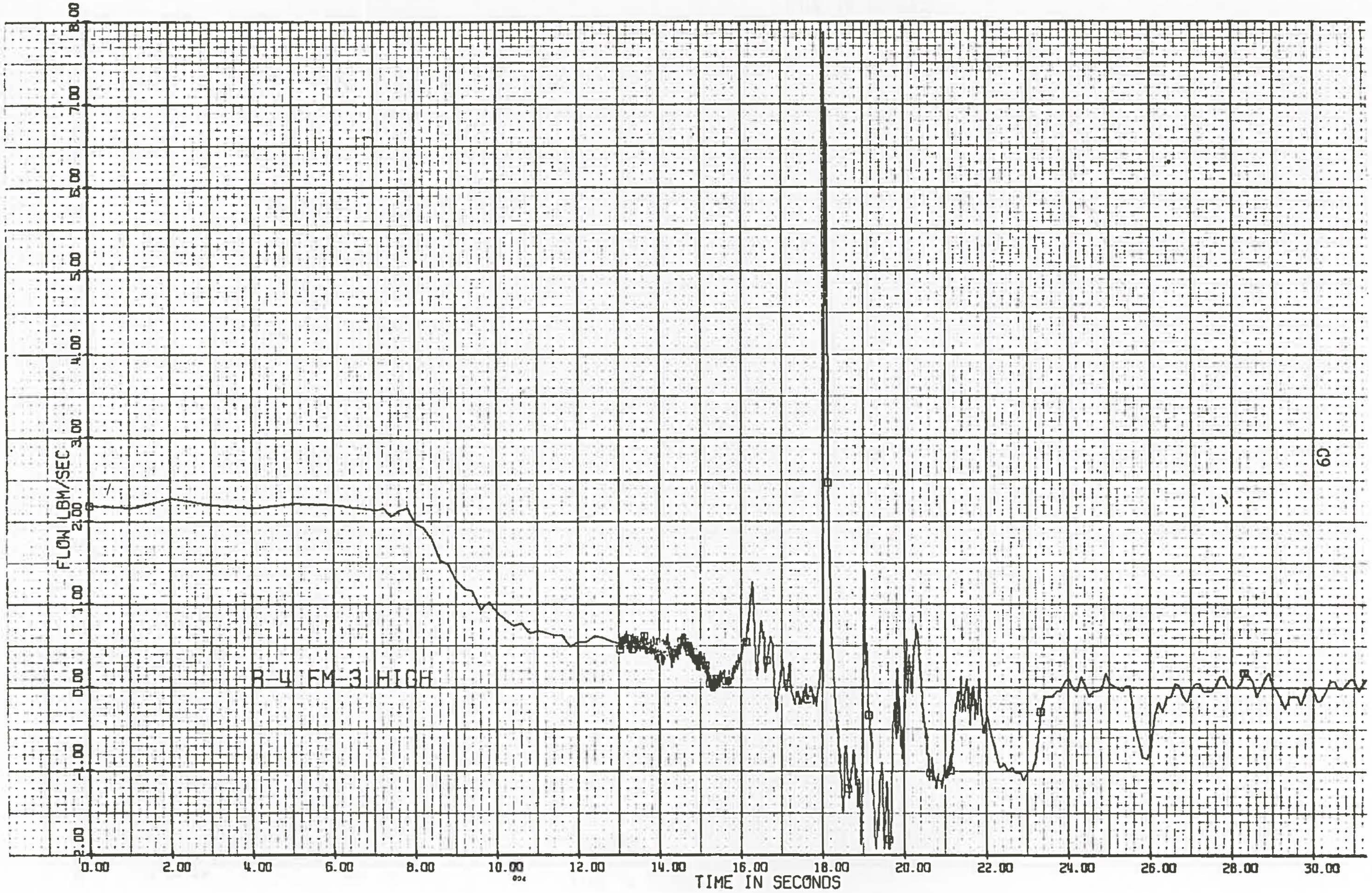

Fig. C8 R4 Sodium Exist Flow Rate on Compressed Scale.

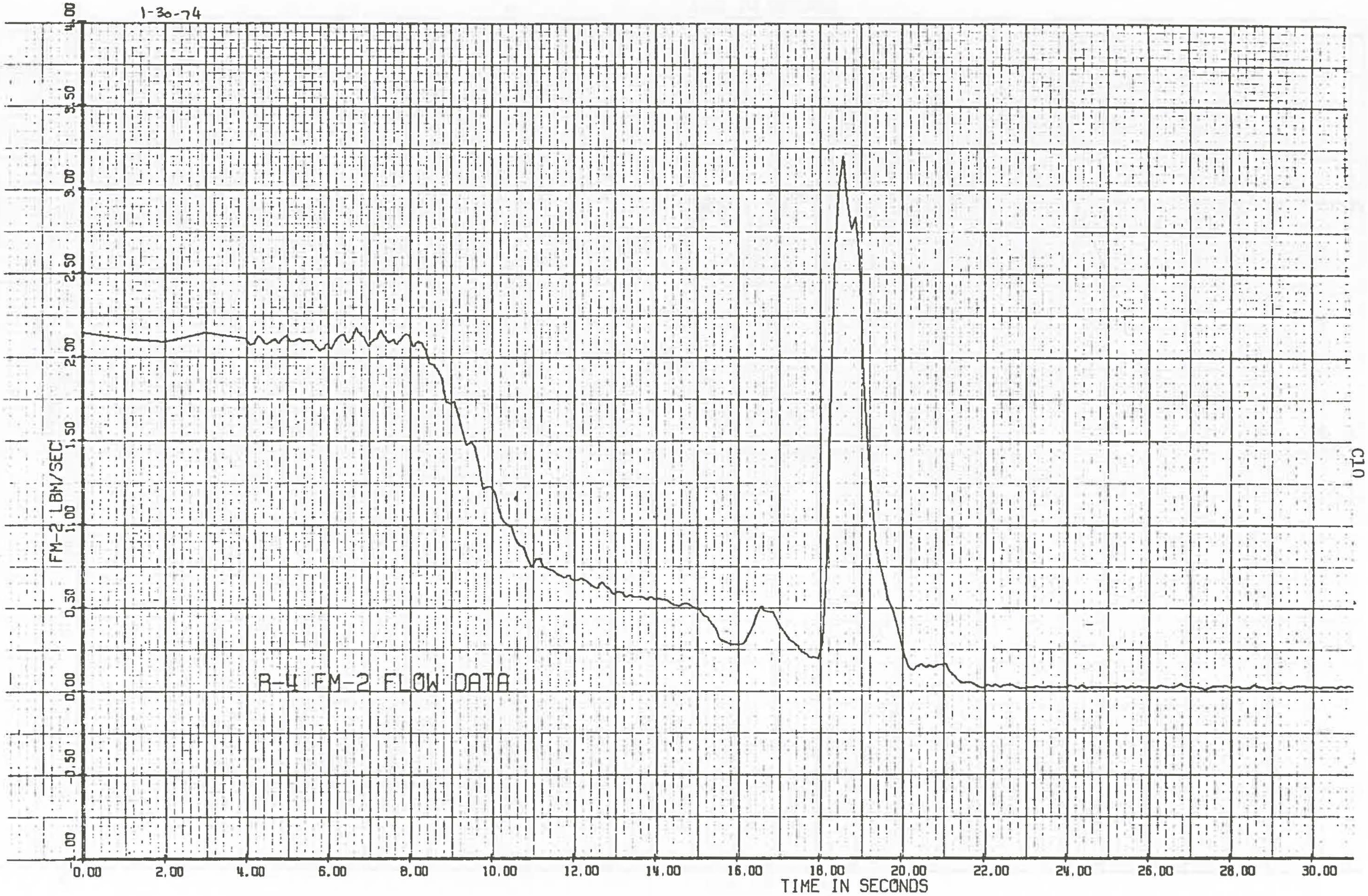

Fig. C9 R4 Plenum Simulator Discharge Flow Rate.

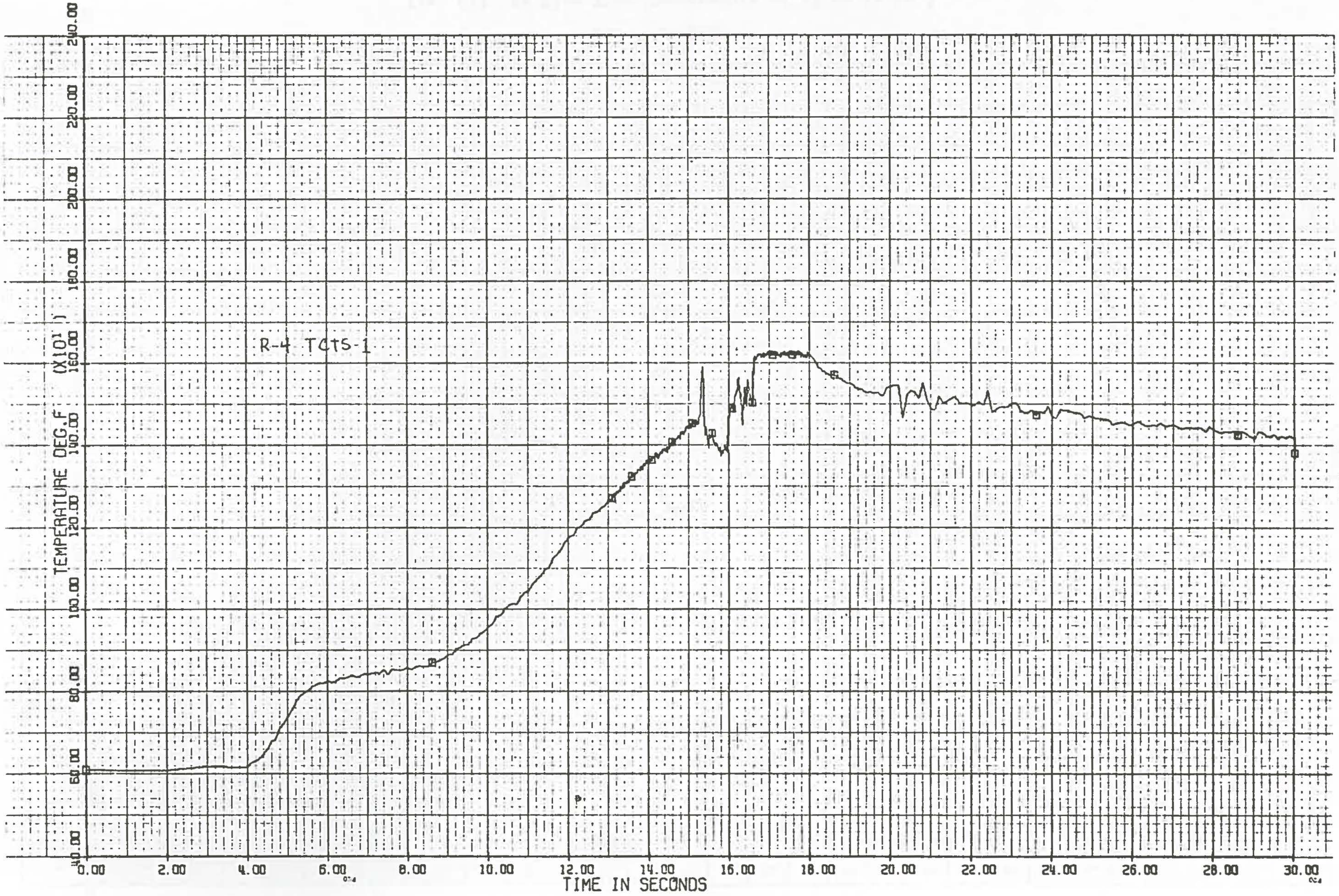

Fig. C10 R4 Flow Tube Temperature 30 cm (12 in.) Above Top of Active Fuel.

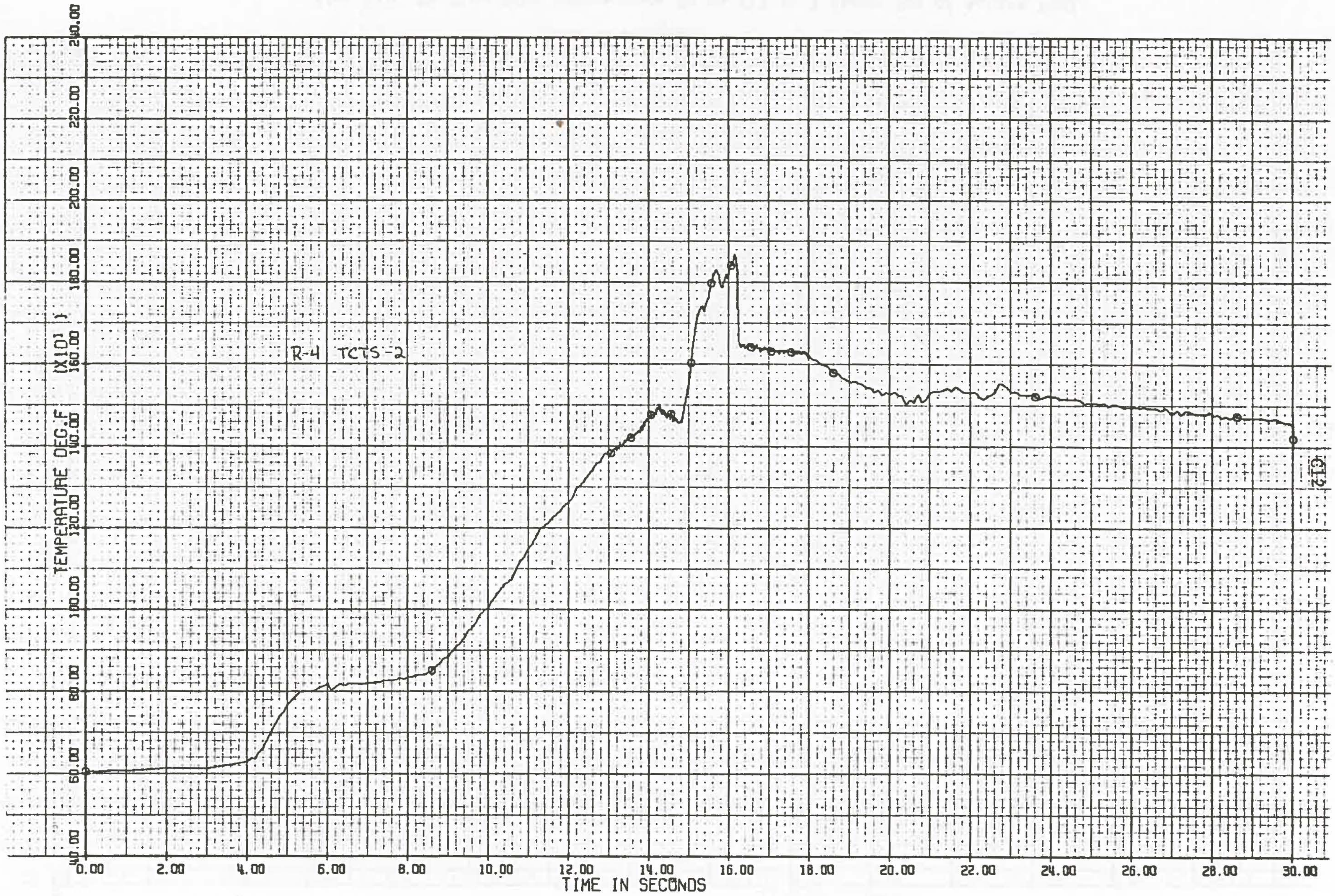

Fig. C11 R4 Flow Tube Temperature at 15 cm (6 in.)

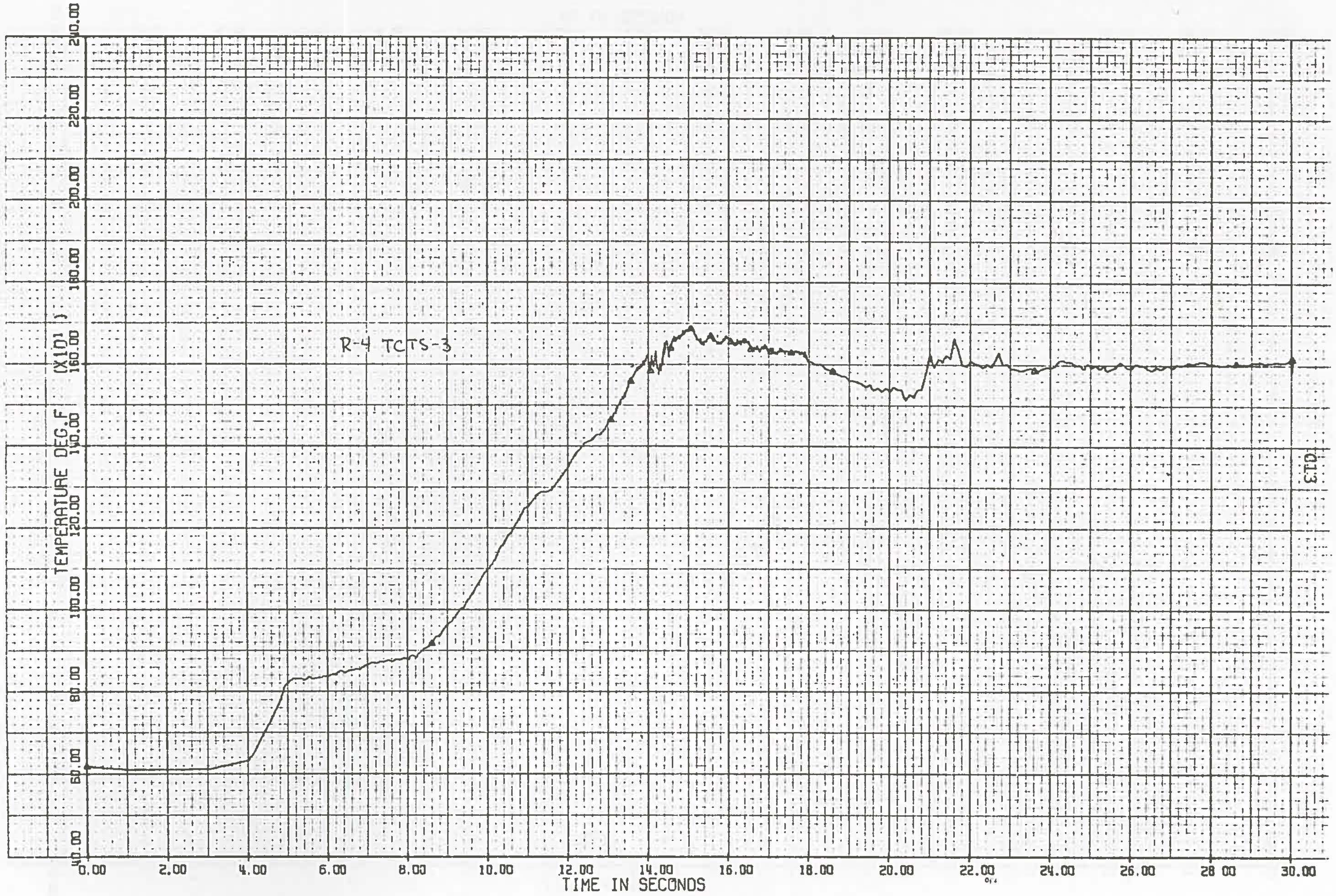

Fig. C12 R4 Flow Tube Temperature at 7.5 cm (3 in.)

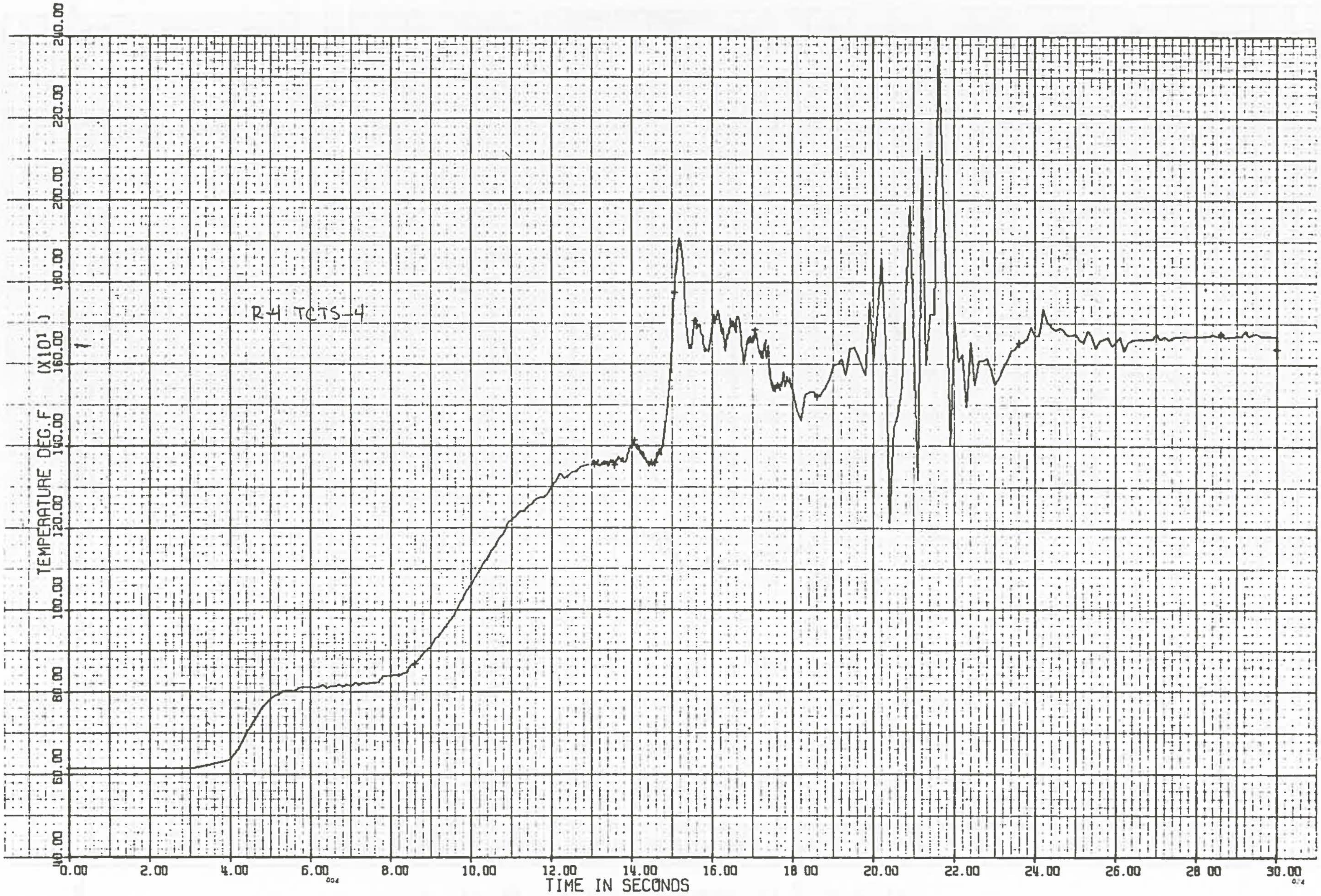

Fig. C13 R4 Flow Tube Temperature at 2.5 cm (1 in.)

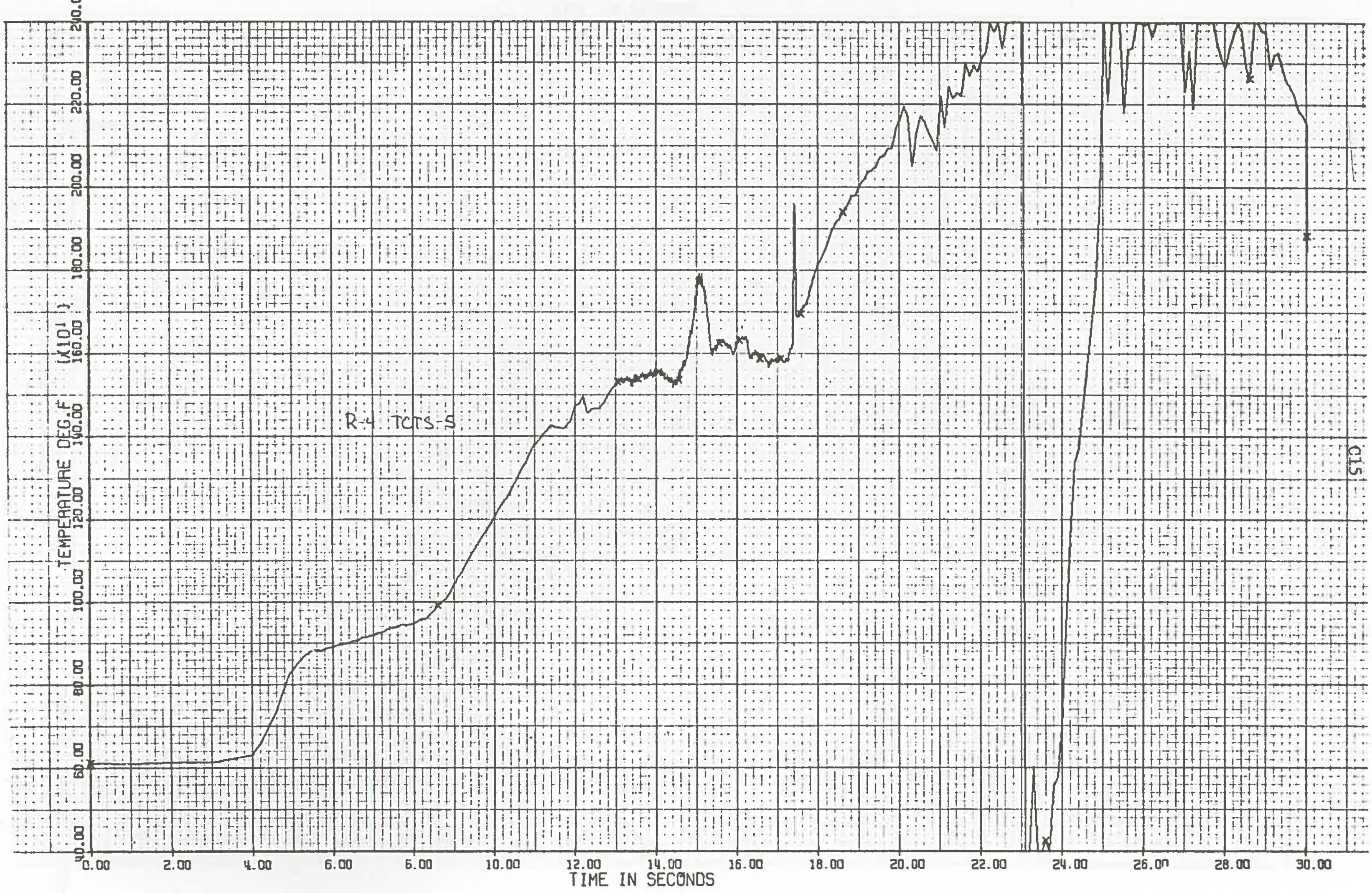

Fig. C14 R4 Flow Tube Temperature at Top of Active Fuel, 0 cm.

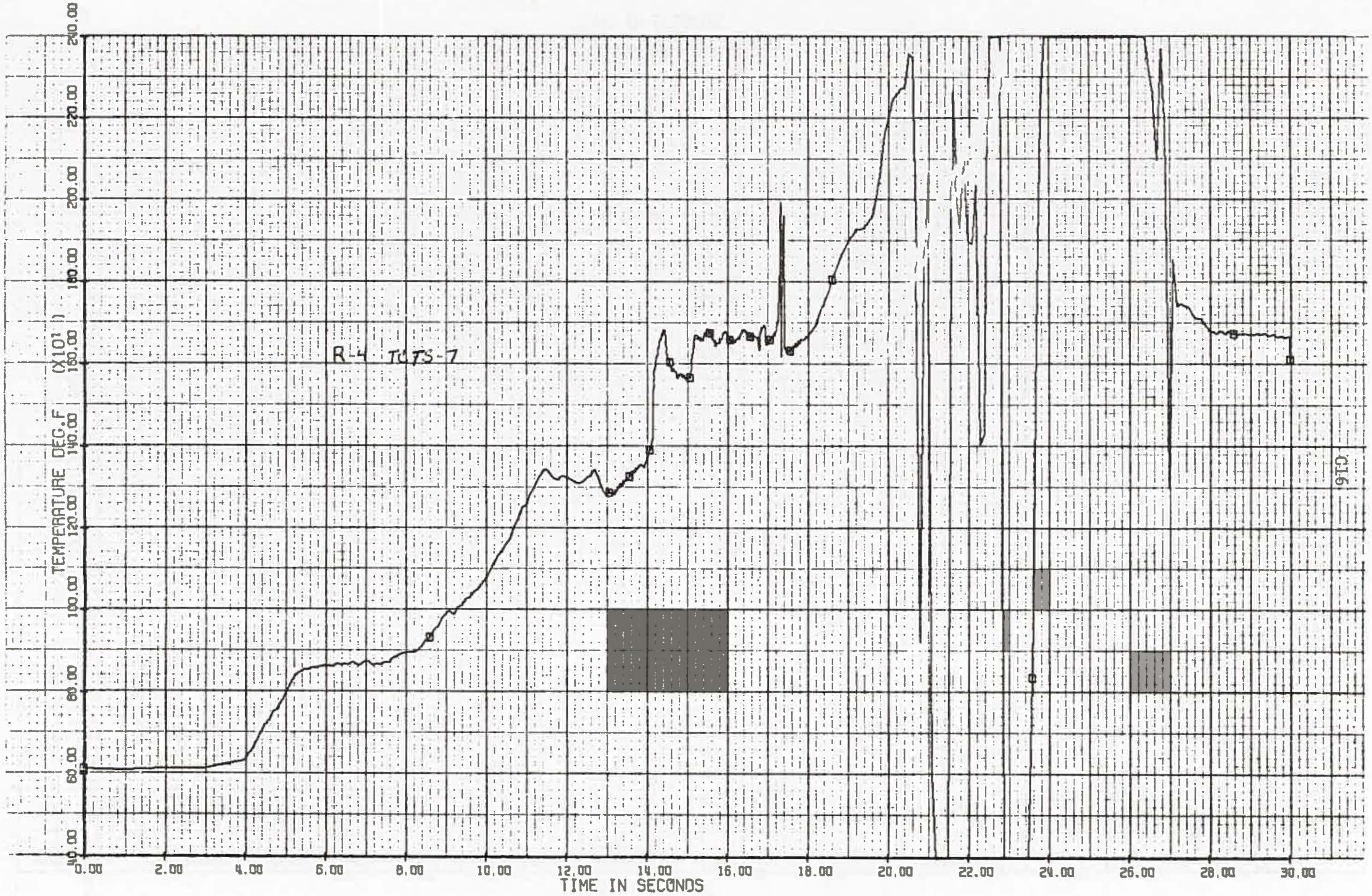

Fig. C15 R4 Flow Tube Temperature at -75 cm (-3 in.)

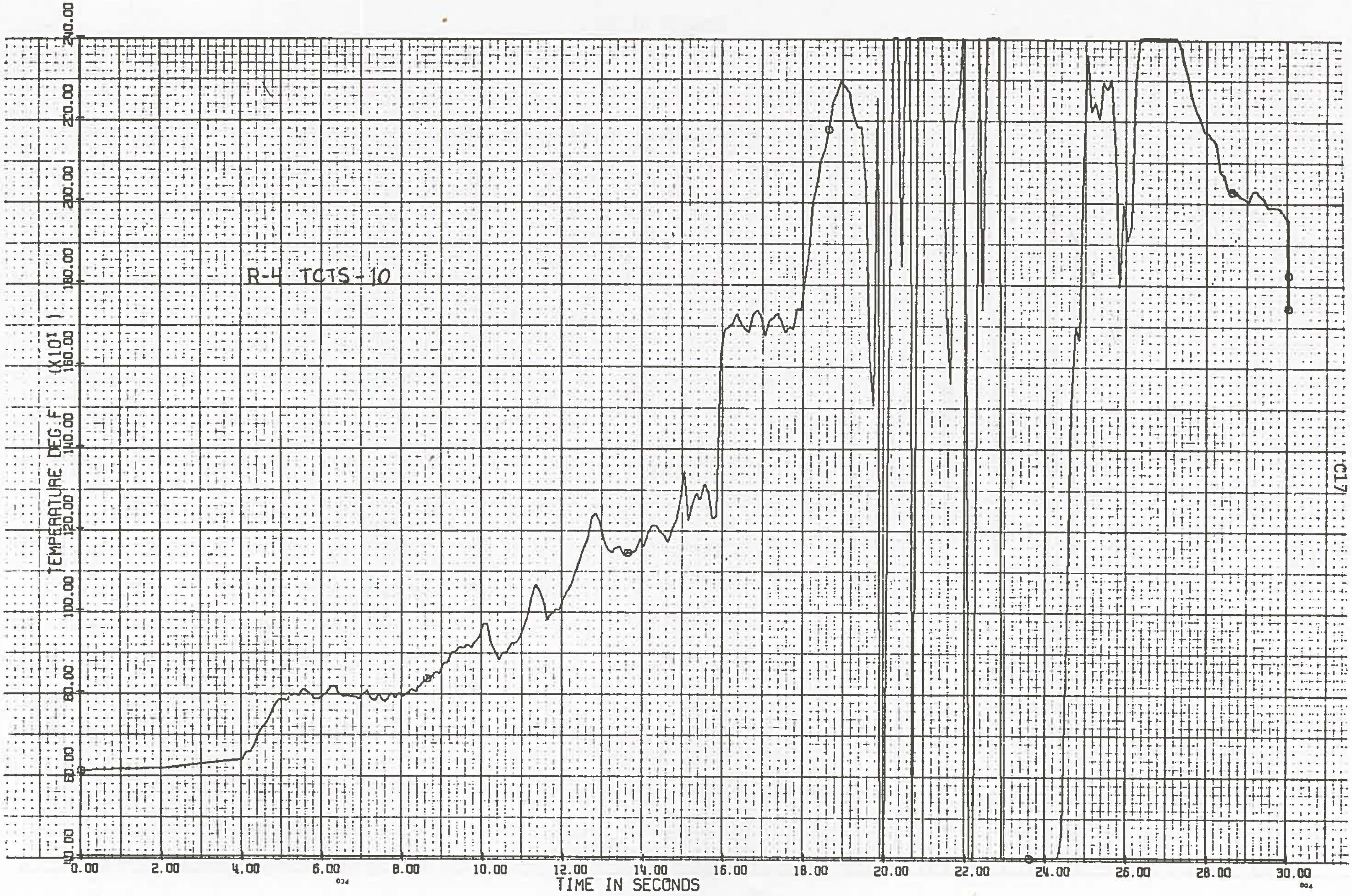

Fig. C16 Flow Tube Temperature at Active Fuel Midplane, -45 cm (-18 in.).

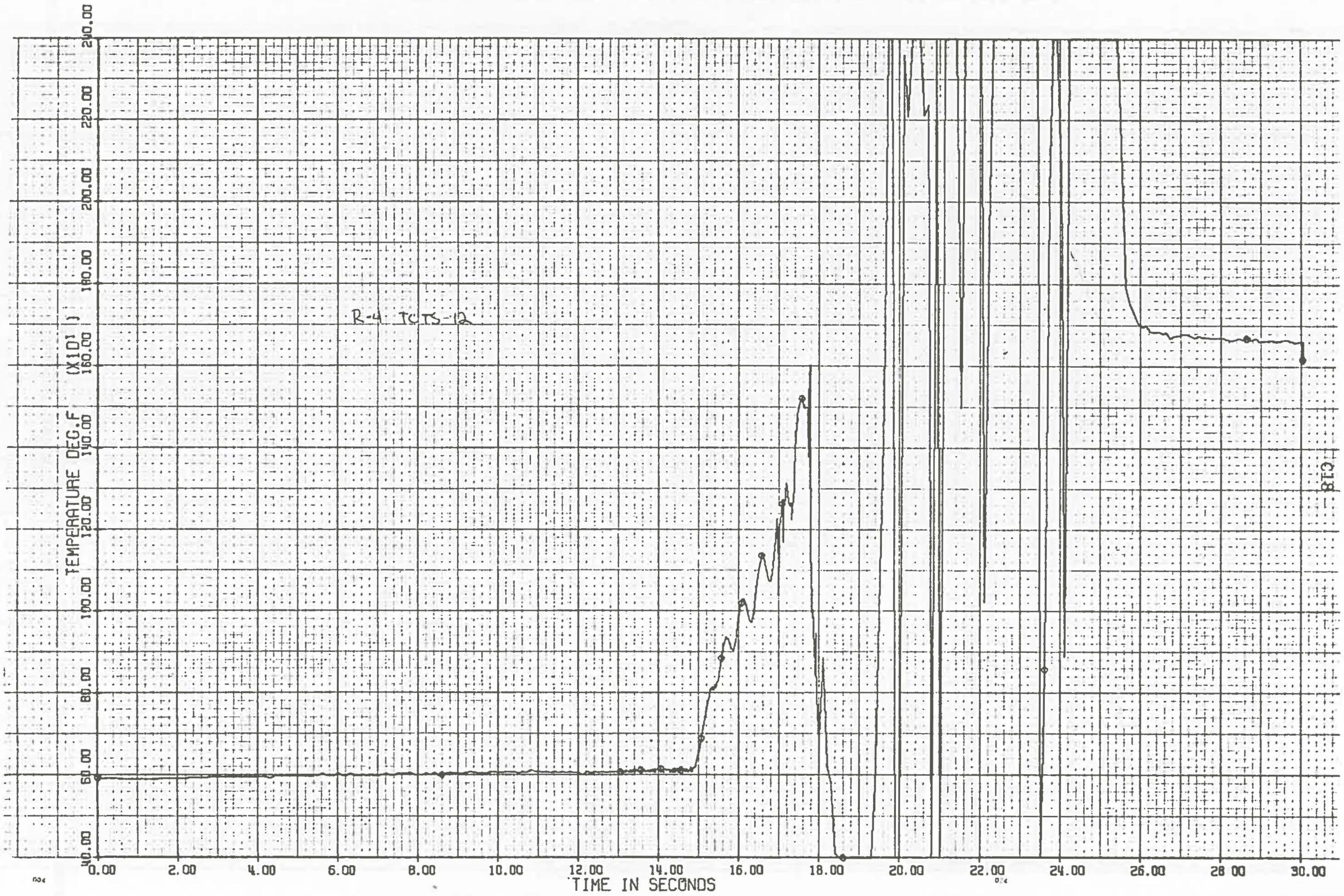

Fig. C17 R4 Flow Tube Temperature at Entrance to Active Fuel Region, -91 cm (-36 in.).

APPENDIX D

R5 DATA PLOTS

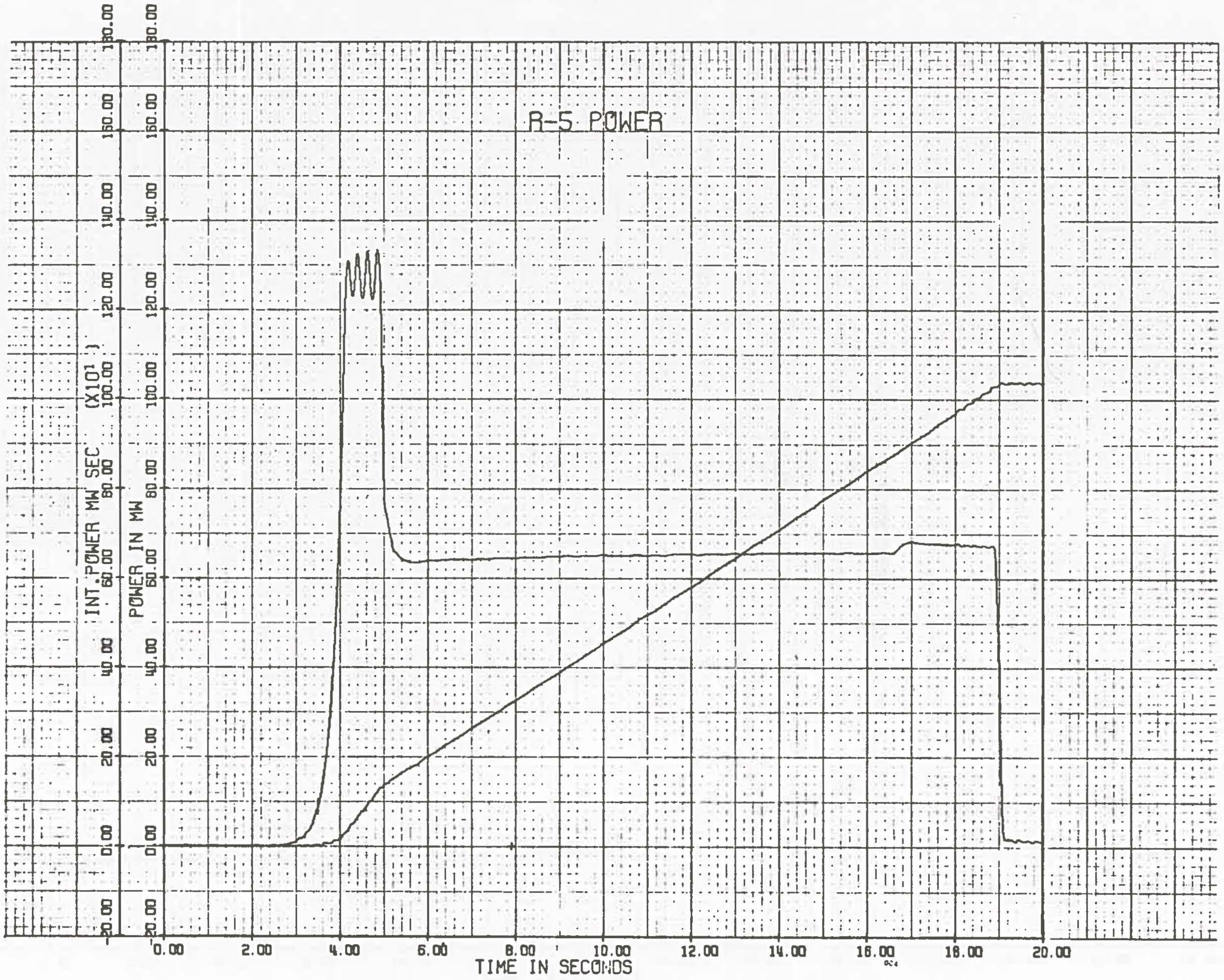

Fig. D1 R5 TREAT Power and Integrated Power.

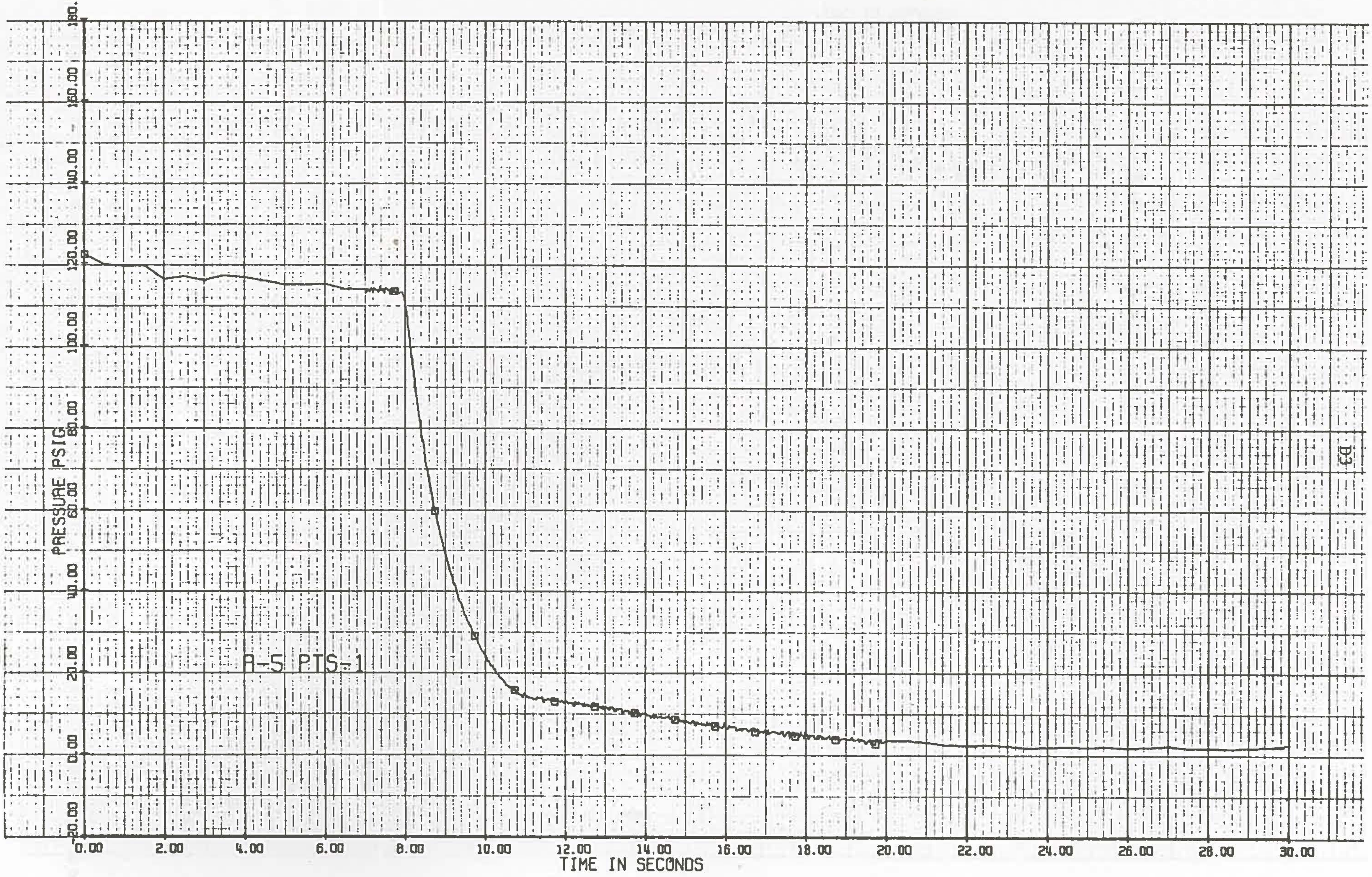

Fig. D2 R5 Supply Tank Pressure.

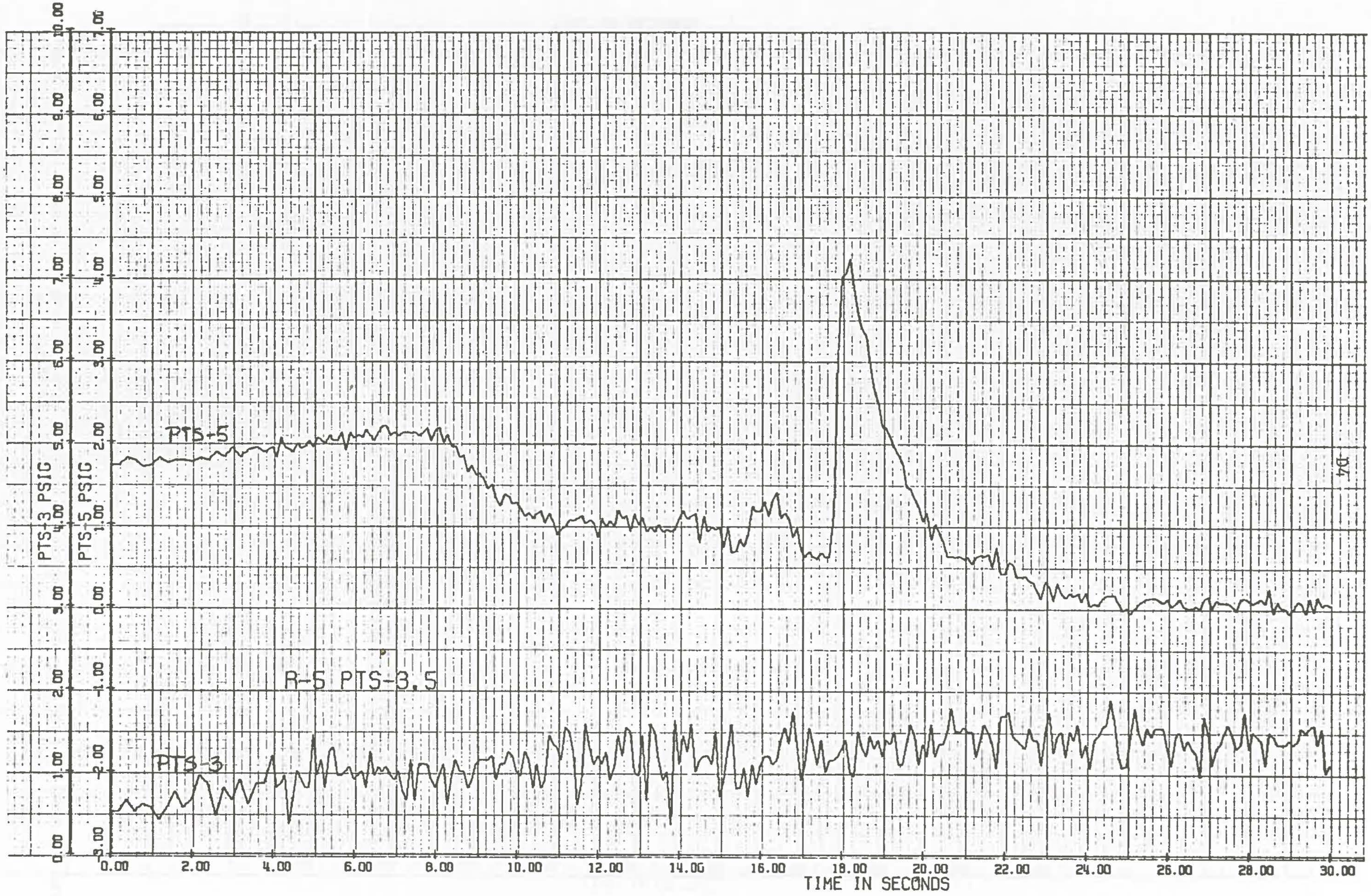

Fig. D3 R5 Plenum Simulator (PTS-5) and Discharge Tank (PTS-3) Pressure.

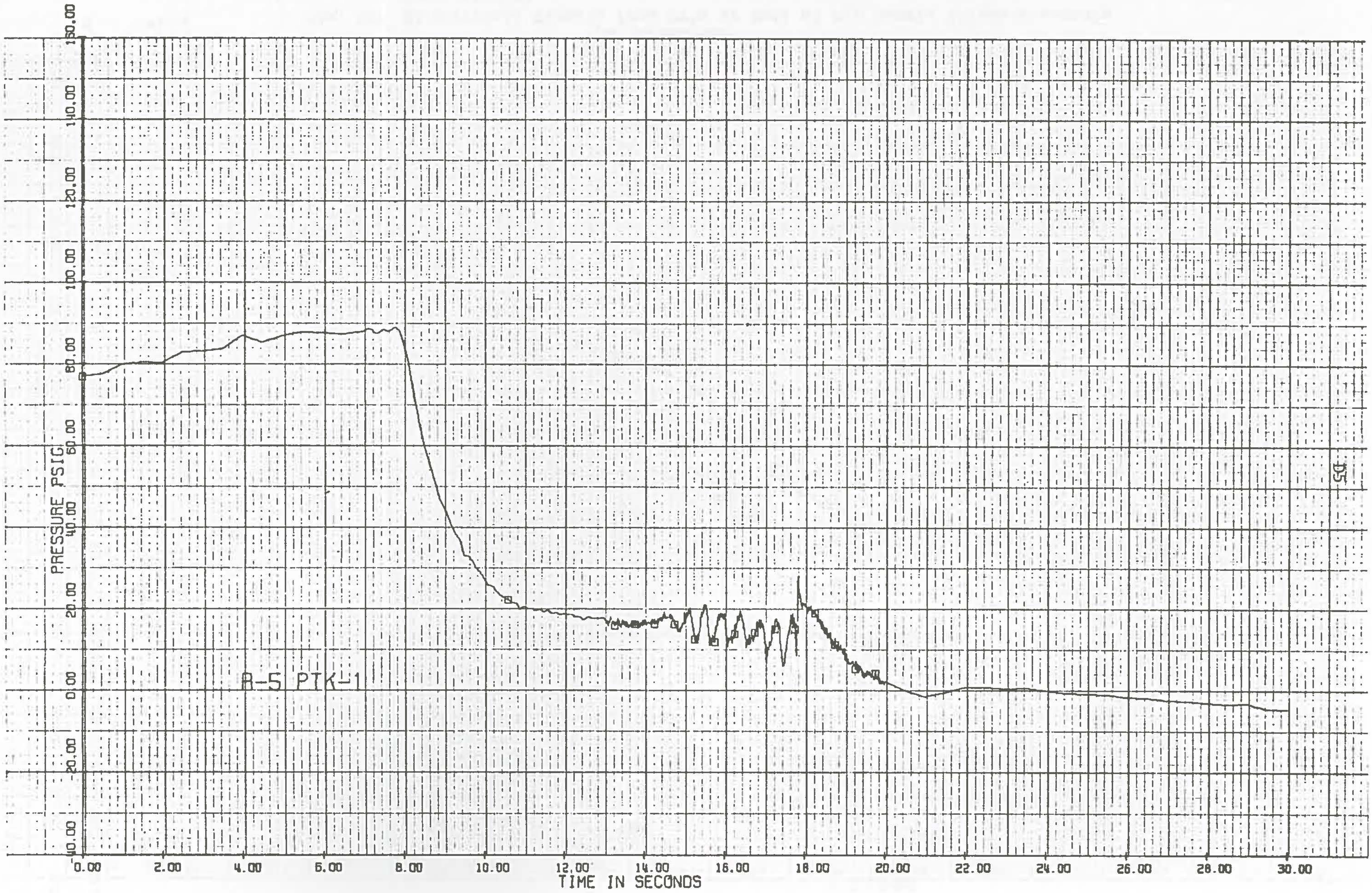

Fig. D4 R5 Pressure at Entrance to Pin Bundle.

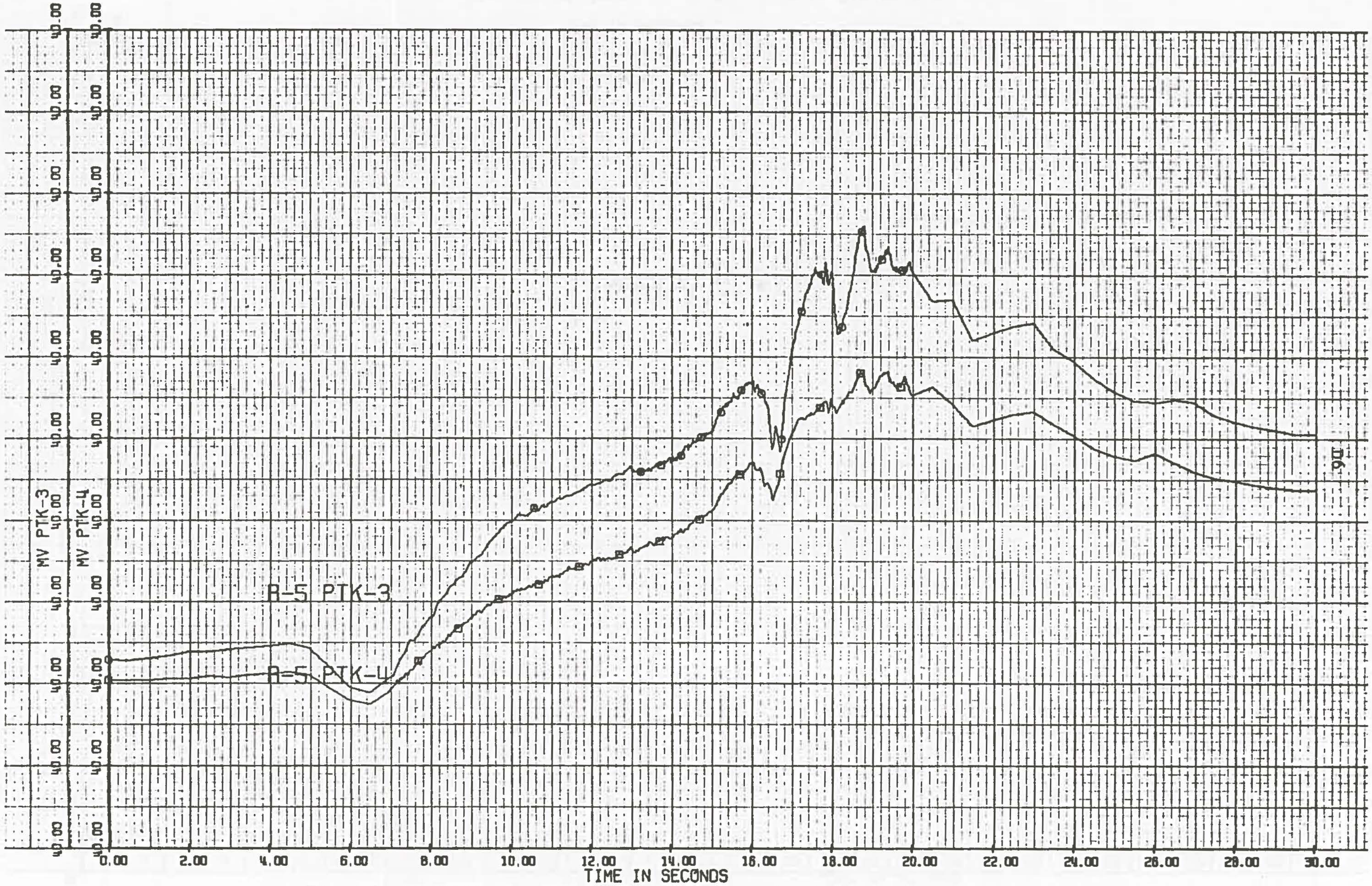

Fig. D5 R5 Millivolt Signals from PT's at Exit of Pin Bundle (Signals contain large effect).

1-24-74

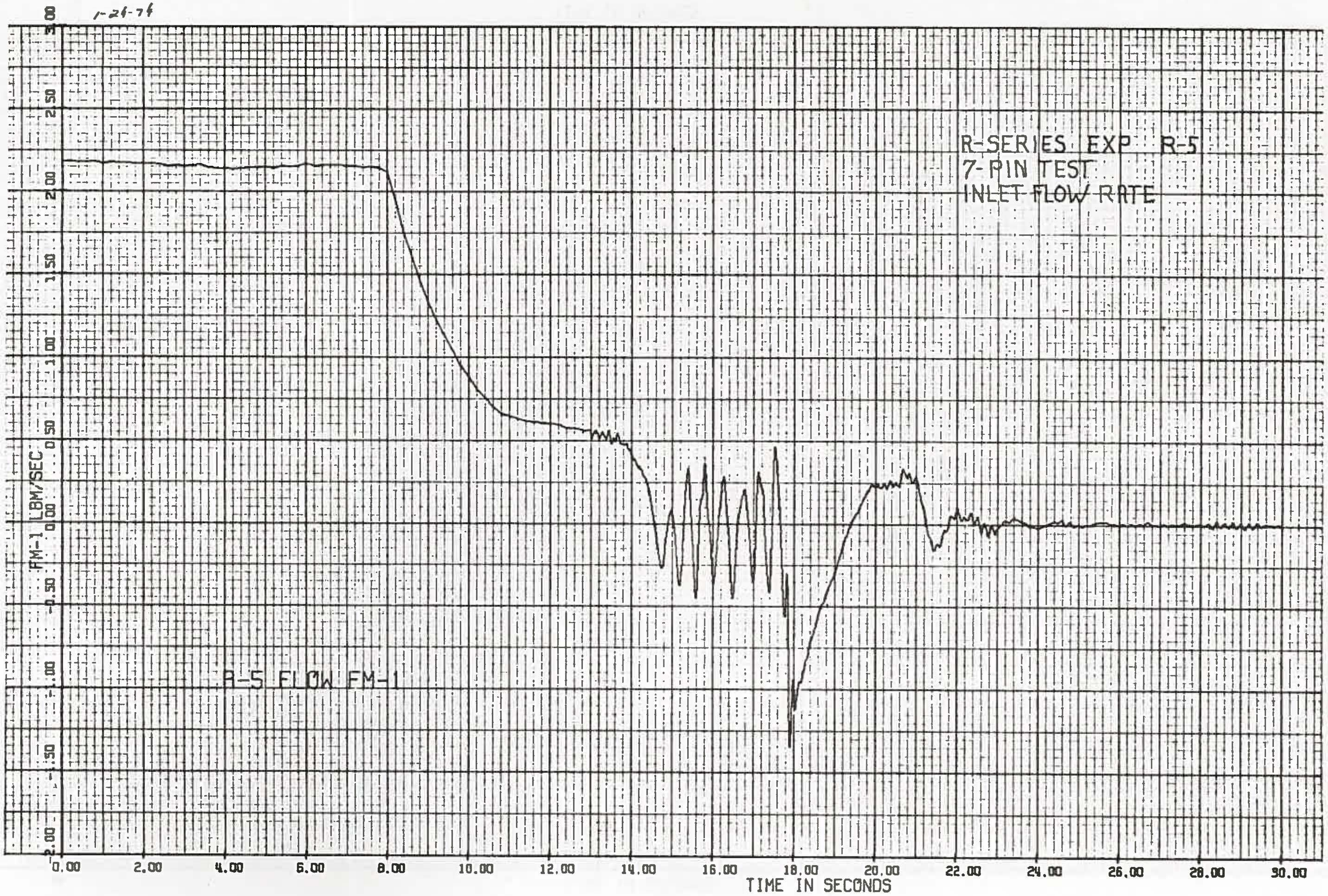

Fig. D6 R5 Sodium Inlet Flow Rate.

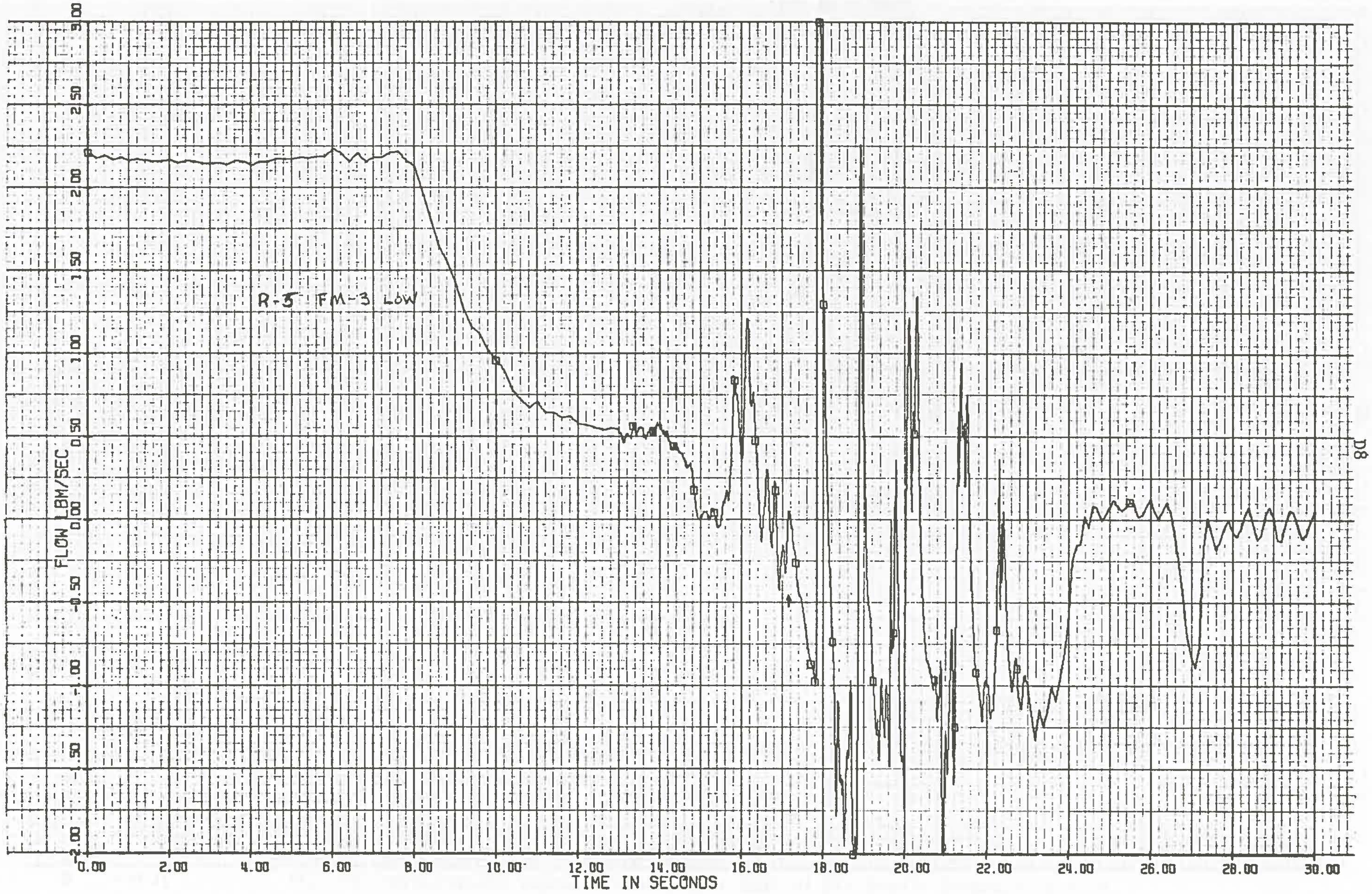

Fig. D7 R5 Sodium Exit Flow Rate.

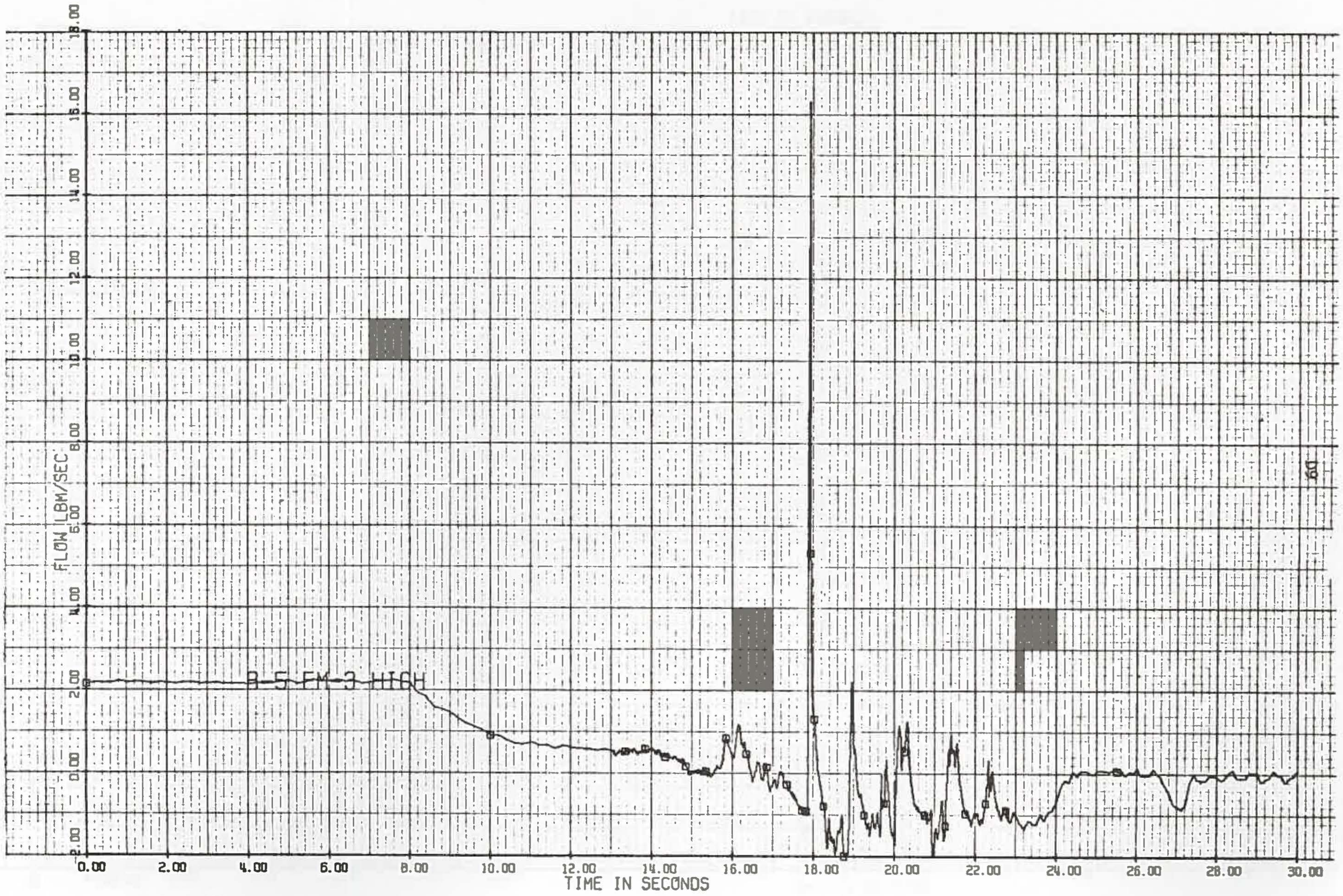

Fig. D8 R5 Sodium Exit Flow Rate on Compressed Scale.

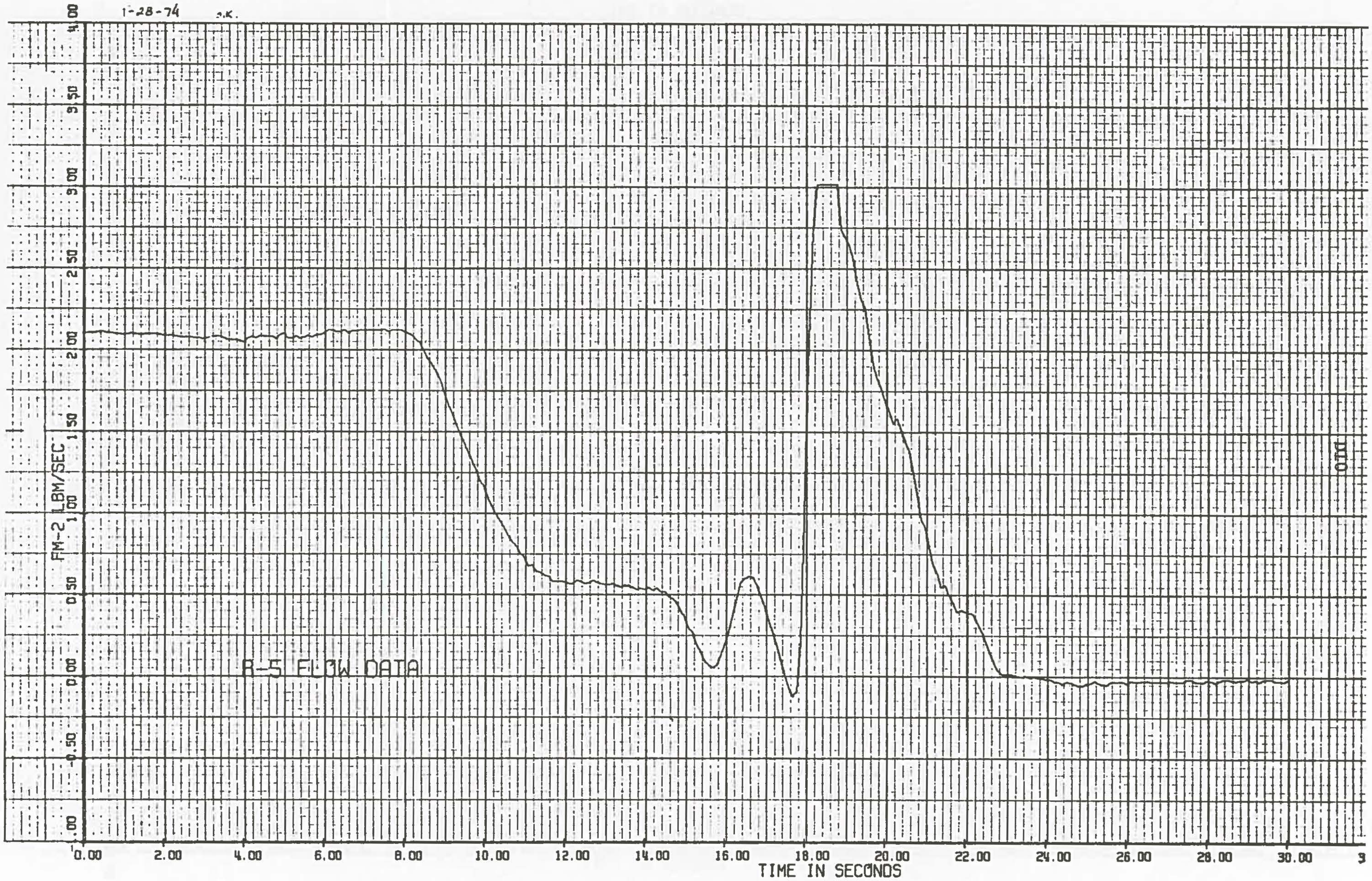

Fig. D9 R5 Plenum Simulator Discharge Flow Rate.

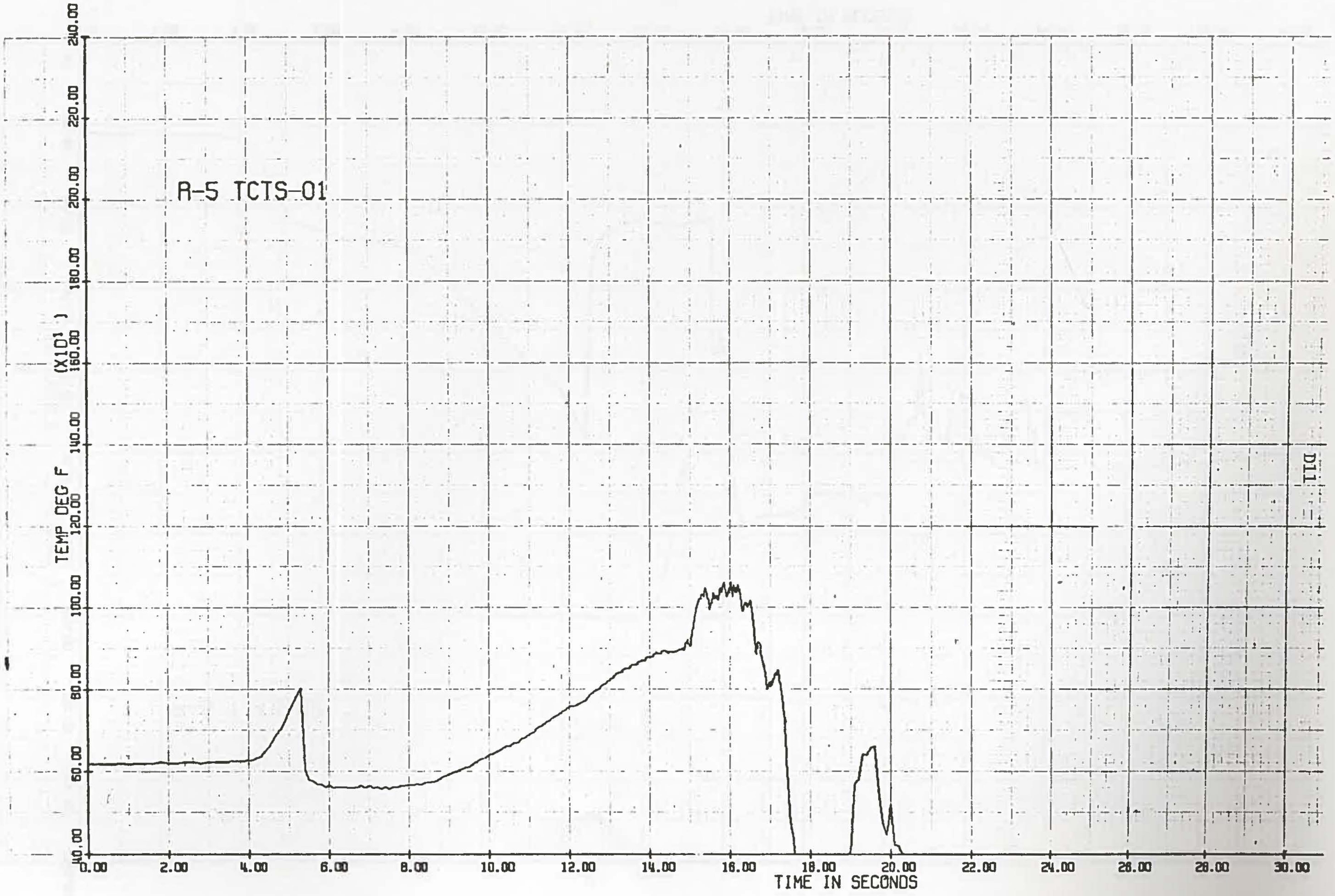

Fig. D10 R5 Flow Tube Temperature 30 cm (12 in.) above top of Active Fuel.

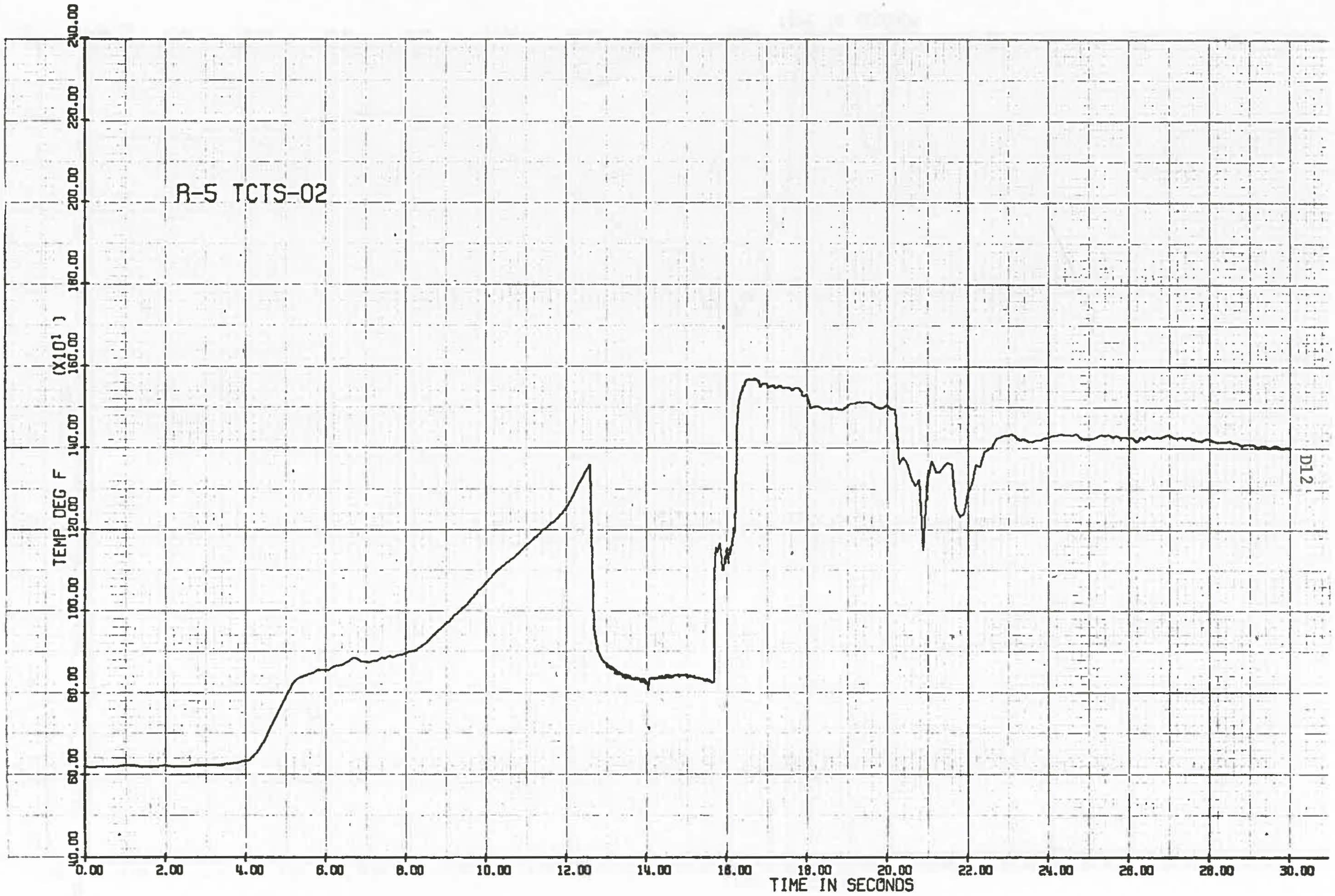

Fig. D11 R5 Flow Tube Temperature at 15 cm (6 in.).

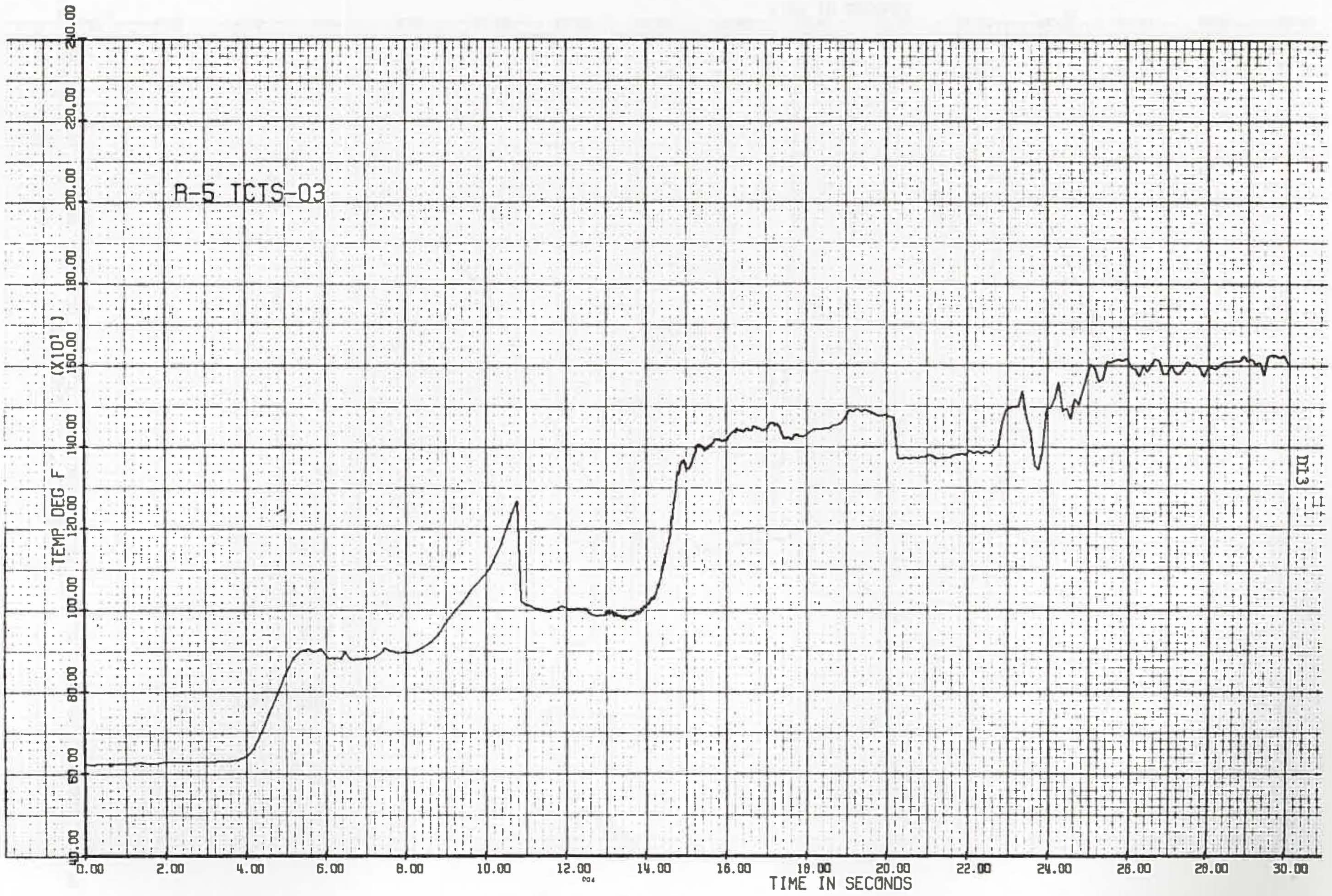

Fig. D12 R5 Flow Tube Temperature at 7.5 cm (3 in.).

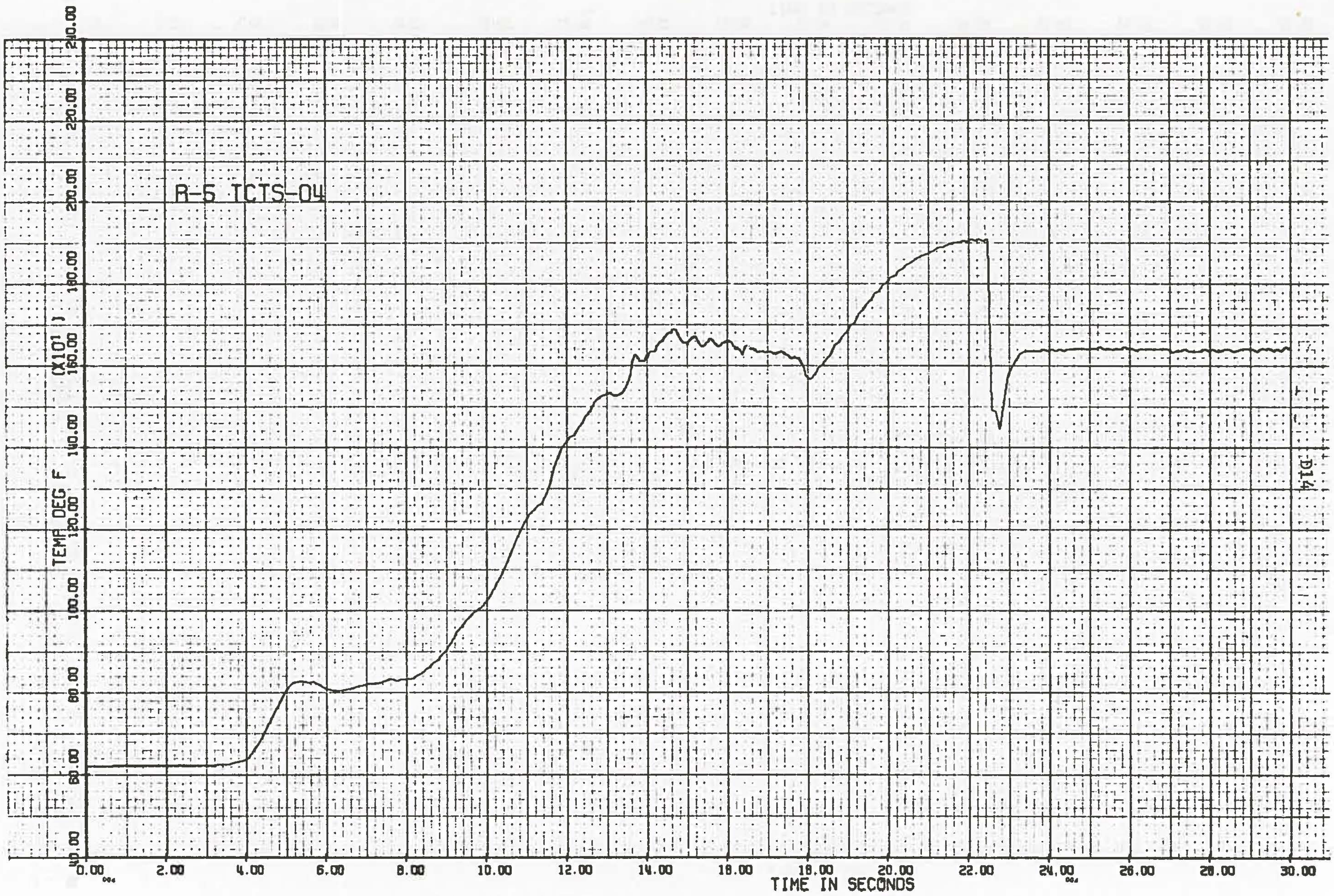

Fig. D13 R5 Flow Tube Temperature at 2.5 cm (1 in.).

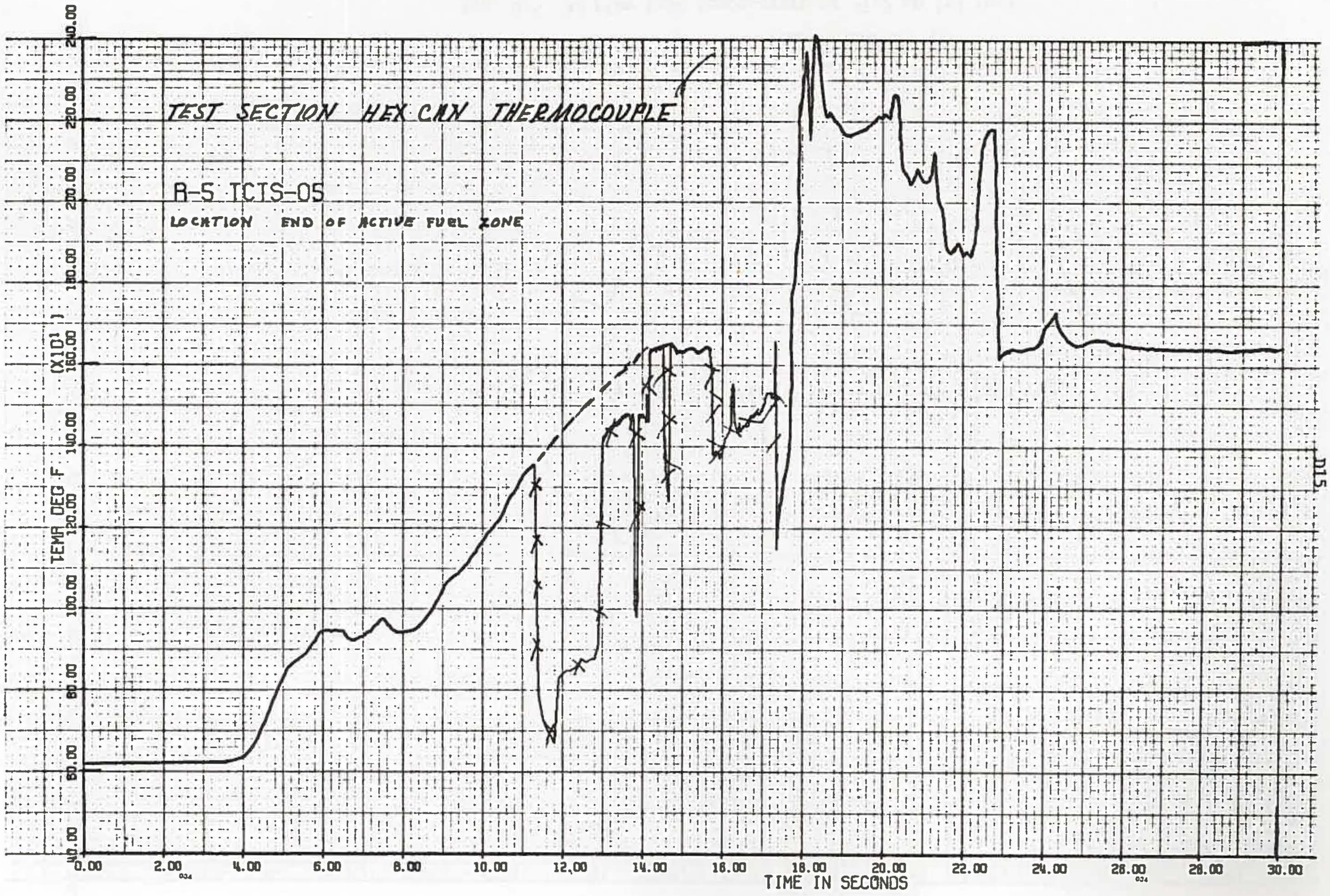

Fig. D14 R5 Flow Tube Temperature at top of Active Fuel, 0 cm.

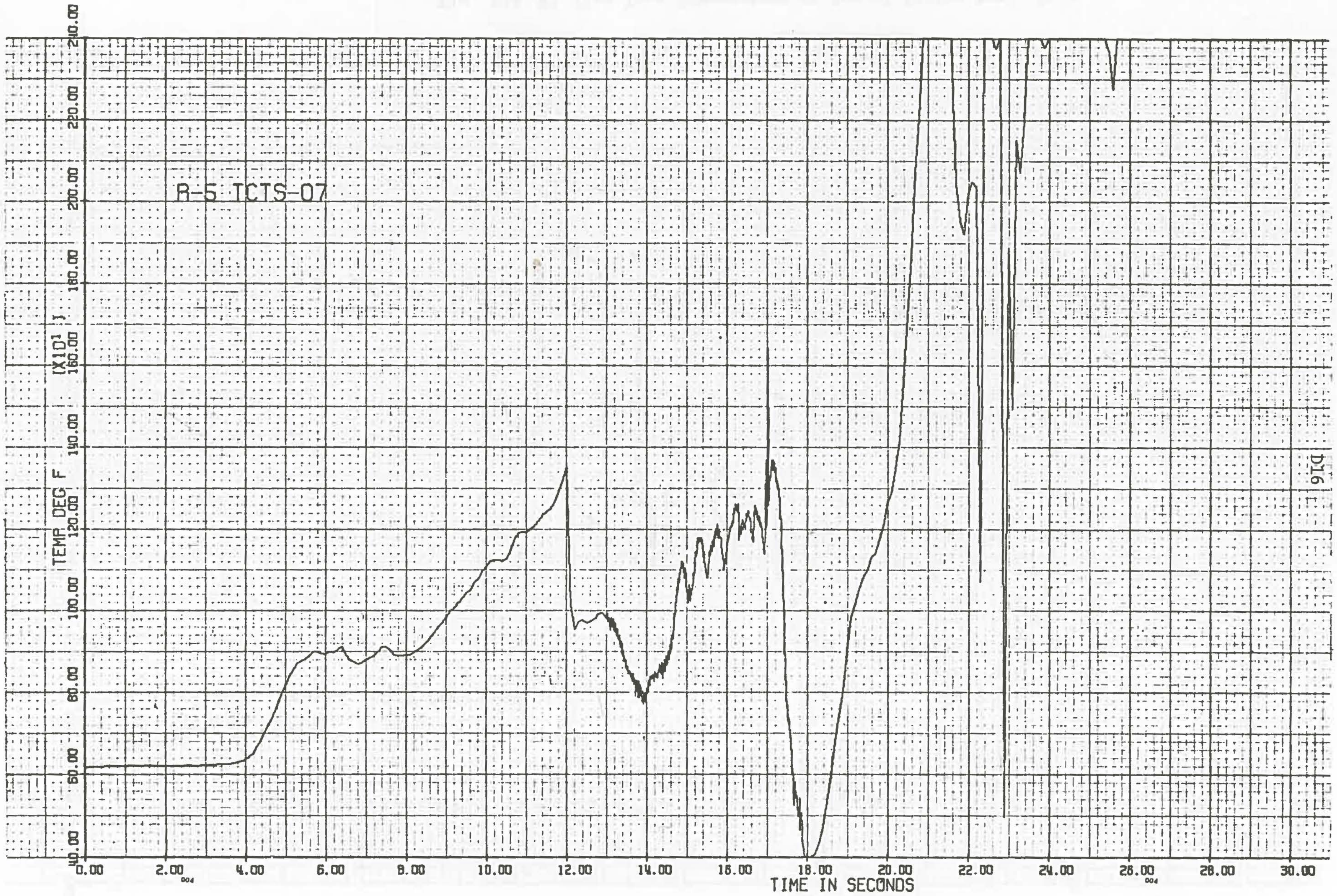

Fig. D15 R5 Flow Tube Temperature at -7.5 cm (-3 in.).

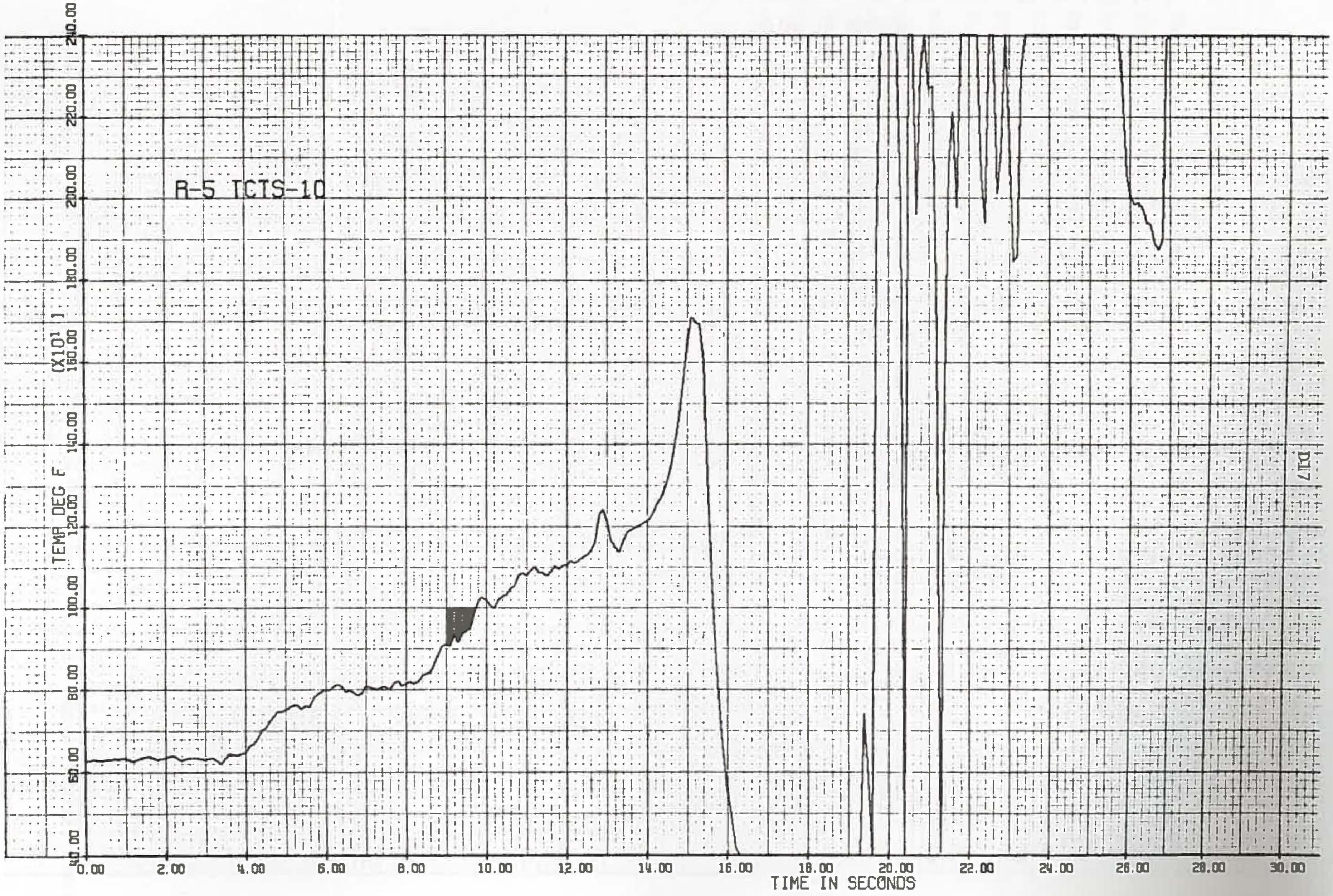

Fig. D16 R5 Flow Tube Temperature at Active Fuel Midplane, -45 cm (-18 in.).

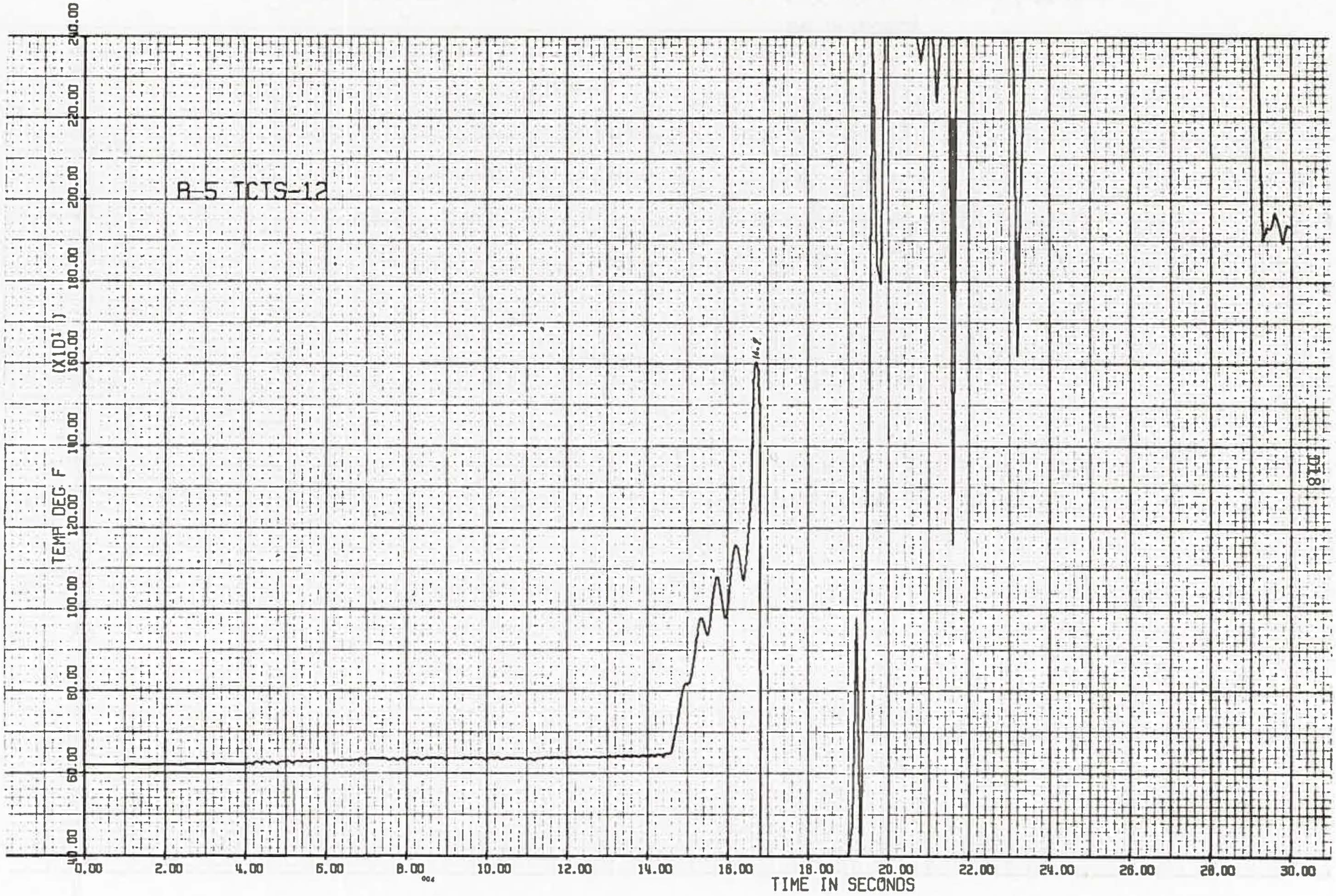

Fig. D17 R5 Flow Tube Temperature at Entrance to Active Fuel Region, -91 cm (-36 in.).

ACKNOWLEDGEMENTS

The authors gratefully acknowledge the many people who have contributed to the success of this effort. The work was under the direction of H. K. Fauske, Manager, Coolant Dynamics Section. The cooperation and assistance of J. F. Boland, L. J. Harrison and their staff at TREAT played a major role in the timeliness and success of the tests. Particular acknowledgment goes to R-series project members C. E. Miller, O. I. Hoff, H. J. Myers, G. M. Hauser, E. G. Erickson, G. A. Lambert, and P. M. Tschamper. R. I. Martell performed the preliminary posttest examination at ANL-W. J. C. Florek assisted with the MSD posttest metalographic examinations. A DeVolpi and his coworkers were responsible for the hodoscope fuel motion monitoring. G. Trahey provided valuable assistance by way of his Quality Assurance duties. The authors also acknowledge the helpful guidance of J. F. Marchaterre and C. E. Dickerman. The manuscript was prepared by K. Wagner; figures were prepared by T. Lucitt and his staff.

REFERENCES

1. F. E. Dunn, et. al., "The SAS3A LNFBR Accident Analysis Computer Code," ANL/RAS 75-17 (1975).

2. L. E. Robinson, et. al., "The Mark-II Integral Sodium TREAT Loop," TANSAO 13, 254 (1970).

3. J. J. Barghusen, et. al., "Fuel-coolant Interaction Effects During Transient Meltdown of LMFBR Oxide Fuel in Sodium-filled Piston Autoclave TREAT Tests S2 to S8," ANL/RAS 74-13 (1974).

4. R. E. Henry, et. al., "Single-pin Expulsion and Reentry Test," TANSAO 16, 180 (1973).

5. C. E. Dickerman, et. al., "Status and Summary of TREAT In-pile Experiments on LMFBR Response to Hypothetical Core Disruptive Accidents," ASME Symp. on Thermal and Hydraulic Aspects of Nuclear Reactor Safety, Atlanta, GA (1977).

6. R. E. Holtz, et. al., "Final Report on TREAT Test R3, A Single-pin Loss-of-flow Experiment, ANL-77-54 (1977).

7. B. W. Spencer, et. al., "TREAT Loss-of-flow Safety Experiment R6," TANSAO 21, 287 (1975).

8. R. E. Holtz, et. al., "TREAT Loss-of-flow Safety Experiment R7," TANSAO 22, 424 (1975).

9. B. W. Spencer, et. al., "TREAT Loss-of-flow Safety Test R8 with Pressurized FTR Fuel Pins," TANSAO 24, 269 (1976).

10. R. E. Holtz, et. al., "The R-series In-TREAT Test Apparatus," TANSAO 19, 238 (1974).

11. B. W. Spencer, R. E. Henry, and B. G. Jones, "System Hydraulic Effects on Fuel Sweepout in the Hypothetical TOP Accidnet," TANSAO 30, 444 (1978).

12. R. E. Hnery, personnal communication.

13. Y. Okamoto, et. al., "Hydraulic Performance in Rod Bundles of Fast Reactor Fuels Pressure Drop, Vibration, and mixing coefficient," IAEA-SM0130/5.

14. R. E. Holtz, personnal communication.

15. B. W. Spencer, et. al., "Final Report on R-series Power Calibration (R8CAL) for 7-pin LOF and TOP-type LMFBR Safety Experiments in TREAT," ANL/RAS IPR Rept. (1975).

16. F. L. Yahhee and G. Dragel, "An Ultrasonic Trepanning Technique for Radial Sampling Ceramic Fuel Pellets for Fission Analysis," TANSAO 19, 263 (1974).

REFERENCES (Con'd)

17. A. DeVolpi, personnal communication.

18. R. E. Henry, et. al., "A Sodium Expulsion Test in a 7-pin Geometry," Proc. ANS Conf. Fast Reactor Safety, USAEC-CONF-740401)1974).

19. M. A. Grolmes, G. A. Lambert, and H. K. Fauske, "Flooding Correlation for Sodium and Clad Motion in Subassembly Voiding," TANSAO 18, 209 (1974).

20. R. E. Henry, et. al., "Cladding Relocation Experiments," Proc. Intl. Meeting on Fast Reactor Safety and Related Physics, USERDA-CONF-761001 (1976).

21. G. Hoppner, et. al., "TREAT R5 Loss-of-flow Experiment in Comparison with SAS Pretest Analysis," TANSAO 18, 213 (1974).

22. H. K. Fauske, "Transient Liquid-metal Boiling and Two-phase Flow," Progress in Heat and Mass Transfer, 1, 451 (1973).

23. B. W. Spencer, et. al., "Cladding Motion and Blockages in R-series Safety Experiments," TANSAO 19, 238 (1974).

24. M. A. Grolmes, R. E. Henry, and H. K. Fauske, "Consideration of Sodium Boiling in LMFBR Subassemblies from 7-pin Test Data," TANSAO 19, 240 (1974).

25. M. A. Grolmes, et. al., "R-series Loss-of-flow Safety Experiments in TREAT," Proc. ANS Conf. Fast Reactor Safety, USAEC-CONF-740401 (1974).

26. B. W. Spencer, et. al., "Summary and Evaluation of R-series Loss-of-flow Safety Tests in TREAT," Proc. Intl. Meeting Fast Reactor Safety and Related Physics, USERDA-CONF-761001 (1976).

27. T. E. Kraft, et. al., "Simulations of an Unprotected Loss-of-flow Accident with a 37-pin Bundle in the Sodium Loop Safety Facility", accepted for presentation at the International Meeting on Fast Reactor Safety, Seattle, WA (1979).

☆U.S. GOVERNMENT PRINTING OFFICE:1979—651-990